2014

Effect of manganese content and microstructure on the susceptibility of x70 pipeline steel to hydrogen embrittlement

Daniel Hejazi
University of Wollongong

EFFECT OF MANGANESE CONTENT AND MICROSTRUCTURE ON THE SUSCEPTIBILITY OF X70 PIPELINE STEEL TO HYDROGEN EMBRITTLEMENT

A thesis submitted in fulfilment of the requirement for the award of the degree of

DOCTOR OF PHILOSOPHY

from

UNIVERSITY OF WOLLONGONG

by

Daniel Hejazi

B.Eng. (Materials Science and Engineering)

M.Eng. (Materials Science and Engineering)

School of Mechanical, Material and Mechatronic Engineering

2014

Thesis Certification

I, Daniel Hejazi, declare that thesis, submitted in fulfilment of the requirements for the award of Doctor of Philosophy, in the School of Mechanical, Materials and Mechatronic Engineering, University of Wollongong, is wholly my own work unless otherwise referenced or acknowledged. The document has not been submitted for qualifications at any academic institution.

Daniel Hejazi

August 2014

Table of Contents

Abstract

A wide range of ferrite-based microstructures were produced for high strength pipeline steels with standard X70 (1.2 wt.%) and lowered MX70 (0.5wt.%) Mn content. These include as-processed X70 and MX70 strips, as well as X70 transfer bar in the as-processed and normalised conditions. In addition, simulated coarse grain heat affected zone (CGHAZ) microstructures were produced. The main objective of the research was to establish and rationalise the differences in hydrogen pick-up and susceptibility to hydrogen embrittlement (HE), both under three point bending (TPB) of notched hydrogen-charged samples and tensile testing of tubular samples pressurized with hydrogen. A particular concern was whether the susceptibility to hydrogen induced cracking (HIC) was compromised by design of a lower Mn steel meeting X70 mechanical property specifications.

The effects of electrolytic hydrogen charging on surface and internal damage, as well as fracture toughness, were studied in relation to grain size, microstructure, composition and the type and distribution of non-metallic inclusions and precipitates. The X70 steel consistently exhibited higher J_Q fracture toughness values (derived from TPB tests) than the MX70 strip, both before and after hydrogen charging.

Electrolytic hydrogen charging experiments on thin strip samples (about 1 mm thick) indicated that the most rapid formation of surface blisters and HIC occurred for the banded ferrite-pearlite microstructures of the as-processed strip, followed by equiaxed TB ferrite-pearlite microstructure in the normalised condition, and then by the as-received TB sample with a ferrite-bainite microstructure, no blistering was observed in the heat affected zone (HAZ) samples for up to 24 hours charging.

In terms of measured diffusible hydrogen content after charging, the equiaxed (normalised) microstructure showed the lowest diffusible hydrogen content, followed by the banded ferrite-pearlite microstructures, the quasi-polygonal ferrite with bainite microstructure and finally the HAZ samples. In relation to residual hydrogen monitored after its release from stronger traps, the HAZ microstructures exhibited the lowest hydrogen content; followed by the equiaxed (normalized TB) microstructure; the quasi-

polygonal ferrite and bainite microstructure of the as-received TB; and the banded ferrite-pearlite microstructures of the as-received strip steels.

HIC in these charged samples often initiated from oxide particles and propagated mainly along intragranular paths, and also along ferrite/pearlite interfaces. The role of ferrite grain size in HIC was also evaluated and it was confirmed that microstructures with an intermediate average ferrite grain size (46 μm) exhibit higher residual and diffusible hydrogen contents than samples with lower and higher grain sizes.

The plastic behavior of the X70, MX70 and normalized TB samples was investigated by tensile testing of tubular specimens under 10 MPa hydrogen gas at 25, 50 and 100˚C, and 10 MPa argon at 25˚C for reference. The results showed that X70 steel is more susceptible to hydrogen embrittlement by external gaseous hydrogen charging than MX70, an opposite finding to the J_Q results obtained from TPB.

It is therefore clear that evaluation of HE can depend on the method of testing, particularly the presence/absence of a notch and the whether the hydrogen is internal or is externally supplied. The investigation overall established that there was no significant loss in resistance to HIC associated with the use of a medium Mn X70 alloy design.

Acknowledgments

I would like to express deepest gratitude to my supervisors, Prof. Elena V. Pereloma, Prof. Druce P. Dunne and Assoc.Prof. Andrej Calka. The successful completion of this thesis is due to their guidance, constant encouragement and stimulating discussions throughout the course of this work. In spite of her busy schedule, Elena always had time to listen to me and responded back at her earliest possible whenever I submitted any draft for corrections; she had been instrumental for seeing through that things are getting done. Druce was always available with his valuable metallurgy knowledge and experience and Andrej's laboratory equipments were every time easy to use with his great experimental information.

My sincere thanks to my colleagues Dr. Ayesha J. Haq, Dr. Nima Yazdipour and Dr. Andrew Carman for their support and valuable advice during my study. Ayesha was always ready to lend me a hand whenever I needed and had an answer to the problem. She had been optimistic and energetic throughout the whole thesis which gave me a lot of energy to continue.

I am also grateful to the help provided to me by Dr. Liang Chen (Gleeble simulations), Drs. Azdiar Gazder and Ahmed Saleh(mechanical testing), Dr Lenka Kuzmikova (hydrogen measurement over mercury), Dr. Mark Ried and Mr. Nick Mackie (SEM), Mr. Greg Tillman (metallography support and being a supporter by all the means) and Mr. Bob De Jong (Gleeble simulation). I greatly appreciate the attention I received from technical staff at the Engineering Workshop for sample preparations and also Mr. John Palinkas from BlueScope Steel research laboratories for hydrogen measurements. Additionally I thank Dr. Frank Barbaro, Dr. David Nolan, Mr. James Williams and Mr. Tom Schambron from BlueScope Steel for their support.

It was a real pleasure for me having great office-mates and friends around; Sujoy, Salar, Shideh, Matthew, Massoud, Michael and especially Ali.

I would like to thank Australian Research Council (APAI scholarship and LP0883546) and BlueScope Steel for financial support of this project.

Finally my deepest regards to my parents for their unconditional love and support and also the sacrifice and endurance of my wife, Paria.

List of Abbreviations

The following table describes the various abbreviations used throughout the thesis. The page on which each one is defined or first used is also given.
Acronyms that are used in some places to abbreviate the names of certain elements or chemical compounds are not in this list.

Abbreviation	Meaning	Page
AF	Acicular Ferrite	6
API	American Petroleum Institute	47
AR_3	Austenite to Ferrite Transformation Temperature	8
BF	Bainatic Ferrite	79
C-J	Crussard–Jaoul	50
CGHAZ	Coarse Grain Heat Affected Zone	viii
CLR	Crack Length Ratio	111
CSR	Crack Sensitivity Ratio	111
CTR	Crack Thickness Ratio	111
COD	Crack Opening Displacement	45
DC-J	Differential of Crussard–Jaoul	50
E_i	Embrittlement Index	144
EDS	Energy Dispersive X-ray Spectroscopy	3
EPMA	Electron Probe Microanalysis	17
FATT	Fracture Appearance Transition Temperature	9
FEGSEM	Field Emission Gun Scanning Electron Microscope	66
F/P	Ferrite Pearlite	24
GB	Granular Bainite	9
HACC	Hydrogen Assisted Cold Cracking	21
HAZ	Heat Affected Zone	viii
HE	Hydrogen Embrittlement	viii
HEAC	Hydrogen Environment Assisted Cracking	22

Abbreviation	Meaning	Page
HEDE	Hydrogen Enhanced Decohesion	135
HELP	Hydrogen Enhanced Local Plasticity	135
HIC	Hydrogen Induced Cracking	viii
IHAC	Internal Hydrogen Assisted Cracking	22
IG	Intergranular	22
J_I	The Crack Tip Energy Release Rate	41
J_{IC}	J_{IC} Fracture Toughness	41
J_Q	J_Q Fracture Toughness	viii
J-R	J resistance	43
K_{IC}	K_{IC} Fracture Toughness	43
M/A	Martensite / Austenite	3
MC-J	Modified Crussard–Jaoul	50
MX70	Medium X70 strip	viii
MVC	Micro Void Coalescence	22
n	Work Hardening Exponent	49
n_H	Hollomon's work hardening exponent	146
n_i	Instant Work Hardening Exponent	151
NTB	X70 Normalised Transfer Bard	4
PF	Pearlite Ferrite	7
QC	Quasi Cleavage	22
SBD	Strain Based Design	48
SCC	Stress Corrosion Cracking	9
SEM	Scanning Electron Microscopy	x
SSRT	Slow Strain Rate Testing	165
SZW	Stretch Zone Width	41
$t_{8/5}$	Cooling time from 800˚C to 500˚C	58
TB	X70 Transfer Bar	158
TMCP	Thermo Mechanical Controlled Processing	12
TPB	Three Point Bending	viii

Abbreviation	Meaning	Page
UTS	Ultimate Tensile Strain	47
X70	X70 rolled strip	viii
YS	Yield Strength	47
Δa	Crack Extension	41
$d\delta/d\varepsilon$	Work Hardening Rate	76

List of Figures

List of Tables

1 INTRODUCTION

Over the last twenty years in Australia the standard gas pipeline grade has moved from X52 through to the present X70, with the maximum operating pressure rising from 6.8 MPa to 15.3 MPa. Higher strength steels allow economic benefits through the use of thinner walled pipe, with lower costs for transport-to-site and field welding; and/or higher operating pressures with lower gas transportation costs[1].

Pipeline steels can hold small amounts of hydrogen because of absorption during pipe welding or as a result of environmental exposure. The presence of hydrogen increases the chance of hydrogen induced cold cracking (HIC) [2]. Once a steel pipeline is exposed to an acidic environment, its surface oxidizes and produces hydrogen. The adsorbed hydrogen atoms diffuse inside the steel and become trapped at certain microstructural features such as inclusions and interfaces between non-metallic inclusions and the steel matrix [3, 4]. If the trapped hydrogen reaches the critical concentration necessary for crack initiation, HIC can take place. The absorbed hydrogen atoms can also recombine and form molecules at inclusions, voids, grain boundaries and dislocations, resulting in pressure build up that can lead to blistering and cracking [5].

In recent years, there have been attempts to shift to lower Mn levels, in the range of 0.2-0.5%, to reduce centreline segregation. At these lower levels of Mn and at a given S level, formation of MnS from the liquid will take place closer to the solidification temperature and thus the particles are smaller in size [6].

Hydrogen-induced degradations have generally been investigated through the ex-situ testing of electrolytically hydrogen-charged specimens. However, the cathodic charging cannot fully replicate the damage caused by gaseous hydrogen in transportation pipelines. Thus, in this work for the first time effect of gaseous hydrogen charging on medium Mn X70 is investigated and the results are compared to the traditional electrolytic hydrogen charging. There was no information in the literature regarding the effect of temperature on the in-situ gaseous hydrogen charging. Thus, the effect of elevated temperature is also investigated, as pipeline could operate at the elevated temperature conditions.

It has been reported that as quenched martensitic microstructure has the least hydrogen embrittlement (HE) resistance, whereas tempered bainitic or tempered martensite structures

have the highest resistance [7]. Pearlitic microstructure sits between these two extremes. The most important elements that control the susceptibility to hydrogen embrittlement of a microstructure are the hydrogen permeability and hydrogen trapping ability of that microstructure. The coarse grain heat affected zone (hereafter refer as HAZ) next to the weld zone is also the critical region for HE [7-9]. The susceptibility to hydrogen cracking can also be related to the steel composition and the processing history as these factors affect non-metallic inclusions (size, morphology and type). Large inclusions such as elongated manganese sulfides and stringers of oxide increase the HIC susceptibility [10]. The concentration of impurities was found to increase the susceptibility of HIC [11].

As pipeline steels could have different microstructure in base metal, HAZ and weld metal, it is important to know how hydrogen affects these areas.

This study was conducted with the aim of investigating the effect of variable parameters on hydrogen embrittlement of X70 pipeline steels with standard (1.14 wt. %) and medium (0.5 wt. %) Mn content. The objectives of this investigation were:

- Assess the role of hydrogen on fracture toughness
- Evaluate the role of microstructure (phases present, grain size, precipitation) in HIC and HE;
- Assess internal and surface damage as a result of hydrogen charging
- Compare the effects of electrolytic and gaseous charging

To achieve this goal, a comprehensive data set of electrolytic and gaseous hydrogen charging has been utilised to assess the medium Mn steel and compare its performance with the standard X70 steel. As a major concern for the designing high pressure gas transmission pipelines made from high-strength steels is the control of long running ductile fractures, fracture toughness is measured to assess the hydrogen embrittlement.

1.1 Thesis Outline

Following this brief introduction, a review of the most recent studies on the hydrogen embrittlement of pipeline steels is presented in Chapter 2, with an emphasis on X70 pipeline. Chemical compositions of X70 steels and the effect of alloying elements, with focus on the role of Mn, are reviewed. The process of fabrication of pipeline steel

fromthermo-mechanically controlled processing in the mill to electric resistance welding (ERW) is explained. Mechanisms of hydrogen embrittlement, the role of precipitates, microstructure, grain size and strain rate on blistering and HIC are evaluated. A brief review on different hydrogen charging methods and hydrogen measurement techniques is carried out. Finally, fracture toughness calculations and work hardening models are discussed.

Chapter 3 presents the experimental procedure. This chapter begins with description of the chemical compositions and fabrication stages of two studied steels containing high and medium Mn content. The techniques used to prepare samples for three point bend (TPB) testing, Gleeble simulations, hydrogen diffusion and tensile tests are then outlined. The simulation of the HAZ structure using the Gleeble thermo-mechanical testing machine is then discussed. The techniques used for microstructure and fractography characterisation are described. In addition, the electrolytic hydrogen charging method used to introduce hydrogen into steels and hydrogen measurement techniques are explained.

Chapter 4 provides descriptions of the microstructures of X70 strip, X70 transfer bar, X70 normalized transfer bar and the HAZ in the as-received condition. In addition, data on grain sizes and hardness are provided. Chapter 4 continues with analysis of precipitates and inclusions present in both studied steels by means of optical metallography, scanning electron microscopy (SEM), energy-dispersive X-ray spectroscopy (EDS) analysis and X-ray mapping.

Chapter 5 begins with evaluation of electrolytic hydrogen charging conditions with respect to electrolyte current density, current, inhibitor and duration of charging. Based on the obtained data, an electrochemical hydrogen charging procedure has been developed. The four electrolytically charged microstructures are: as-received X70 strip with banded ferrite-pearlite microstructure; as received transfer bar of X70 steel with quasi-polygonal ferrite and granular bainite; normalised transfer bar of X70 with an equiaxed ferrite-pearlite microstructure; and simulated HAZ microstructure with coarse bainitic ferrite laths and martensite/austenite (M/A) islands. The chapter reports the measurement of the diffusible and residual hydrogen contents using the mercury and melt extraction methods. In addition, the role of microstructure in internal and surface damage (blistering) by hydrogen is

discussed. The chapter closes with an analysis of the nature of blisters and cracks based on the results from EDS and X-ray mapping.

In Chapter 6 the effect of electrolytic hydrogen charging on the fracture toughness of X70, MX70, normalised transfer bar (NTB) and their HAZ is investigated. Notched and fatigue pre-cracked samples were charged with hydrogen prior to TPB tests. The conditional fracture toughness J_Q was determined. The results are discussed in relation to grain size, microstructure, composition, fracture surface and the type and distribution of non-metallic inclusions and precipitates.

In Chapter 7, gaseous hydrogen embrittlement of X70, MX70, NTB samples and the ERW region of X70 steel were studied through tensile tests of sealed hollow cylindrical samples with 10 MPa hydrogen gas at 25, 50 and 100˚C. All samples were also tested under 10 MPa of argon for comparison. It is shown that 10 MPa hydrogen reduced the strength and ductility of all samples. Hydrogen tests at elevated temperatures demonstrated reduced strength but increased elongation compared to the room temperature tests. As the yield strength of the pipe is influenced primarily by work hardening during forming and expansion of pipes, the work hardening behaviour of the above steels was also investigated.

Chapter 8 presents discussion highlighting the contribution to the knowledge, general conclusions and suggestions for future work.

2 LITERATURE REVIEW

This Chapter begins by detailing typical compositions of pipeline steels and considers the effects of the alloying elements. The effect of thermo-mechanical controlled processing on pipeline manufacturing is also discussed. The review then focuses on factors underlying the concept of using a reduced Mn content in pipeline steel.

An overview of hydrogen embrittlement mechanisms, together with parameters affecting these phenomena, forms an important part of this review. In this context, different methods for hydrogen measurement and fracture toughness calculations are presented. Finally, the importance of work hardening parameters and various models for the work hardening behaviour of pipeline steels are discussed.

2.1 Compositions of X70 Pipeline Steel

The microstructure of API 5L-X70 welds can be a mixture of acicular ferrite (AF), grain boundary ferrite, Widmanstätten ferrite, bainite and ferrite with martensite/austenite (M/A) microconstituents. Use of a relatively high concentration (~>1 wt%) of Mn helps to refine and homogenise the weld microstructure [12].

When metals are joined by welding the material is heated above its melting point and then cooled down rapidly under conditions of restraint imposed by the geometry of joint. As a result of such a severe thermal cycle the original microstructure and properties of the region close to weld area are significantly changed. This volume of metal is known as the HAZ. The HAZ is conventionally divided into different sub-zones as illustrated in Figure 2-1 [13]. The part of the HAZ that experiences the maximum thermal shock is that closest to the molten weld bead and is called the HAZ. This region transforms rapidly from ferrite to austenite and back again and has a microstructure which has a high hardness and is susceptible to hydrogen embrittlement. Hydrogen cracking is mostly found in this region [14].

Ferrite is the main phase of these types of steel, but there is a series of possible ferrite morphologies. Ferrite can nucleate at austenite grain boundaries and grow in the form of packets containing parallel plates with the same crystallographic orientation. Ferrite can also nucleate heterogeneously on small intragranular non-metallic inclusions and grow in different directions. This kind of ferrite is referred to as acicular ferrite (AF) [15].

The presence of AF in the weld metal and HAZ is considered to be a desirable microstructure for steel pipelines because it is tougher and stronger than conventional ferrite-pearlite microstructures [16]. The higher strength and toughness of AF is due to its finer grain size and higher density of dislocations and sub-boundaries, which decrease the cleavage fracture unit and result in an irregular crack path that requires increased energy for crack propagation [17].

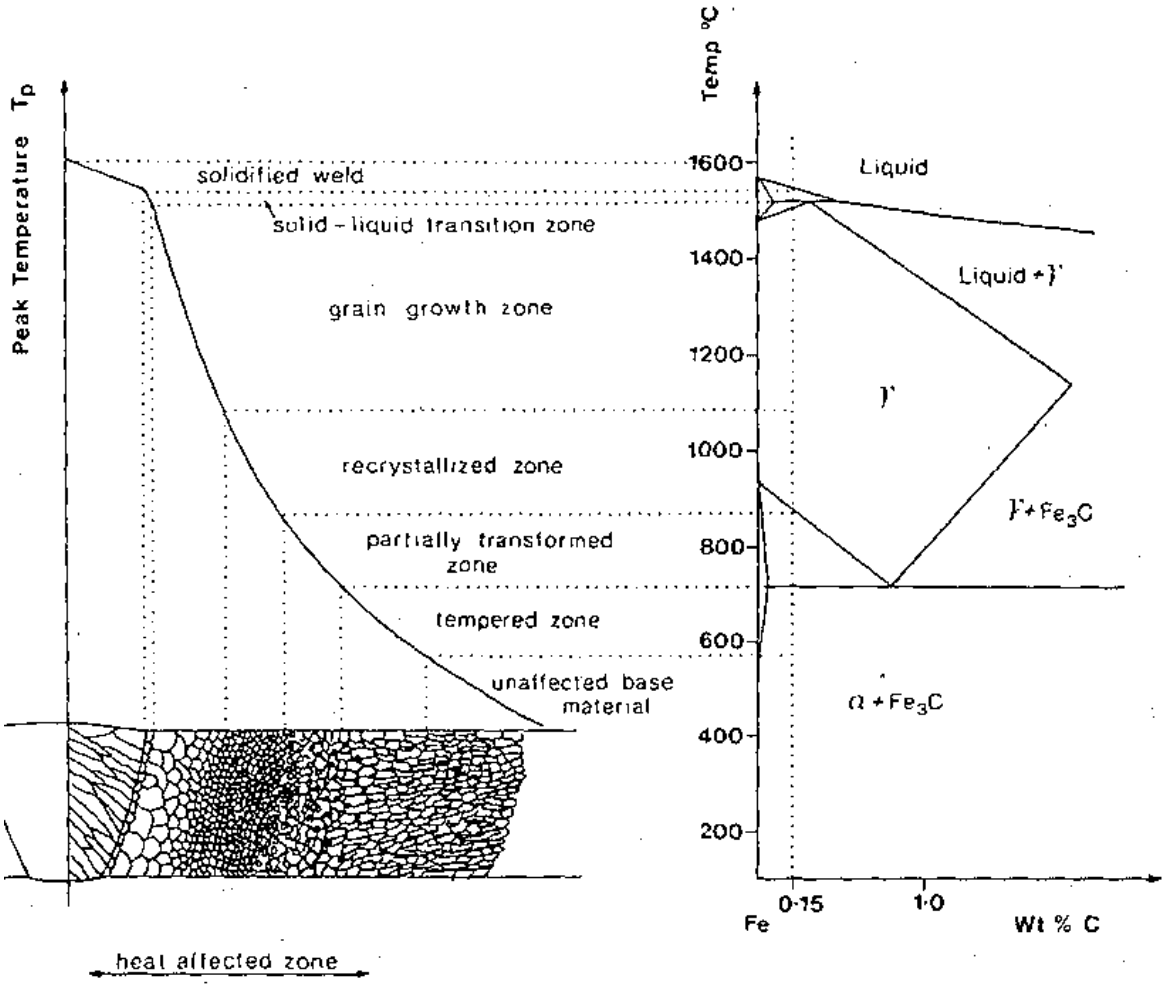

Figure 2-1 Schematic diagram of the various sub-zones of the HAZ for a welded 0.15 wt % C steel [13].

Polygonal ferrite (PF) forms at the highest temperatures in the transformation range and for the slowest cooling rates. It nucleates as grain boundary allotriomorphs and grows into roughly equiaxed grains with smooth and continuous boundaries under the scale of the light microscopy [17].

The volume fractions of AF, PF and the M/A microconstituent have a significant effect on steel strength. In the controlled hot rolling of pipeline steels, the volume fractions of these microstructures are determined by hardenability parameters and cooling conditions. The steel composition, the hot rolling schedule, and particularly the temperature range of finish rolling and the finishing reduction, control the hardenability of the steel [18].

2.2 Role of Alloying Elements

2.2.1 Manganese

Manganese is one of the most important alloying elements in pipeline steels because it combines with sulphur to form MnS. Sulphur is very harmful in steel and can cause hot shortness. Therefore, the addition of manganese and formation of MnS reduces the susceptibility of a steel to hot shortness [19]. Manganese is not only added to steel to improve hot working properties, but it can also increase the strength, toughness and hardenability. Manganese, like nickel, is an austenite forming element. As iron sulphide has a lower melting point than MnS, it tends to form along austenite boundaries in the absence of manganese and provides potential crack sites during hot working the addition of manganese improves [20]. The low carbon high manganese (Mn = 0.8-1.5%) approach to steel design is also based on manganese contributing solid solution strengthening, enhancing grain refinement and lowering the impact transition temperature. These changes are largely due to the effect of Mn of lowering the Ar_3 temperature (austenite to ferrite transformation temperature) [20]. A relatively high concentration of manganese helps to refine and homogenize the weld microstructure in X70 pipe-line steel [12].

2.2.2 Silicon

Silicon is one of the deoxidisers used in steelmaking. Silicon exerts a solid solution hardening effect on ferrite and is used to increase strength and toughness [19]. The rate of strengthening of low carbon steels by Si is higher in coarse-grained than fine-grained steels. However, silicon decreases the prior austenite grain size which leads to a fine ferrite grain size. Silicon up to 0.7 wt.% improves the impact behavior of steel [21]. Increasing the silicon content causes a decrease in the rate of recrystallisation as well as an increase in the strength of austenite due to the effect of solid solution hardening. The silicon increases both the A_{r3} temperature and also the activity of carbon in austenite [22].

2.2.3 Molybdenum

Molybdenum has a powerful effect on increasing the high-temperature strength and retarding grain growth at temperatures above the critical temperatures of steel [19]. Molybdenum increases the steel hardenability and improves its resistance to hydrogen embrittlement and stress corrosion cracking (SCC) in high sulphur content steels [23]. It has been reported that addition of 0.40 wt% Mo to low-carbon microalloyed steel results in slowing down the bainite transformation and reducing the B_s and B_f temperatures (bainite start and finish transformation temperatures, respectively). As a result, the microstructure of bainite becomes finer [24]. Also, the addition of Mo in the range of 0.82–0.88 wt. % results in a decrease of fracture appearance transition temperature (FATT) and an increase of impact toughness. Mo addition to steel promotes formation of AF and granular bainite (GB), but can also lead to the appearance of grain boundary ferrite (GBF) in weld metal [25]. Molybdenum retards the precipitation of Nb(CN) (niobium carbonitride) in the presence of high Mn levels. This phenomenon is due to the effect of molybdenum on the activity coefficients of niobium, carbon and nitrogen and the consequent increase of the solubility of carbonitride [26]. Molybdenum along with copper, chromium and nickel improves resistance to hydrogen embrittlement of high sulphur microalloyed steels in a H_2S environment by promoting the formation of fine precipitates, uniformly distributed in the matrix. These precipitates can trap hydrogen in the steel [23].

2.2.4 Niobium

Niobium is the main microalloying addition for stabilising carbon and has strong effects on austenite recrystallization and hardenability. Nb affects recrystallization by solute drag effect and strain-induced precipitation, as well as refines both the austenite and ferrite grain sizes [19]. The rate of initial transformation of austenite to ferrite in high niobium steels is reduced by the solute drag effect of niobium and the pinning effect of the Nb(CN) precipitates [27].

2.2.5 Vanadium

Vanadium is used to inhibit austenite grain growth at high temperatures and therefore results in finer grains and hence improved toughness and strength [19]. However, it has been found that steels that are precipitation hardened by vanadium carbide exhibit lower wear resistance than vanadium-free steels [28]. Vanadium and silicon have a significant influence on the microstructure and hardness of air cooled medium carbon low alloy steels. The volume fraction of proeutectoid ferrite increases with the level of silicon and the presence of vanadium carbonitrides, both of which control the austenite grain size and thereby promote grain boundary formation of ferrite on cooling [29].

2.2.6 Titanium

Microalloying with titanium can promote retardation of austenite recrystallisation and precipitation strengthening of ferrite. Titanium combines with carbon and forms titanium carbides, which are relatively stable and difficult to dissolve in austenite. It also promotes more efficient precipitation strengthening of ferrite in Mo-Nb steels. Titanium also removes nitrogen as TiN and can form precipitates of (Ti, Nb) (C, N) in austenite and ferrite. Titanium can improve the weldability and resistance to HAZ cold cracking because TiC precipitate particles (as well as MnS inclusions) are well known as effective traps for hydrogen atoms [18].

2.2.7 Chromium

Chromium is added to steel to increase its resistance to oxidation. Chromium also increases the hardenability and abrasion resistance of steel. Chromium in amounts above 4 wt. % in steel increases the corrosion resistance but decreases the weldability. Chromium can form Cr_3C_2 and other carbides that promote high wear resistance [19]. Chromium polarizes the cathodic polarization curve of pipelines, reduces the corrosion rate and helps to avoid the uneven corrosion of pipeline weldments [30].

2.2.8 Nickel

Nickel improves resistance to oxidation and corrosion. It also improves the toughness and impact resistance and solid solution strengthens the ferrite. Nickel also causes more and finer pearlite to form, so the pearlite is consequently stronger and tougher. This element has no adverse effect on welding [19]. The combined presence of Ni (2.03–2.91 wt.%) and Mo (0.7–0.995 wt.%) in the weld metal, leads to a high volume fraction of fine AF with good toughness [25].

2.2.9 Aluminium

Aluminium is added to steel as a deoxidising element. However, for more than 0.05 wt. % Al the toughness is reduced and, moreover, the deoxidizing function is saturated. Aluminium tends to form aluminium nitride (AlN) in austenite which has harmful effects on the hot ductility of different grades of steels. More than 0.02 wt.% of aluminium promotes precipitation of AlN rather than vanadium nitride (VN) in steel [31]. For the same level of aluminium and vanadium, VN precipitates are more soluble in austenite than AlN particles [32, 33]. This means the solubility temperature of VN is lower than that of AlN and that AlN is more stable. However, the existence of AlN in the austenite can cause harmful effects on the hot ductility of different grades of steels [34, 35].

2.2.10 Copper

Copper is generally regarded as a harmful element because it promotes hot shortness as a result of ductility loss at high temperatures (1100 ~1300 °C). Copper also causes surface defects during hot processing and it has been reported by Savov [36] that hot cracks begin to form in austenite during hot processing at copper contents above 0.2 wt.%. However, copper increases corrosion resistance, as well as the tensile strength of steel.

2.2.11 Phosphorus

One of the most common embrittling impurity elements in commercial low alloy steels is phosphorus. Phosphorus promotes grain boundary segregation and degrades the toughness. It also increases the tendency to cracking during welding. For this reason, the phosphorus content is usually specified to be lower than 0.015 wt% [37]. It has been reported that phosphorus in iron-phosphorus alloys increases the hydrogen activity and the hydrogen uptake in acid sulphate or sulphide electrolytes [38]. However, when present as a phosphate, it retards hydrogen uptake [38].

2.2.12 Sulphur

Sulphur is an unwanted element in steel which forms sulphide inclusions with manganese and other elements and degrades the toughness. Sulphur can segregate to grain boundaries causing intergranular fracture [20].

2.2.13 Nitrogen

Nitrogen has been classified as a crucial and low-cost alloying addition to steels. Nitrogen can be present in steel as an interstitial atom and as nitrides of iron, titanium, aluminium, niobium, vanadium, and some other alloying elements. Nitrogen, depending on the form in which it is found, can be either beneficial or harmful to the physical and mechanical properties of steel. Because it is a small atom, nitrogen (like carbon) can readily diffuse into the surface of steels and produce surface hardening [29].

2.3 Processing and Manufacturing of Pipeline Steel

2.3.1 Thermo-mechanical controlled processing (TMCP)

From a metallurgical aspect, correct control of the whole rolling process from slab reheating to coiling is necessary to develop the suitable strength and fracture toughness.

2.3.1.1 Slab reheating

The aim of this stage is to homogeneously heat the slab to obtain complete solution of niobium carbonitrides. Treatment conditions should be controlled carefully for each steel grade as solution of micro-alloying elements depends on the soaking temperature and time. The target slab reheating temperature is usually 1250°C. Consistent slab heating inside the walking beam furnace leads to uniform mechanical properties from coil to coil [18].

2.3.1.2 Rough rolling/coil box

The rough rolling stage is accomplished at temperature higher than 1030°C. The aim of this stage is to gain the finest possible recrystallised austenite grain size. To achieve this purpose, particles of (Ti,Nb)(C,N) are used to inhibit growth of recrystallised grains [39].

2.3.1.3 Finish rolling

The target during this stage of rolling is to accumulate rolling strain within the non-recrystallised austenite grains. The austenite non-recrystallisation temperature is typically below 1000°C for Mo-Nb steels. The transfer bar thickness is adjusted at this stage and normally is about 26-30 mm, if the final thickness of strip ranges from 5 to 10 mm. Therefore, the total reduction required for the transfer bar is about 70-80% [18]. On cooling after finish rolling, ferrite nucleation sites are abundant within the deformed austenitic structure and a very fine ferrite grain size is produced during the controlled cooling and in the final coiling stage.

The volume fractions of AF, PF and M/A constituent have a significant effect on strength of steel and these are determined by austenite hardenability factors and the cooling conditions. The austenite hardenability is mainly controlled by the levels of Mn, Mo, Nb and C (as reflected in the CEQ for the steel), together with the amount deformation and the temperature range of finish rolling [38].

2.3.1.4 Run-out table cooling/Coiling

Control of coiling temperature and cooling conditions are essential for achieving optimum strength in hot rolled strip since these parameters control ferrite grain refinement and precipitation hardening. Installation of high intensity laminar sprays on the run-out table assists in obtaining more consistent properties across the width and along the length of the coil. The availability of high rate cooling also helps to achieve better microstructural control [18] . Figure 2-2 presents a schematic image of steel processing from reheating furnace to hot roll strip coiling [40].

2.3.2 Effect of TMCP on pipeline steels

Lowering the finish rolling temperature below the Ar_3 temperature extensively increases the strength of the hot strip. Pipe tensile strength often varies from the strip tensile strength, which depends upon the level of work hardening and the Bauschinger effect developed during pipe forming. The outer layers of the pipe wall are subjected to a tensile stress whilst the inner layers experience a compressive stress. The resulting final pipe strength depends upon the combination of effects from these tensile and compressive stresses (i.e. work hardening vs. the Bauschinger effect). After forming the strip into the pipe, the strength decreases due to the Bauschinger effect. In order to counteract this effect molybdenum is added to more easily obtain the higher strength levels required for high strength pipe steels, such as X70 and X80. The amount of the Bauschinger drop in different Mo-Nb steels, for a constant pipe thickness/diameter (t/D) is a function of the Lüders elongation as shown in Figure 2-3 [18].

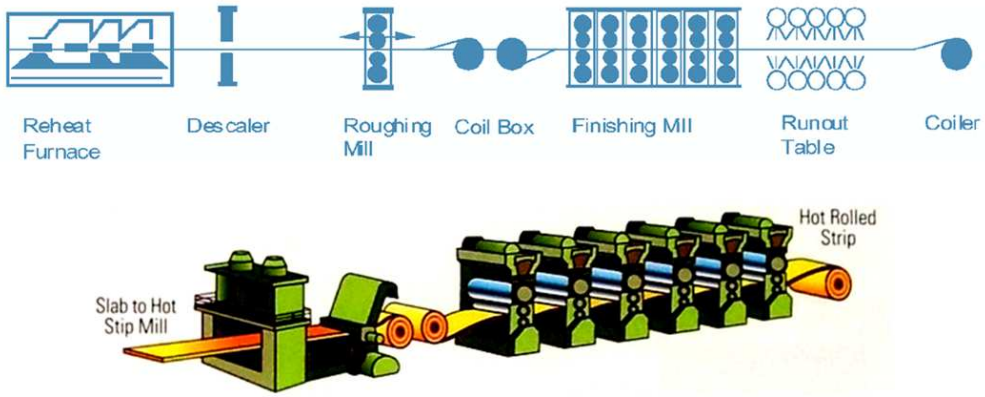

Figure 2-2 Making steel from reheating furnace to hot roll strip coiling [40].

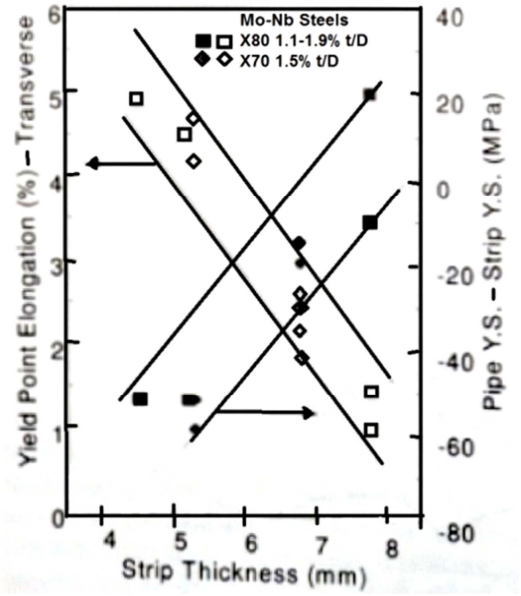

Figure 2-3 Relationship between Lüders elongation (Yield point elongation), strip thickness and Bauschinger drop (Pipe Y.S-Strip Y.S) for X70 and X80 pipeline steel [18].

2.3.3 Electric resistance welding

ERW is usually defined as “a process of forming a seam by electric-resistance or electric-induction welding” [41]. The ERW process starts with uncoiling the hot-rolled strip produced through TMCP and deforming it plastically, in the direction transverse to the rolling direction to form it into the shape of a tube. These steps are implemented without heating. After deformation to a tube shape, the edges of the tube are forced together by pulling or pushing through a pair of C-shaped rolls so that an electric current

can be applied to the edges to weld them together. The final stage is the application of postweld heat treatment to normalize the pipe microstructure [41, 42].

The low frequency current that was originally used for seam welding of pipe has been replaced recently by the use of high frequency current. The ERW welds are stronger and locally thicker than the pipe material [43]. Figure 2-4 presents a schematic diagram of ERW process from hot strip uncoiling to welding.

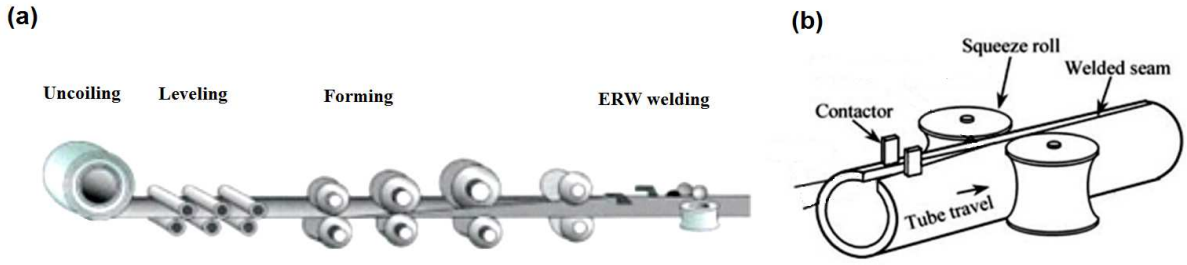

Figure 2-4 (a) Schematic diagram showing pipe forming from uncoiling to ERW [40]; and (b) details of the ERW stage [42].

2.4 Metallurgical Aspects of Manganese in Steel

2.4.1 Basic concept of low manganese approach

Improved properties in some high strength steels are possible as a result of a reduction in the manganese level of the steel. The enhancement is obtained mostly due to the changes in the size and type of sulphide inclusions that form at low manganese contents along with a reduced level of centreline segregation [1].

Manufacturers of pipeline steels around the world generally consider that the optimum manganese level is about 0.8 - l.5 wt. %. Recently, attention has been focussed on a shift in manganese level to about 0.20 - 0.50 wt. % in an attempt to reduce the effects of segregation and also the cost of comparatively expensive steelmaking processes required to produce ultra-low sulphur levels. At these levels of manganese and at a constant sulphur level, creation of MnS inclusion from the melt will take place closer to the solidification temperature and hence the MnS size is smaller. In addition, the solubility of MnS in austenite and delta ferrite is higher [44]. These factors result in the average

size of the MnS particles being smaller in low Mn steel than in high Mn steel. The smaller MnS inclusions are also less elongated by hot rolling and consequently, through-thickness bendability, ductility and fracture toughness are improved. More recent investigations show that titanium, chromium, copper and niobium have increased sulphide forming capacities as the activity of manganese is reduced. These compositionally modified sulphides are less plastic during hot rolling than MnS and potentially less harmful to the steel. The small size, morphology and behaviour of these sulphide inclusions under strain are advantageous for fracture toughness [1].

The segregating trend of Mn in the centreline region of the steels with different Mn levels is presented in Figure 2-5a which is based on Electron Probe Microanalysis (EPMA). Figure 2-5b shows the reduced extent of centreline segregation at low Mn levels compared to high Mn levels, as measured by EPMA [6].

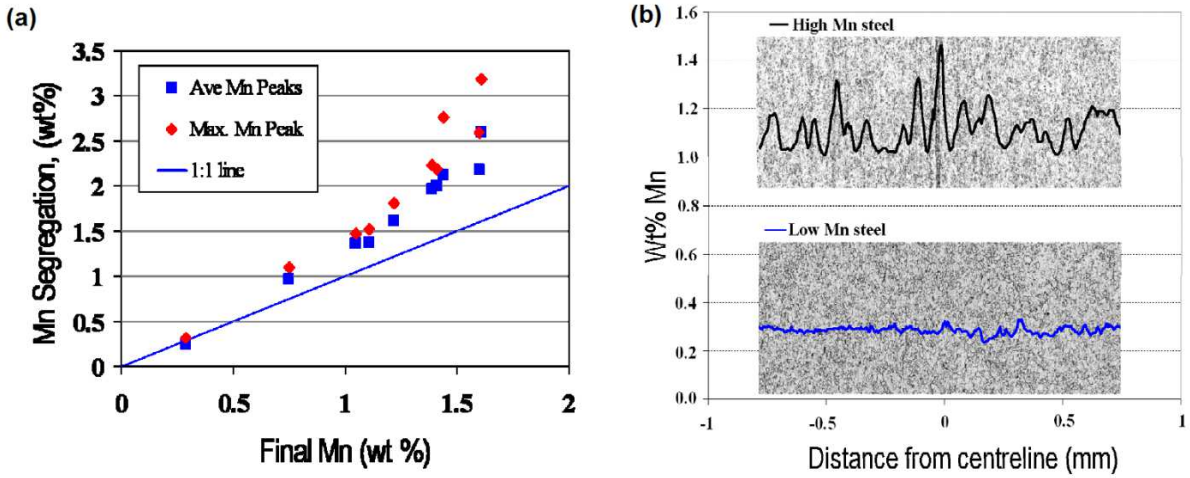

Figure 2-5 (a) Effect of Mn content on average and peak segregation levels in centreline segregation regions of various hot rolled strip steels as measured by EPMA and (b) X-ray line scans across the centreline regions of high and low Mn hot rolled strip samples [6].

For TMCP steels produced for pipeline applications, strengthening by Mn is mainly augmented in steels up to X65 grade by the addition of Nb. However, for higher strength grades (e.g. X70 and X80) the addition of other alloying elements, such as Mo and Cr, is also required. Mo is a key hardenability improving element in pipeline grades like X70, but it is an expensive alloying element. The addition of Cr in hot rolled steels must be controlled to avoid precipitation of Cr carbides during slow coil cooling and also to avoid forming oxides with high melting point on the weld-line of ERW pipe steels [1].

2.4.2 Low manganese alloy design in pipeline steels

The anomalous centreline area microstructures and elongated MnS inclusions in high manganese pipeline steels can have harmful effects on the mechanical properties of the ERW pipelines produced from centre slit strip. In order to address the requirements for weld line toughness in small diameter pipes, the low manganese alloy approach has been investigated to overcome the adverse effects of centreline segregation on ERW weld line toughness. The ERW weld line Charpy toughness requirements can be much more easily accomplished by the reduction in the centreline segregation banding and the size and shape of the MnS inclusions. The general pipe body toughness of these steels is also improved at a given S level, because of the smaller, less elongated sulphide inclusions. Figure 2-6 schematically shows how low manganese contents extensively reduce the harmful effects of anomalous microstructures occurring in the strip weld zone where the segregation band is diverted towards the plane of the weld as a result of the ERW process [1].

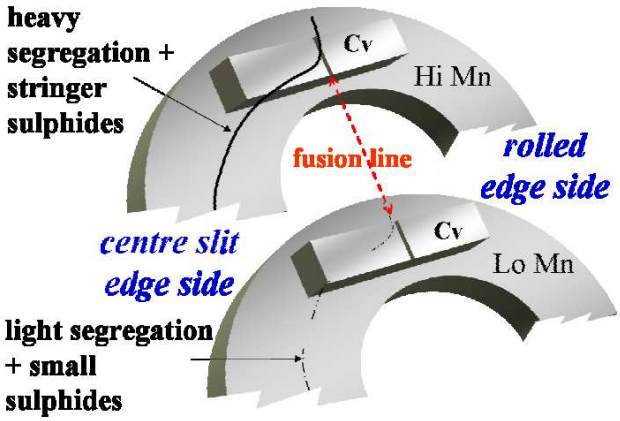

Figure 2-6 Schematic representation of ERW pipe ring sample showing reduced effect of centreline segregation and sulphide inclusions on weld line Charpy toughness[1].

The AF-PF balance is an important contributing microstructural factor in controlling the strength and toughness properties of low Mn X70 steels. Thicker strips accordingly require careful balancing of top versus bottom cooling sprays to minimise microstructural variations. Resistance to both brittle and ductile fracture propagation are prime requirements for pipeline steels. Modern low carbon alloy designs combined with the high deformation levels in non-recrystallisation temperature range and the high cooling

rates achievable on hot strip mills ensure the base strip and resultant pipe body has an extremely high resistance to brittle fracture. From plant and laboratory trials to date, a level of Mn nearer to 0.5% rather than 0.3% would appear to be more amenable for achieving the necessary low temperature toughness for pipeline steels particularly for thicknesses above 6mm [1].

2.4.3 Effect of TMCP variables on pipe yield strength

The major metallurgical and process drivers for optimising and controlling the strengthening components in Mo-Nb steels are schematically represented in a causal tree diagram such as Figure 2-7.

2.5 Hydrogen Embrittlement

Development of high-strength pipeline steels used for transportation of oil and gases has resulted in considerable cost savings. However, one of the most important considerations in their usage is their susceptibility to hydrogen embrittlement.

It was reported by Wang et al. [45] that buried underground pipeline steels, which are used for natural gas transportation, absorb hydrogen from the localized corrosion and cathodic protection. When the hydrogen reaches a critical level in pipeline steel, they lose their strength and ductility. This phenomenon of the loss in ductility or strength is known as HE. It has been reported that more than a sixfold increase in the concentration of hydrogen can occur in the external surface of pipes after 1 to 2 years of service, with about a tenfold increase after 15 years. These amounts of hydrogen entering in the steel structure could induce cold cracking [45]. Therefore, close pipeline monitoring is required to detect HIC and to ensure reliability and safety [46, 47].

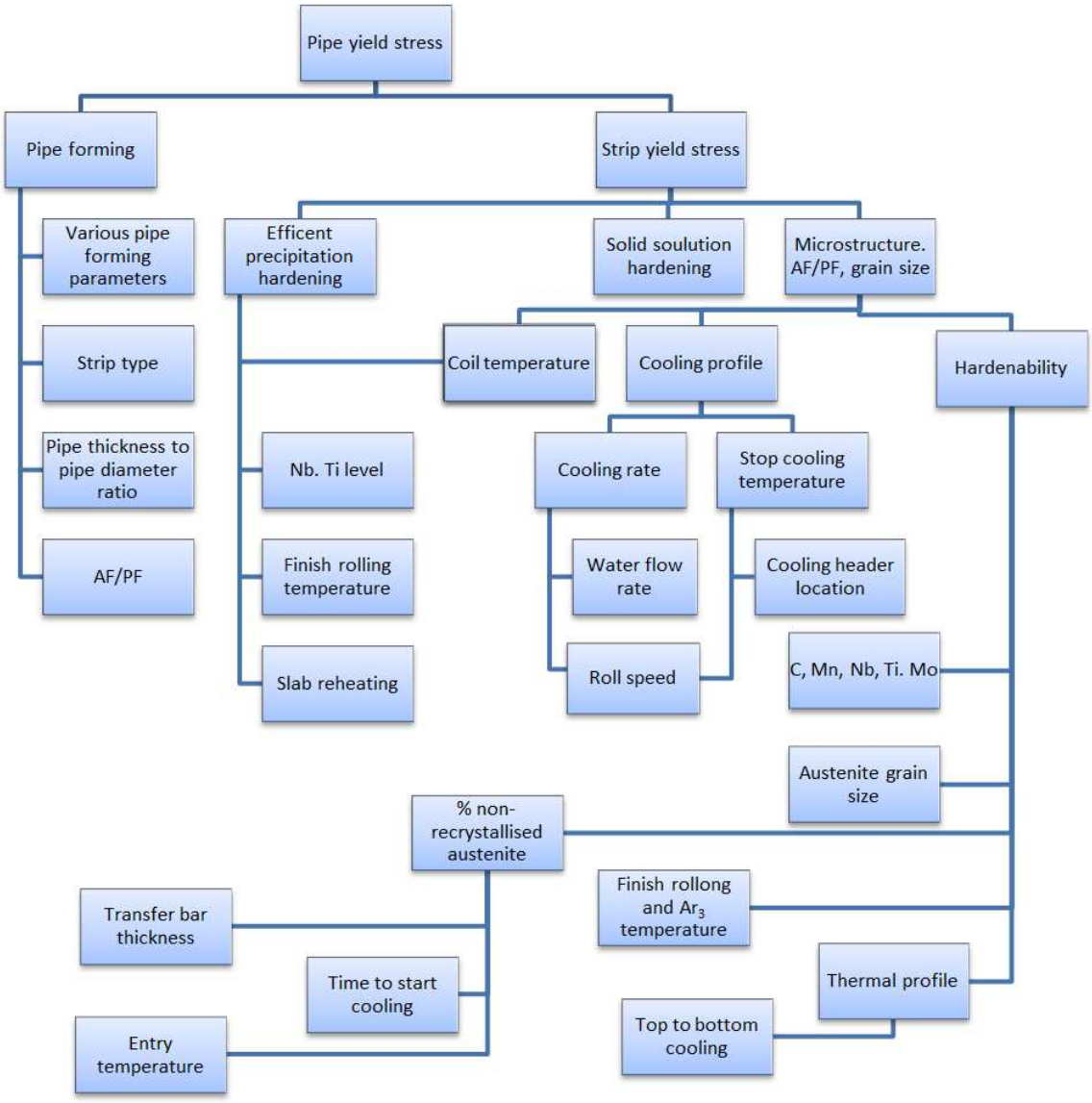

Figure 2-7 Causal tree for pipe yield strength [18].

In-service welding repair has a significant economic advantage of continuity of supply to customer without disrupting pipeline operation. There are two factors that make in-service welding difficult. Firstly the high cooling rate of the weld due to large heat loss from the pipe wall which will increase the hardness and susceptibility of the steel to HAZ cracking. The loss of material strength in the weld process is the second factor. Considering the gas pressure inside the pipeline, bursting can occur if the strength is reduced dramatically [48, 49]

2.5.1 Source of hydrogen

Hydrogen can be introduced to steel by absorption from a hydrogenous atmosphere during steelmaking, casting, welding, hot working, pickling, heat treatment and electroplating. Under service conditions, hydrogen can be picked up by exposure to hydrogenated liquids or gases. The presence of diffusible hydrogen of only a few ppm is known to cause steel embrittlement and induce cold cracking in steel. Microstructure is one of the key factors affecting the resistance of steel to hydrogen embrittlement [50].

2.5.2 Susceptible microstructures

It has been reported that high strength steels with the microstructure of bainite or martensite or M/A constituent are more likely to be subject to hydrogen embrittlement than mild steel. In general, the higher the strength or hardness of a steel, the lower is its resistance to hydrogen assisted cold cracking (HACC) [14].

Other key elements reducing the steel resistance to hydrogen embrittlement are:

- Inclusions or coarse carbides at grain boundaries;
- Coarse prior austenite grains,
- High dislocation density.

However, some microstructures also provide a number of irreversible hydrogen traps, such as incoherent interfaces between particles/inclusions and matrix. By taking hydrogen atoms out of circulation at low temperatures, these hydrogen traps can reduce the susceptibility of steel to HACC. It has been reported that in hot rolled, normalised and heat treated steels, nitrides or carbides can act as effective hydrogen traps. However, at sufficiently high hydrogen levels, the incoherent particle/matrix interfaces can act as nucleation sites for microvoid formation, leading to decohesion, crack initiation and failure [48, 49].

2.5.3 Effect of hydrogen on crack growth

Gangloff [51] has categorized the hydrogen effects on crack growth into the following two types: internal-hydrogen-assisted cracking (IHAC) and hydrogen-environment-assisted cracking (HEAC). Figure 2-8 is a graphical representation of the above two mechanisms. IHAC and HEAC are distinguished by the source of the hydrogen that causes cracking. In HEAC, atomic hydrogen is produced on the crack surface and diffuses to the crack tip. In IHAC, atomic hydrogen diffuses through the crystal lattice to the crack tip from other regions.

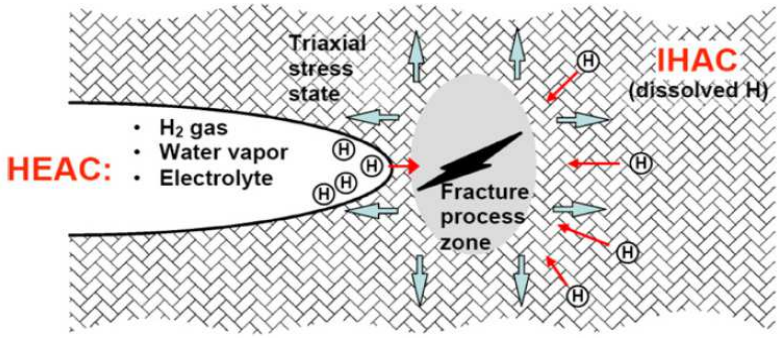

Figure 2-8 Schematic diagram, showing hydrogen embrittlement by both environmentally assisted cracking (HEAC) and internal hydrogen assisted cracking (IHAC) [51].

2.5.4 Hydrogen assisted cold cracking

HACC is a major failure mode in high strength steels. Beachem *et al.* [52] have recognised that hydrogen assisted stress corrosion cracking is very much related to HACC and that both are hydrogen embrittlement processes which demonstrate the same changes in fracture mode with changing stress intensity at the crack tip. They proposed a model for hydrogen embrittlement based on the increase in solubility of hydrogen with tensile stresses. Their model also classifies possible cracking mechanisms at the crack tip as micro void coalescence (MVC), quasi-cleavage (QC) and intergranular (IG) fracture, which all require microscopic plastic flow. Figure 2-9 schematically presents this transition in cracking mode and the contracting zone of plastic deformation.

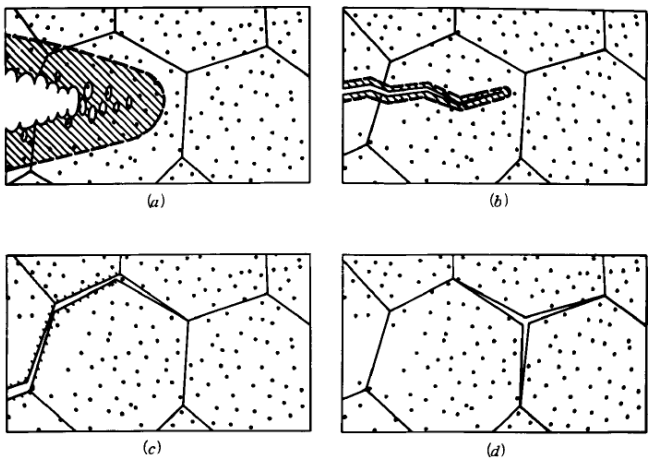

Figure 2-9 Schematic microstructural views of fracture by: (A) micro void coalescence (MVC); (B) quasi-cleavage (QC) at intermediate stress intensity; (C) intergranular fracture; and (D) intergranular fracture assisted by hydrogen pressure [52].

2.5.5 Hydrogen embrittlement mechanisms

There are several theories that have been proposed for hydrogen embrittlement. A summary of major models is as follows.

- The Zapffe model based on internal hydrogen gas pressure in microvoids [53];
- The Troiano model based on decohesion of atoms in lattice regions with a high hydrogen concentration [54];
- The Beachem model based on slip softening due to enhanced dislocation mobility [52].

In recent years, support has grown for the Beachem and Troiano models. There is also little doubt that precipitation of molecular hydrogen or methane in microvoids can exert sufficiently high pressures to enlarge the voids and initiate cracking [55]. Beachem pointed out that the essential action of hydrogen is to diffuse into the lattice ahead of the crack tip and to promote whatever plastic deformation processes the system displays [52].

Bastien and Azou [56] asserted that dissolved hydrogen can be carried along by moving dislocations and precipitated elsewhere. Concentration of hydrogen can also generate gas pressure and promote intergranular fracture, see Figure 2-9d.

It is frequently assumed that hydrogen increases the mobility of screw dislocations; decreases the mobility of edge components; promotes planar slip by inhibiting cross-slip of screw dislocations; and reduces the cohesive energy of the crystal lattice. Using these hypotheses McMahon [57] has argued that plastic rupture is enhanced at particle-matrix interfaces where hydrogen is irreversibly trapped and the concentration builds up by "sweeping-in" of reversibly trapped hydrogen by mobile screw dislocations. Further analysis of fracture at particle-matrix interfaces by Thompson and Bernstein [58] resulted in the proposed modes of fracture:

- Void growth and MVC;
- Particle fracture and/or decohesion, producing cleavage;
- Particle fracture/decohesion and void growth, leading to quasi-cleavage; and
- Fracture/decohesion/void growth associated with intergranular particles, resulting in grain boundary fracture.

Although decohesion at particle-matrix interfaces is expected to be prevalent in steels, particle fracture is far less likely to occur because of the relatively high fracture strengths and small sizes of the common carbide, nitride and oxide particles [58].

2.5.6 Effect of microstructural anisotropy on hydrogen permeation

A banded structure consisting layers of ferrite and pearlite typically exists in steel after controlled rolling. Banding causes a loss in tensile ductility and a drop in the impact energy. Hydrogen promotes the stepwise cracking of banded ferrite/pearlite (F/P) structural steel [59]. Lee *et al.* [60] studied the effects of anisotropy on the hydrogen diffusivity and cracking of AISI 4130 steel with a banded F/P. Hydrogen charging was carried out in a H_2S saturated saline solution and after 2 hours of hydrogen charging, more hydrogen was occluded for diffusion in the longitudinal direction than other directions. The smallest amount of hydrogen was occluded in specimens sectioned parallel to the through-face direction (i.e. parallel to the sheet normal, with the banding perpendicular to the direction of hydrogen entry). However, the hydrogen reached the same saturation level as for other directions after 8 hours of charging. These permeation results disclosed that the effective hydrogen diffusivity along the through-face direction was nearly an order less than that

along the longitudinal and transverse directions. The results show that the permeation flux of hydrogen along the longitudinal direction was higher than that along the transverse direction whilst hydrogen diffusivity was similar. Figure 2-10 presents the microstructure of banded F/P in an isometric view. The banding arrangement in the longitudinal direction exhibits a more regular structure than that in the transverse direction; pearlite blocks alternating with the ferrite layers are also found in the transverse F/P bands. Figure 2-11 compares the permeation of hydrogen in F/P banded and F/P random microstructure. The relative ease of hydrogen atom movement for these structures is shown schematically in this figure.

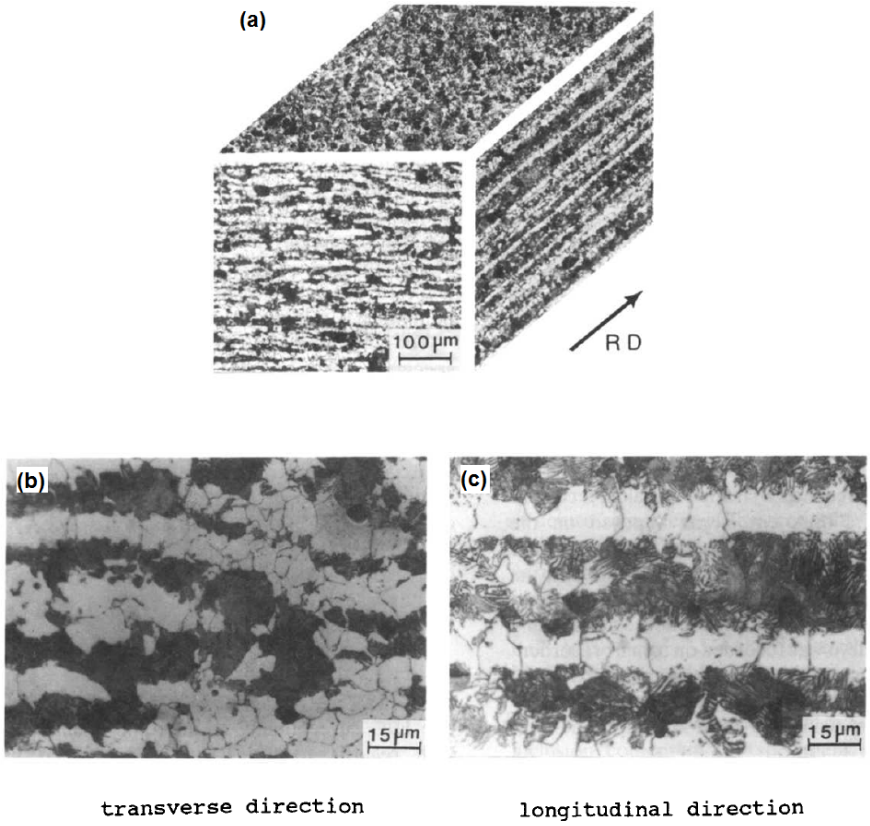

Figure 2-10 Micrographs showing (a) the banded F/P structure (b) microstructure in transverse direction and (c) microstructure in longitudinal direction [60].

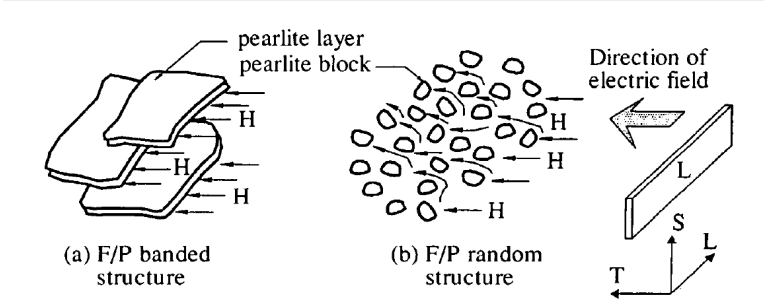

Figure 2-11 Schematic diagram indicating the paths of hydrogen movement in both random and banded F/P structures [61].

2.5.7 Hydrogen charging

Two different methods are often used to introduce hydrogen into the steel, namely gaseous charging [62] and electrolytical or cathodic charging. Cathodic charging represents the more severe charging process and therefore has more harmful effects on steel properties. Cathodic charging and corrosion reactions are the techniques commonly used for introducing hydrogen to specimens for measurement of hydrogen embrittlement [63].

In order to more accurately represent conditions that pipeline steels are likely to material experience in practice, gaseous hydrogen charging should be employed. Compared to electrolytic charging, gaseous charging provides a reduced concentration gradient more representative of what would be encountered in service [62].

2.5.7.1 Electrolytic (cathodic) hydrogen charging

During electrolytic charging, hydrogen exists in the electrolyte as positive ions (protons) and can be adsorbed as hydrogen atoms on the metal surface [64]. As a hydrogen atom is adsorbed onto the surface of the metal, it will either combine with another atom to form a hydrogen molecule or it will migrate into the bulk of the material [65].

The surface energy of the material will dictate which of the possibilities is more likely. The kinetics of the permeation is governed by the nature of the metal, applied potential, cathodic surface characteristics, pH, and chemical composition of the charging solution. Generally, the rate of hydrogen absorption into the metal is governed by the coverage of

hydrogen on the steel surface. Applying a current provides added driving force for the diffusion of hydrogen. A very large hydrogen concentration is produced at the surface, with a gradient into the bulk of the material [66].

Poisons or inhibitors such as sulphur, arsenic and thiourea are added in the electrolyte to inhibit molecular hydrogen formation and as a result, to promote hydrogen absorption. Ren *et al.* [67] used As_2O_3 in sulphuric acid during hydrogen charging, Rozenak [68] used arsenic-based poisons ($NaAsO_2$) in sulphuric acid, Vigdorovich *et al.* [69] studied the effect of thiourea with HCl–LiCl electrolyte on the hydrogen evolution at an iron surface and Han *et al.* [70] studied the effect of thiourea in NaOH on the hydrogen absorption at a palladium electrode.

The hydrogen concentration in ferrous alloys reaches a saturation level after a certain charging time. The saturation time depends on the electrolyte, charging current, charging temperature, steel type and sample geometry. Dong *et al.* [4] found that the amount of hydrogen increased with increasing current density and H_2SO_4 concentration in API5L X100 steel. The amount of hydrogen increased with charging time for 0.1 M H_2SO_4 but when the solution concentration was increased to 0.5 M H_2SO_4, the amount of hydrogen decreased after longer charging. This effect occurred because of the formation of a large number of hydrogen bubbles on the electrode surface, reducing the pick-up of hydrogen atoms.

2.5.7.2 Gaseous Hydrogen Charging

Molecular gaseous hydrogen cannot enter into the steel. In order for hydrogen molecules to be absorbed, it must dissociate into hydrogen atoms. This typically occurs due to the reaction of metal hydrides or from electrochemical reactions [71]. As reported by Liu and Ficalora [72], an energy of 434.2 kJ/mol is required for the dissociation of a hydrogen gas molecule. It was proposed that the energy requirement may be supplemented at the specimen surface via a terminating dislocation. From there, the atomic hydrogen can be transported through the atomic lattice by diffusion or by dislocation movement.

In the case of high-pressure gaseous charging, diffusion is the main method of transport. Diffusion of hydrogen is driven both by temperature and chemical potential gradients [73-75].

The mechanism of hydrogen absorption into a metal lattice involves several steps [76]**.** In the case of gaseous hydrogen the 6 steps involved are the following (Figure 2-12):

- Adsorption of hydrogen molecules on the high pressure feed side;
- Dissociation of the molecules into atomic H consisting of a proton and an electron;
- Dissolution of the hydrogen atoms H (proton and electron) into the lattice of the metal;
- Diffusion of the hydrogen atoms H (proton and electron) through the lattice from the high hydrogen pressure side to the low hydrogen pressure side of the metal;
- Recombination of protons and electrons and re-association of two atomic H with formation of hydrogen molecules H_2 at the low hydrogen pressure side;
- Desorption of hydrogen molecules from the low hydrogen pressure side [76].

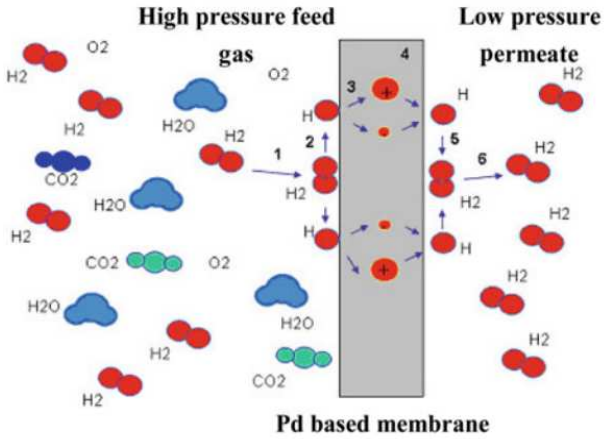

Figure 2-12 Mechanism of permeation of hydrogen through metal: adsorption, dissociation, ionization, diffusion, recombination and desorption [76].

Lee *et al.* [77] designed hollow cylindrical specimen made from API X65 which enabled an *in-situ* tensile test containing gaseous hydrogen. They observed reductions of 3.4 % in ultimate tensile strength and 4.1 % in fracture strain after exposure to 20 MPa of hydrogen gas. They used the same hollow cylindrical specimen filled with 20 MPa of nitrogen for comparison purpose. The fracture surface of hydrogen charged sample, showed quasi-cleavage perpendicular to the loading direction and a fracture wall thickness that was close to the initial wall thickness. In contrast, the nitrogen charged sample was quite different with a complex dimpled fracture surface and a highly reduced fracture thickness.

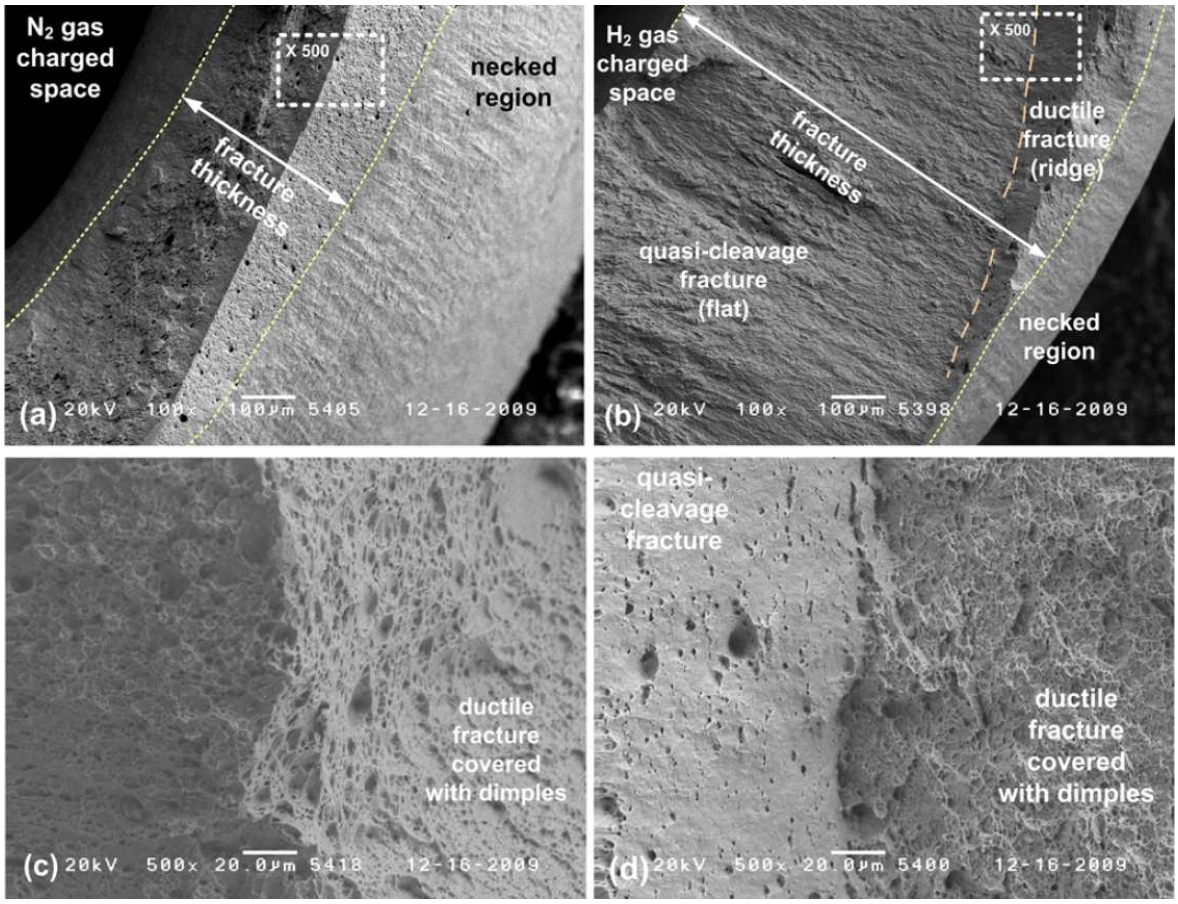

Figure 2-13 Fractured surfaces from (a) N_2 and (b) H_2-charged ampule specimens subjected to a tensile stress at an elongation rate of 0.01 mm/min. Micrographs of the fracture morphologies are shown for gas environments of N_2 (c) and H_2 (d) [77].

2.5.8 Blistering

Hydrogen-induced blistering in steel has been reported by several researchers [5, 78-81]. Blisters not only appear during hydrogen charging of steel, but are also observed after cathodic hydrogen charging in brass [82] and nickel [83]. The progress of hydrogen-induced blisters during the cathodic charging of medium strength steel has also been reported [78]. Rozenak and Watson [68, 84] studied the effect of cathodic charging on the mechanical properties of aluminum. Rozenak reported the existence of a considerable number of hydrogen bubbles around the surface during electrochemical charging. He concluded that these could lead to the creation of blisters and micro-cracks in aluminum samples. Ren *et al*. [85]observed blisters on the sample surface for a wheel steel after charging.

It has been reported by Huang *et al.* [86] that cold work reduces hydrogen diffusivity and increases the hydrogen concentration and blistering effects in steel. The increase in trap density as a result of cold work was proposed to be the reason for the increase in hydrogen concentration and the decrease in the hydrogen diffusivity which leads to less resistance to hydrogen embrittlement.

Matsui *et al.* [87]concluded that blistering was related to the interaction of hydrogen and other impurities at the grain boundary. Garofalo *et al.* [88] suggested that the hydrogen gas in voids or microcracks formed by plastic deformation promotes the propagation of hydrogen-induced internal cracks in iron and steel. Chen [89] regarded blister formation to be caused by remnant porosities in the ingot. Dong *et al.* [4] found that that the size, length and depth of blisters increased with the hydrogen charging time of API5L X100 steel. Wilde *et al.* [90] studied the hydrogen-induced blister cracking of pipeline steels in sulphide environments and found that hydrogen-induced blister cracking initiated at stretched Mn sulphide inclusion and glassy silicate inclusions or substantial niobium carbonitride precipitates. Domizzi [91] also worked on the same subject and found that HIC linked with the elongated Mn sulphide inclusions. The hydrogen charging kinetics depends on the microstructure and the current density applied during cathodic hydrogen charging. As presented in Figure 2-14, the damage of the surface increases by enhancing the current density [92].

Jin *et al.* [81] worked on hydrogen charging of an API5L X100 steel and found that the number of blisters increased with the cathodic charging current density. Furthermore, they reported that some blisters were ruptured, leaving apparent signs on the steel surface, as shown in Figure 2-15.

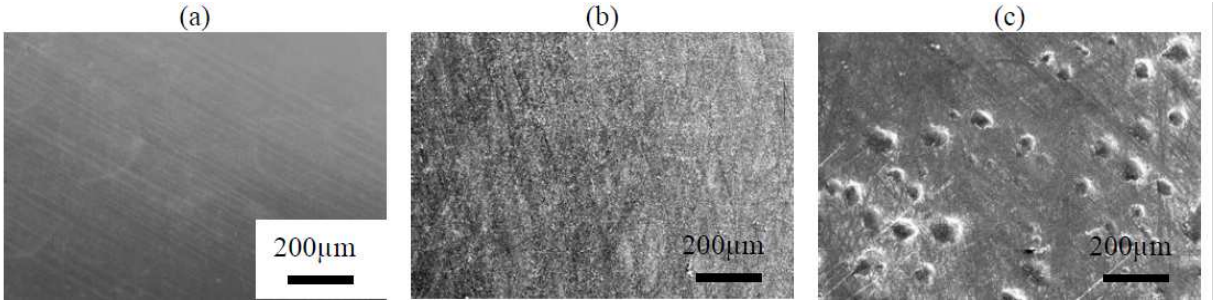

Figure 2-14 SEM images showing increasing damage at the surface of DC03ED steel with increasing current density: (a) not charged, (b) j= 0.8 mA/cm^2 and (c) j=62.5 mA/cm^2 [92].

Escobar *et al.* [93] found that blister formation in pure iron occurred after 1 hour of cathodic charging at 50 mA/cm^2 with arsenic-poisoned electrolyte. Figure 2-16 shows the blisters on pure iron (the TD-RD surface) after charging whilst Figure 2-17 shows crack propagation underneath the same blisters for a cross-section containing the ND-RD directions.

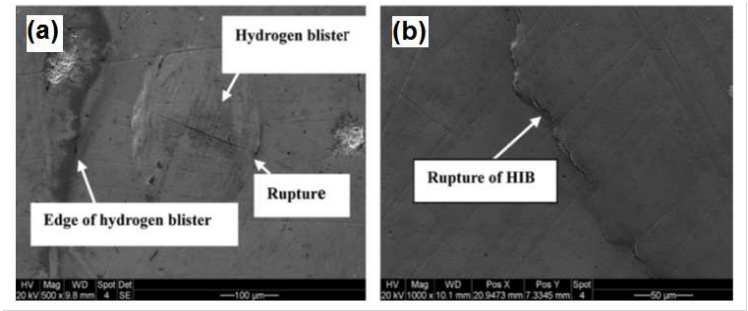

Figure 2-15 Ruptured blisters in an API5L X100 steel after 20 hours of cathodic charging [81].

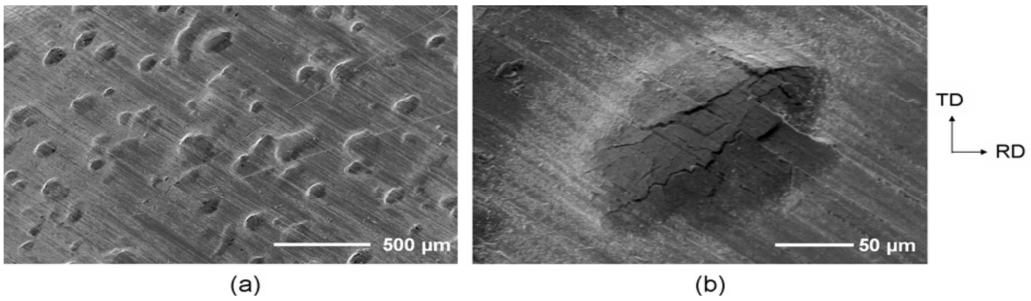

Figure 2-16 SEM micrographs of the pure iron after charging with the arsenic-based electrolyte at 50 mA/cm^2 for 1 hour [93].

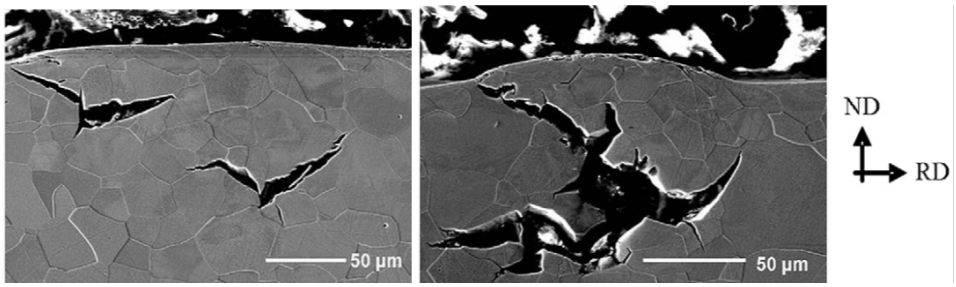

Figure 2-17 Crack propagation underneath the blister in pure iron with the arsenic based electrolyte at 50 mA/cm^2 for 1 hour [93].

2.5.8.1 Mechanism of blistering

McLellan and Galvele [94, 95] observed that hydrogen-affected metals have a greater concentration of vacancies than hydrogen-free metals. So combination of vacancies into vacancy clusters is easy [96]. Osono *et al.* [97] also observed voids in Ni hydrogenated under a hydrogen pressure after removing hydrogen by heat treatment.

The hydrogen atoms in a hydrogen-vacancy cluster combine to form hydrogen molecules and release some energy [85]. Once hydrogen atoms enter an existing defect such as a small cavity (Figure 2-18a), a nucleus is formed which can grow with increasing hydrogen pressure (Figure 2-18b). The build-up of hydrogen atoms and vacancies will make the cavity larger, as illustrated in Figure 2-18c. Plastic deformation around the blister cavity will cause cracks to initiate and propagate out from the cavity (Figure 2-18d). If the cavity is closely adjacent to the metal surface, its growth can displace the layer of material between the cavity and the surface thereby forming a surface hydrogen blister. The blister can grow and then fracture, releasing the pressure inside the underlying cavity [93].

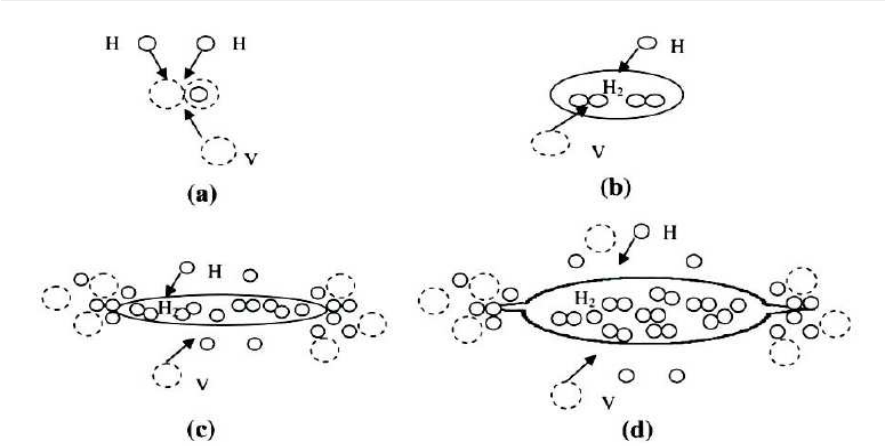

Figure 2-18 Schematic diagrams showing the formation of a hydrogen-vacancy cavity (a) vacancies and hydrogen atoms combine to a hydrogen cluster; (b) hydrogen atoms in the cluster form hydrogen molecules; (c) the cavity grows through build-up of hydrogen and vacancies; and (d) cracks initiate from the walls of the cavity as a result of internal hydrogen pressure [85].

Blistering has been identified as a problem in steel pipelines in sour gas environments which can cause leaking, as illustrated in Figure 2-19 [98].

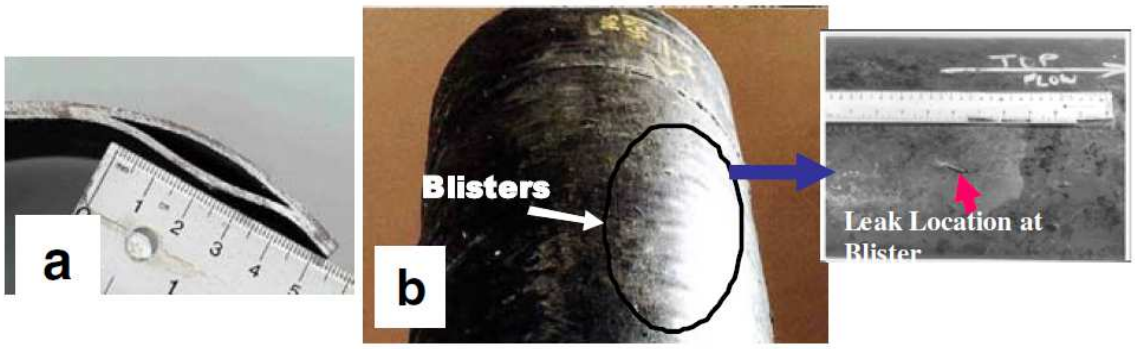

Figure 2-19 (a) Hydrogen blister formed in a sour gas pipeline; (b) blistering and surface cracking at the outer pipe surface in a seamless pipeline (the arrow shows the location the crack in the blister that resulted in a gas leak [98].

2.5.9 Hydrogen trapping

On entering the steel, hydrogen may be present in a diffusible (mobile) form at interstitial sites within the ferrite crystal structure or become trapped at defect sites such as inclusions and grain/phase boundaries [99]. The presence of diffusible hydrogen is

essential for hydrogen embrittlement. A large number of investigations have been carried out with the aim of increasing the density of hydrogen traps in the steel structure in order to trap diffusible hydrogen and reduce the likelihood of hydrogen embrittlement [100-103]. It has been reported that elastic stresses facilitate hydrogen diffusion, but plastic deformation reduces hydrogen diffusion because dislocations act as hydrogen traps [104].
Defects such as grain boundaries, dislocations, microvoids, precipitate-matrix interfaces and non-metallic inclusions can trap hydrogen [105]. These traps can be reversible or irreversible depending on their trap activation energy and trap binding energy for hydrogen atoms (see Table 2-1) [106].

Irreversible traps that permanently trap hydrogen at low temperatures display high binding energies ≥ 60 kJ.mol^{-1}. So the energy needed for hydrogen atom to escape from the trap site to a normal lattice site is very high. The interface between the ferritic steel matrix and non-metallic inclusions is classified as an irreversible trap site.
Reversible traps are temporary sites for hydrogen atoms because their binding energies are lower. Dislocations, grain boundaries and microvoids have lower trap activation energies and are classified as reversible traps.

Table 2-1 Trap activation energies for various trapping sites in steels [107].

Classification of trapping site	**Trap activation energy (kJ mol^{-1})**
Grain boundary	16-18
Cementite Interface	18
Dislocation	26
Microvoid in cold-worked iron	35-40
Microvoid in AISI 4340 steel	56
Interface of Al_2O_3	79
Interface of MnS	72
Interface of Fe oxide	47
Interface of TiC	87

The traps can also be categorised based on their binding energies as strong, and weak traps [108, 109].

- Weak traps: Dislocations with binding energy of 20-28 kJ/mol and fine precipitates in the matrix and also solute atoms like Cr and Mo which have binding energies of about 10 kJ/mol.
- Strong traps: Hydrogen can escape these traps only at elevated temperatures. These traps have high binding energies (above 50 kJ/mol). Spherical precipitates, non-metallic inclusions, interfaces of martensitic laths and prior austenite grain boundaries and segregated impurities are classified as strong hydrogen traps.

2.5.10 Effect of grain size on hydrogen embrittlement

It has been reported by several researchers that hydrogen diffusion rate increases with enhancement of the grain boundary density [110-112]. However, other researchers have proposed that grain boundaries, nodes and junction points act as reversible hydrogen trap sites and decrease the diffusion rate [113, 114]. Therefore, there appears to be two opposing effects. As the grain size decreases, the mobility of hydrogen atoms increases because a larger amount of grain boundary area is available as a diffusion path. However, the larger amount of grain boundary area per unit volume and the higher density of nodes and junctions associated with a smaller grain size can act as possible traps for hydrogen atoms and reduce the hydrogen mobility. Due to these two opposing effects, Ichimura *et al*. [115] suggested that there is an optimum grain size for which hydrogen diffusion coefficient is maximised in pure aluminium. These researchers called these phenomena the cross-boundary effect. This concept is supported by the experimental results of Yazdipour *et al.* [116] for the dependence of hydrogen diffusion rate on grain size in pipeline steels. These results are demonstrated in Figure 2-20.

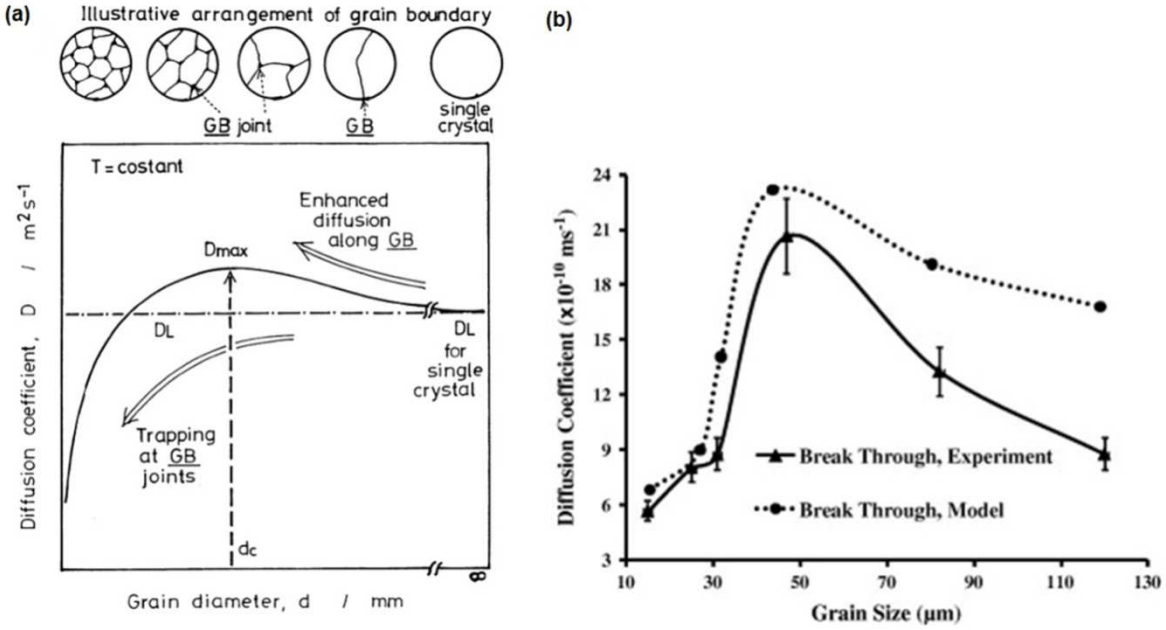

Figure 2-20 The effect of average ferrite grain size on the diffusion coefficient: (a) model for grain cross-boundary effect on hydrogen diffusivity of pure aluminium [115]; and (b) experimental results from permeability studies and modelling for microstructures with different grain sizes (d_0 = 10–117 μm) for pipeline steel [116].

2.5.11 Effect of inclusions and precipitates on hydrogen embrittlement

Inclusions are known to be one of the leading factors affecting hydrogen embrittlement and are considered to be irreversible trap sites in steel [117]. Several different types of inclusions have been identified in pipeline steels [118]. The types of inclusions reported in the steels are mostly MnS, Al_2O_3, complex (Fe, Mn)S compounds and $FeO.Al_2O_3$ double oxide inclusions. Pressouyre and Bernstein [108] investigated MnS inclusions and reported them to be strong irreversible trapping sites for hydrogen. However, Garet *et al.* [119] classified MnS inclusion as reversible traps as their binding energies are only moderate. Carbide and nitride precipitates such as TiC and TiN are regarded as irreversible traps [108, 109]. Takahashi *et al.* [120]reported that fine coherent TiC particles smaller than 10 nm were the most effective trapping sites, whilst Valentini *et al.* [121] reported that coherent Ti(C,N) precipitates smaller than 35 nm are the most favourable irreversible traps in microalloyed steels.

2.5.12 Effect of strain rate on hydrogen embrittlement

Völkl and Wipf [122] found that the diffusivity of hydrogen in steel can vary widely from 10^{-7} to 10^{-11} m^2/s at room temperature. They observed that for diffusion controlled fractures, an increase in the strain rate decreases the time for hydrogen diffusion and decreases the extent of hydrogen embrittlement.

Toribio [123] also studied the embrittlement in steels at different strain rates in the presence of hydrogen. He found that the harmful effect of hydrogen decreased with increasing strain rate. This result is demonstrated in Figure 2-21 in which the ratio of the fracture load in the presence of hydrogen (F_c) to that in air (F_o) is plotted as a function of the strain rate. It can be seen that below a certain strain rate, hydrogen embrittlement was independent of the strain rate. Hydrogen embrittlement is restricted by the capacity of the hydrogen atoms to travel through the metallic structure by interstitial diffusion. Hydrogen diffusion also depends on dislocation motion as diffusion of hydrogen can be accelerated by dislocation transport. However, it is difficult to determine the critical transport speed of the hydrogen due to dislocation motion. This phenomenon depends on the dislocation density and the presence of inclusions. A high density of dislocations together with a high volume fraction of inclusions would slow down dislocation movement and hence decrease the rate of hydrogen mobility.

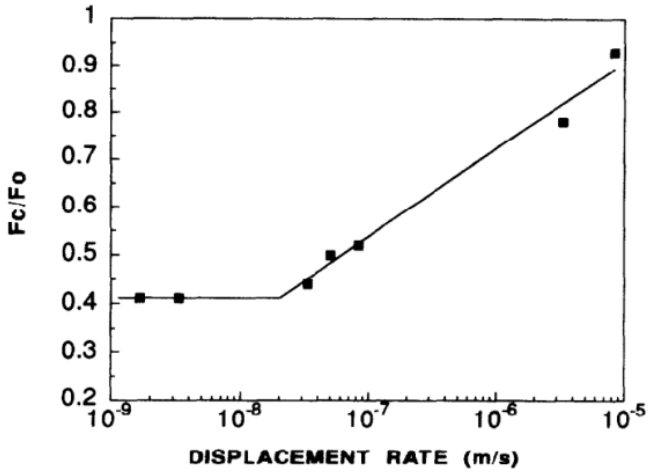

Figure 2-21 Ratio of the fracture load in the presence of hydrogen (F_c) to that in air (F_o) as a function of strain rate for steels [123].

2.5.13 Effect of microstructure

The final microstructure of the steel after TMCP of pipeline steel plays a significant role in the diffusivity of hydrogen [124] and can consist of a combination of quasi-polygonal or polygonal ferrite with pearlite, or bainitic ferrite with martensite-austenite constituent. Park *et al.* [125] found that bainitic ferrite is the most efficient microstructure for trapping hydrogen. Lunarska *et al.* [126] studied the diffusion rate of hydrogen in different microstructures and concluded that the efficiency of trapping decreases in the following order: martensite, bainite, fine pearlite, coarse pearlite and small second phase particles.

2.6 Hydrogen Measurement Techniques

There are several established methods for determination of hydrogen content. The primary method is based on collection and measurement of desorbed hydrogen over mercury, as described in ISO 3690:2000(E) [127], AS/NZS 3752:2006[128] and AWS A4.3-93 [129].

2.6.1 Collection of hydrogen over mercury

The method is based on the correct positioning of a test sample in a gas burette that is filled with clean mercury. Over time, atomic hydrogen diffuses out of the test sample and forms molecular hydrogen, which is collected in a calibrated volume segment of the gas burette. The volume of hydrogen is measured over several days, until change in the hydrogen volume is less than 1% of the total volume collected. As there are some health concerns with the use of this method at elevated temperatures, a range of ambient temperatures from 20-40 ˚C is recommended [127].

2.6.2 Japanese glycerin method

The Japanese glycerine method [130] is another technique similar to the mercury method, but with environmental and health advantages. However, as glycerine is prone to

contamination by moisture and atmospheric gases, the reliability of this method in not widely accepted [129].

2.6.3 Gas chromatography method

Gas chromatography is the most commonly used technique and does not involve any environmental and health concerns. The gas chromatography technique is defined in Australian, American and Japanese standards [127-131] and can provide results with a high level of accuracy, being capable of resolving hydrogen to 0.01 ml. Gas chromatography involves the extraction of hydrogen by holding at a temperature below 150˚C for 6 to 72 hours. The test chamber is then connected to the calibrated gas analyser and the amount of hydrogen is calculated in ppm in the sample being analysed. Incomplete purging of the test chamber and moisture contamination in the dehumidifier or chromatographic column are possible sources of error in this method.

2.6.4 Hot extraction method

The hot extraction technique has been shown to provide trustworthy and comparable test results, regardless of the comparatively high extraction temperature. The temperature used to extract the hydrogen content is below the melting point (500°C-1200°C) during the entire measurement. At a temperature in this range, substantial extraction of both diffusible and trapped hydrogen can be effected in less than half an hour, providing a significant benefit from an industrial viewpoint. Another advantage of this method is that the same crucible can be re-used for a number of analyses, thus decreasing the cost of analysis [132].

2.6.5 Melt extraction method

The melt extraction is a reliable and fast method which covered by AS/NZS 1050 [133]. The system includes a pulse furnace where a pre-weighed sample is heated as quickly as possible up to 2000 ˚C in a nitrogen atmosphere. At this temperature, the metallic sample melts and releases its hydrogen as gaseous hydrogen which is picked up

by flowing nitrogen with the hydrogen-nitrogen mixture being sent to a thermal conductivity measuring cell. The thermal conductivity of the mixture depends on the hydrogen concentration because of the substantial difference in conductivity of hydrogen and nitrogen. The hydrogen concentration is then calculated by software that uses the thermal conductivity variation and the weight of the sample. The advantage of this technique is that the total hydrogen content is extracted and measured in less than 2 minutes. It is not possible to re-use the crucibles in this method [134].

2.6.6 Other methods

Other measurement techniques are the vacuum extraction technique [126], the Arnacle electrode technique[135] and secondary ion mass spectrometry (SIMS) [136].

2.7 Fracture Toughness (J) Calculation

The correct estimation of ductile fracture behaviour is an essential task in structural reliability assessment of steel pipelines. An important consideration about the safety of pipelines is susceptibility to hydrogen embrittlement. A number of research investigations of hydrogen embrittlement of pipelines have performed. A majority of these studies utilise techniques that replicate slow strain rates in the presence of high pressure hydrogen. However, these qualitative results are not adequate from a safety viewpoint as the fracture toughness properties need to be recognised. Fracture toughness testing is most commonly performed using relatively large samples so as to maintain conditions of plane strain and maximum constraint [137].

2.7.1 Why J_{IC}?

In steel research, sometimes the particular region of interest, such as the HAZ, may be quite small and its exact location may be unknown. In addition, the microstructures are heterogeneous. This makes preparing bulk samples very difficult, in that the notch and pre-crack must be directed at the region of interest and the subsequent crack growth must penetrate that region of interest during the test. This problem can be overcome by reducing

the size of the sample to ensure that the entire region being tested is of the desired microstructure. However, reducing the size of the sample runs the risk of no longer satisfying the conditions of plane strain and maximum constraint. As the sample dimensions are reduced, it is difficult to maintain predominantly elastic conditions during fracture testing in metals. In large samples, the plastic zone at the crack tip is relatively small compared to the specimen dimensions and its effect on the elastic conditions of loading is negligible. However, in small samples, this plastic zone at the crack tip becomes significant and the loading conditions are considered plastic-elastic in nature. Therefore, it may be necessary to measure the crack tip energy release rate (J_i) under elastic-plastic conditions [138]. This can be achieved by calculating the critical crack tip energy release rate (J_{IC}) using the J-integral [139] or stretch zone width (SZW) measurement method [140].

2.7.2 J integral method

The J-integral method was proposed by Rice [141] as an energy integral that can be used as an diagnostic tool to describe the crack tip stress and strain region under elastic and plastic conditions. During initial crack extension, many steels commonly show a considerable rise in fracture toughness which can be described by the J-integral method. Common testing methods to determine crack propagation resistance normally utilize TPB or compact specimens containing deep and sharp cracks [141, 142].

The J-integral method involves determining the J-integral as a function of crack extension (Δa). The J-integral is calculated from the area under the load-displacement curve and the crack extension can be measured by either multiple specimen techniques (where different samples are tested to different loads and broken open to measure the crack length) or single sample in-situ techniques (where the crack length is determined by compliance measurements or electric potential drops during a progressive series of loading/unloading cycles of the sample (Figure 2-22 a)).

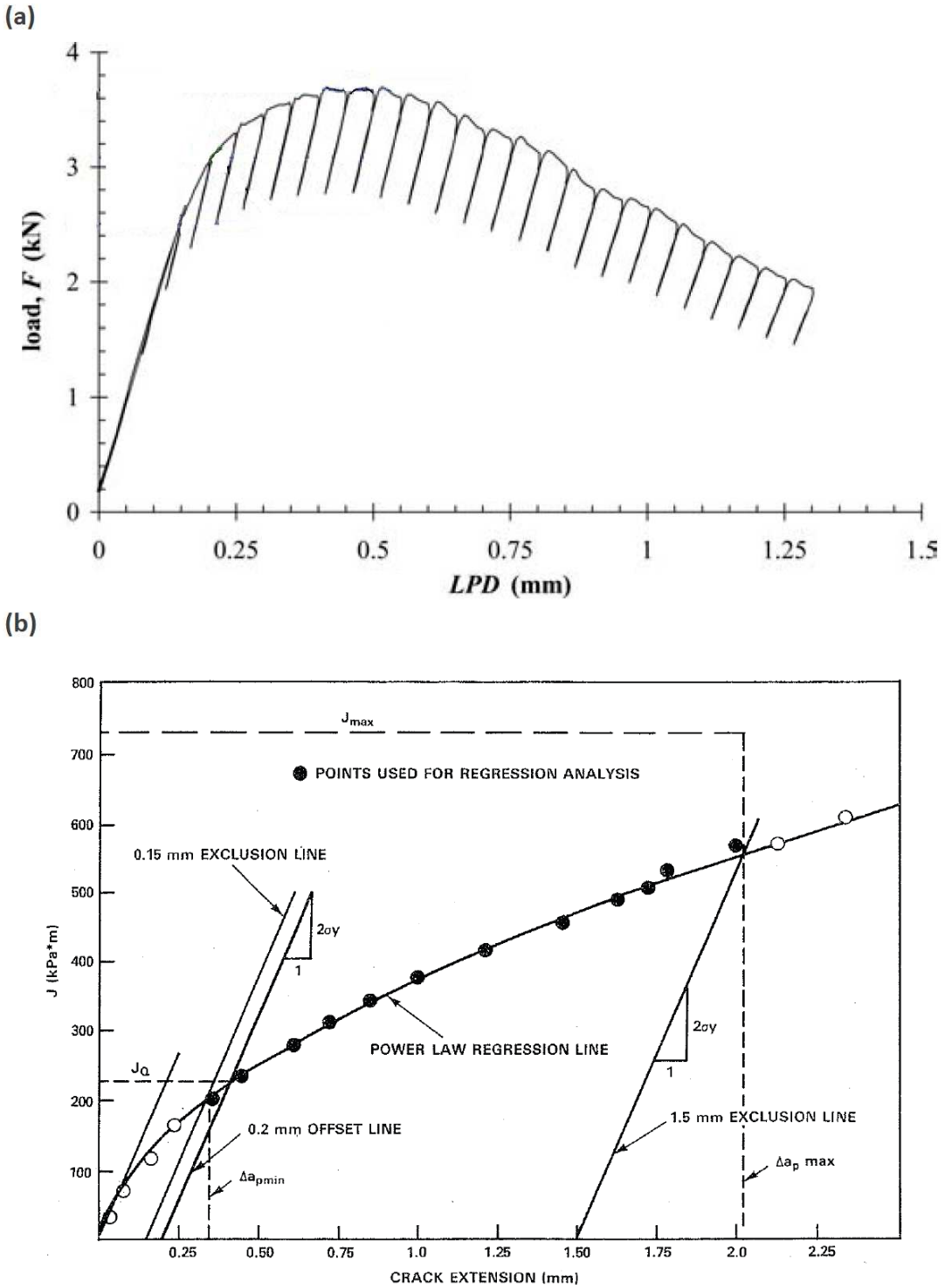

Figure 2-22 (a) Load vs. LPD (load point displacement) graph for single specimen method [143] and (b) a J-R curve used to determine J_{IC} [139].

The relationship between the J-integral and the crack extension is given by the J-resistance curve (generally called the J-R curve, as illustrated in Figure 2-22b), which is extrapolated back to a line corresponding to crack blunting, thereby giving a value of J corresponding to crack initiation (J_{IC}). Since the J-integral is path independent [141], it can be related to the fracture toughness (K_{IC}) in a large specimen by equation 2-1 [144]:

$$K_{IC} = \sqrt{\frac{J_{IC} E}{1 - \nu^2}} \qquad 2\text{-}1$$

where E is the Young's modulus and ν is the Poisson's ratio.

Such methods have been used to determine the fracture toughness of a number of sub-sized specimens down to thicknesses as small as 1.02 mm with very little effect on the obtained J_{IC} values [144-147].

A standard test specimen, such as a compact tension specimen and fatigue pre-cracked, notched TPB specimen, typically has a high constraint at the crack-tip, whilst most actual cracked pipelines and non-standard specimens have a low crack-tip constraint. Therefore, the J-R curve results commonly depend on geometry. However, the J_{IC} curve is size-independent, as described in ASTM E 1820-99 [148]. In general, the J-R curve and J_{IC} may possibly be a function of specimen geometry, thickness, size, and loading stresses [149]. A large number of experiments have been carried out to understand the crack-tip constraint effects on the fracture behaviour of ductile cracks [150-154]. Experimental trials have been carried out for ductile crack extension tests of sub-sized fracture specimens [155-157], for large-size fracture specimens [158-160] and for non-standard size fracture specimens [149, 161, 162]. These researchers did not find any substantial constraint effect on the crack initiation toughness; however, after relatively large extensions by crack propagation, a higher constraint effect on the fracture toughness was observed. The results supported the conclusion that the J-integral value on the J-R curve for low constraint specimens is higher than those for high constraint specimens. This means that after crack initiation, the gradient of the J-R curve decreases with increasing crack tip constraint. This effect has been simulated by several researchers with finite element analyses [152, 163-167].

For steel pipelines containing gaseous hydrogen up to 34.5 MPa, critical J-integral values J_{IC}, calculated from J-R curves are available in the literature [168-170]. Due to the

effect of hydrogen, a decrease in J_{IC} values by up to a factor of three has been reported. For the purpose of moderating this effect, addition of inhibiting gaseous mixtures like oxygen to the hydrogen is recommended by Kussmaul *et al.* [171], who worked with the same concept on 15 MnNi 6 3 steel. The load line-displacement and J-R graph obtained in this work (Figure 2-23) clearly illustrate the effect of hydrogen and also the moderating effect of oxygen on hydrogen embrittlement. The same results have been reported for X70 steel using high pressure hydrogen gas with admixtures of oxygen [172] as well as in other cyclic crack growth experiments [168, 173, 174].

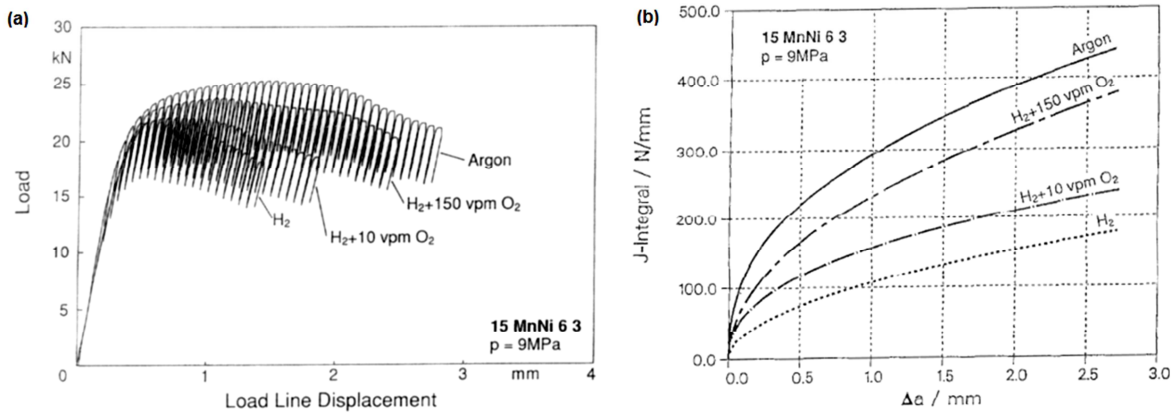

Figure 2-23 The effect of hydrogen and hydrogen-oxygen mixtures on load line-displacement (a) and J-R curves (b) for 15 MnNi 6 3 steel [171].

2.7.3 Stretch zone width method

This method is an alternative technique to determine J_{IC} by using measurements of the stretch zone width (SZW). The same samples used for the determination of the J-R curves can be used for SZW measurements. Since the SZW is indicative of the amount of plastic blunting at the crack tip, it can be influenced by a change in microstructure as a result of the activation of mobile dislocations in the earlier strain cycles. The stretch region is the transition region linking the end of the fatigue pre-crack and the region of steady crack growth. It is characterised by significant plastic deformation just before crack initiation. This region can be identified between the fatigue pre-crack region and the stable crack growth region in fractography [175].

Assuming a symmetric blunt crack, Nguyen-Duy and Bayard analysed the SZW and found an equation to describe the SZW-based crack opening displacement (COD). The model is illustrated in Figure 2-24.

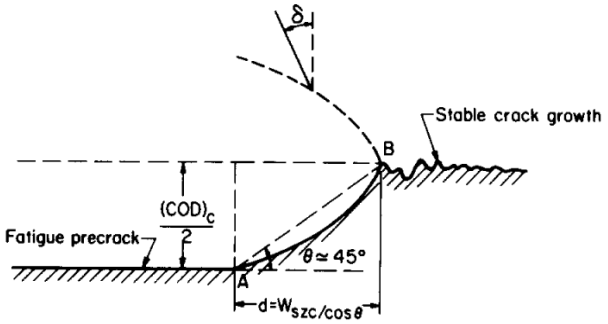

Figure 2-24 A schematic diagram illustrating the model proposed by Nguyen-Duy and Bayard to describe the measurement of the SZW-based COD [175].

If the line AB defines the critical stretch zone width, the SZW and COD are given by equation 2-2 and (2-3 respectively:

$$W_{strech\ zone} = \frac{d}{\cos(\theta - \delta)} \times \frac{1}{G} \qquad 2\text{-}2$$

$$COD = \frac{2d}{\sin\delta + \cos\delta} \times \frac{1}{G} \qquad 2\text{-}3$$

where d is the measured extent of the stretch zone on the Figure 2-24, δ is the bending angle of the specimen, $\theta = 45°$ and G is the magnification. Hayes and Turner [176] proposed that the critical value of the J under plane strain conditions is given by equation 2-4:

$$J_{IC} = 2\sigma_f . COD \qquad 2\text{-}4$$

where σ_f is the average of yield and tensile strength. If equation 2-3 is substituted in equation 2-4, it will appear as equation 2-5:

$$J_{IC} = \frac{4\sigma_f . d}{\sin\delta + \cos\delta} \times \frac{1}{G} \qquad 2\text{-}5$$

J_{IC} can be calculated in most of the cases by considering that $\delta = 45$, G=250~ 380 and *d* is the average stretch width measurement along the crack front.

Tarpani *et al.* [177] used SEM fracture analysis to characterize the SZW as illustrated in Figure 2-25.

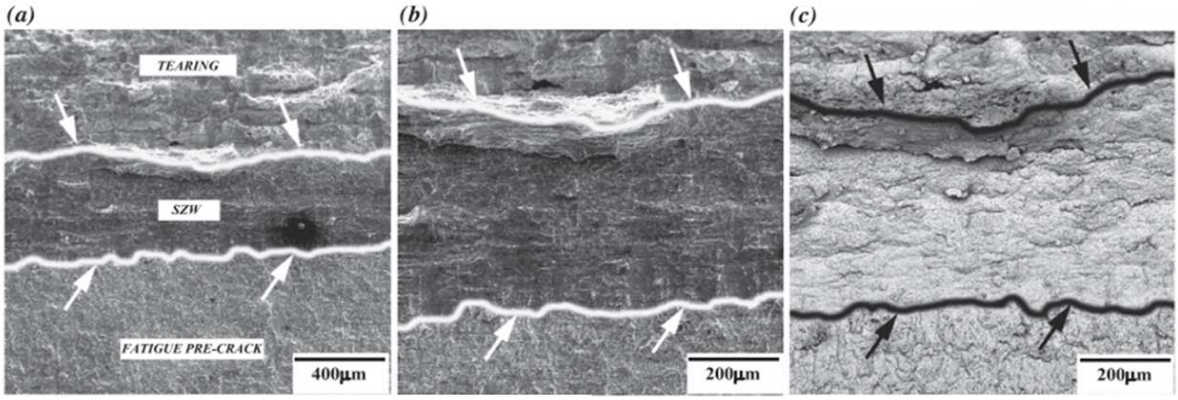

Figure 2-25 SEM fractographs taken from fractured Charpy impact specimens: (a) general view of SZW; (b) magnified view; and (c) back scatter image. The beginning and end of the SZW are arrowed. Crack growth direction is from the bottom to the top of the figure [177].

2.7.4 J calculation for X70 pipeline steel

Olden *et al.* [178] studied hydrogen diffusion and hydrogen influenced critical stress intensity in an API X70 pipeline steel welded joint. In order to identify the energy required for the initiation of ductile crack growth in as received base metal, HAZ and weld metal, multiple specimen J integral and SZW techniques were employed. For the base metal and weld metal specimens, the SZW method was used. The stretch zone widths were determined by optical micsoscopy to be 0.1 mm and 0.04 mm, respectively. As given in Figure 2-26a and b these crack extension values correspond to J values of 300 N/mm and 250 N/mm, respectively. For the HAZ specimen, the J integral method was employed using an analytical blunting line [179] since recognition of the SZW was difficult with optical microscopy. The blunting line crosses at 0.1 mm and gives a J value of 400 N/mm. Therefore, according to Olden *et al.* [178] the J_{IC} value for X70 weld metal is greater than

that for the base metal whilst the J_{IC} value for the HAZ is smaller than that for the base metal.

2.8 Work Hardening in Pipeline Steel Design

2.8.1 Importance of yield to tensile strength ratio

The American Petroleum Institute (API) specifications for line pipe steels commonly require a yield to tensile strength ratio (YS/UTS) that is smaller than 0.93. Higher YS/UTS ratios mean that there is not enough plasticity for strain rearrangement in thinned areas during line pipe service. Although lower YS/TS ratios result in a broad strain range for material forming, the yield strength still should be high enough for the transport of liquid or gas at high pressures. The YS/UTS ratio is affected by the steel microstructure which can be optimized by controlling the hot rolling, cooling and coiling procedures [180].

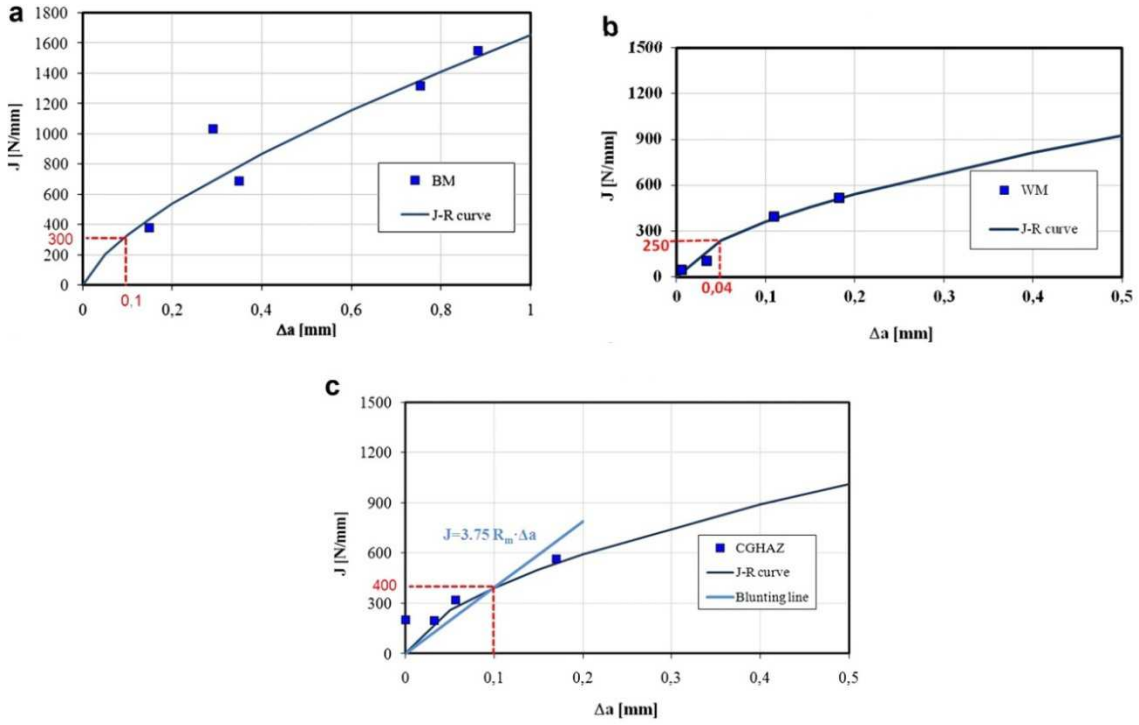

Figure 2-26 J-R curves for an uncharged welded specimen of X70. (a) Base metal specimen with observed stretching zone width of 0.1 mm. (b) Weld metal specimen with observed stretching zone width of 0.04 mm. (c) HAZ specimens with SZW of 0.1mm obtained using the analytical blunting line [178].

Buried high-strength pipelines are prone to plastic circumferential stresses as a result of pressure containment where mainly circumferential and radial components of strain undergo plastic deformation. In addition, differential ground movements may cause large longitudinal strains. Differential ground movements can be caused by soil sinking, landslides and tectonic faults. In hostile environments, pipelines can be exposed to longitudinal strains (tensile, compressive or complex) that exceed the elastic limit, as presented in Figure 2-27 [181]. These factors place restrictions on the pipeline material and the related design. With the intention of pipeline safety and reliability it is not sensible to design based on acceptable stress because the driving parameter is strain, 'Strain Based Design' (SBD) may assist as the key to such difficult pipeline applications.

The main design parameters for pipeline intended for applications with a substantial strain demand are the resistance to buckling (compressive strain) and the tensile tearing capacity of field girth welds (tensile strain)[182].

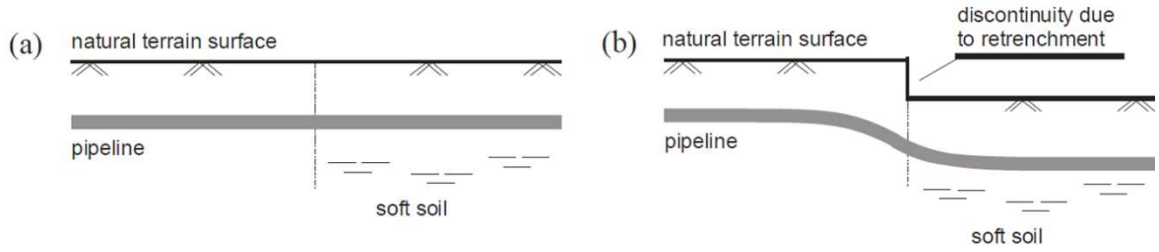

Figure 2-27 Typical strain based design situations (a) just after pipe installation and ((b) after a few years [181].

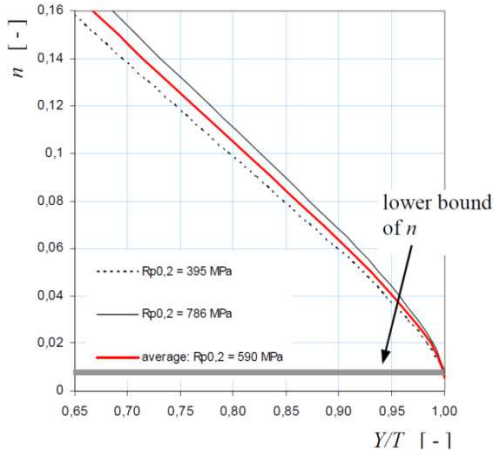

Figure 2-28 Strain hardening exponent n plotted against yield to tensile ratio [181].

In the initial stages of pipeline design it is very desirable to have access to relevant stress-strain information, especially in the elastic-plastic area. However, in early stages of design, the strength of pipeline material in the axial and transverse directions might have been calculated based upon specific pressure requirements, whereas the final stress-strain graph is still unidentified. Knowledge of the work hardening exponent is beneficial for any strain based valuation of safety, strain capability. The work hardening exponent can be important in the axial as well as in the circumferential direction because of the variety of service stresses (internal pressure alone or the presence of external stresses). Liessem *et al.* [181] analysed the way work hardening properties can be estimated based on classical material characteristics, such as yield and ultimate tensile strength or uniform elongation. Their analysis was directed at the question whether results from a classical stress-strain graph can elucidate the strain hardening characteristics. They found that the yield-to-tensile ratio might be appropriate for a first approximation of work hardening exponent, regardless of using the engineering or true stress-strain graph.

Figure 2-28 shows the plot of work hardening exponent against yield-to-tensile ratio. Moderate values of yield-to-tensile ratio generally indicate that the metal has sufficient plastic strain capability, and therefore, substantial work hardening properties. Other than YS/UTS, uniform elongation is known to have significant effect on work hardening exponent since it is the range over which work hardening takes place. A mathematical model for estimating the work hardening exponent as a function of YS/UTS and uniform elongation has been proposed by Liessem [181], (equation 2-6):

$$n = -0.0293 + \sqrt{\frac{0.0696}{Y/T} - 0.0683} \qquad 2\text{-}6$$

where n is the Holloman work hardening exponent, Y is yield stress and T is tensile stress. The graphs in Figure 2-28 suggest that the strain hardening exponent may not just be a function of yield-to-tensile alone but of the yield stress as well. Moreover at YS/UTS=1, the work hardening exponent is still above zero, the grey line indicates the minimum value of n.

2.8.2 Modeling of work hardening

A variety of empirical equations of stress–strain correlation have been used to model the work-hardening characteristics of steels. These models are summarized in Table 2-2. Models by Hollomon [183], Ludwik [184], Swift [185], Hockett/Sherby [186], Voce [187] or Ghosh [188] are commonly used.

Among these models, the most accepted ones in relation to pipelines are Hollomon [183], Ludwik [184] and Swift [185]. However, the Ludwik and Swift equations are commonly used with a few modifications. The Crussard–Jaoul (C-J) [189] analysis based on Ludwik model [184] is commonly known as the differential C-J (DC-J) method [190]; and the modified C-J (MC-J) method [190-192] is based on the Swift equation [185]. Ramos showed that the efficiency of the Hollomon equation is limited in explaining the work hardening of steels [193]; however, he successfully analyzed the same steel by the DC-J method. Jiang and Jha [191, 194] reported that the MC-J method is more appropriate than the DC-J technique for modeling the work hardening behaviour of dual phase steels with different martensite volume fractions.

Several researchers have attempted to distinguish the different stages of hardening. Nes, Zehetbauer and Kocks [195-198] comprehensively studied the different stages of hardening and found up to four different stages in some cases. However, most researchers have reported two stages [191, 192, 194, 198-204] and three stages [193, 198, 200, 203, 205-207]. There is also some evidence of a single stage of work hardening in the literature [198, 201, 203, 204].

Table 2-2 Empirical equations for the stress–strain correlation used to model the work-hardening behavior of steels.

Model	Equation	Eq. No.
Holloman [183]	$\sigma_H = C_1 . \varepsilon^{C_2}$	2-7
Ludwick [184]	$\sigma_L = C_1 + C_2 . \varepsilon^{C_3}$	2-8
Swift [185]	$\sigma_S = C_1 . (C_2 + \varepsilon)^{C_3}$	2-9
Voce [187]	$\sigma_V = C_1 + (C_2 - C_1) . exp(-C_3 . \varepsilon)$	2-10
Hochett/Sherby [186]	$\sigma_{H/Sh} = C_2 - (C_2 - C_1) . exp(-C_3 . \varepsilon^{C_4})$	2-11
Ghosh [188]	$\sigma_G = C_1 + C_2 . (C_3 + \varepsilon)^{C_4}$	2-12
Swift-Voce [208]	$\sigma_{S-V} = C_1 . \sigma_S + (1 - C_2) . \sigma_V$	2-13
Bergström [209, 210]	$\sigma_B = C_1 + C_2 . (C_3 . (C_4 + \varepsilon) + \{1 - \exp[-C_5 . (C_4 + \varepsilon)]\}^{C_6}$	2-14
El-Magd [211]	$\sigma_{E-M} = C_1 + C_2 . \varepsilon + C_3 . [1 - exp(-C_4 . \varepsilon)]$	2-15
Voce generalized [212]	$\sigma_{V.g} = C_1 + (C_2 + C_3 . \varepsilon) . [1 - \exp(-C_4 . \varepsilon)$	2-16

In an attempt to create a universal model to predict the work hardening behaviour from the processing conditions, Umemoto *et al.* [204] studied mechanical properties of the four most common single structures found in steel (ferrite, pearlite, bainite, and martensite). They tried to describe the work-hardening behaviour and found that DC–J method can describe the work-hardening behaviour of these steels reasonably well. They found that steels containing ferrite or pearlite deform with two stages and martensitic steels show a single stage of work hardening. Work hardening behaviour in bainite was found to be dependent on transformation temperature; upper bainite acts similar to pearlitic steels and lower bainite deforms like quenched martensite. Each stage is coupled with an individual work hardening exponent (*n).*

2.9 Summary

- The literature review indicates that HE is a prevalent and critical problem for pipeline steels.
- Fabrication welds, ER seam welds and girth and in-service welds change the local microstructure and properties and provide a means of hydrogen entry into the steel.
- Pipeline transport of hydrogen provides a permanent source for hydrogen pick-up.
- Mn in steels in the normal content range of 0.8-1.2% for pipeline steels results in significant centre-line segregation, impacting on HIC resistance.
- Microstructure and mechanical properties, particularly work hardening characteristics, are important in determining susceptibility to HE.
- Relatively little research has been conducted on the effect of lower Mn content (0.4-0.6%) in X70 pipeline steels, and the consequently reduced segregation, on the susceptibility to HE.

This thesis addresses the issues of the effects of X70 steel microstructure, as well as lower Mn content, on the susceptibility to HE and HIC.

3 EXPERIMENTAL PROCEDURES

This chapter begins with characterisation of chemical composition and fabrication stages of tested steels. The techniques used to prepare samples for TPB test, Gleeble simulations, diffusion and tensile tests are then presented. The simulation of the HAZ structure using the Gleeble thermo-mechanical testing machine is then discussed. The techniques used for microstructure and fractography characterisation are described. In addition, the electrolytic hydrogen charging method used to introduce hydrogen into steels and hydrogen measurement techniques are explained.

The chapter closes by describing the experimental set-up used for each mechanical test used: hardness, fatigue, TPB and tensile testing.

3.1 Materials and Samples Preparation

3.1.1 As-received material

Two API X70 grade samples were received from the BlueScope Steel Ltd. in the form of transfer bar and strip.

The as-received strip and transfer bar are shown in Figure 3-1. The pipe sample photograph was taken after the seam welded region was removed. Table 3-1 presents the chemical compositions of the steels. The main difference in chemical composition of the strips is the level of Mn and Cr. Hereafter, the steels with higher Mn (1.14wt. %) and lower Mn (0.5wt.%) are referred to as X70 and MX70, respectively. The MX70 has a higher level of Cr as it was added to provide a hardenability to offset the reduction in Mn. The transfer bar (referred to as TB) was supplied only in the X70 composition. Table 3-2 and Table 3-3 show the fabrication stage, thickness and TMCP parameters of the samples.

Figure 3-1 As-received material.

Table 3-1 Compositions (wt%) of the standard and medium manganese steels

	C	P	Mn	Si	Ni	Cr	Mo	Cu	Al	Nb	Ti	V	S	N
X70	**0.074**	**0.012**	**1.14**	**0.22**	**0.024**	**0.029**	**0.1**	**0.023**	**0.019**	**0.06**	**0.02**	**0.002**	**0.002**	**0.004**
MX70	**0.085**	**0.01**	**0.5**	**0.19**	**0.018**	**0.26**	**0.11**	**0.011**	**0.04**	**0.059**	**0.035**	**0.003**	**0.002**	**0.005**

Table 3-2 Conditions and dimensions of as-received samples

	Mn%	Fabrication stage	Thickness
X70	1.14	Transfer bar	28~30mm
X70	1.14	Strip/Plate	10mm
X70	1.14	Strip HAZ	10mm
MX70	0.5	Strip/Plate	8mm

Table 3-3 TMCP parameters

	X70	MX70
Soaking Temperature (°C)	1250	1250
Soaking time (hours)	3	3
Rough rolling temperature (°C)	1075-1100	1060-1095
Finish mill entry temperature (°C)	1000-1040	950
Finish mill exit temperature (°C)	800-840	820
Coiling temperature (°C)	600	600

3.1.2 Three point bending sample preparation

3.1.2.1 As-received samples

All samples were machined into 5 × 5 × 25 mm bars. Samples then were wire cut in the bar centre to produce a 1 mm deep notch with a maximum width of 0.3 mm to meet ASTM E813 requirements [139] (Figure 3-2). Samples were then fatigue pre-cracked, as described in section 3.5.2, to achieve a total notch plus crack depth of 2.5 mm along the notch.

Immediately before hydrogen charging, TPB samples were ground on SiC paper to an 800 grit finish (including notch walls) using ethanol as a lubricant, so as to minimise oxidation of the surface of the steel samples.

The as-received strip samples (X70 and MX70) were used for TPB test without any further treatment.

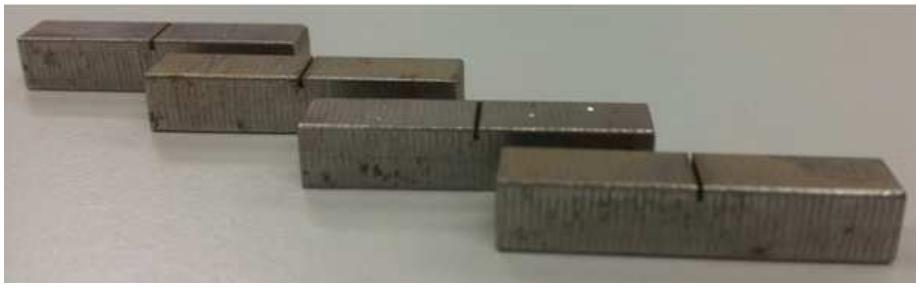

Figure 3-2 TPB samples with a 1 mm deep notch of 0.3 mm width.

3.1.2.2 Gleeble HAZ thermal cycle simulation

Simulation of the HAZ thermal cycle during in-service welding was achieved on a Gleeble 3500 thermo-mechanical testing machine. Samples were machined to a rectangular bar with a cross-section of 9×5 mm and a length of 80 mm. A small neck 10 mm long with a reduced width of 5 mm was machined in the centre of the bar to achieve a more uniform temperature profile along the sample and obtain a more uniform HAZ microstructure. These dimensions were dictated by the amount of material available and the thicknesses of the pipeline steels studied, as well as the need to achieve rapid heating and cooling for the thermal cycle simulations. The sample geometry and dimensions are shown in Figure 3-3.

After HAZ simulation, the sample was machined into the standard 5×5×25 mm TPB shape. Figure 3-4 shows the machining stages of HAZ samples.

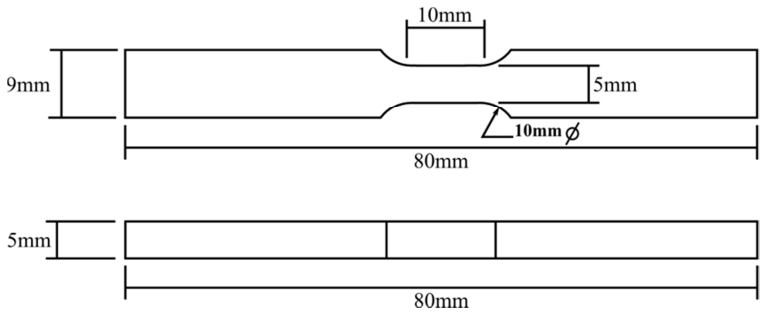

Figure 3-3 Gleeble sample geometry and dimensions for HAZ thermal cycle simulations.

Figure 3-4 Machining stages of samples for TPB for simulated HAZ.

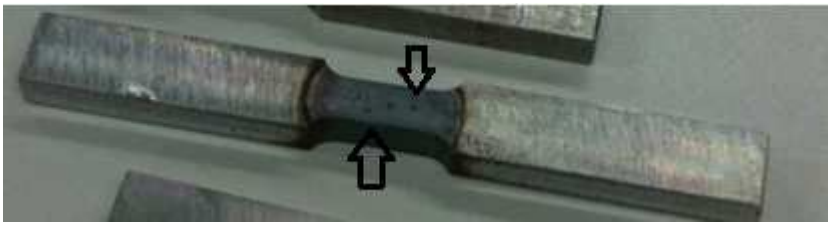

Figure 3-5 Dog bone sample, arrows show the connection points for the 2 thermocouple wires which were separated by ~ 1mm.

A K type thermocouple was welded in the centre of the Gleeble sample **(**Figure 3-5**)** and connected to thermocouple points on the Gleeble (Figure 3-6). Samples were set up in the Gleeble Pocket Jaw with specially machined copper grips; making sure that the ends of the dog-bone Gleeble samples were flush with the outside faces of the copper grips.

A current was applied to resistively heat the sample according to the required temperature cycle. The thermal cycle was performed under vacuum before the argon cooling gas was turned on. The cycle designed to simulate that experienced by the HAZ during in-service welding by replicating the thermal cycle reported by Nolan *et al.* [213]. The heating rate was maximised whilst maintaining adequate control to avoid overshooting the peak temperature of 1350°C. The heating rate was 30°C/s (0 to 150°C) and 300°C/s (150° to 1350°C). The hold time at the peak temperature was minimised whilst allowing the temperature to stabilise and the sample was cooled rapidly through the use of two high-pressure argon gas quenching jets located on opposite sides of the neck of the Gleeble samples. Through the use of the argon jets, a high cooling rate was obtained. Samples were subjected to a cooling time of 3 seconds between 800 ºC and 500 ºC ($t_{8/5}$), consistent with that obtained for a heat input of 0.77 kJ/mm on 10 mm thick pipeline. This is at the lower end of the range of cooling times typically observed during in-service welding procedures ($t_{8/5}$ of 2-10 seconds) [213].The program was run under force control, so that no force was applied to the sample (any force would cause the sample to buckle at 1350ºC). A typical thermal cycle achieved during the HAZ simulation is shown in Figure 3-7.

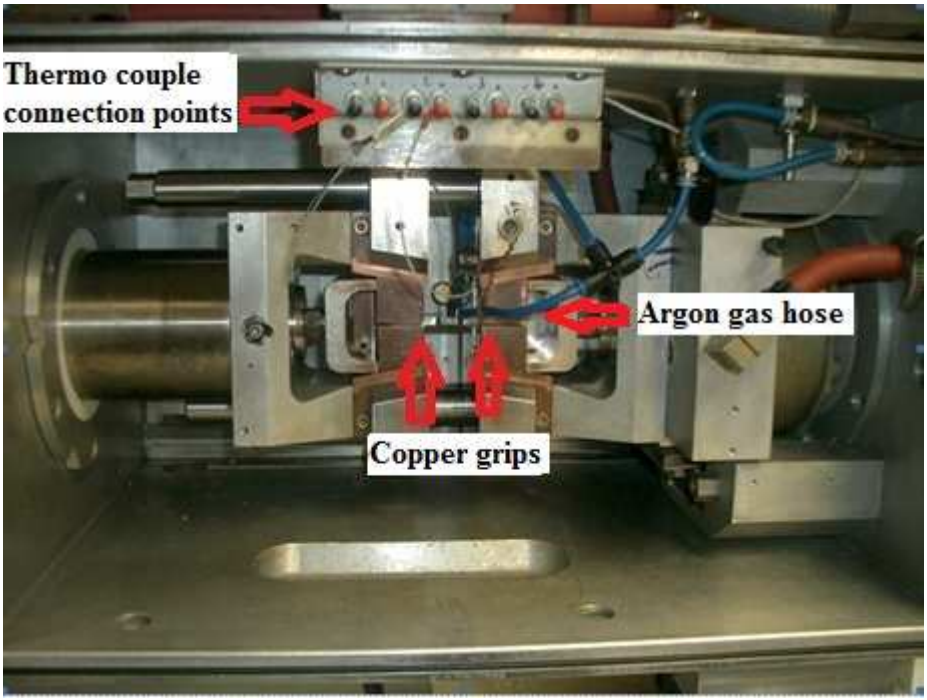

Figure 3-6 Experimental setup for HAZ welding simulation in Gleeble.

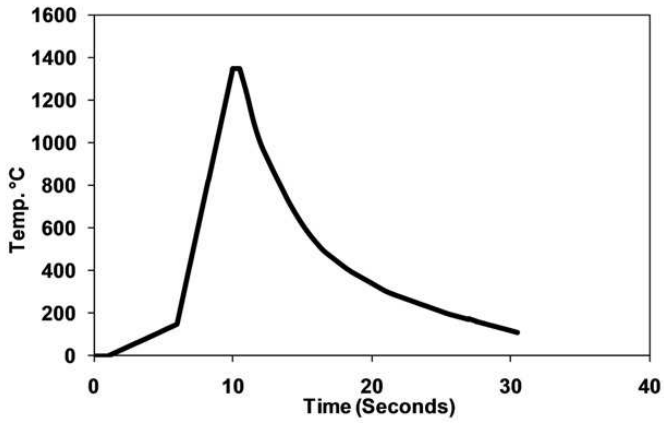

Figure 3-7 Typical HAZ thermal cycle used for Gleeble simulations.

Once the HAZ microstructure was produced by the HAZ thermal cycle simulation, the Gleeble sample was machined into a small TPB sample bar 5 × 5 × 25 mm in size. The TPB bar utilised the neck of the Gleeble sample and was centred along its length so that the HAZ microstructure was situated in the centre of the bar. All samples were wire cut to produce a 1 mm deep notch with a maximum 0.3 mm width to meet ASTM E813

requirements. The Gleeble HAZ samples were prepared from X70, MX70 and TB. To verify the heat treatment cycle on Gleeble machine, one reference weld metal sample was obtained from the BlueScope Steel. The microstructure of the Gleeble simulated HAZ was compared with the HAZ of the reference sample (Figure 3-8). The grain size and microstructure of the HAZ samples were found to closely match the actual weld HAZ.

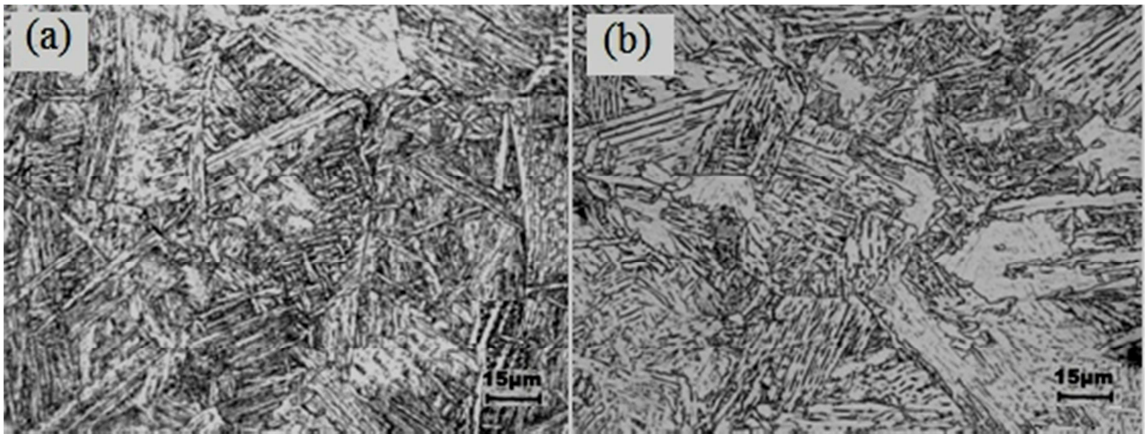

Figure 3-8 (a) Gleeble HAZ simulated sample and (b) HAZ of BlueScope Steel weld sample.

3.1.2.3 Normalised transfer bar TPB samples

Transfer bar samples were encapsulated in quartz tubing **(**Figure 3-9**)** and then normalised in a KTL1600 electric furnace. The furnace was first heated up to 950ºC and then the samples were inserted in the furnace for 20 minutes. The samples were then air cooled to room temperature.

Figure 3-9 Encapsulation for normalising the transfer bar TPB samples

3.1.3 Heat treatment of transfer bar samples

In order to investigate the effect of grain size on hydrogen embrittlement, rectangular samples parallel to the rolling plane of the X70 transfer bar and strip with thicknesses ranged from 0.2 to 5 mm were obtained by wire cutting. The size of samples was different from sample to sample, hence the current was adjusted to compensate. The transfer bar samples were sealed in quartz tubes and subjected to the heat treatments following the annealing program given in Figure 3-10 to produce different grain sizes. Except for HAZ samples, which were water quenched immediately, all the samples were initially cooled from the respective annealing temperatures to 700 ˚C and held at this temperature for 2 hours before final cooling to the room temperature in order to prevent the transformation of austenite to bainite during cooling. Cross-sections of the samples were cut and prepared for optical metallography.

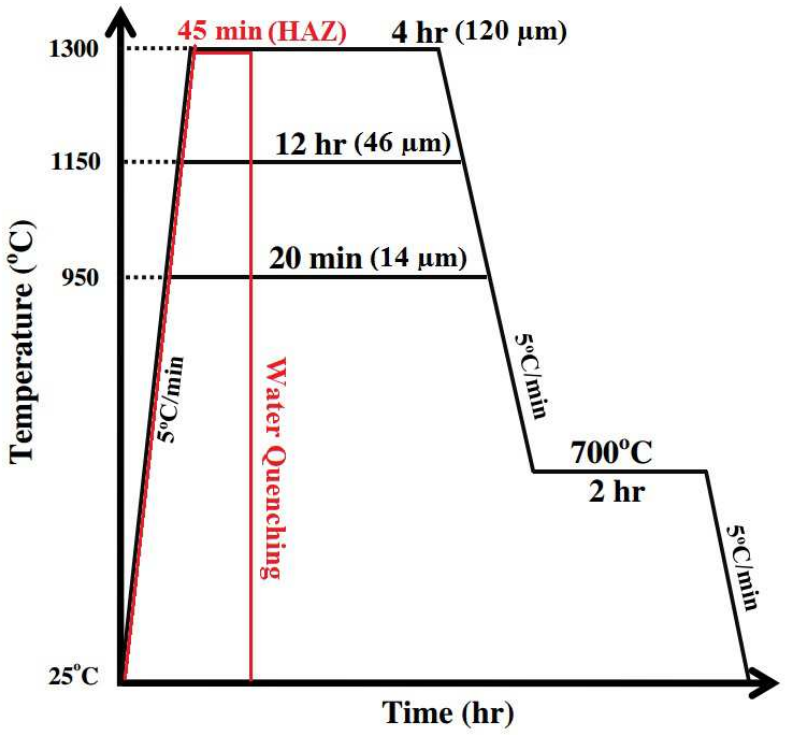

Figure 3-10 Annealing program to obtain microstructures with different grain sizes and also HAZ samples

The samples were etched with 2% Nital solution and the microstructures were examined in an optical microscope and the grain sizes were measured by the linear intercept technique according to ASTM E112-10 [214]. The samples were classified based on average grain sizes to 14, 46 and 120 µm. The annealing program resulted in approximately the same pearlite volume fraction in all the samples. As the microstructure and annealing program of 14µm was almost the same as normalised transfer bar sample for TPB test, this microstructure is also referred to as NTB in this study.

3.1.4 Preparation of samples for tensile testing in presence of hydrogen

Normalising of TB was carried out before machining the tensile samples. The whole transfer bar was put in the oven at 950°C for 20 minutes and then air-cooled to room temperature. 2 mm of metal was removed by machining from the sample sides in order to remove the oxide layer.

Hollow cylindrical samples were machined along the rolling direction. Figure 3-11 and Table 3-4 show the dimensions of specimens.

Table 3-4 Hollow cylindrical sample dimensions

External diameter	Internal diameter	Wall thickness	Gauge length	Parallel length
6mm	4mm	1mm	40mm	36mm

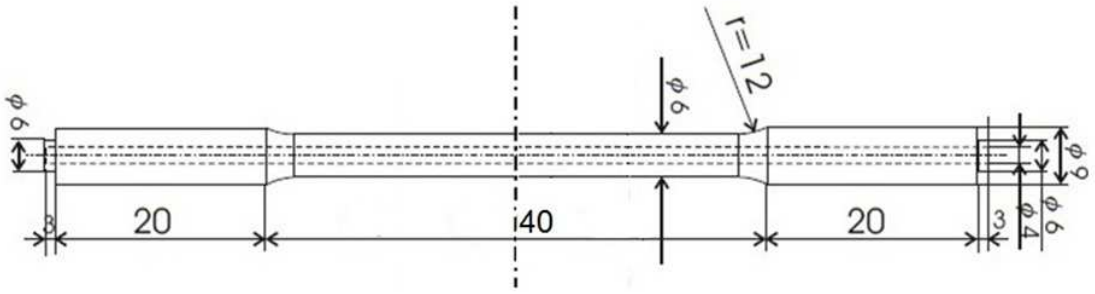

Figure 3-11 Schematic of hollow cylindrical sample dimensions.

After machining, hollow cylindrical samples were welded to two stainless steel hollow cylindrical pipes as extensions. Because of the limitations in size of the test samples and the amount of as-received material, stainless steel pipes were chosen for extensions. The welding was performed carefully to avoid heating the centre area of the samples. The stainless steel extensions were bent for exit of the tensile test line. (Figure 3-12). Once the specimen was connected to the hydrogen (99% purity) or argon (99% purity) cylinders, the connections were sealed and sample was purged three times with hydrogen or argon and then pressurised to 10 MPa.

In all experiments gaseous charging was carried out within 2 minutes before the tensile test. Tensile test itself took between 6 to 11 minutes depending on fracture strain. The amount of hydrogen gas before and after tensile test was below detection limit.

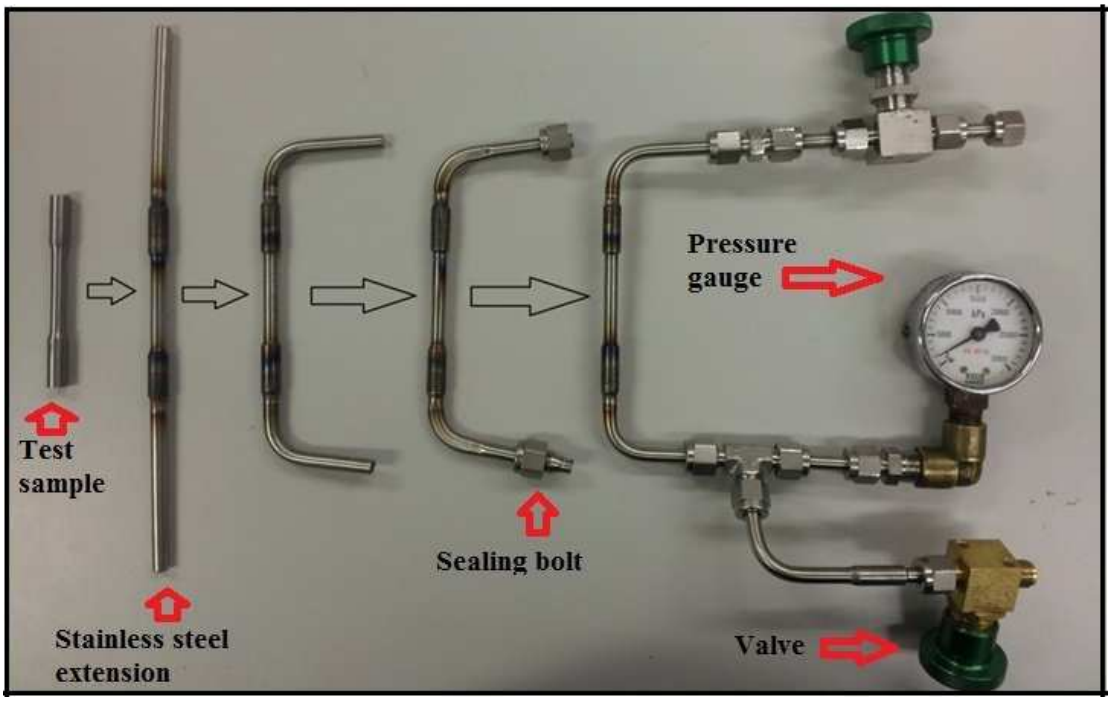

Figure 3-12. Stages in manufacturing of tensile samples and set-up for tensile testing with gas under pressure inside the sample.

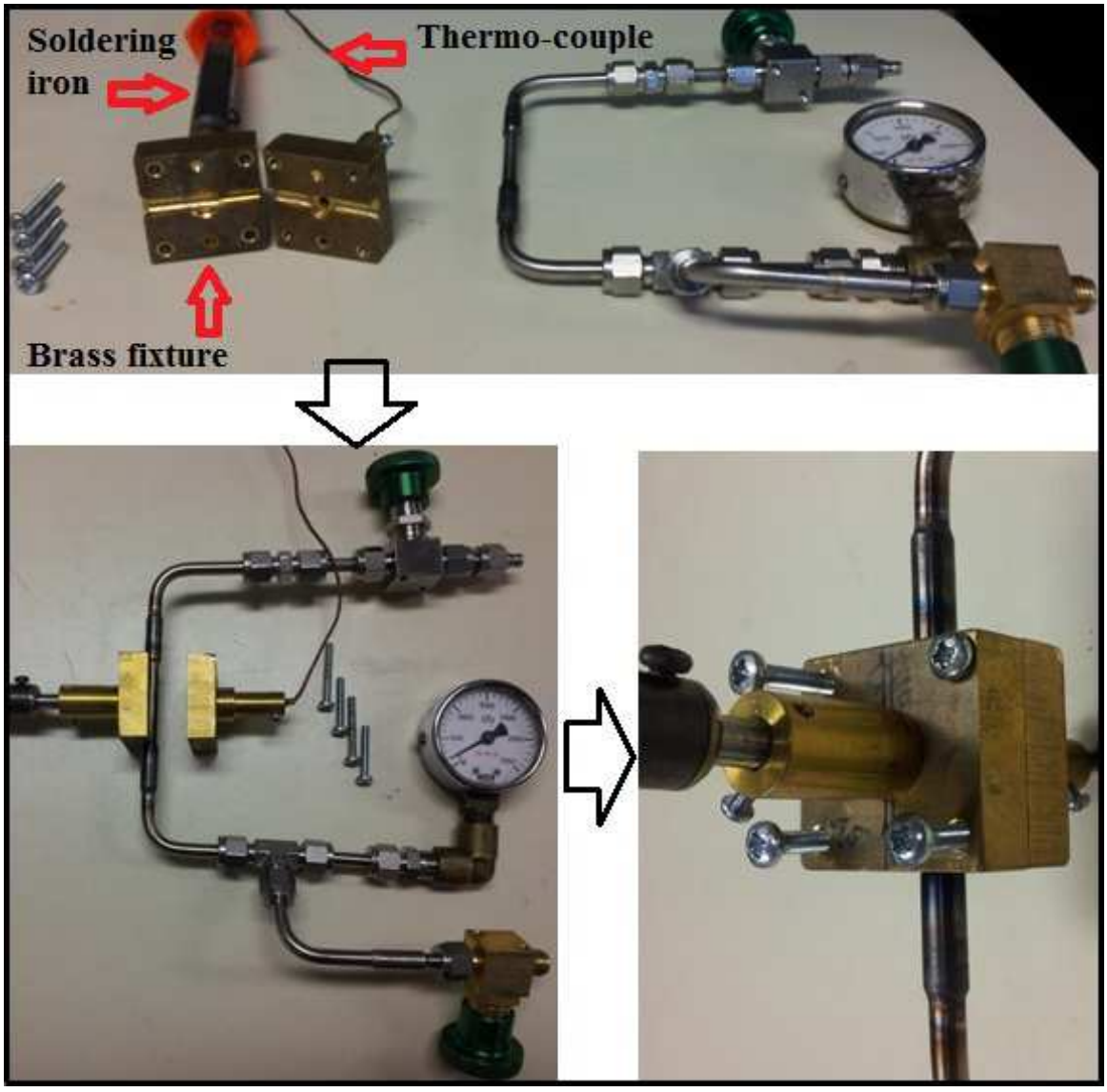

Figure 3-13 Set-up for elevated temperature tests.

To perform tensile tests at elevated temperatures, a brass fixture was designed and machined to surround tightly the gauge length of the sample (Figure 3-13). The fixture was connected to an 80 watt Duratech TS-1485 soldering iron. The power source of the soldering iron was supplied by a West MC 30/3D temperature controller, which monitored the temperature through the K type thermo-couple (with 0.75% error in temperature reading), connected to the brass fixture and controlled the heating current to soldering iron to maintain a consistent temperature. The temperature controller had a digital screen, which showed the temperature of the sample.

3.2 Electrolytic Hydrogen Charging

Electrolyte was made with high purity milli-Q water and concentrated H_2SO_4 in different normalities. $NaAsO_2$ was added as a hydrogen recombination inhibitor. Specimens were spot welded to a stainless steel wire for holding and current conductivity purpose. An AC to DC adaptor with ability to supply a constant current at two outlets was used to ensure that a constant current density was obtained (Figure 3-14a). The samples were suspended in the centre of a platinum mesh anode in an electrolyte inside a glass beaker (Figure 3-14a), and a current was passed through the circuit.

Cathodic hydrogen charging of the samples at a current density of 50 mA/cm^2 was performed in 0.5 N H_2SO_4 with 250 mg/L of $NaAsO_2$. Calibration curves were obtained by charging the samples for different times. To prevent the loss of hydrogen, the samples were stored in liquid nitrogen immediately after electrolytical charging. Since 1 to 5 ppm was reported [215] as the main range of hydrogen pick up during pipeline girth welding and installation, the hydrogen charging rate over time was then extrapolated to estimate the times needed for 2 and 4 ppm for TPB samples. These charging times were then verified experimentally.

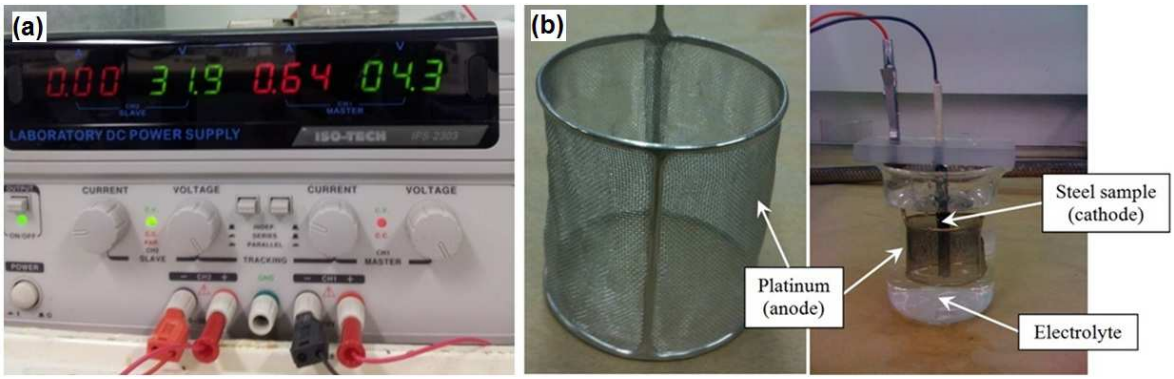

Figure 3-14 Constant current supply unit for electrochemical charging (a) and electrolytical hydrogen charging set-up (b).

TPB specimens were subjected to electrolytic charging immediately after the fatigue pre-cracking to ensure that crack surface was fresh.

3.3 Microstructure Characterisation Techniques

Samples for metallographic analyses were hot mounted in Bakelite, ground and polished according to standard metallographic methods for C-Mn steels [216]. The Struers TegraPol-21 machine was used for automatic grinding and polishing. Table 3-5 presents the program used for polishing test samples on this machine. The polished samples were etched using 2 % nital solution. Optical microscopy was performed on a Leica DMR optical microscope fitted with a DFC295 digital camera using Video Pro 32 version 6.003 software. Measurements of pearlite area fraction and ferrite grain size were performed using the standard point count method according to ASTM E 562 [217]. A total of 10 fields were counted using grids of 10×10.

Semi-quantitative Energy Dispersive X-ray Spectroscopy (EDS) analysis of the samples was carried out using a JEOL JSM-7001F field emission gun scanning electron microscope (FEGSEM). To analyse the type and distribution of inclusions and precipitates, automated particle analyser software, Esprit Steel (Bruker, Germany), was employed. An area of 5 mm × 2 mm of each sample was scanned. Scanning electron microscopy of the fracture surfaces was performed on a JEOL LV6490 SEM operating at 20kV. Prior to observation, specimens were subjected to an ultrasonic cleaning. For TPB samples, in order to achieve the best correlation only a region within 1 mm of the root of the fatigue crack was analysed.

Table 3-5 Polishing sequences for metallogeraphy samples

1	SiC paper	#220	2 minutes
2	Largo polishing plate	9µm	5 minutes
3	Dur polishing plate	6µm	5 minutes
4	Dap polishing plate	3 µm	5 minutes

3.4 Hydrogen Measurement Techniques

3.4.1 Inert gas melt extraction method

Measurement of the hydrogen content was performed on a ELTRA ONH-2000 machine (Figure 3-15a) located in the Central laboratory at BlueScope Steel, Port Kembla, approximately 12 km away from the mechanical testing lab at the University of Wollongong. The delay time between the end of the test and measurement was between 30 to 60 minutes, which was large enough for hydrogen to escape. In order to prevent loss of hydrogen before testing, the samples were kept in liquid nitrogen [178]. The hydrogen was measured by a fusion process, whereby the sample is melted and the released gases are analysed. This measurement method was selected because of its accessibility, accuracy and availability of trained and experienced operator.

The Eltra ONH-2000 machine is designed for the rapid and accurate determination of oxygen, nitrogen and hydrogen in steel and other materials. For hydrogen, it has sensitivity of 0.01 ppm and an indication range of 0-100%. The water cooled high power electrode impulse furnace uses a graphite crucible (Figure 3-15b) to heat the sample up to a temperature of 3000° C. Test pieces were taken from a small localised region (~2mm x 2mm x 5mm) of the charged TPB samples around the crack tip. This is the region where the crack grows during TPB testing, and hence is the most relevant to the fracture toughness results presented. Samples were dried, weighed and placed into the loading head and the graphite crucible is positioned on the lower electrode tip. The furnace closes, the crucible is outgassed, and then the sample is dropped into the crucible and the analysis proceeds. Due to the electrical resistance of the graphite, the graphite tip heats up the bottom of the crucible. This effect moves the hot zone from the middle of the crucible down to the bottom where the sample is located. Hydrogen concentrations are determined by a thermal conductivity detector (Figure 3-15c) and results are displayed on the monitor in ppm. The Eltra ONH-2000 was equipped with Uni software (Actual version 2.4.3.6). This software uses the same approach described in 3.4.2 to calculate the hydrogen amount in ppm.

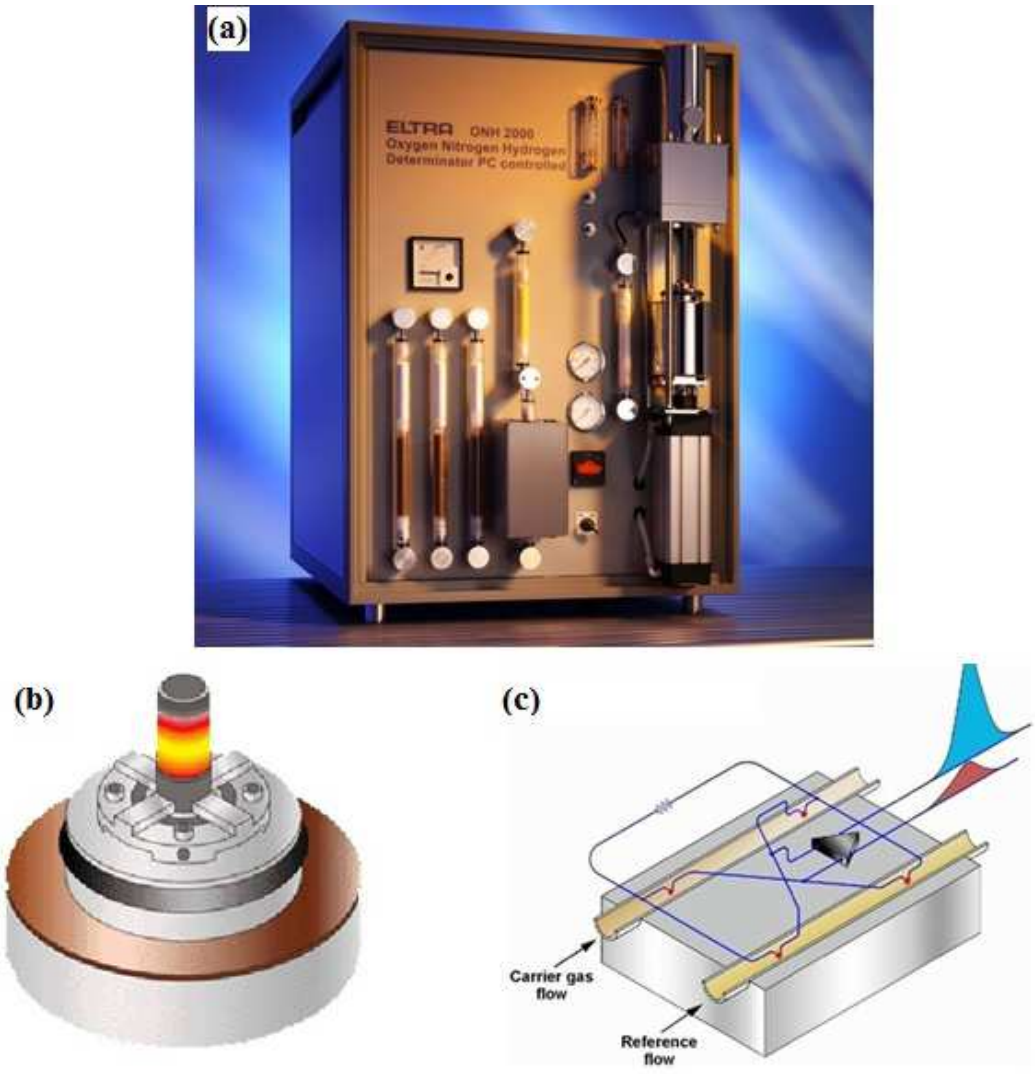

Figure 3-15 Eltra ONH 2000 machine (a), crucible placed on a graphite tip (b); and thermal conductivity detector (c) [218].

3.4.2 Mercury method for hydrogen measurement

The set-up for collection of hydrogen gas over mercury is shown in Figure 3-16. Testing was performed according to AS/NZS 3752:2006 [128]. To ensure the consistency of the results, three tests were conducted for each condition.

After hydrogen charging, the samples were immediately dried with a jet of air, weighed to the nearest 10 mg and left undisturbed in the Y-tube for 3 days at room temperature (around 20ºC). During this period of time the majority of diffusible hydrogen escaped and was collected in the capillary tube. The atmospheric pressure and room

temperature were recorded daily prior measuring the volume of hydrogen. The corrected volume of released hydrogen was calculated after considering the room temperature and barometric pressure, using Eq. 3-1:

$$V = \frac{273(P-H)(\pi r^2 \times C)}{760(273+T)\times 100} \quad 3\text{-}1$$

where: V is the corrected volume of collected hydrogen; P is barometric pressure in mm of Hg; H is the height difference of the top head of mercury between the two limbs of the Y-tube in mm; C is the height of hydrogen gas column above the mercury in mm; r is the inner radius of the capillary tube in mm; and T is ambient temperature at time of hydrogen measurement in °C.

In order to calculate the amount of hydrogen in ppm, the weight of hydrogen was needed. The equation of state for an ideal gas is Eq. 3-2:

$$pV = NkT \quad 3\text{-}2$$

where, p = atmospheric pressure, V = corrected volume of collected hydrogen, N= number of molecules in the gas, k = Boltzmann constant = 1.38×10^{-23} J.K^{-1} and T = temperature.

The formula for calculation of N is (Eq. 3-3):

$$N = nN_A = {}^{m}/_{M_m} \times N_A \quad 3\text{-}3$$

where n = number of moles in the gas, N_A = Avogadro constant = 6.03×10^{23} mol^{-1}, m = weight of collected hydrogen and M_m = molar mass.

The weight of collected hydrogen can be calculated using Eq. 3-4:

$$m = \frac{pVM_m}{N_A kT} \quad 3\text{-}4$$

Then the amount of hydrogen in ppm was calculated (Eq. 3-5) considering the total weight of the sample:

$$H_{ppm} = {}^{m}/_{m_t} \times 10^6 \quad 3\text{-}5$$

where m_t = total weight of sample [128].

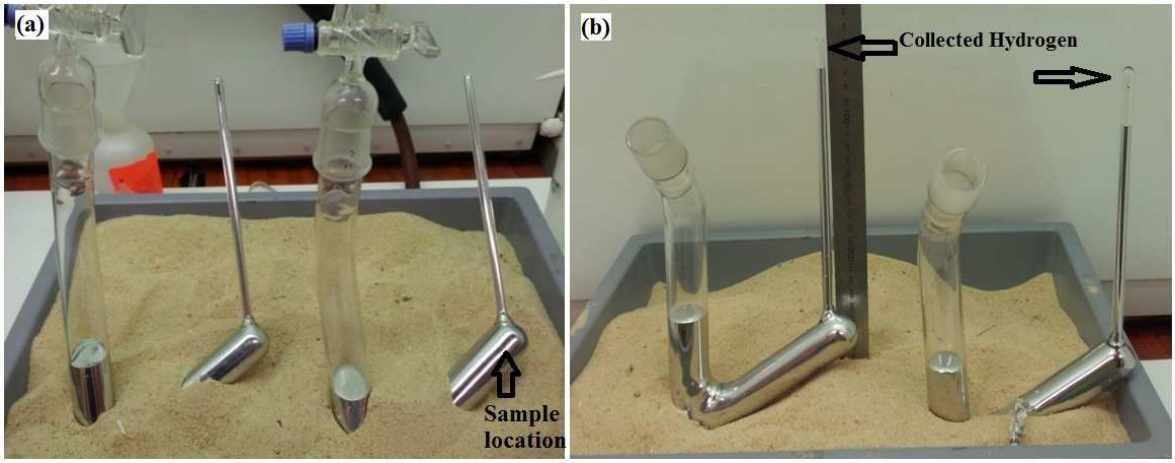

Figure 3-16 Apparatus for hydrogen measurement using mercury: (a) sample insertion and (b) hydrogen measurement.

3.5 Mechanical Tests

3.5.1 Hardness Test

Samples for hardness measurements were hot mounted in bakelite and polished using the method described in Section 3.3. The hardness values were determined through Vickers indentation hardness testing (Indentec Vickers machine) with a 20 kg load, using 5 measurements to give an average value. The standard deviation was also calculated. Hardness profiles of HAZ samples were taken along the rolling direction (ND-RD) on polished sections. The sections were located at the longitudinal centre of the samples.

3.5.2 Fatigue Test

The notched TPB samples were subjected to fatigue pre-cracking on an Instron 1341 machine using 4 KN load cell. The Syncrack software (Syncrack Version 1, developed by Arthur Carlton Synapse Technology Pty Ltd) was employed to carry out cyclic loading (Figure 3-17). The software used image processing via a Scout Basler video camera to measure the instant crack opening displacement. All specimens were pre-cracked according to ASTM E813 [139].

In general, Syncrack performs a fatigue test that repeatedly loads and unloads TPB samples to force the growth of a wire cut notch. The test is run until the crack has reached 1.5 mm, or until a specified number of cycles has elapsed, at which time a number of test results values are reported. The program allows a single shape of specimen to be used with crack opening determined by optically measuring the position of 2 contrasting dots located near the machined notch ends (Figure 3-18). The actual crack opening is calculated from the measured horizontal dot separation compensated for rigid movement of the slot opening corners. Initially a slow linear force ramp is used to apply the maximum cyclic load to the specimen. This fixes the sample in place. A cyclic force ramp (sine wave) is then started and the controller automatically ramps to the cycle mid-point before starting the periodic wave form.

The load used for pre-cracking, P_L, is a function of yield strength and is given by Eq. 3-6:

$$P_L = \left[\left(\frac{4}{3} \right) \left(\frac{B b_0^{\,2} \sigma_Y}{S} \right) \right] \qquad 3\text{-}6$$

where B, b_0, S and σ_y are effective thickness, original uncracked ligament, span and effective yield strength, respectively. To obtain a fatigue crack of 1.5 mm depth, maximum loads of 850 N and 1350 N were applied for the as-received and HAZ samples, respectively. The stress ratio and cycling frequency were 0.4 and 50 Hz, respectively. A range from 50,000 to 100,000 cycles was used for each specimen. The accuracy of flatness of fatigue crack was verified with heat tinting. For this purpose a few samples were put in the furnace at 400°C for 20 minutes, then put in liquid nitrogen for 10 minutes and broken in super cold brittle manner. The depth of the crack was measured at different positions.

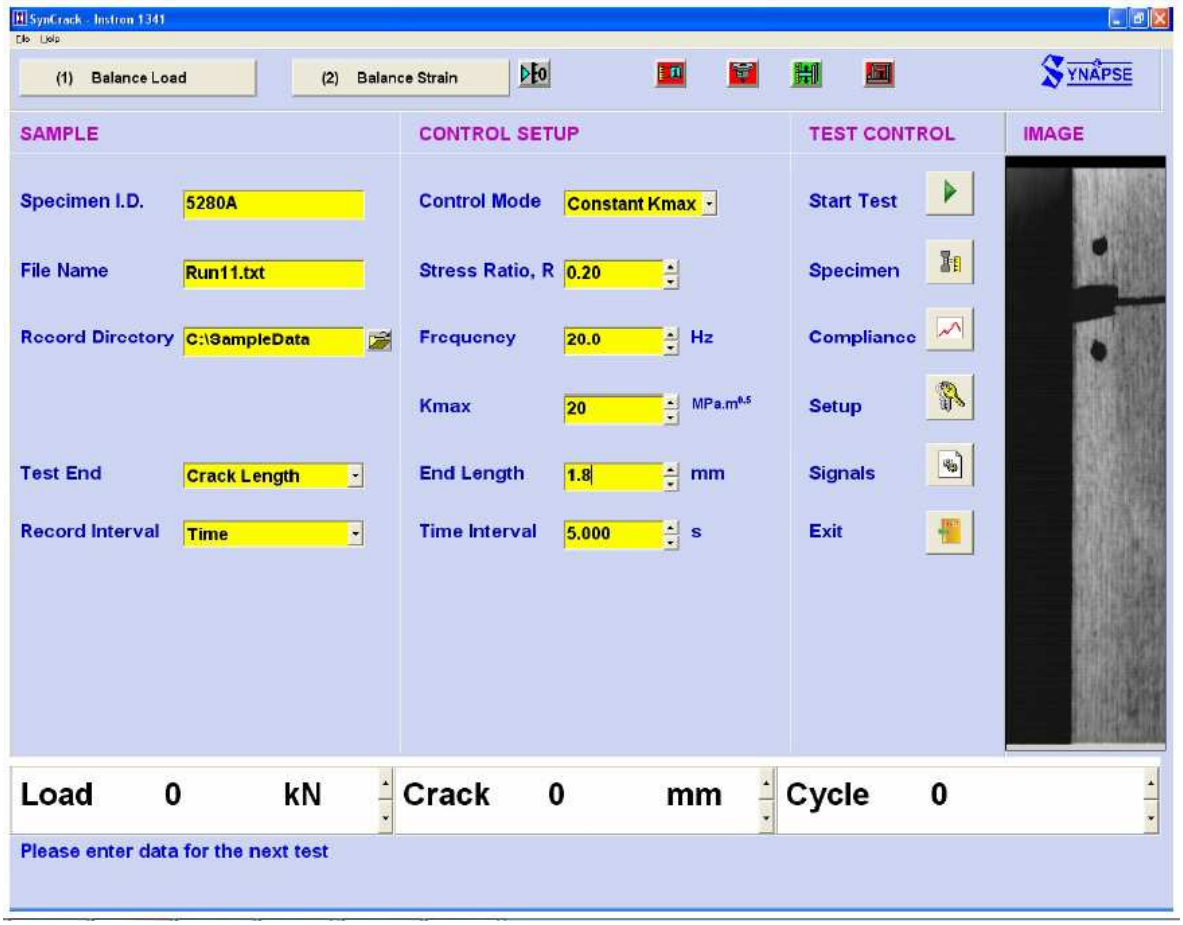

Figure 3-17 Syncrack main menu with instant optical monitoring the the crack length.

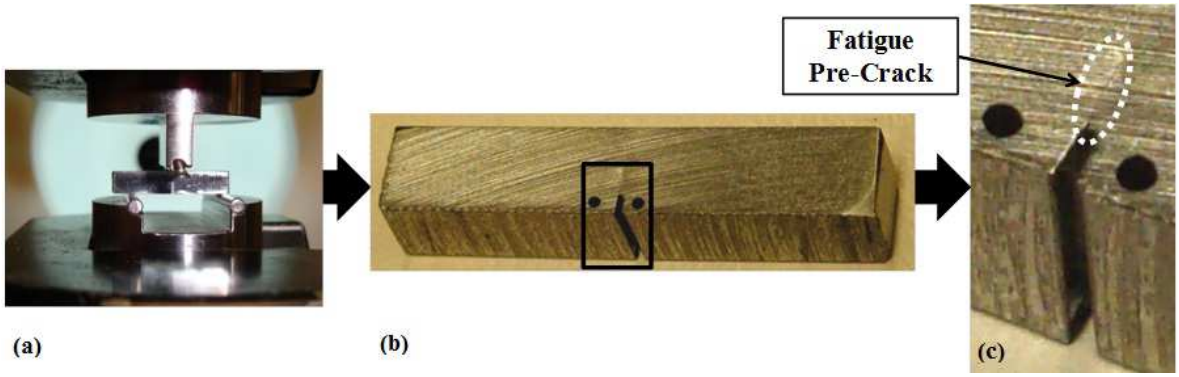

Figure 3-18 Fatigue test setup with digital camera and light source in background (a), TPB sample with fatigue crack and black dots to measure CTOD (b, c).

3.5.3 Three point bend test

The machining of the TPB setup including rollers and fixture was done to meet machined ASTM E813 requirements for tolerance [139] (Figure 3-19).

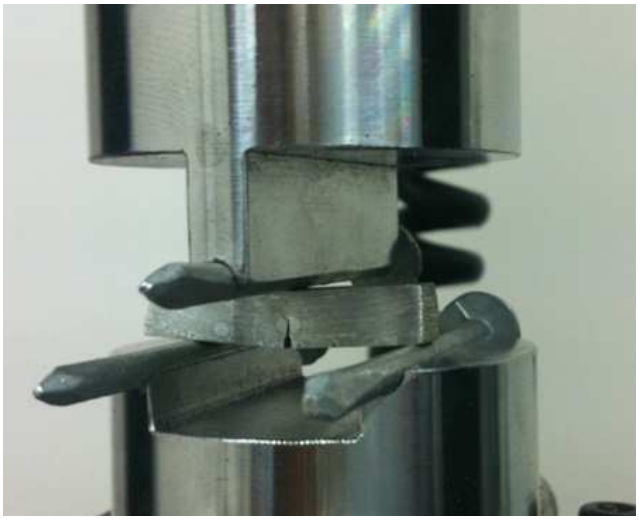

Figure 3-19 The designed fixture for TPB including rollers, top and bottom jaws.

Fracture toughness testing is most commonly performed using relatively large samples so as to maintain conditions of plane strain and maximum constraint [137]. In this study of the mechanical property of steels, the particular region of interest, such as the HAZ, may be quite small and its exact location may be unknown. In addition, the microstructures are heterogeneous. This makes preparing bulk samples from HAZ material very difficult, in that the notch and pre-crack must be directed at the region of interest and the subsequent crack growth must penetrate that region of interest during the test. This can be overcome by reducing the size of the sample to ensure that the entire region being tested is of the desired microstructure. However, reducing the size of the sample runs the risk of no longer satisfying the conditions of plane strain and maximum constraint.

As the sample dimensions are reduced, it is difficult to maintain predominantly elastic conditions during fracture testing in metals. In large samples, the plastic zone at the crack tip is relatively small compared to the specimen dimensions and its effect on the elastic conditions of loading is negligible. However, in small samples, this plastic zone at the crack tip becomes significant and the loading conditions are considered plastic-elastic

in nature. Therefore, it may be necessary to measure the crack tip energy release rate (J_I) under elastic-plastic conditions [138]. This can be achieved by calculating the critical crack tip energy release rate (J_{IC}) using the J-integral method [139]. This method involves determining the J-integral as a function of crack extension (Δa). The J-integral is calculated from the area under the load-displacement curve and the crack extension can be measured by either multiple specimen techniques (where different samples are tested to different loads and broken open to measure the crack length) or single sample in-situ techniques (where the crack length is determined by compliance measurements or electric potential drops during progressive loading/unloading of the sample).

The relationship between the J-integral and the crack extension is given by the J-resistance curve (illustrated in Figure 3-20), which is extrapolated back to a line corresponding to crack blunting, thereby giving a value of J corresponding to crack initiation (J_{IC}). Since the J-integral is path independent [141], it can be related to the fracture toughness (K_{IC}) in a large specimen by [144]:

$$K_{IC} = \sqrt{\frac{J_{IC} E}{1-\nu^2}} \qquad 3\text{-}7$$

where E is the Young's modulus and ν is the Poisson's ratio.

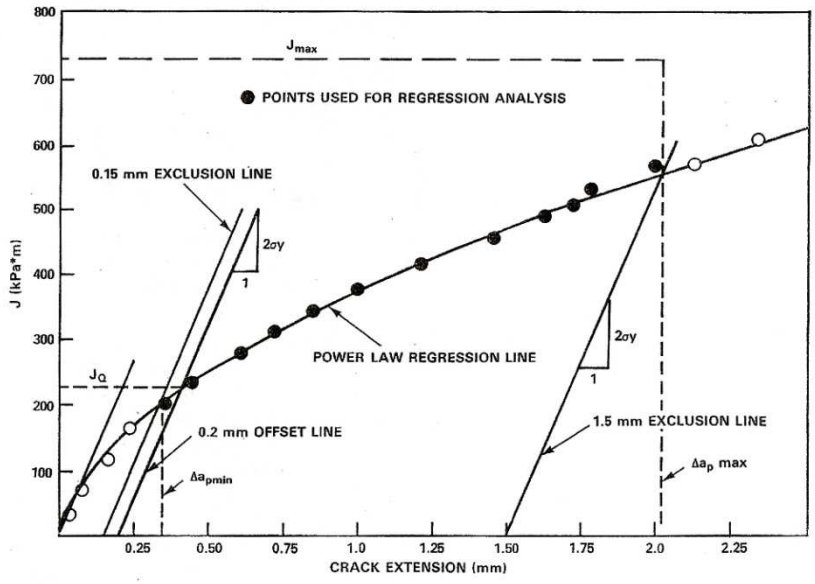

Figure 3-20 J-resistance curve used to determine J_{IC}.

Such methods have been used to determine the fracture toughness of a number of sub-sized specimens down to thicknesses as small as 1.02mm with very little effect on the obtained J_{IC} values [144-147].

In order to minimise hydrogen loss, TPB tests were conducted within 10 minutes of charging and samples were kept in liquid nitrogen immediately after hydrogen charging. The test was carried out on an Instron 5566 machine with 10 KN load cell, using Bluehill 2 version 2.14 software. Before testing, the samples were washed in ethanol to bring the samples to room temperature, then quickly dried and placed in the three-point bend rig for testing. The samples were subjected to a series of loading-unloading cycles according to ASTM E813 [139] using the single specimen method at a speed of 0.2 mm/min and load vs. load line displacement curves were obtained. Crack extension was calculated from the load line displacement as follows:

$$a = W \times \left(0.997 - 3.58\,U - 1.51U^2 - 110\,U^3 + 1232\,U^4 - 4400\,U^5\right) \qquad 3\text{-}8$$

where, a is the crack length, W is the sample width and U is given by Eq. 3-9:

$$U = \frac{1}{\left(1 + \sqrt{EB\delta / F}\right)} \qquad 3\text{-}9$$

where, δ, E, B and F are crack opening displacement, the elastic modulus, sample thickness and the applied load, respectively. A six megapixel Canon IXUS 60 digital camera was installed on the side of the instrument to monitor crack opening displacement during load-unloading. The data collected by a digital camera during the TPB tests were used to verify δ. The J integral versus crack extension curves were obtained in accordance with the method specified in ASTM E813 [139] and the conditional value of fracture toughness, J_Q, was calculated. After calculation of crack extension and J_Q, the J-R curves were then plotted.

3.5.4 Tensile test

In order to test the effect of gaseous hydrogen, hollow cylindrical tensile samples from X70, MX70, NTB and ERW zone of pipe were pulled in uniaxial tension at 25, 50 and 100 ºC with 10 MPa pressure of gaseous hydrogen inside. The tests were performed on

an Instron 1341 tester using Syntest software (Syntest Version 1, developed by Arthur Carlton Synapse Technology Pty Ltd) (Figure 3-21). For comparison, the samples were filled with 99% high purity either 10 MPa hydrogen or argon. A safety plastic glass shield was installed around the tensile jaws to avoid projection of metal pieces after necking when hydrogen possibly can explode the thin remaining pipe wall.

Assuming a local equilibrium of hydrogen will exist directly at the surface, its concentration depends only on temperature and pressure. Therefore, by performing tensile tests in a gaseous hydrogen environment, the immediate effect of hydrogen can be established.

To allow time for hydrogen diffusion, all samples were pulled at the slowest possible cross head speed (0.003 mm/s) until fracture. At least 3 samples were tested per condition. Force and displacement were recorded and converted to equivalent engineering strain and stress with Instron software assuming ideal plane strain compression conditions. Inhomogeneities in strain distribution are known to form through the specimen thickness in plane strain condition experiments. However, these inhomogeneities were ignored, since the objective of these experiments was to compare the behaviour of different steels.

The true stress-strain curves were plotted. The standard deviation was calculated based on tensile strength and maximum strain. To investigate the work hardening behaviour, the work hardening rate ($d\delta/d\varepsilon$) is plotted against true strain. As an alternative to physical modelling, several empirical stress–strain equations have been used to describe plastic deformation behaviour.

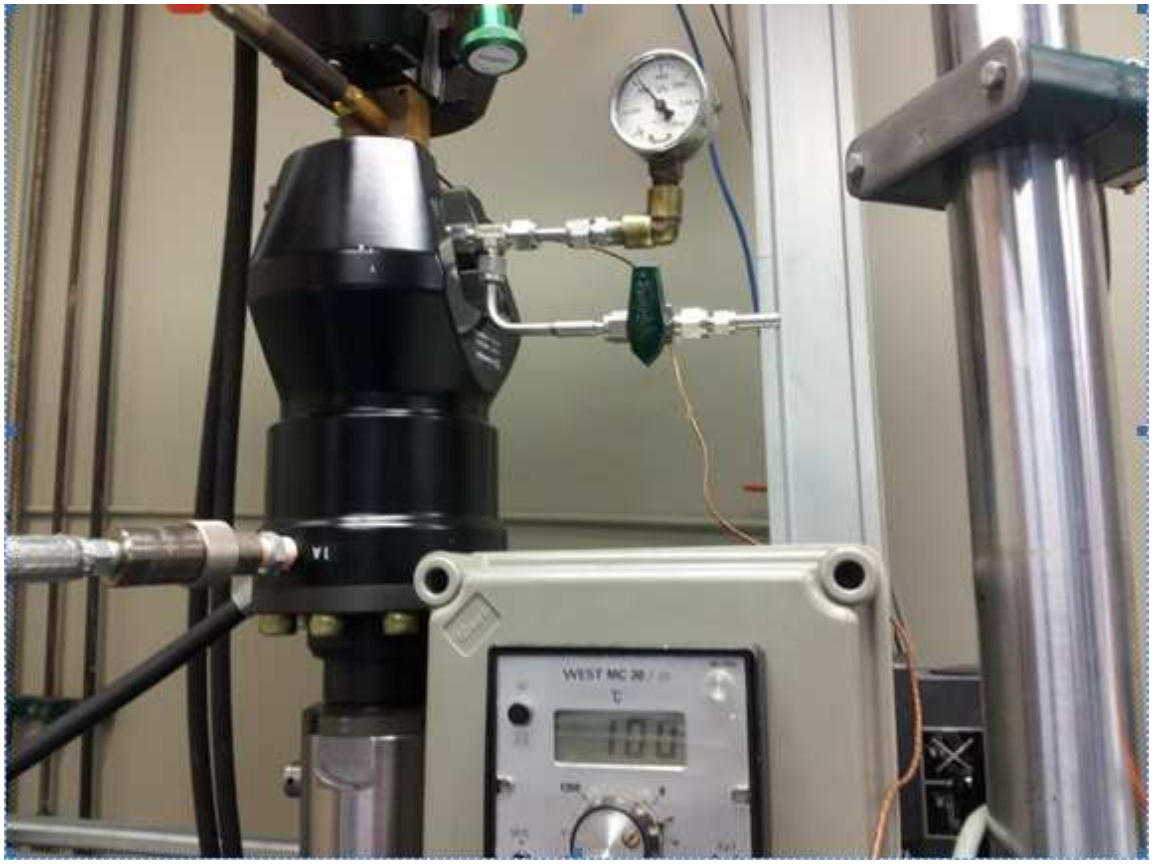

Figure 3-21 Tensile test on the sample with 10 MPa hydrogen inside at 100°C.

4 MICROSTRUCTURE CHARACTERISATION

This chapter begins with characterisation of microstructures of X70 strip, X70 transfer bar, X70 normalised transfer bar and the HAZ. In addition, data on grain sizes and hardness are provided.

The chapter closes with the description of precipitates and inclusions present in both studied steels by means of optical metallography, SEM, EDS analysis and X- ray mapping.

4.1 Microstructure Characterisation

4.1.1 X70 transfer bar

The microstructure of as-received X70TB in transverse direction was characterised by optical metallography, Figure 4-1. The photographs were taken from the upper edge towards the lower edge in 2 mm steps. The microstructure changes from predominantly polygonal ferrite (PF) with islands of pearlite near the edge of the top surface of transfer bar to granular bainite (GB) with a bit of bainitic ferrite (BF) in the centre.

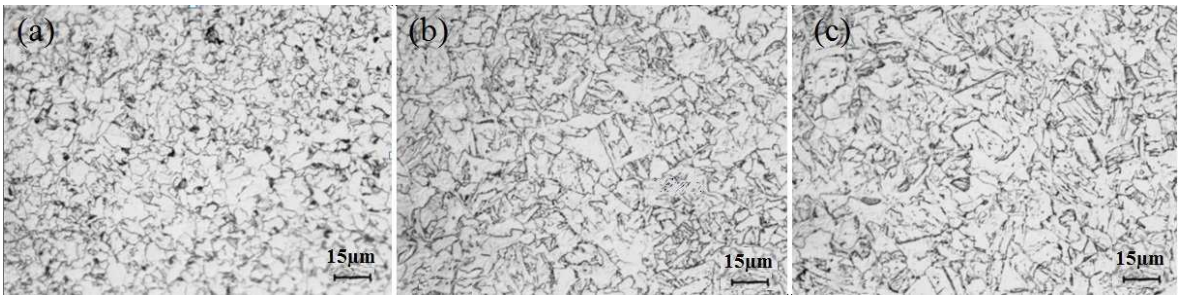

Figure 4-1: Evolution of the microstructure in X70TB sample cut perpendicular to the rolling direction: edge (a), 1/4 thickness (b) and centreline (c).

Considering the different microstructures across the transfer bar, normalising at 900ºC for 20 minutes was carried out to obtain a more uniform microstructure. The microstructure of normalised transfer bar is an equiaxed ferrite-pearlite microstructure with an average grain size of 14±0.5 µm (Figure 4-2). The area percentage of pearlite was determined to be 12±1%.

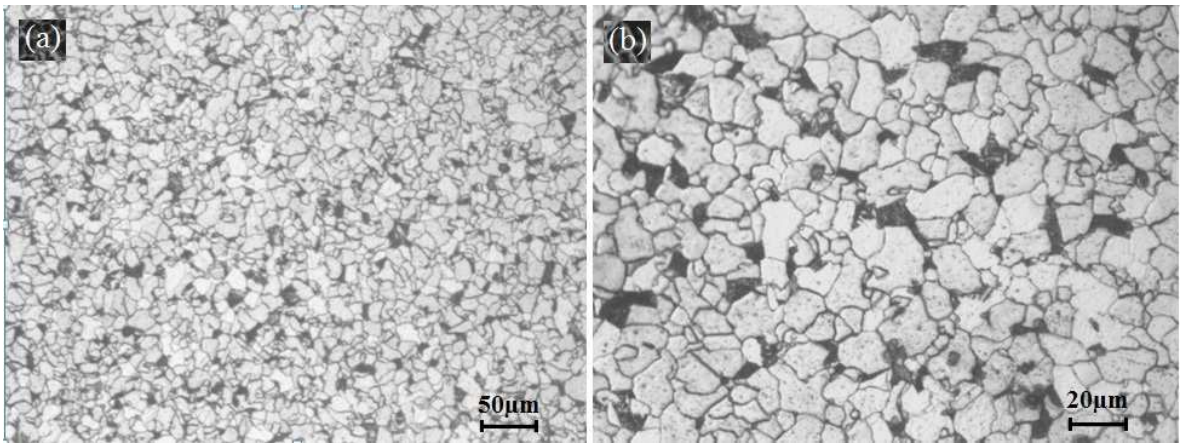

Figure 4-2: Microstructure of X70TB after 20 minutes normalizing at 900ºC.

4.1.2 X70 strip

The microstructure of X70 strip samples was characterized at the edge (Figure 4-3 a,b) and centreline (Figure 4-3 c,d) of a 10 mm thick sample. The microstructure was a mixture of ferrite and pearlite grains (Figure 4-3 and Figure 4-4). The ferrite-pearlite grains were present in bands parallel to the rolling direction in the centreline region. The edge region consisted of a combination of fine ferrite grains with an average size of 5.1±1.3 µm and some coarse ferrite grains with an average size of 12.7±3.5 µm. The grain size distribution in the centreline region was also bimodal with a mean size of 5.4±0.6 µm for fine ferrite grains and 11.8±4.8 µm for the coarse grains. The overall average ferrite grain size was 8.1±4.8 µm for the edge region and 8.9±4.9 µm for the centreline of the strip. The coarse ferrite grains were more prevalent at edges than centreline region. The area fraction of pearlite was determined to be 9±0.8%. These results are consistent with data in literature [2, 219].

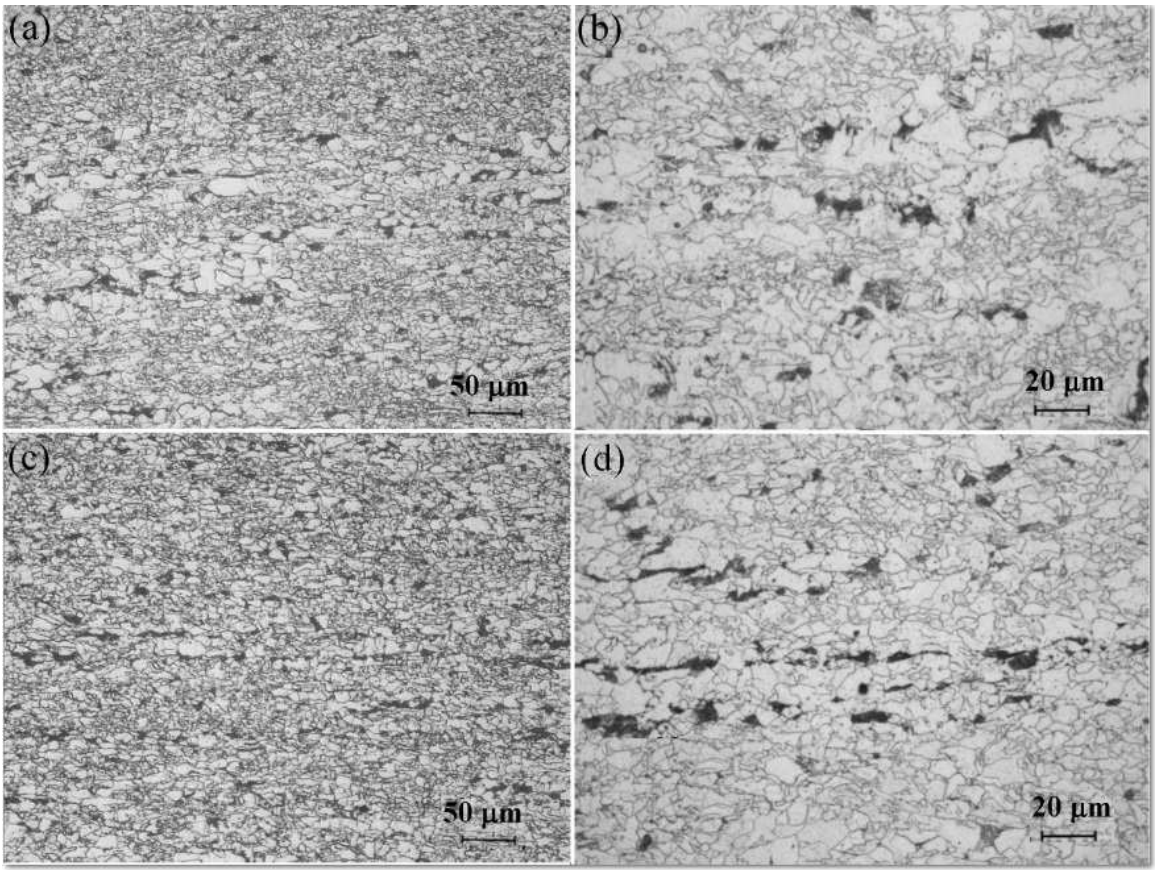

Figure 4-3: Optical micrographs taken from (a), (b) edge and (c), (d) centreline regions of X70 strip.

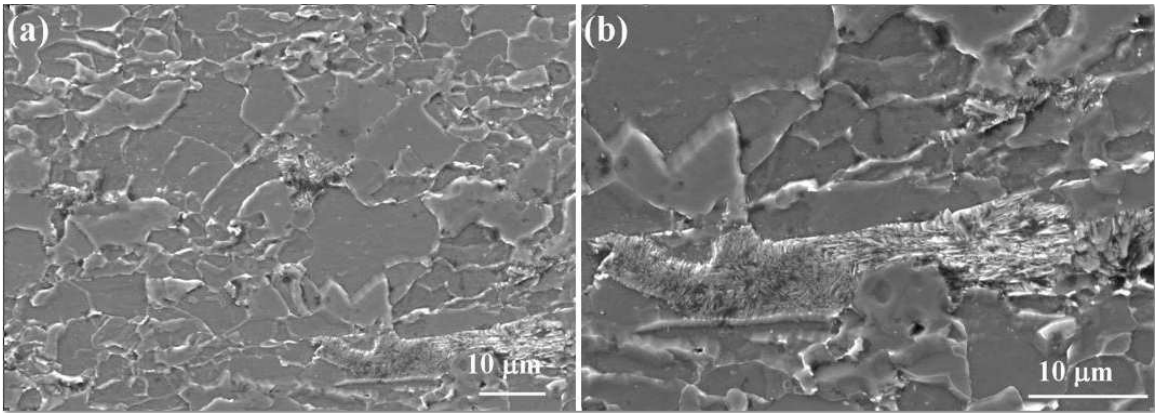

Figure 4-4 Secondary electron micrographs of X70 strip showing ferrite-pearlite microstructure

Inclusions were observed in the centreline region of sample. The inclusions had elongated, spherical or irregular morphologies, as shown in Figure 4-5.

EDS analysis carried out on these inclusions, indicated that inclusions were mostly MnS. A few particles such as the one marked by an arrow in Figure 4-5a, also contained Fe, Ca and very small amounts of Al and Mg (Figure 4-6), in addition to Mn and S.

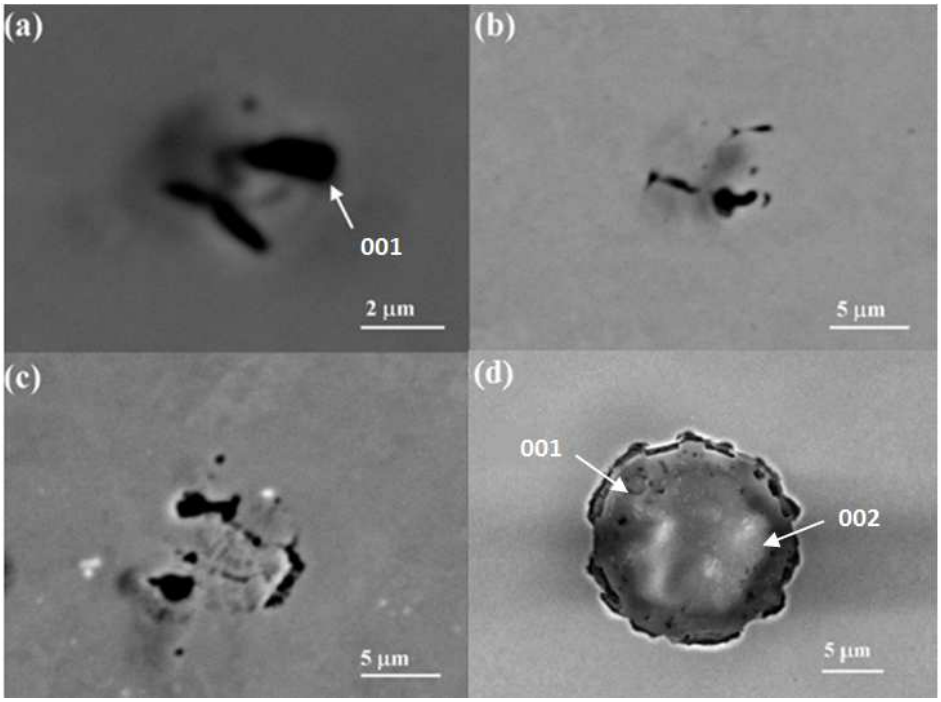

Figure 4-5: Back scattered electron images of inclusions in the centreline region of X70 strip.

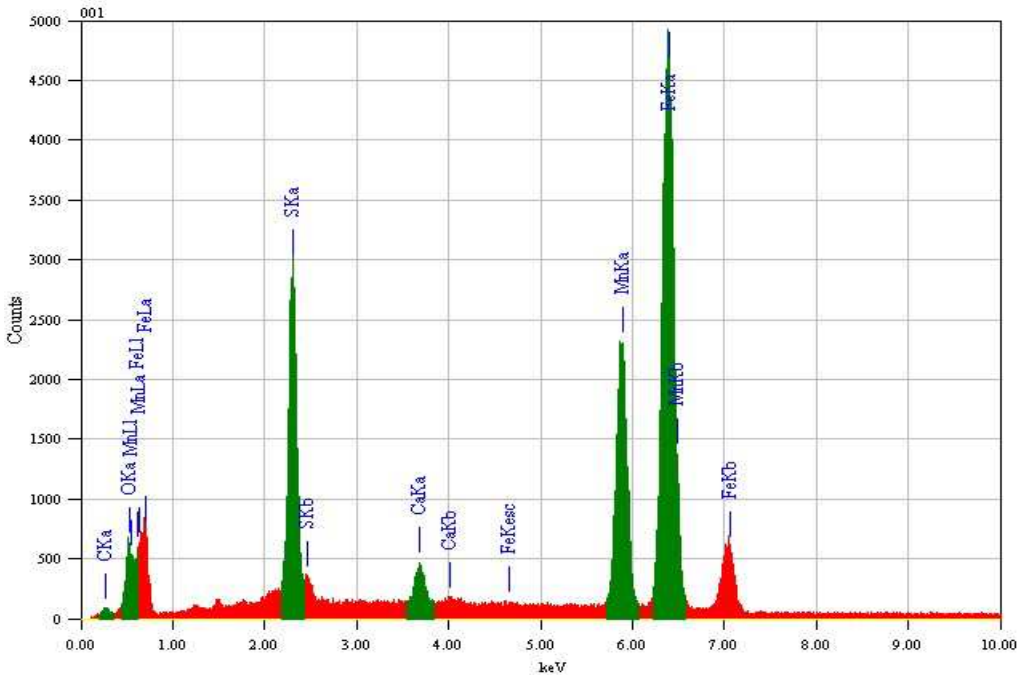

Figure 4-6 EDS spectrum of the particle indicated by the arrow in Figure 4-5 a.

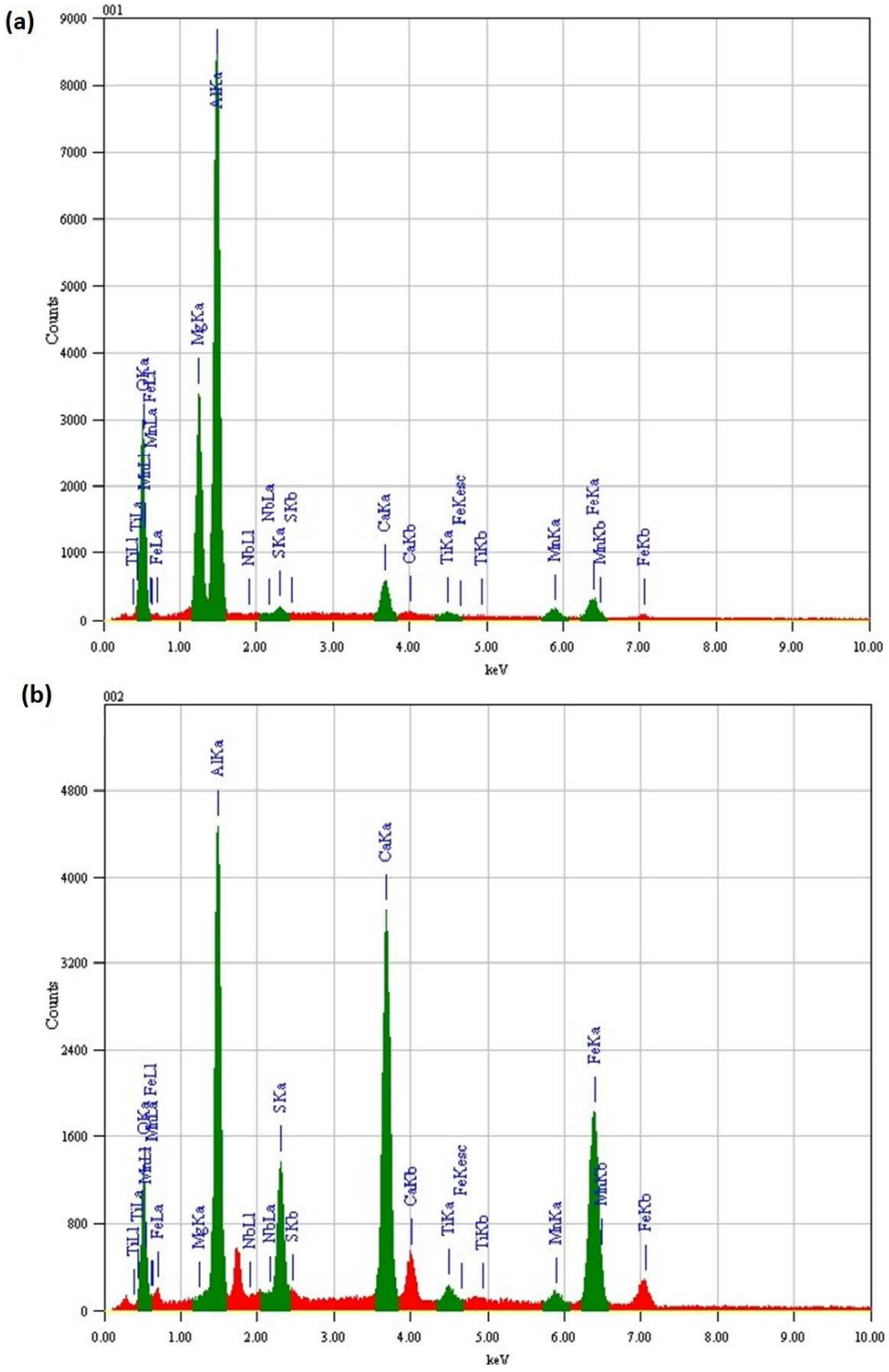

Figure 4-7 Point EDS spectra taken from different regions of the inclusion in Figure 4-5 d

Figure 4-5d shows one large inclusion with a diameter of ~15 µm and Figure 4-7 presents point EDS spectrum taken from different regions of this inclusion. The results revealed that this inclusion is an AlCa oxysulphide containing a large amount of Mg and Fe in some regions and small amounts of Ti and Mn in some other regions.

Figure 4-8 shows the distribution of elements in another large inclusion by x-ray mapping. Fe, Al and Ca are the major elements in this inclusion.

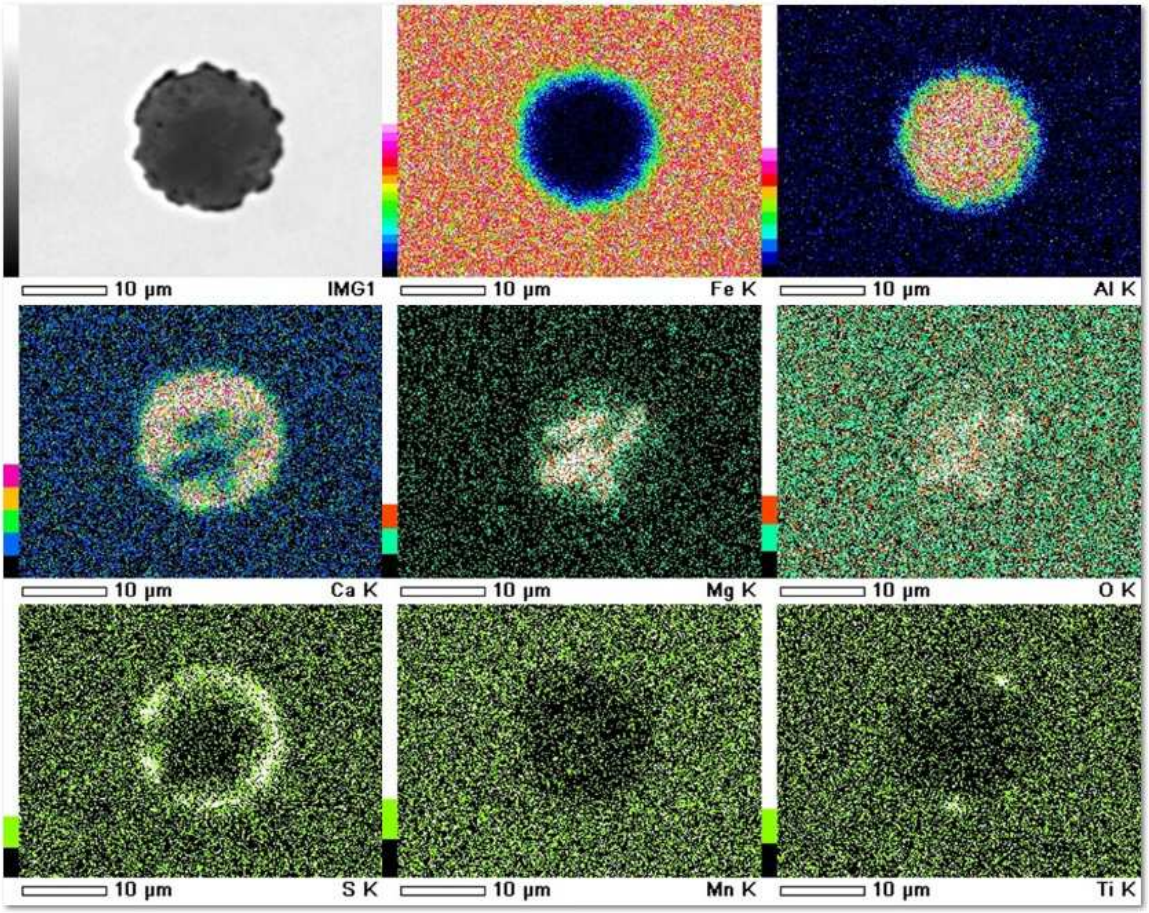

Figure 4-8 X-ray maps showing the distribution of different elements in a large inclusion.

4.1.3 MX70 strip

The microstructure of the hot rolled MX70 pipeline steel is shown in Figure 4-9. As for X70 steel, ferrite - pearlite structure was dominant. The bimodal type grain size distribution found in edge and centreline regions of X70 was not found in MX70, which had more uniform ferrite grains than X70. The average ferrite grain size was 8.5±1.8µm for

edge and 9.4±1.8µm for centreline. The area fraction of pearlite was determined to be 11±1 % Unlike X70, several elongated MnS stringers with some blocky inclusion among these stringers, were observed in the centreline region of the sample but there was no banding of ferrite and pearlite there (Figure 4-9c,d).

Figure 4-10a shows a SEM image of the inclusions and the mentioned stringers can be found in Figure 4-10b and c. Figure 4-10d shows a magnified image of blocky inclusion found along the MnS stringers.

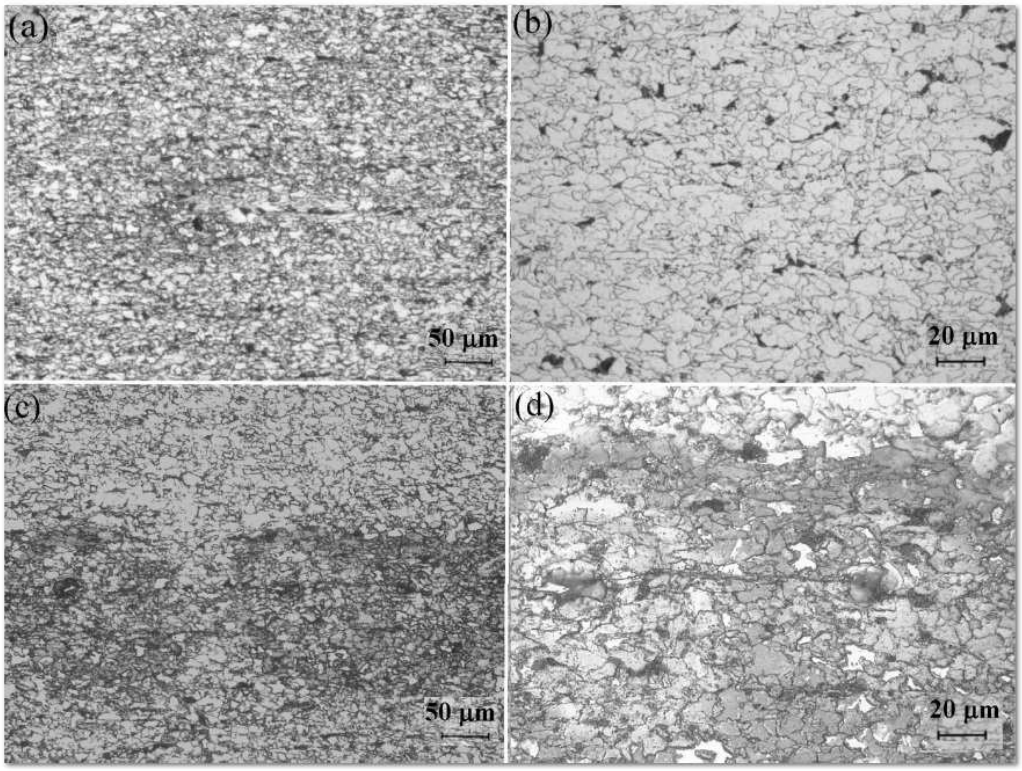

Figure 4-9 Optical micrographs taken from (a), (b) edge and (c), (d) centreline regions of MX70 strip.

The x-ray maps of the stringers (Figure 4-11) confirm that the stringers are MnS. X-ray maps of the blocky inclusions that were found in line with the stringers are shown in Figure 4-12, which reveals the presence of Nb, Ti, C and S. In addition to MnS stringers and the associated blocky inclusions shown in Figure 4-13, several independent inclusions that had spherical or irregular morphologies, were also observed (Figure 4-13 a,b). Some of these were very large in size, up to 20 µm in diameter. These were the typical CaAl

oxysulphides and they also contained some Mn and S, as revealed in the x-ray spectra (Figure 4-14).

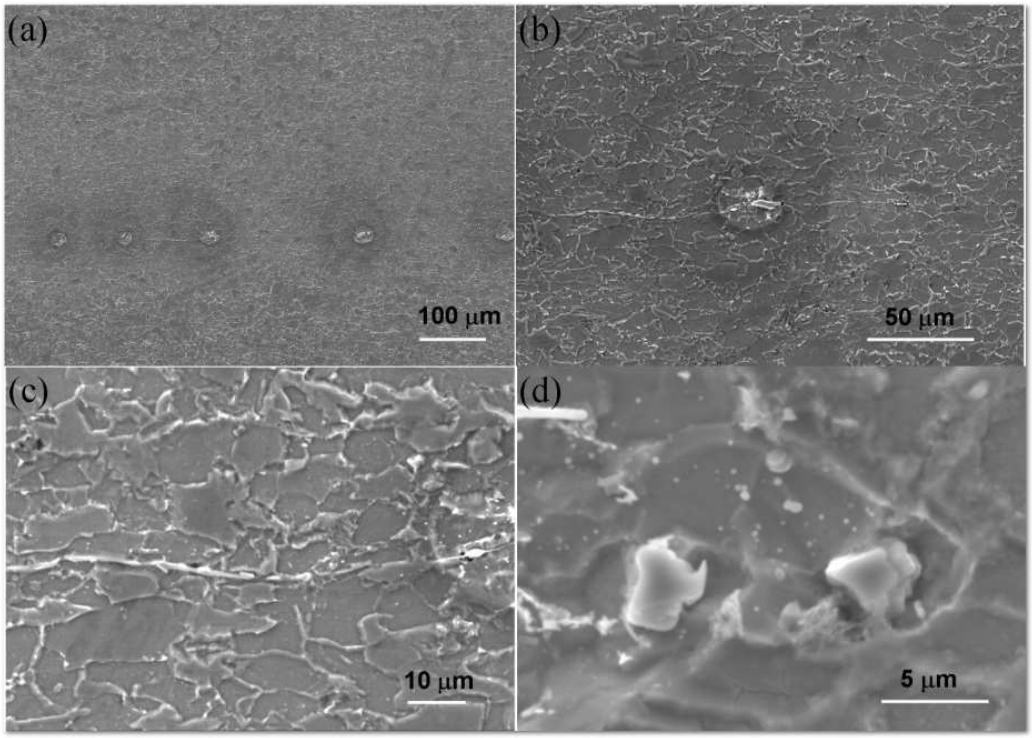

Figure 4-10 Secondary electron micrographs of the centreline region of MX70 strip showing MnS stringers and the blocky inclusions along the stringers.

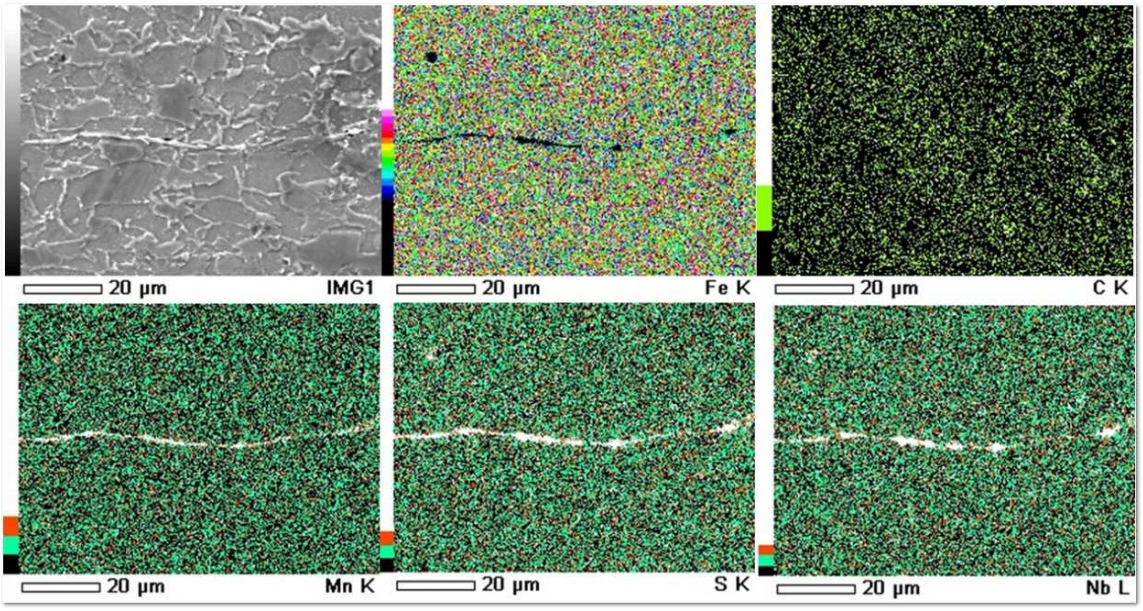

Figure 4-11 X-ray maps of centreline region of MX70 strip showing the distribution of elements in the stringer.

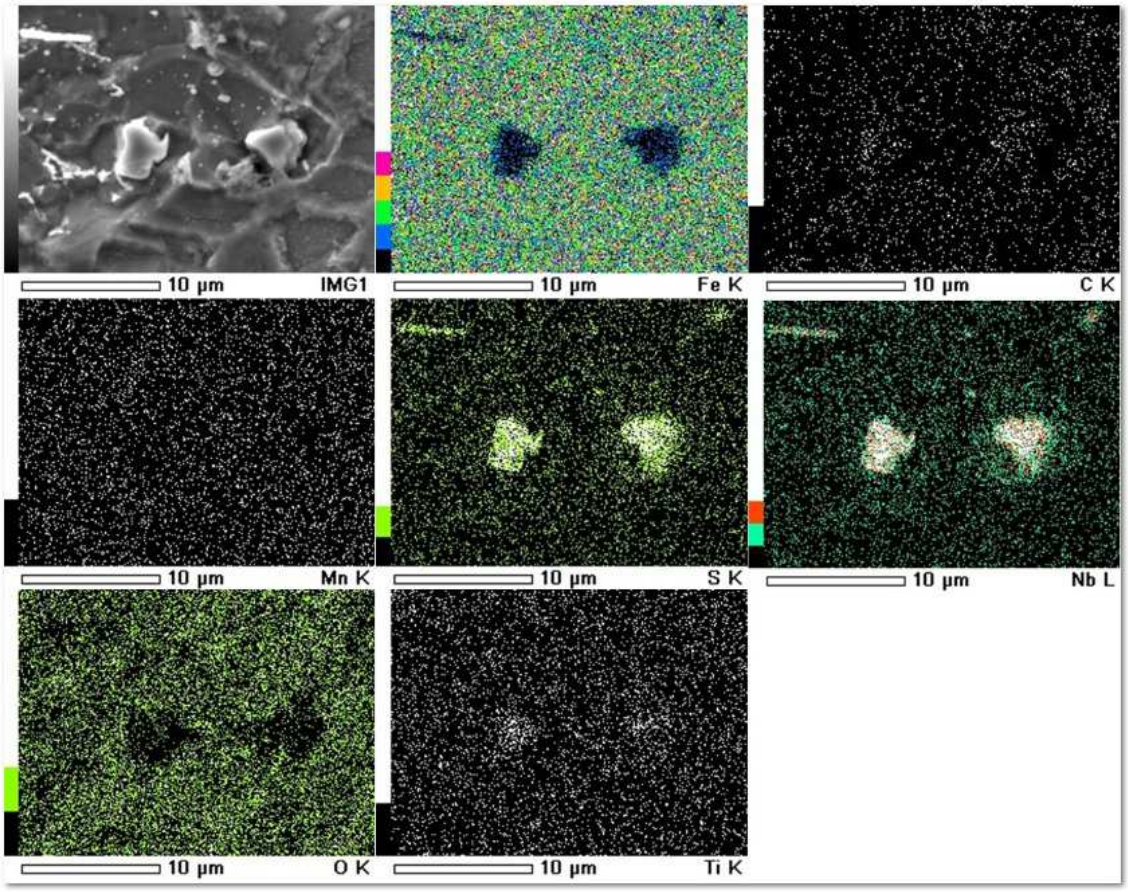

Figure 4-12 X-ray maps showing the distribution of different elements in the blocky inclusions that were present in line with the stringers.

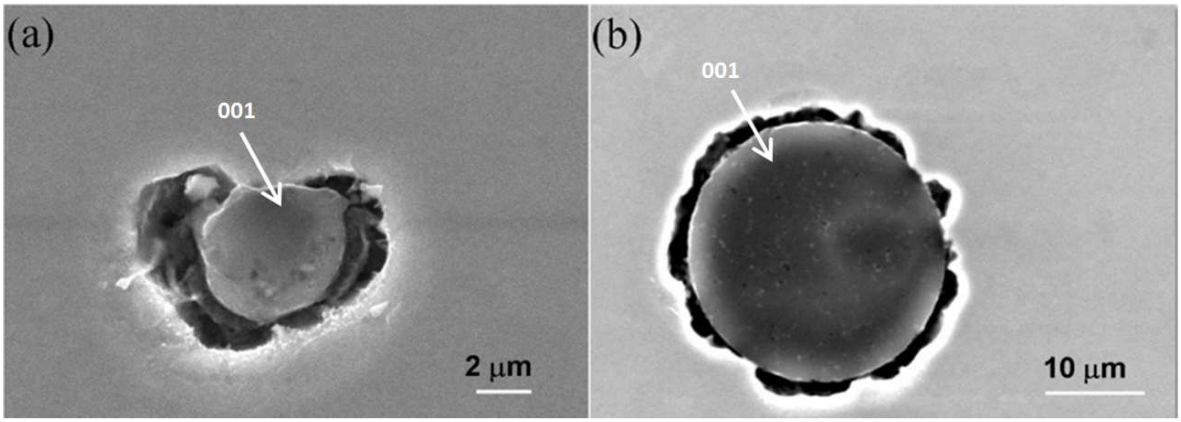

Figure 4-13 Secondary electron images of inclusions in the centreline region of MX70 strip.

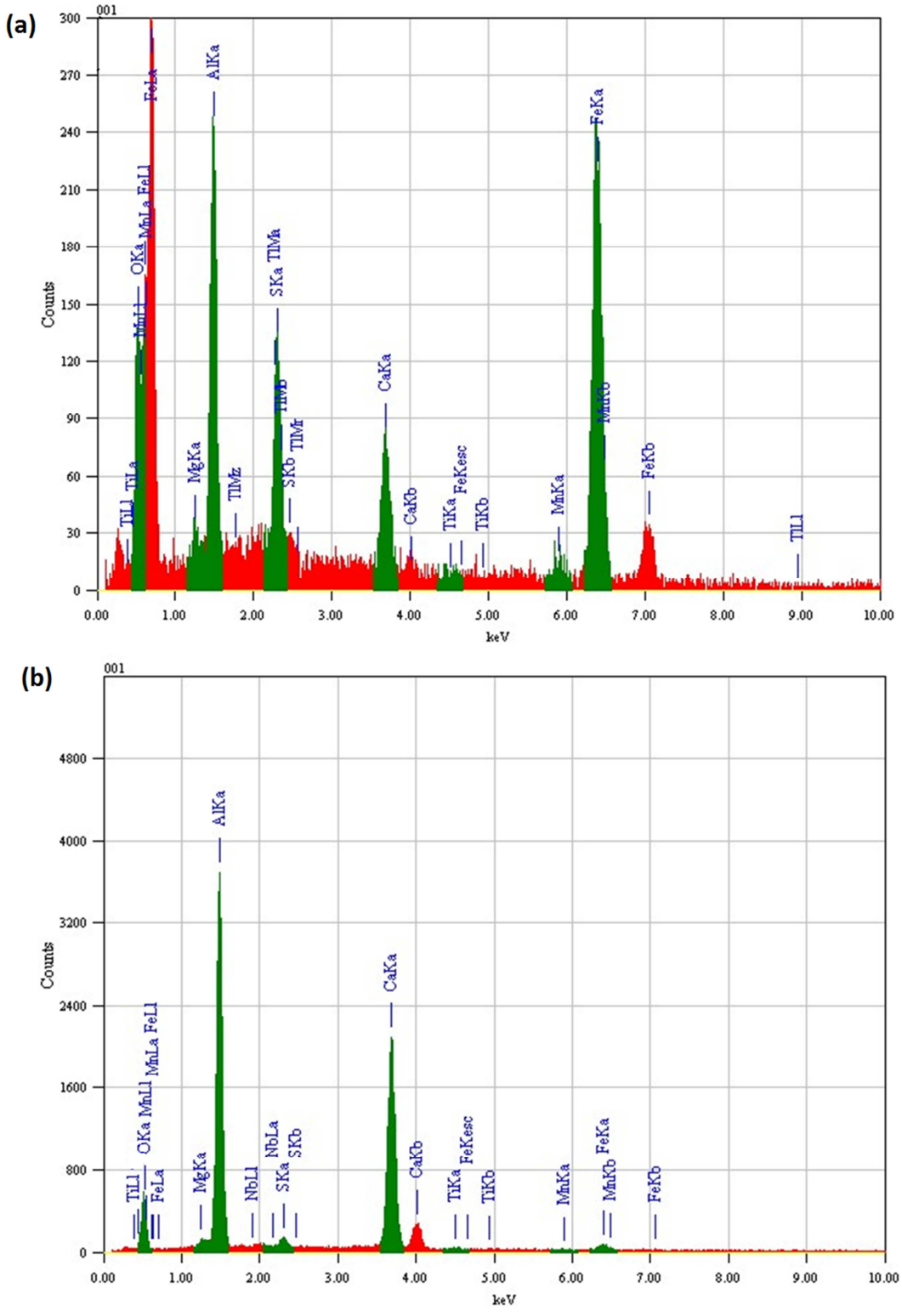

Figure 4-14 Point EDS spectrum taken from different regions of the inclusion shown in (a) Figure 4-13a and (b) Figure 4-13b.

4.1.4 Gleeble HAZ samples

Figure 4-15a and b show a comparison between the simulated HAZ structure of X70 and MX70. The HAZ microstructure (Figure 4-15) consisted predominantly of coarse bainitic ferrite laths with aligned interphase M/A islands. The ferrite laths formed in the X70 HAZ sample were finer than those present in MX70 HAZ (Figure 4-15 a and b), this is possibly due to higher hardenability and carbon equivalent of the X70 steel which causes the transformation on cooling starts at lower temperature range.

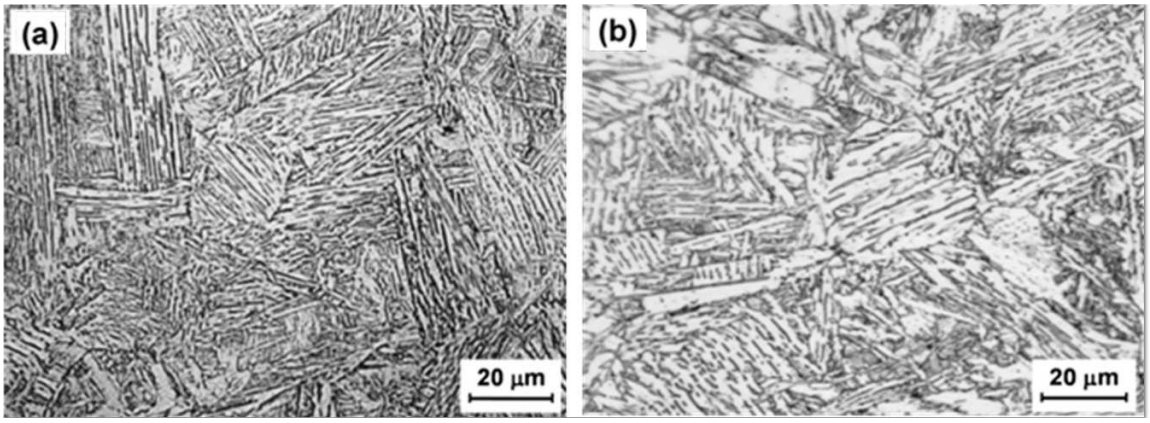

Figure 4-15 Microstructures of (a) X70 HAZ and (b) MX70 HAZ

4.2 Hardness Profile

Figure 4-16 shows the hardness profiles for the two steels after HAZ simulation. The gradients indicate that the simulated HAZ extended over a distance of about ± 10 mm from the sample centre. The approximately constant hardness of this central zone was about 265 HV for X70 and 222 HV for MX70, indicating that, for the same cooling rate during Gleeble simulation, the X70 transformed to a structure with a higher strength than the MX70 steel. This could be due to more Mn in solid solution causes solid solution strengthening. The X70 HAZ region exhibited a hardness about 50 HV points higher than the base metal, whereas the difference was ~ 20 HV points for MX70.

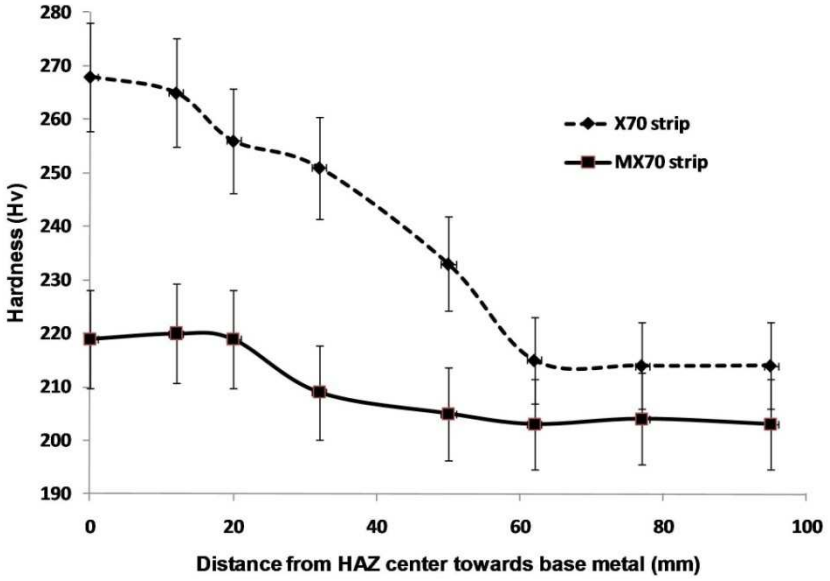

Figure 4-16: Hardness profile of X70 and MX70 from base metal to HAZ.

4.3 Further Analysis of Precipitation and Discussion

The average ferrite grain size was slightly larger in MX70 compare to X70 steel. This supports Schambron *et al.* work [220] who found the Ar_3 of the Low Mn X70 was about 50°C higher than for the higher Mn X70. The higher Ar_3 promotes the formation of coarser ferrite grains. Simulations of their entire hot rolling process showed the high Mn X70 had a finer ferrite grain size compared to the low Mn X70.

Although there was little difference in the amount of pearlite for the X70 and MX70 steels, pearlite banding was more evident in the hot rolled X70 strip, consistent with its higher Mn level and more pronounced compositional segregation.

The number of precipitate particles per square mm was determined using SEM with particles $\geq$ 0.25 μm being counted. Since the number of particles per mm^2 was found to be significantly higher in the MX70 sample (77 mm^{-2}) than in X70 (38 mm^{-2}), the X70 steel is much "cleaner" than the medium Mn version, in terms of areal density of inclusions/precipitates. The results of EDS microanalysis of the precipitates are shown in Figure 4-17, which is a plot of the numbers of the different types of precipitates detected in the test area for the two steels. A major difference, evident in this plot, is that the areal

density of nitrides in MX70 was more than an order of magnitude higher than for X70. Most of these nitrides were complex (Ti,Nb)(C,N) precipitates. This striking difference between the standard and medium Mn steels is likely to be due to the higher Ti, C and N contents of the MX70 steel (see Table 3-1), which resulted in a significantly larger fraction of carbonitride precipitates. The numbers of sulphide inclusions per unit area, particularly MnS and complex MnS, were almost the same for both steels. Since the S contents of the two steels were the same (0.002%) and both Mn contents are well in excess of that required for the stoichiometric ratio (Mn:S = 1.71:1), the volume fractions of sulphides in the two steels would be expected to be approximately the same. The volume fractions were not determined, but the total numbers of S-containing precipitates per unit area were similar for the two steels (Figure 4-17b). In contrast, the number of oxides in the MX70 strip was almost double that observed for the X70 strip. These oxide inclusions usually contained Fe, Ca, Al, Mg and Mn, and a small amount of Ti was present in about 50% of these precipitates. These results are consistent with the literature [221].

The mean sizes and the size distributions of the (Ti,Nb)(C,N), Ca-Al oxides, and the aspect ratio of MnS precipitates in the two steels are shown in Figure 4-18. The (Ti,Nb)(C,N) precipitates in MX70 strip exhibited a unimodal distribution with an average diameter of 0.8±0.8 μm. The size distribution of the precipitates was very broad with a long tail (not shown in Figure 4-18a), with some precipitates having diameters in the range 3-5 μm. On the other hand, the X70 strip showed a bimodal distribution with mean sizes of 0.6±0.2 and 2±0.3 μm. However, it should be noted that the number of the nitrides per unit area for the MX70 sample was significantly higher than that for the X70 strip.

The mean aspect ratio of MnS particles in the MX70 strip was larger than that of the X70 strip. The distribution of aspect ratios of MnS particles in the MX70 strip was also wider and had a long tail (Figure 4-18b). Although the aspect ratio for MnS particles in MX70 extended up to about 20:1, the mean ratio was 7±5. For X70, the mean aspect ratio was 3.2±2. The present results are not consistent with the reported trend of reduced plasticity and lower aspect ratio of MnS particles with decreasing Mn content [1].

The average sizes of the Ca-Al oxide precipitates in the X70 and MX70 strips were similar: 3.6±3.8 μm and 3.8±2.6 μm, respectively. Compared to the carbonitrides, the standard deviations of the average values of the diameters of the oxide inclusions and the

aspect ratios of MnS precipitates were relatively high, because these particles were less abundant and showed a considerable spread in particle size/aspect ratio.

The higher hardness increment for the X70 HAZ sample indicates transformation at a lower temperature to finer bainitic ferrite with higher density of dislocations. The finer lath structure for the X70 HAZ sample is evident in Figure 4-15 (compare Figure 4-15a and b). In the hot rolled condition, the hardness of X70 was about 10 HV points higher than of MX70, but the difference was amplified to 43 HV points for the simulated HAZ samples. Lee *et al.* [222] reported a similar simulated HAZ hardness for X70 grade steel (238 HV), for the same peak temperature (1350 °C) and $\Delta t_{8\rightarrow5}$ = 4 s (c.f. 3 s in the current work). The alloy composition in [222] was: 0.05 C 0.26 Si 1.48 Mn, 0.17 Mo, and 0.05 Nb ($C_{E\ (IIW)}$ =0.3).

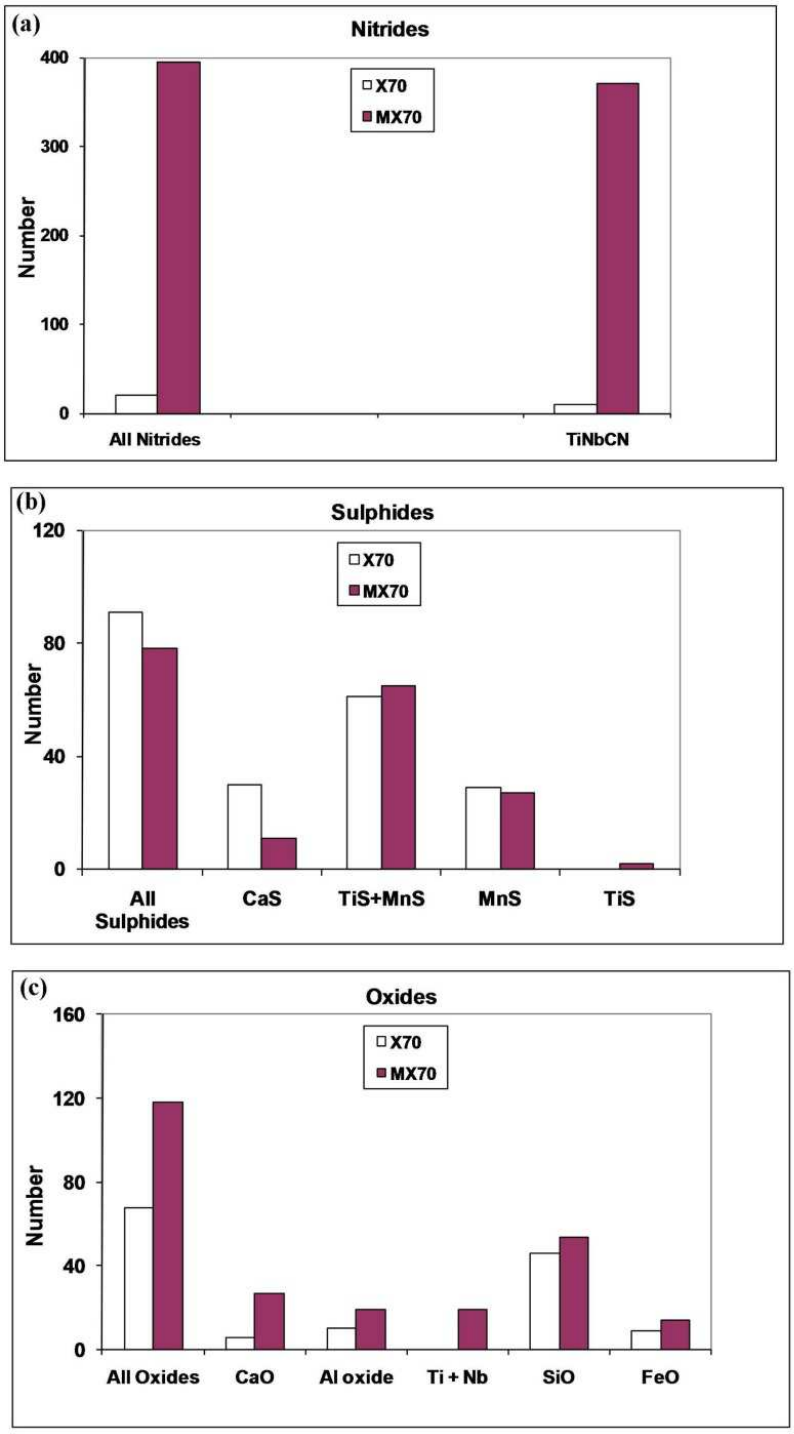

Figure 4-17 Plots showing the number per unit area and types of (a) nitrides, (b) sulphides and (c) oxides present in the two steels.

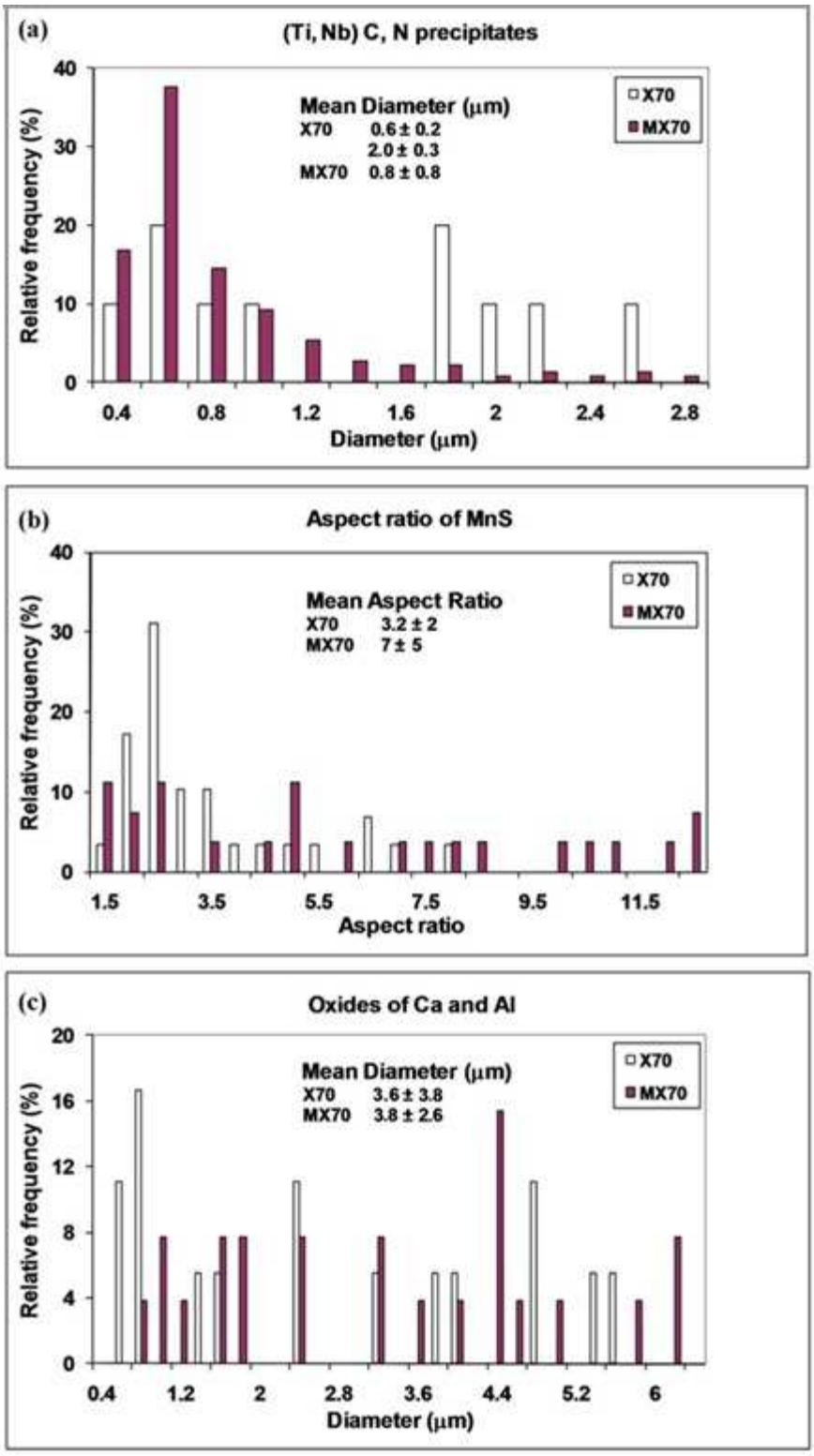

Figure 4-18 Plots showing the mean values and distribution of (a) size of (Ti,Nb)(C,N) precipitates, (b) aspect ratio of MnS and (c) size of oxides of Ca and Al.

4.4 Conclusions

- The optical microscopy revealed that the microstructure of as received X70 transfer bar changed from predominantly PF with islands of pearlite near the top surface of transfer bar to GB with a bit of BF in the centre. After normalising, the microstructure is uniform consisting of an equiaxed ferrite-pearlite.
- As-received X70 and MX70 strips displayed inhomogeneous ferrite-pearlite microstructures, whereas the HAZ microstructures compromised coarse bainitic ferrite laths and M/A islands.
- Although there was little difference in the amount of pearlite for the X70 and MX70 steels, pearlite banding was more evident in the hot rolled X70 strip, which is consistent with its higher Mn level and more pronounced compositional segregation.
- The number of particles per square mm was found to be significantly higher in the MX70 than in X70, so in terms of density of inclusions/precipitates the standard X70 steel is much “cleaner” than the MX70 version.
- The EDS microanalysis of the precipitates revealed that the density of nitrides in MX70 was more than an order of magnitude higher than that for X70. The number of oxides in the MX70 strip was also found almost double of that observed for the X70 strip. However the average sizes of oxide precipitates were similar and the number of sulphides per unit area was almost the same in both steels.
- The X70 HAZ sample has a substantially higher hardness than MX70 HAZ due to finer lath structure and solid solution strengthening by Mn.

5 HYDROGEN UPTAKE DURING ELECTROLYTICAL CHARGING

This chapter begins with characterisation of electrolytic hydrogen charging regarding electrolyte density, current, inhibitor and duration of charging. Hydrogen embrittlement is discussed with respect to the effect of ferrite grain size and steel microstructures. The four tested microstructures are: as received X70 strip with banded ferrite-pearlite microstructure; as received transfer bar of X70 steel with quasi-polygonal ferrite and granular bainite; normalised transfer bar of X70 with an equiaxed ferrite-pearlite microstructure; and simulated HAZ microstructure with coarse bainitic ferrite laths and M/A constituents.

The chapter reports the measurement of the diffusible and residual hydrogen contents using the mercury and melt extraction methods. In addition, the role of microstructure internal and surface damage (blistering) by hydrogen is discussed.

The chapter concludes with an analysis of the nature of blisters and cracks based on the results for EDS and X-ray mapping.

5.1 Electrolytical Hydrogen Charging Parameters

5.1.1 Effect of charging time on hydrogen absorption

Curves for electrolytical hydrogen charging were obtained to study the effect of charging duration (Figure 5-1). No differences in the rate of charging were observed for the X70 and MX70 TPB samples; and the charging rates for the TPB HAZ samples were also the same. However, the hydrogen charging curve for the HAZ TPB samples was displaced to shorter times that than that for the as-received TPB samples (Figure 5-1). The hydrogen content varied with charging time, reaching a maximum value after about 5 hours of charging, and then decreasing with further charging. This phenomenon has been described by several researchers as saturation of hydrogen in the metal [4, 93, 223-225]. However, although some researchers reported a decrease in hydrogen content after saturation [4, 225], others found no variation in hydrogen content after saturation [93, 223]. For longer times of charging, Dong *et al.*[4] reported a drop in hydrogen content for X100 pipeline steel using an electrolyte of higher concentration than that used in the current study. These authors attributed the decrease to the formation of bubbles on the sample surface which hinder the permeation of hydrogen. Also since samples looked slightly darker after hydrogen charging, it could be suggested that a thin film of oxide might prevent the further entry of hydrogen after its appearance. The effect of these thin films in reducing the hydrogen entry to the steel is discussed in literature [226].

The difference in the charging rates between as received and HAZ TPB samples is associated with the bainitic microstructure of the HAZ samples, whereas as received samples have a ferrite-pearlite microstructure. The faster charging rates for the HAZ samples could correlate with the increased tendency for trapping in the bainitic ferrite plate microstructure due to higher residual stresses caused by the displacive phase transformation compared to the diffusional transformation to ferrite and pearlite microstructure [178]. These higher residual stresses in HAZ have been reported in the literature [226] to reduce hydrogen permeation and diffusion coefficient because of dislocations acting as reversible traps, slowing down hydrogen permeation. The X70 and NTB consist of ferrite, while the HAZ consists of a mixture of bainite and martensite.

During both bainitic and martensitic transformation, transformation strains are accommodated leading to the increase in the density of dislocations, thus the number of trap sites for hydrogen is higher in such microstructures compared to ferrite/pearlite ones. Consequently the diffusion rate will slow down and the hydrogen concentration becomes higher. Thus the effective diffusion coefficients are lower in HAZ compare to X70 and NTB [126]. Escobar *et al.* [227] also found that for electrolytical hydrogen charging of martensitic microstructures the pick-up of hydrogen is higher compared to ferrite-pearlite microstructures of the same steel composition and for the same charging time .

Charging was focused on achieving 2 and 4 ppm of hydrogen in the samples for TPB testing in order to simulate the possible hydrogen pick-up during processing and under in-service condition (Figure 5-1). It was estimated from calibration curves that the maximum hydrogen content of about 9 ppm for TPB as-received samples was reached in about 5 hours; and that 20 and 90 minutes of charging time were required to reach 2 and 4 ppm, respectively. Correspondingly, for HAZ samples the charging times were 8 and 30 minutes. Although Dong *et al.* [2] also reported about 5 hours to reach maximum hydrogen content on charging of X70 pipeline steel, there is no evidence in the literature for the charging times required to reach 2 and 4 ppm hydrogen in X70 steel.

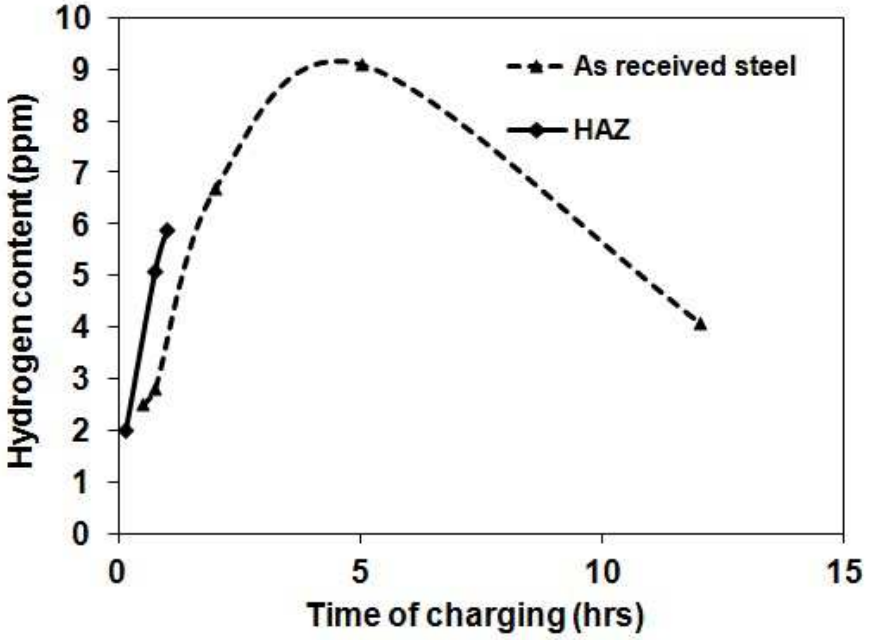

Figure 5-1 Hydrogen calibration curves for hydrogen charging of TPB samples of X70 steel in as received condition and for simulated HAZ samples.

5.1.2 Effect of sample thickness and promoter (poison)

Arsenic based solutions are frequently used as a promoter (poison) to delay the recombination of hydrogen atoms to hydrogen gas on the surface of the sample. The most common arsenic solutions are $NaAsO_2$ (sodium arsenite) [68, 228] and As_2O_3 (arsenic trioxide) [2, 11]. Figure 5-2a shows the results for hydrogen content determination using melt extraction of samples of 0.25 mm and 1 mm thickness, and also for the 5 mm thick TPB test samples, after electrolytic charging in 1 mole H_2SO_4 + 250 mg $NaAsO_2$ solution at 50 mA/cm^2 for various times. Regardless of the sample thickness, the hydrogen content of the sample increased with time of charging until it reached saturation and then decreased.

Figure 5-2a also shows that samples of different thickness not only exhibited similar charging curves, but that there was no significant difference in the maximum amount of hydrogen that was absorbed in these samples (9 - 9.5 ppm). This observation suggests that the samples have absorbed the maximum amount of hydrogen to the saturation limit of the material [4]. However, the time required to reach the maximum was slightly longer for the thicker (5 mm) samples because of the longer time required for hydrogen diffusion into the centre of the sample.

In contrast to the effect of sample thickness, an increase in concentration of $NaAsO_2$ (promoter concentration), shifts the curves to shorter charging times as shown in Figure 5-2b. In other words, similar concentrations of hydrogen are absorbed in the samples for shorter times of charging. This effect is likely to be due to the action of the promoter in preventing recombination of hydrogen [229]. However, the maximum amount of hydrogen absorbed remained almost the same since it corresponds to the amount of hydrogen required to saturate the material.

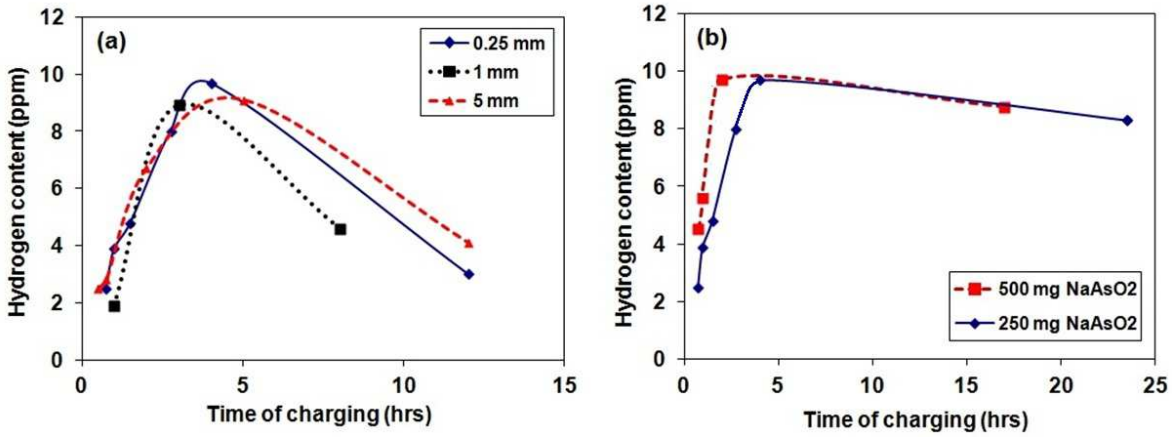

Figure 5-2 Hydrogen charging curves for X70 steel: (a) the effect of thickness on hydrogen pick up and (b) the effect of inhibitors on hydrogen pick-up in 5 mm thick samples.

5.2 Effect of Ferrite Grain Size

5.2.1 Effect of grain size on the hydrogen content

To investigate the effect of grain size on the diffusible and residual hydrogen contents, three ferrite grain sizes with the same pearlite volume fraction were used. Figure 5-3 shows the microstructure of the samples having three different average ferrite grain sizes and pearlite volume fraction of about 12%.

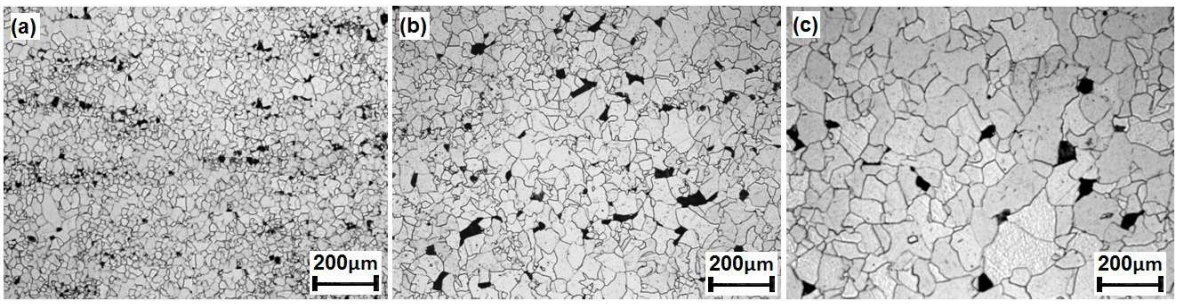

Figure 5-3 Ferrite-pearlite microstructures with pearlite volume fraction of about 12% and average ferrite grain sizes of (a) 14 µm, (b) 46 µm and (c) 120 µm.

The diffusible hydrogen contents for these samples, estimated by measuring the quantity of hydrogen collected over mercury, are presented in

, which also lists the residual (trapped) hydrogen present in these samples. The residual hydrogen was measured by melt extraction after removal of diffusible hydrogen. It can be seen from this

, that the samples with an intermediate value of average ferrite grain size showed higher quantities of diffusible, as well as residual hydrogen, as compared to finer and coarser grained samples. The larger value of diffusible hydrogen for the intermediate grain sizes can be attributed to the dual role played by grain boundaries as faster diffusion paths for hydrogen transport as well as traps for hydrogen at triple junctions and nodes. Ichimura and Sasajima [115] worked on pure aluminium specimens and found that samples with an average grain size (15mm) show higher diffusion coefficients compared to samples with finer or coarser grains. This finding is consistent with the data presented in

. According to Yazdipour *et al*. [116], for ferrite grain sizes smaller than 46 μm, the diffusion of hydrogen being retarded by trapping of hydrogen at nodes and triple junctions, resulting in diffusion coefficient values that decrease with decreasing grain size. Although the effect of trapping decreases for larger ferrite grain sizes, so also does the grain boundary area per unit volume and consequently grain boundary hydrogen diffusion is limited, resulting in a lower diffusion coefficient. The finest (14 μm) grain size sample showed higher residual hydrogen content compared to the coarsest (120 μm) grain size sample, due to its more efficient trapping of hydrogen by the larger density of triple junctions and grain boundaries. The highest diffusion coefficient at intermediate grain size explains the highest total amount of hydrogen in this sample. However, considering the residual/total hydrogen ratios, there is a continuous decline in ratio with increase in grain size, which correlates with the reduction in grain boundary area and number of triple junctions.

5.2.2 Effect of microstructure on hydrogen diffusivity

Figure 5-4 shows the different microstructures reported in this chapter. The details are explained in Chapter 4. Table 5-2 shows the effect of microstructure on diffusible and residual hydrogen contents of the samples examined. The equiaxed microstructure showed the lowest diffusible hydrogen content followed by the banded ferrite-pearlite microstructure, the quasi-polygonal/bainitic microstructure and finally the HAZ bainitic ferrite microstructure. In contrast, the HAZ microstructure exhibited the lowest residual hydrogen content followed by the equiaxed microstructure, the quasi-polygonal ferrite and granular bainite microstructure and the banded ferrite-pearlite microstructure. Since the residual hydrogen content reflects the trapping efficiency of the microstructure, it is inferred that the interfaces of the fine lamellar carbide structure of the pearlite in the as received strip provide strong trapping sites. The more highly dislocated bainitic ferrite structures evidently provide weaker traps which can release hydrogen under mercury and contribute to the "diffusible" (mobile) hydrogen content. Hence, the diffusible hydrogen content is highest for the simulated HAZ microstructure and lowest for the equiaxed ferrite-pearlite structure. Other microstructural features can also contribute to trapping and affect hydrogen diffusion as discussed below.

Table 5-1 Measured amounts of diffusible and residual hydrogen in X70 as a function of ferrite grain size .

Grain size	**14 μm**	**46 μm**	**120 μm**
Diffusible (ppm)	2.9 ± 0.3	9.05 ± 1.6	4.29 ± 0.02
Residual (ppm)	1.5 ± 0.1	3.2 ± 0.42	0.73±0.3
Residual / Total	34%	26%	15%

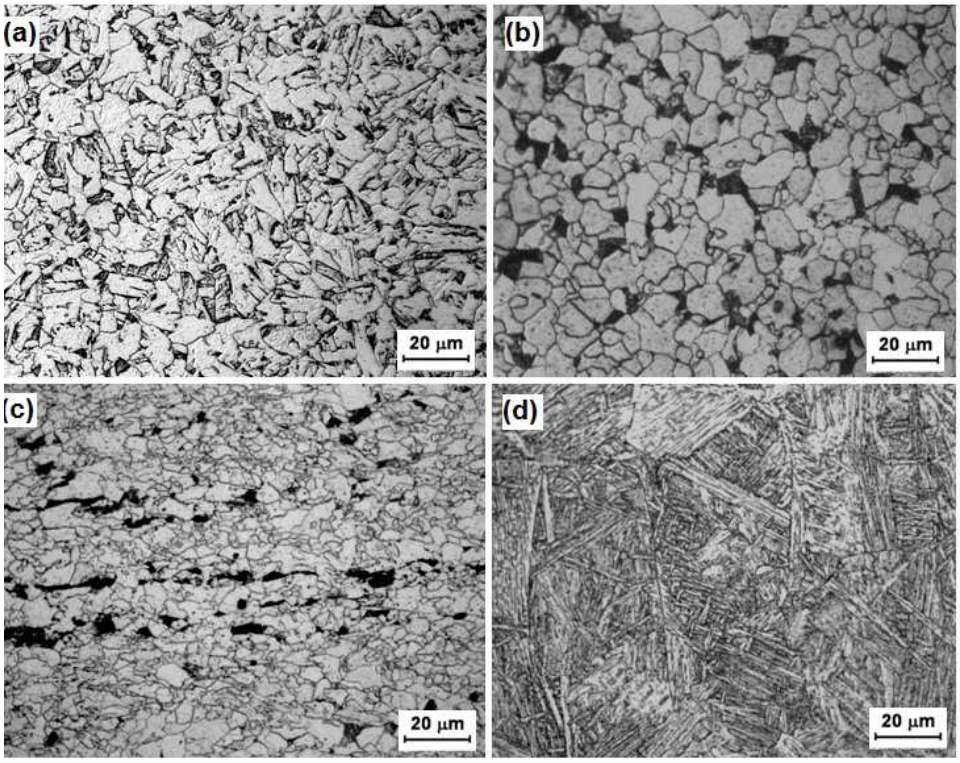

Figure 5-4 Microstructures of steel samples investigated: (a) as received transfer bar of X70 steel with quasi-polygonal ferrite and granular bainite; (b) normalised transfer bar of X70 with an equiaxed ferrite-pearlite microstructure; (c) as received X70 strip with banded ferrite-pearlite microstructure; and (d) HAZ microstructure with coarse bainitic ferrite laths and martensite-austenite (MA) constituents.

Table 5-2 The effect of microstructure on diffusible and residual hydrogen contents in X70 pipeline steel

X70	**Diffusible Hydrogen (ppm)**	**Residual Hydrogen (ppm)**	**D_{tb} ($\times 10^{-10}$ m^2s^{-1})[182]**
Strip (banded F-P)	3.61 ± 0.8	3.02 ± 0.07	3.02 ± 0.07
TB(F + BF)	3.57 ± 0.4	1.77 ± 0.4	4.87 ± 0.74
NTB (Equiaxed F-P)	2.9 ±0.3	1.5± 0.1	5.66 ± 0.23
HAZ (BF+M)	6.29 ± 0.8	1 ± 0.1	-

Features that affect the diffusion of hydrogen in ferrite-pearlite structures are grain boundaries, ferrite-pearlite interface, precipitate particles, inclusions and dislocations. Of these, the boundaries between ferrite-pearlite interfaces were found to be the main trapping sites by Hardie *et al.* [230]. The microstructures investigated here were all obtained from the same steel at different stages of processing. Therefore it can be assumed that the inclusion content is approximately the same for all the microstructures. However, the volume fraction of carbonitride precipitates in the hot rolled strip is expected to be higher than in TB due to the thermo-mechanical processing of the steel. As reported by Yazdipour *et al.* [116] and also discussed in chapter 2, the trapping effect of grain boundaries increases with a decrease in grain size.

The hot rolled strip with bands of pearlite in a ferrite matrix has a finer (14 µm compared to 46µm) average grain size than the equiaxed microstructure. Further, it also has a larger fraction of ferrite-pearlite interfaces and carbonitride precipitates compared to the normalised sample as discussed in Chapter 4. Therefore, the combination of all of these factors promotes trapping of hydrogen in the banded ferrite-pearlite structure, giving rise to a larger amount of residual hydrogen than that in the equiaxed microstructure. In spite of this, it displays a relatively high amount of diffusible hydrogen, which can be explained as follows. The hot rolled strip transforms at a relatively low temperature resulting in dislocations generated to plastically accommodate the transformation volume change. These dislocations act as reversible traps which releases hydrogen on standing under mercury to contribute to the measured diffusible hydrogen content.

It has been suggested by several researchers [9, 59, 60, 81] that, in a banded structure, the dominant diffusion paths for hydrogen are ferrite layers, the ferrite grain boundaries and the ferrite-pearlite interfaces. Pearlite, when present as individual/separate blocks in a random F-P structure, can also reduce the mobility of hydrogen. Further, Tau and Chan [59] showed that diffusion is faster in a banded pearlite microstructure when the banding is parallel to the direction of hydrogen diffusion as compared to a random ferrite structure, since hydrogen can diffuse undisturbed along the ferrite bands. Based on the above, the larger amount of diffusible hydrogen observed in the banded structure correlates with the relatively high calculated diffusivity. However, these results contradict the results

of permeability measurements by Haq *et al.* [182] which indicated a higher diffusivity for the normalised sample compared to the sample with banded structure. This difference arises because the banded pearlite structure for permeability measurements [3] was perpendicular to the direction of hydrogen diffusion. Therefore, the sample showed a lower diffusion coefficient, consistent with the results of Tau and Chan [59]. In the case of diffusible hydrogen measurement, prior hydrogen charging was conducted parallel to the direction of banding in the microstructure. Therefore, a pathway was present for easy diffusion along the ferrite layers and the measured residual content of diffusible hydrogen was higher**.**

The diffusible hydrogen content of the microstructure comprising a mixture of quasi-polygonal ferrite and bainitic ferrite was almost the same as that of the banded ferrite microstructure and is in between that of the equiaxed ferrite and the bainitic ferrite microstructures. In addition to the quasi-polygonal ferrite grains being significantly finer than the ferrite grains in the equiaxed microstructure, this microstructure has a higher density of dislocations than the normalised equiaxed microstructure. Both these factors affect the amount of diffusible hydrogen.

The HAZ microstructure showed the highest amount of diffusible hydrogen and the lowest quantity of residual hydrogen which suggests the presence of only weak reversible traps. This is consistent with the structure of HAZ which comprises of bainitic ferrite laths with a high density of dislocations. The bainitic ferrite laths are easy paths for hydrogen diffusion and the dislocations act as weak, reversible traps and facilitate the diffusion of hydrogen compared to ferrite-pearlite interfaces, which irreversibly trap hydrogen and retard hydrogen transport. Since weak traps do not hold hydrogen permanently, the residual hydrogen content is also low.

5.3 Role of Microstructure In The Internal And Surface Damage

5.3.1 Blister formation (surface damage)

Blisters observed on the surface of the samples of the different microstructures are shown in Figure 5-5 to Figure 5-7. These blisters appeared on the surface of the samples having different microstructures after different times of charging. The dependence of blisters on charging time is also supported by reports in the literature [92, 93, 231]. For example, blisters appeared in the banded ferrite-pearlite–microstructure (Figure 5-5 and Figure 5-6) after charging for 1.5 – 2 hours as shown in Table 5-3. In the case of the quasi-polygonal ferrite with bainite microstructure blisters were present after charging for 15 hours (Figure 5-7a and b) and after 3 hours for equiaxed ferrite-pearlite microstructure (Figure 5-7c and d). For the HAZ microstructure, however, no blisters appeared even after charging for 24 hours.

Table 5-3 Blister formation time in different microstructures

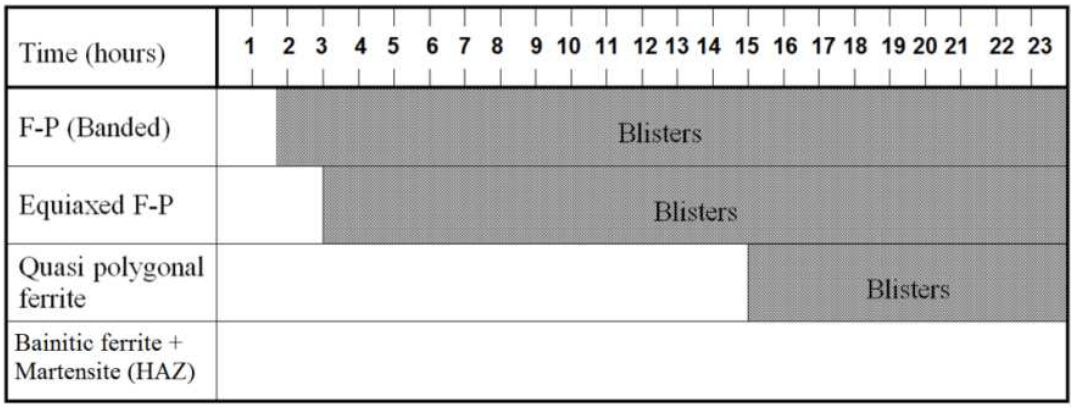

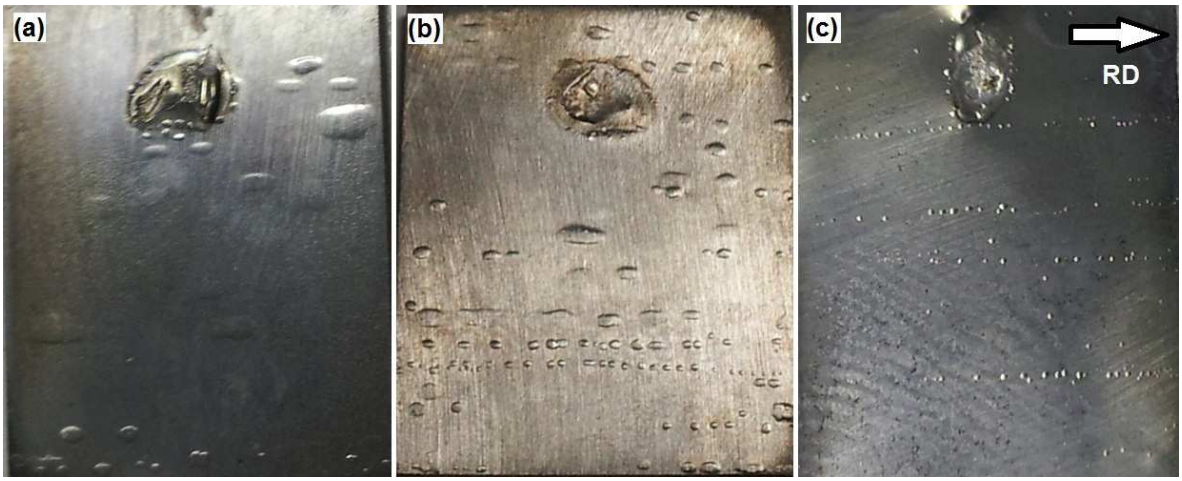

Figure 5-5 Blisters along directions parallel to microstructural bands in 1 mm thick sample after charging for (a) 2 hours and (b) 3 hours; and (c) in 0.25 mm thick sample after 3 hours charging.

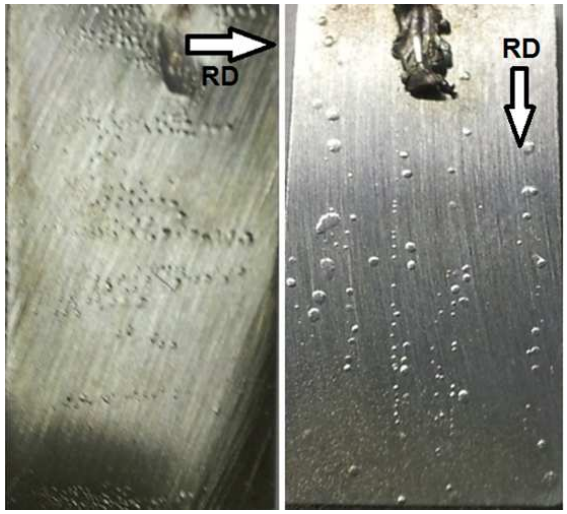

Figure 5-6 Blisters along banded ferrite-pearlite regardless of sample cutting orientation in respect to the rolling direction.

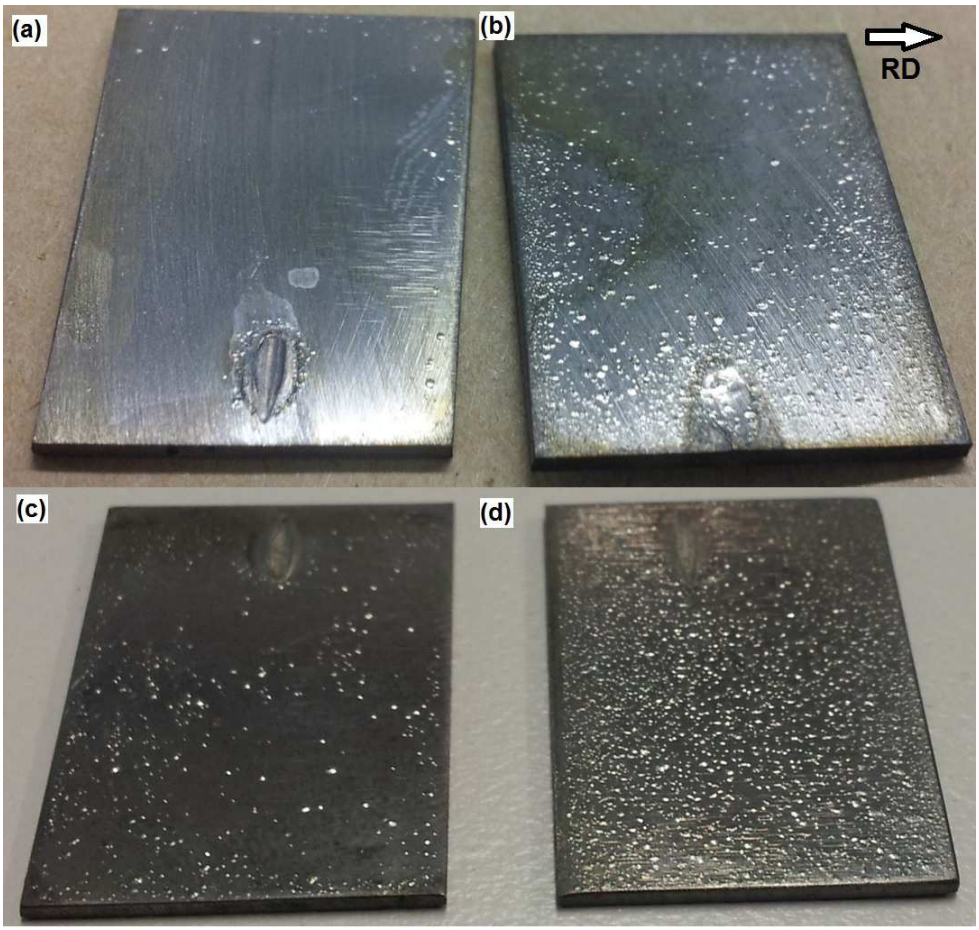

Figure 5-7 Appearance of blisters in1 mm thick samples with a structure of quasi-polygonal ferrite and granular bainite after charging for (a) 15 and (b) 17 hours; and samples with a structure of equiaxed ferrite-pearlite after charging for (c) 3 hours and (d) 5 hours.

5.3.2 Blister morphology and distribution

Ren *et al.* [85] have reported that blisters form parallel to the rolling direction. Consistent with this conclusion, Figure 5-5 shows that the blisters in the banded ferrite-pearlite microstructure are parallel to the rolling direction of the sample. However, in the other samples, the rolling direction is not dominated, as they were subjected to subsequent heat treatments or only low level of hot deformation for TB sample (Figure 5-7). Moreover, blisters in all the other microstructures were circular or oval in shape, whereas those in the banded structure were mostly oval with many of them being large with high aspect ratios. This oval shape is reported in the literature for bainitic and pearlitic steels and

described as having a bubble-like shape [227]. Consistent with the observations by Escobar *et al.* [93], it was also found that for samples other than those with a banded structure, at early stages of blisters appearance when only a few blisters were present, blisters were typically located near the edges of the sample, but at later stage when many blisters were present, blisters distributed uniformly over the sample. These observations indicate that the hydrogen content is higher near the sample edges and that blisters preferentially form in these regions, Figure 5-7. It could be speculated that more hydrogen could be accumulated faster close to the surface/edges at trapping sites during the charging than within the sample due to the diffusion-controlled nature of the process.

It was also found that when the samples were charged for longer times at the same current density, the number of blisters increased significantly. This result correlates with more hydrogen entering the sample and creating internal cracks that act as reservoirs for gaseous hydrogen and increasing the internal pressure, which is relieved in part by bulging (blistering) in surface regions and the development of surface-breaking cracks [93].

The shape and size of the blisters was found to be independent of the charging time but dependent on sample thickness. Figure 5-8 shows the effect of sample thickness on blistering.

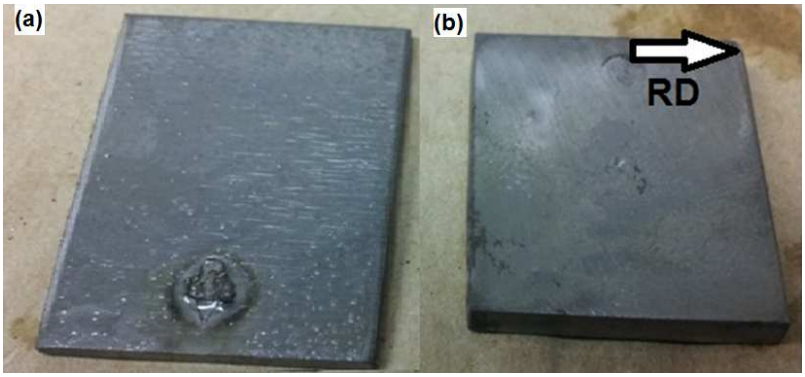

Figure 5-8 Effect of sample thickness on the formation of blisters in samples with an equiaxed F-P microstructure after 3 hours charging at the same current density: (a) 1 mm and (b) 3 mm.

Thinner (1mm) sample showed blisters after 3 hours of charging while thicker (3mm) sample did not show any blisters for the same charging conditions. This effect is likely to be due to the greater sample volume available to accommodate the solute hydrogen and therefore insufficient local hydrogen concentration to create cracks and build-up of hydrogen gas pressure [11, 92, 93, 98]. Figure 5-5b and c also show the effect of sample thickness on blisters with banded ferrite-pearlite microstructure. It is evident that blisters in the thinner (0.25mm) sample are smaller than in the thicker (1mm) one. As both samples were charged at the same current density, the thinner sample accumulated a higher hydrogen concentration than the thicker sample for the same charging time, leading to the activation of a larger number of crack initiation sites. As a consequence, more and finer blisters were formed. The secondary electron images in Figure 5-9 and Figure 5-10 show the surfaces of blisters. These SEM images are similar to those reported by other researchers [11, 92, 93, 98]. When hydrogen atoms are trapped near the surface at inclusions and micro-voids, the concentration can build up to a critical level and cause hydrogen cracking.

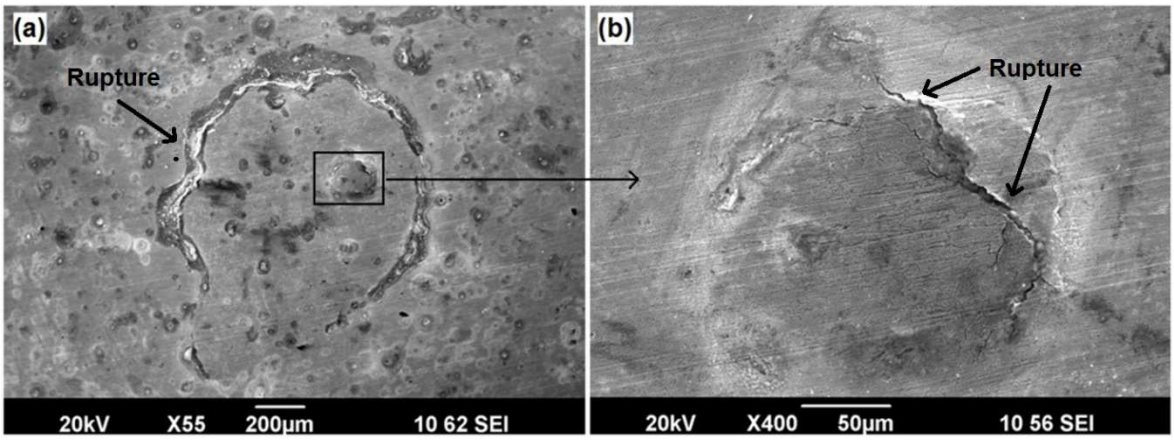

Figure 5-9 SEM micrographs of blisters in equiaxed F-P microstructure after 17 hours electrolytical hydrogen charging: (a) low magnification view of large and small blisters; and (b) higher magnification view of the smaller blister.

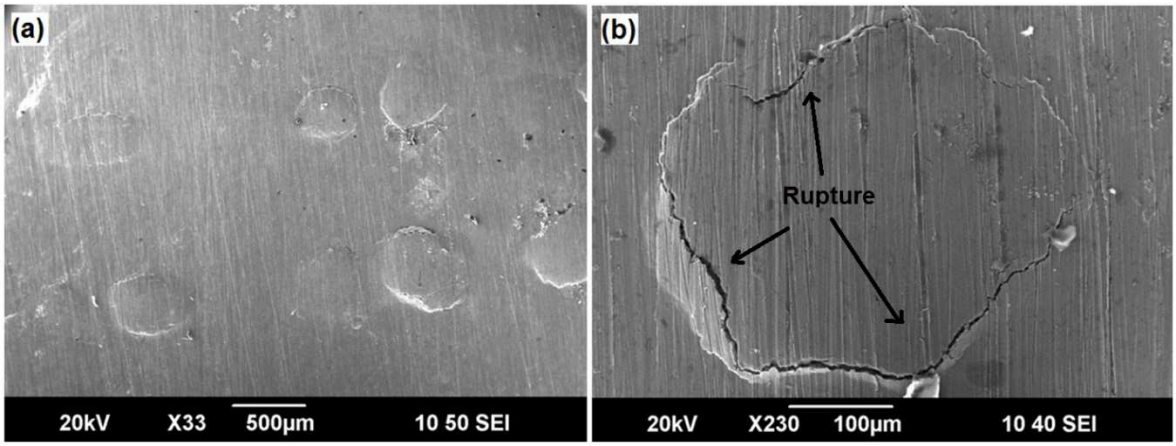

Figure 5-10 Blisters formed in a sample with a banded F-P microstructure at different magnifications after 2 hours electrolytical hydrogen charging.

The voids produced can act as reservoirs for hydrogen molecules that form by recombination of atomic hydrogen. When the internal pressure caused by the hydrogen gas molecules is greater than the yield strength of the steel, the steel deforms plastically to form blisters at the steel surface. Entry of more hydrogen into the metal results in formation of more hydrogen molecules and increases the gas pressure under the blisters. Eventually hydrogen cracking propagates to the surface around the blister, causing rupture of the blisters and attenuating the local internal stress [232].

There is still much debate on the role of hydrogen in crack and blister formation and several mechanisms have been proposed and discussed. Most of them are based on the internal pressure theory suggested by Zapffe *et al.* [53], which propose that hydrogen atoms combine into hydrogen gas molecules at or near the interface of second phase particles and the metallic matrix. The hydrogen molecules cause a pressure build-up and induce microcracks. The propagation and connection of these microcracks leads to macroscopic cracks in which hydrogen gas pressure increases, followed by the formation of the hydrogen blisters. Hydrogen cracking in the centres of samples is less likely to produce blistering because of its remoteness from the surface.

5.3.3 Evaluation of hydrogen induced cracking

For pipelines intended for sour gas or oil transport, HIC testing in accordance with NACE procedures is mandatory. Maximum values for crack sensitivity ratio (CSR), crack length ratio (CLR) and crack thickness ratio (CTR) must be determined and recorded. In order to calculate these values, metallographic sectioning was used to assess the HIC susceptibility with the results being recorded in terms of CSR, CLR and CTR as defined in Figure 5-11 and equations 5.1 – 5.3[60, 233].

$$\text{Crack Sensitivity Ratio (CSR)} = \frac{\sum a \times b \times 100\%}{W \times T} \quad 5\text{-}1$$

$$\text{Crack Length Ratio (CLR)} = \frac{\sum a \times 100\%}{W} \quad 5\text{-}2$$

$$\text{Crack Thickness Ratio (CTR)} = \frac{\sum b \times 100\%}{T} \quad 5\text{-}3$$

where a is the length of the rectangular field containing the crack, b is the width of the rectangular field around the crack, W is the length of the sample and T is the sample width .

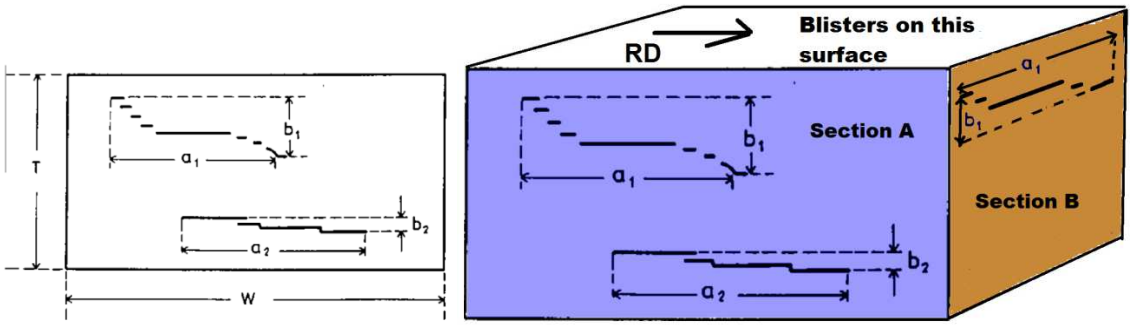

Figure 5-11 Crack parameters used to calculate crack sensitivity [60] for the two transverse sections A and B.

The results for section A are presented in Table 5-4. The banded F-P microstructure showed the maximum CLR, which indicates that cracks are located parallel to the sample surface. This is due to the orientation of the pearlite bands parallel to the rolling direction. The equiaxed F-P microstructure yielded the maximum CTR due to the random orientation of the recrystallised ferrite grains and the presence of more cracks at an angle to the sample

surface. The banded F-P microstructure showed the maximum CSR which indicates more crack affected area under the surface. Kushida [234] studied hydrogen induced cracks in X80 pipeline steel and found that the acceptable maximum values of CLR, CTR and CSR are 15%, 5% and 2%, respectively. According to Table 5-4 the values, the banded F-P microstructure experienced the most severe hydrogen cracking damage as it had the maximum density of cracks in the bulk sample and also the strongest orientation of cracks parallel to the rolling direction. The values recorded are far higher than the maxima proposed by Kushida [234] because the samples were subject to prolonged electrolytic hydrogen charging.

Table 5-4 Crack sensitivity results for different microstructures on section A

Specimen	CSR (%)	CLR (%)	CTR (%)
F-P (Banded)	4.6±1.2	67.2±3.5	8.9±1.4
Ferrite + Bainitic ferrite	3.8±1.5	55.2±4.6	13.2±2
Equiaxed F-P (14 μm)	2.9±1	48±3.2	14.3±1

5.3.4 Evaluation of crack formation

It has been reported that the HIC that leads to the initiation of blisters occurs at trapping sites such as grain boundaries and interfaces between the matrix and inclusions/ second phase particles [235, 236]. Ren *et al*. [85] proposed a mechanism for formation of a cavity that involves the aggregation of hydrogen atoms and vacancies at trapping sites to form a “blister nucleus”, followed by cracking at the surface of the cavity due to the internal hydrogen pressure when the blister nucleus grows to a critical size. This subsequently leads to the blister formation on the surface of the sample. Several publications [4, 81, 85, 98, 118] have shown that second phase particles are the most common nucleation sites for cracks that result in formation of internal cavities while others [237] believe that second phase particles are not an absolute prerequisite for crack

initiation. The mechanism of propagation of hydrogen-induced cracks in different microstructures is presented and discussed below.

Cross-sections of a banded ferrite-pearlite sample containing a surface blister are presented in Figure 5-12. It is evident from these images that hydrogen charging has resulted in internal damage in addition to the formation of surface blisters. Several hydrogen induced cracks can be seen below the surface of the blister. Figure 5-12a shows a blister and some cracks formed close to the surface at the edge of the blister. In addition, a long crack, parallel to the rolling direction, is present at a depth of about 150 μm from the surface. Escobar *et al*. [93] have also reported HIC cracks below surface blisters in samples of industrial multiphase steels. They suggested that the cracks initiated inside the sample and propagated to the surface in order to release the internal pressure.

A slightly magnified image of the tip of this crack reveals that the crack is along a pearlite band. Magnified images shown in Figure 5-12(c) and (d) of this region reveal that there is preferential cracking along the bands containing pearlite colonies. However, in Figure 5-12b it is clear that the crack has propagated partly through a pearlite region, suggesting that the cracking can occur also along boundaries of pearlite colonies. Similar observations have been reported by Albarran *et al.* [238], Lee and Chan [60] for the banded ferrite-pearlite structures. Three carbonitride precipitates (indicated by arrows) are also indicated in Figure 5-12c and d. Figure 5-13 presents the EDS analysis of two inclusions in Figure 5-12d, which indicates that the particles are Nb and Ti-rich and are probably NbTi carbonitrides. The elemental mapping of the inclusion in Figure 5-12(c) also reveals that it is a Ti or Nb carbonitrides. Cracking was not specifically associated with these carbonitrides, as they are located at some distance from the observed cracks. However, it should be remembered that these figures are two-dimensional and it is not known whether crack could be associated with carbonitride/matrix interface somewhere below the surface. Although, it was reported in the literature [11] that Nb and Ti carbonitrides are not preferential sites for hydrogen trapping (or less preferential) compared to oxides and oxysulphides.

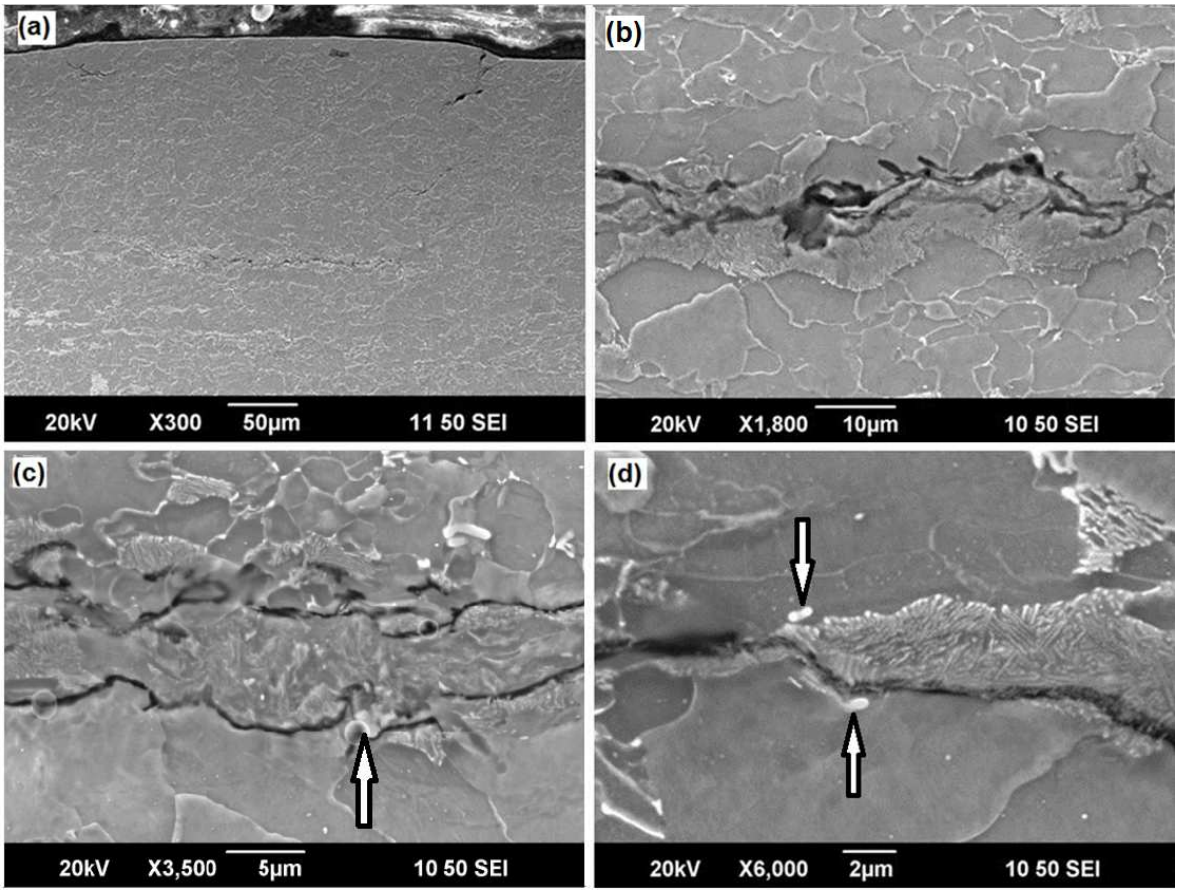

Figure 5-12 Cross-section of F-P structure with banded pearlite grains under a surface blister: (a) general view showing the raised surface due to the formation of a blister and (b, c and d) details of microstructures below the blister shown at different magnifications). Arrows indicate particles.

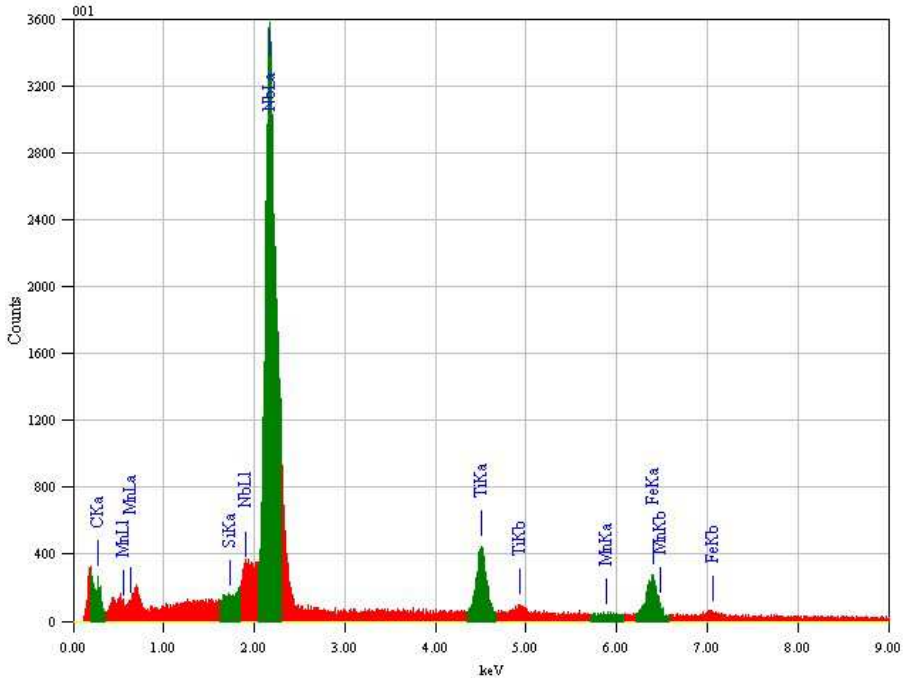

Figure 5-13 Representative EDS spectrum of particles shown in Figure 5-12(d)

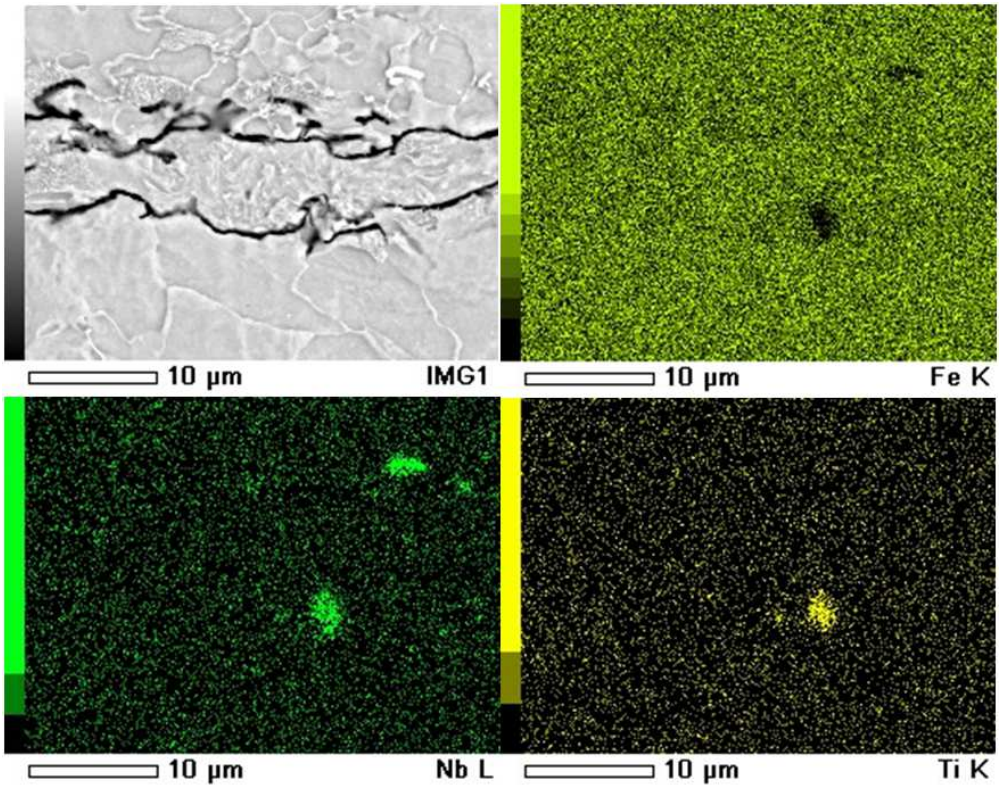

Figure 5-14 Elemental mapping corresponding to Figure 5-12(c) showing that both particles are Nb-rich and the lower one is also or Ti-rich.

Figure 5-15 shows HIC under the surface blister in an equiaxed ferrite-pearlite microstructure. Again the blister and cracks below it are clearly visible in Figure 5-15a. Moreover, the cracks in this microstructure appear to be closer to the surface than those observed in the banded F-P microstructure. Figure 5-15b is a magnified image of the large crack shown in Figure 5-15a. An inclusion marked with an arrow is also seen close to the crack. The cracks in Figure 5-15c are associated with a large inclusion (~ 10 μm) which is located at the site of a branch crack, approximately normal to another the crack extending on either side of the particle. EDS analysis (Figure 5-16) of this inclusion and another inclusion close by indicated that they are oxides of Al and Ca. Figure 5-17 shows the elemental mapping of these inclusions. Decohesion has occurred around the large particle and cracking could have initiated at this site then extended in two main directions due to the local stress state.

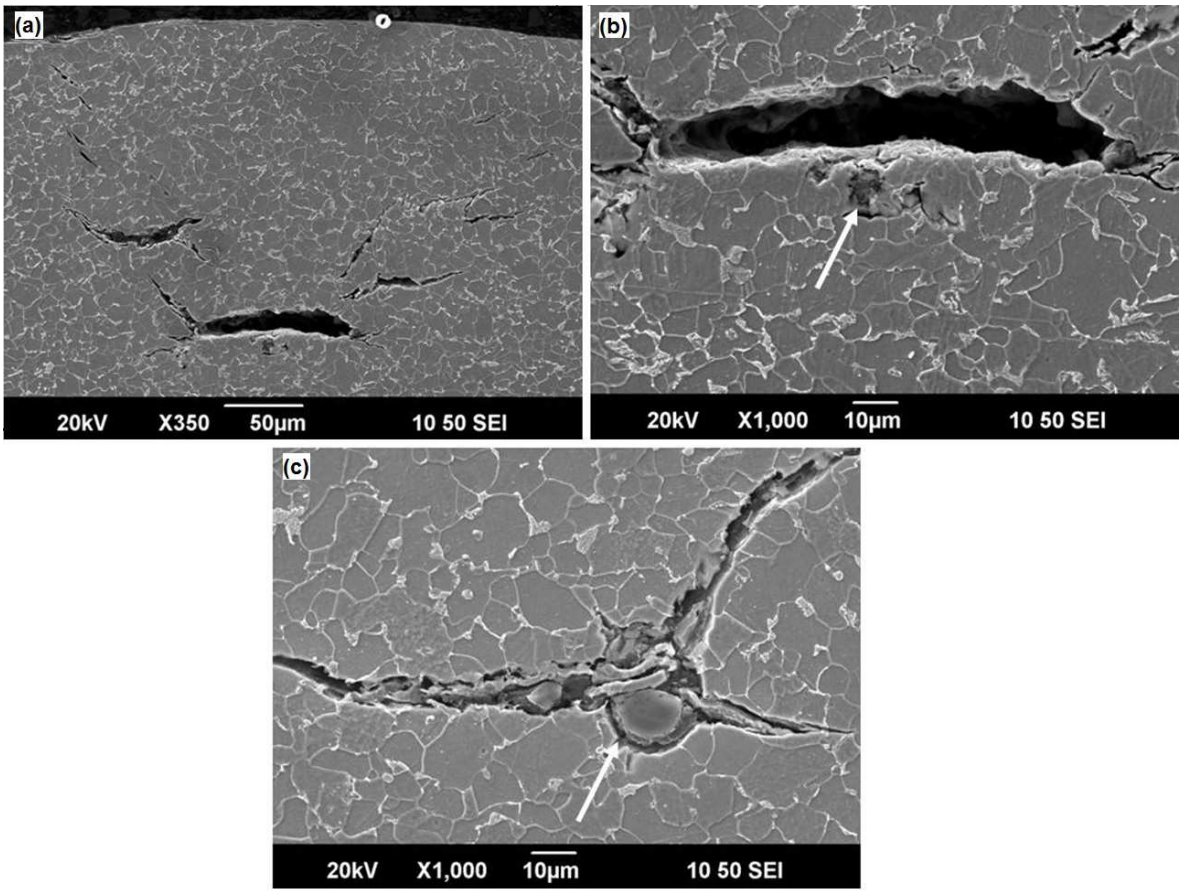

Figure 5-15 Cross-section of equiaxed F-P microstructure under a surface blister: (a) general cross section view showing cracks, (b) higher magnification of a large crack with an inclusion close to crack marked with arrow and (c) an inclusion (arrowed) associated with transgranular crack.

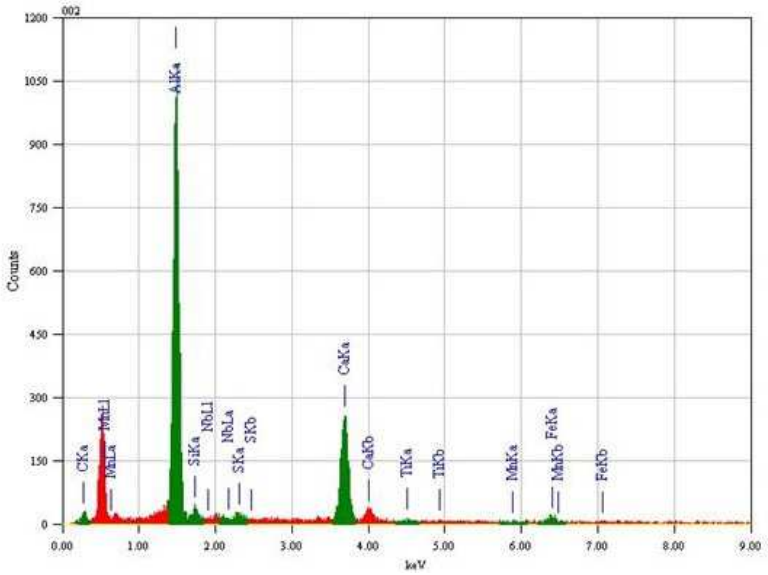

Figure 5-16 EDS analysis of inclusion shown by the arrow in Figure 5-15c.

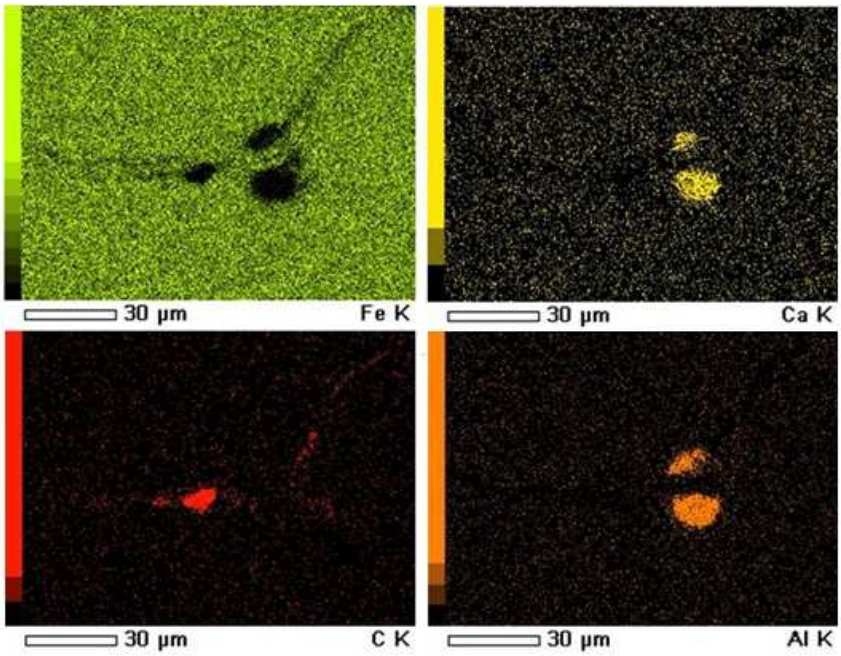

Figure 5-17 Elemental mapping of three inclusions in the equiaxed F-P microstructure showing Al and Ca as main inclusion elements in two of the inclusions.

Figure 5-18 is the cross-section of the granular bainite sample charged for 17 hours. Again the hydrogen induced cracks in this microstructure are quite close to a surface blister, unlike in the banded ferrite-pearlite microstructure. The cracking in this microstructure appears in some cases to follow ferrite/MA islands interfaces, as well as possibly prior austenite grain boundaries. There is also one crack which started from an inclusion (Figure 5-18b). The elemental mapping and EDS analysis of this inclusion shows that that it is an oxide of Al and Ca. The higher number density of reversible traps for hydrogen in this microstructure (dislocations, finer microstructure and high grain boundary area) spreads hydrogen atoms more homogeneously and reduces local hydrogen concentration. Hence the probability is lower for accumulation of hydrogen in a particular site to cause cracking, pressure build-up and blister formation.

Saleh *et al.* [239] carried out trace analysis on the same set of samples used in this work. The results of trace analysis showed that transgranular cracking was observed on the cleavage {001} planes and on {110}, {112} and {123} slip planes, without a clear preferential trend. Branching of HIC also followed the same crystallographic planes. They analysed the grain orientations and found that there was no preferential orientation for

crack development in grains with the same crack plane. They also found that the susceptibility to HIC decreased in the microstructures with higher fraction of low angle grain boundaries, as low angle boundaries were shown to arrest crack propagation.

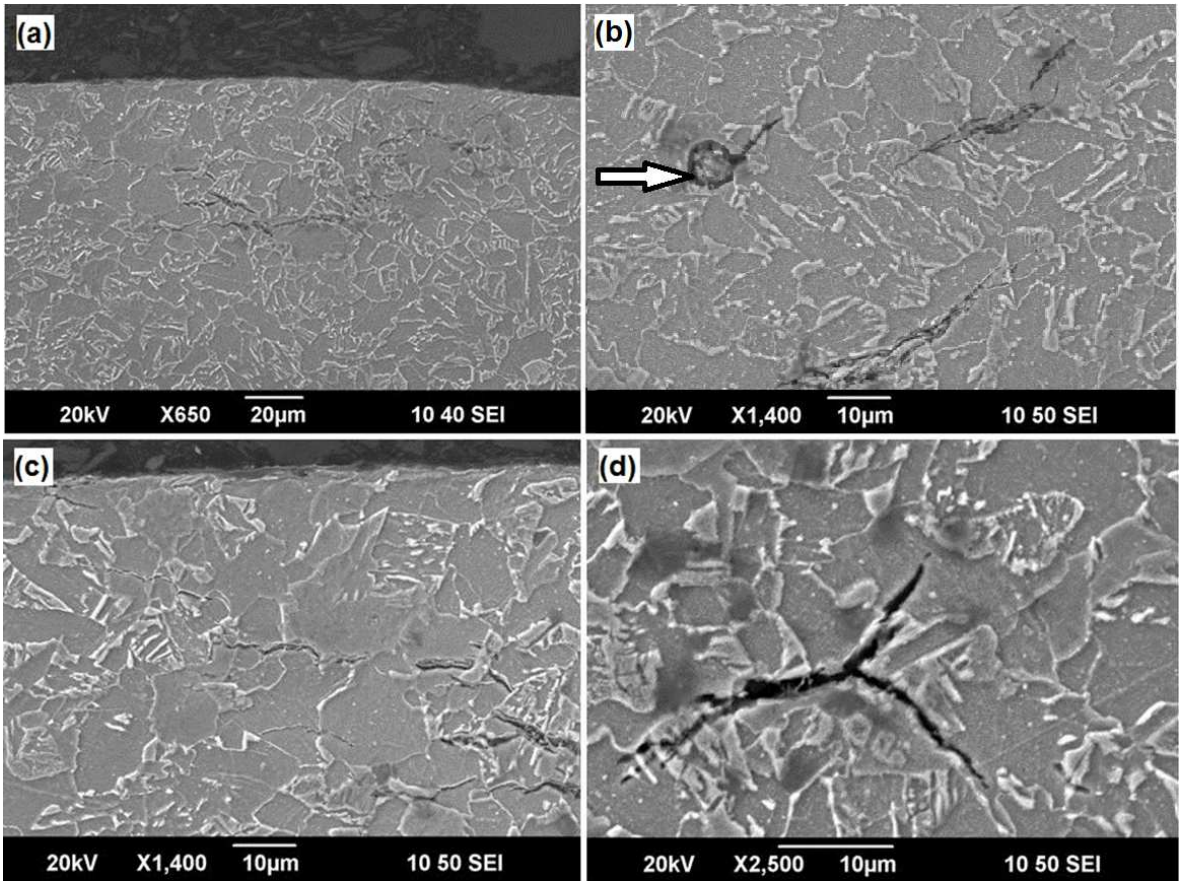

Figure 5-18 Cross-section of granular bainite microstructure under a surface blister: (a) general cross section view showing small blisters, (b, c) examples of cracks at higher magnification and (d) higher magnification of cracks forming a triple junction.

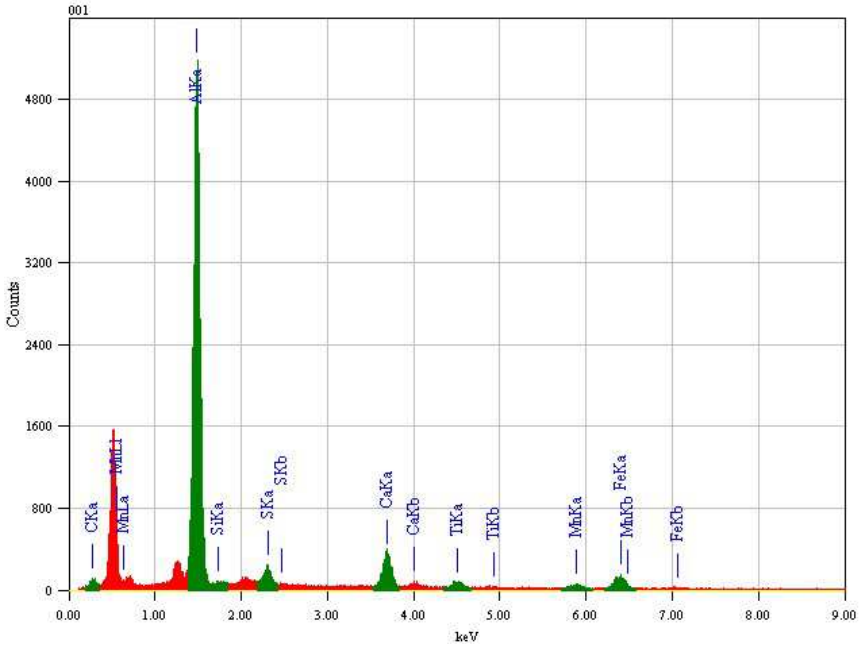

Figure 5-19 EDS analysis of inclusion shown with an arrow in Figure 5-18b.

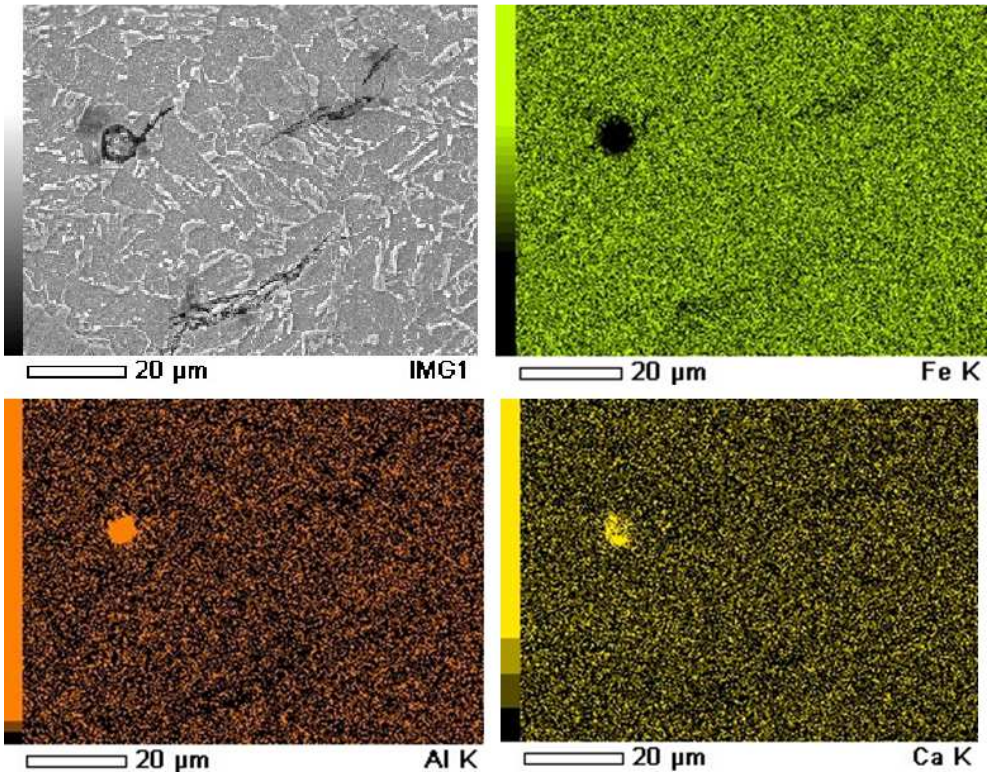

Figure 5-20 SEM micrograph of inclusion in Figure 5-18b showing crack initiation at Al, Ca oxide (a) with corresponding X-ray maps of Fe (b), Al (c) and Ca (d).

5.3.5 Effect of grain size on cracking

In order to investigate the effect of grain size on cracking, SEM images were taken from a cross-section containing a surface blister in an equiaxed F-P microstructure with average ferrite grain size of 46 µm (Figure 5-21). For a grain size of 120 µm almost no blisters were observed in cross sections despite the presence of grain boundary cracks (Figure 5-23). The samples were charged with hydrogen under the same charging conditions (current density and time). Comparing Figure 5-21 and Figure 5-23 with Figure 5-14, there was almost no blistering effect in equiaxed F-P microstructure with average ferrite grain size of 120µm, while there was blistering in both the 14 and 46 µm samples. The cracking seems to have occurred preferentially along boundaries perpendicular to the surface in equiaxed F-P microstructure with average ferrite grain size of 120µm. It is possible that these grain boundaries provide easy hydrogen migration paths to the surface where effusion can occur. These routes are unavailable for the finer P/F structures, and thus subsurface cracks expand due to hydrogen filling, leading to surface bulging. The CSR, CLR and CTR values for the 46 µm sample in section A are presented in Table 5-5. These results suggest that compared with the 14 µm sample, there is a higher crack density underneath the blister surface in the 46 µm sample and the cracks are also more open. The cracks in the 46 µm microstructure were also generally closer to the blister surface than for the 14 µm samples.

Table 5-5 Crack sensitivity results for equiaxed F-P structure with average ferrite grain sizes of 14 and 46 µm (section A)

Specimen	CSR	CLR	CTR
Equiaxed F-P (46 µm)	3.7±2	50.4±6.2	25.3±1.3
Equiaxed F-P (14 µm)	2.9±1	48±3.2	14.3±1

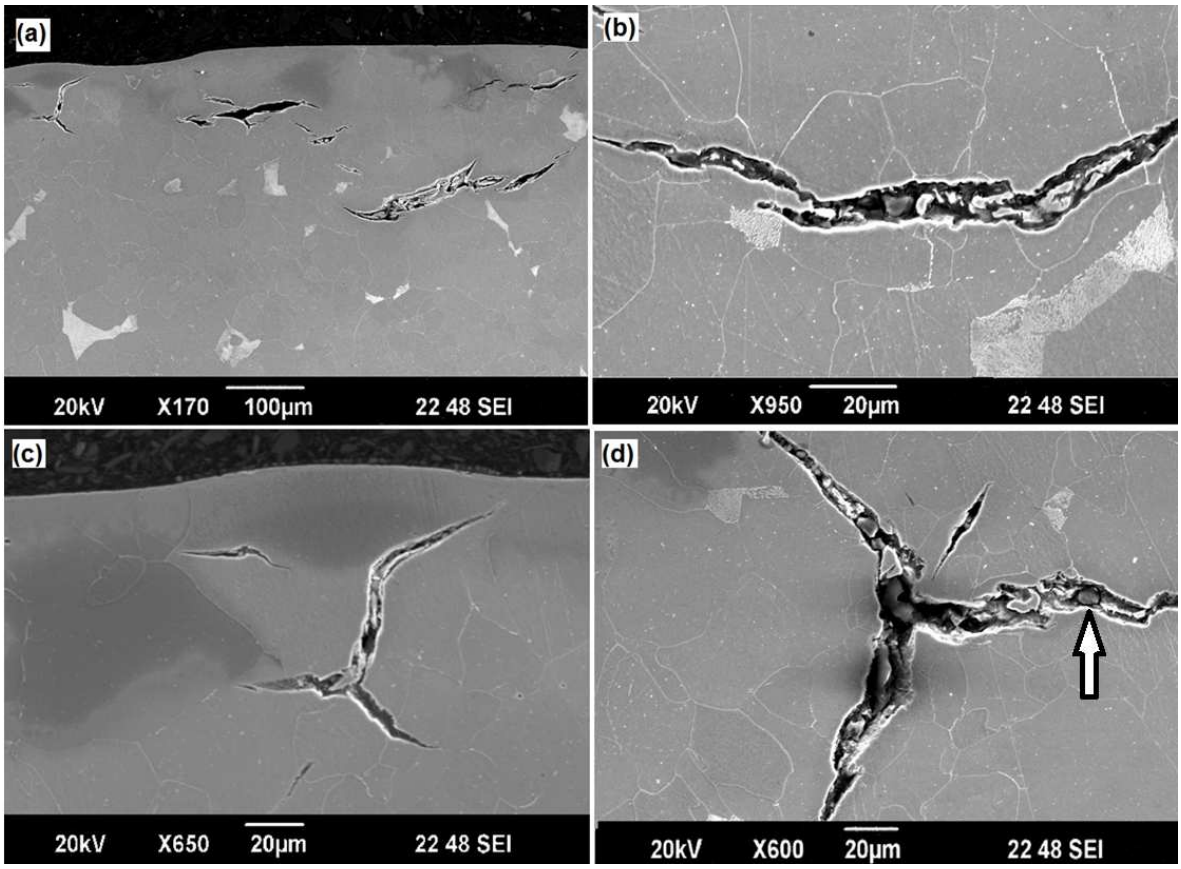

Figure 5-21 Cross-section of equiaxed F-P microstructure with 46 µm average ferrite grain size under a surface blister. (a) General cross-section view showing cracks close to blister surface, (b) higher magnification of a crack, (c, d) triple junctions of intergranular cracks. Arrow in (d) shows an inclusion in the crack.

.

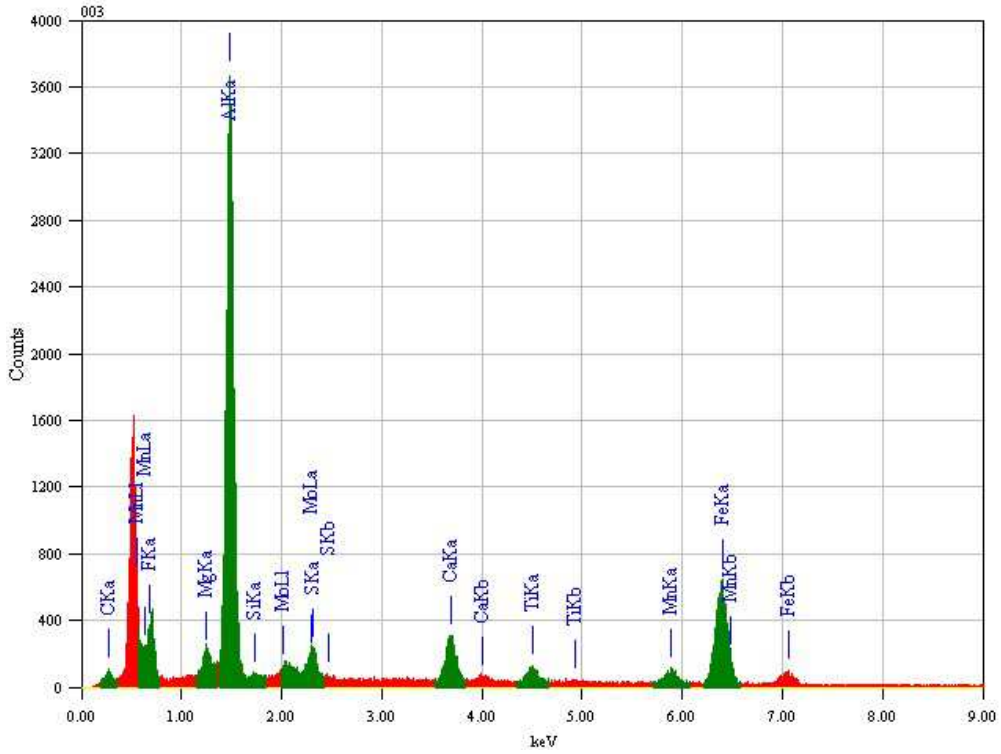

Figure 5-22 EDS analysis of inclusion shown by the arrow in Cross-section of equiaxed F-P microstructure with 46 µm average ferrite grain size under a surface blister. (a) General cross-section view showing cracks close to blister surface, (b) higher magnification of a crack, (c, d) triple junctions of intergranular cracks. Arrow in (d) shows an inclusion in the crack.

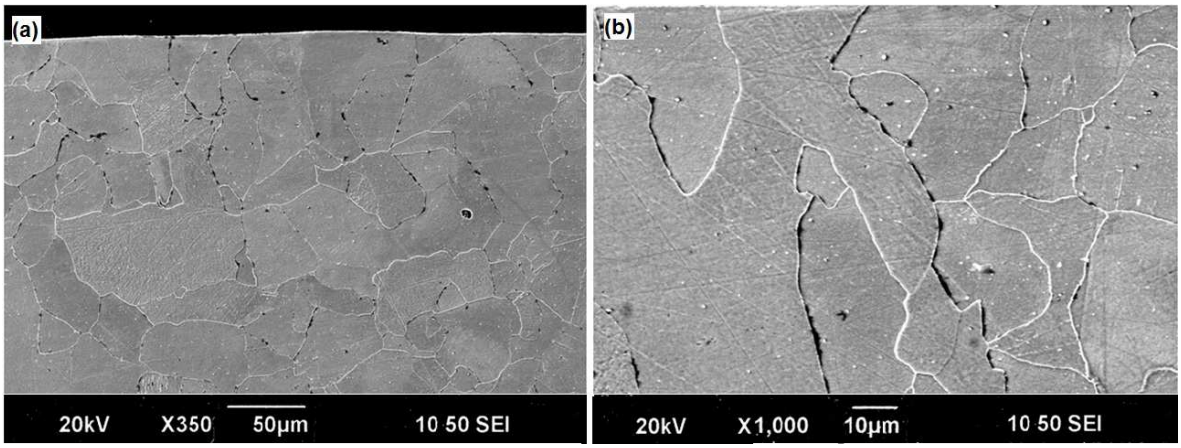

Figure 5-23 Cross-section of equiaxed F-P microstructure with 120 µm average ferrite grain size under a surface. (a) General cross section view showing no blisters, (b) higher magnification.

5.4 Conclusions

- The hydrogen charging experiments demonstrated that the total amount of hydrogen in the charged sample increased during electrolytic charging until a saturation level was reached and then the hydrogen content decreased.
- For the same charging conditions (charging time; electrolyte, current density and sample geometry) the equiaxed microstructure showed the lowest diffusible hydrogen content followed by the banded ferrite-pearlite microstructure, the granular bainite microstructure and finally the HAZ bainitic ferrite microstructure. In contrast, the HAZ microstructure exhibited the lowest residual (trapped) hydrogen content followed by the equiaxed microstructure, the quasi-polygonal ferrite with bainite microstructure and the banded ferrite-pearlite microstructure.
- The experiments revealed that accumulation of hydrogen at trapping sites inside the material produced during electrolytical charging, in the absence of externally applied stress, led to the formation of micro-cracks within the samples and blisters on the surface.
- The results support the hypothesis that grain boundaries can exert opposing effects on the diffusivity of hydrogen atoms and that the highest diffusible and residual hydrogen is expected for an intermediate grain size (~46 μm).
- No blistering was found for the HAZ samples after 24 hours of hydrogen charging.

6 EFFECT OF HYDROGEN ON FRACTURE TOUGHNESS

This chapter begins with the TPB test results. The load-line displacement plots from different steels are presented. The TPB tests plots are followed by calculation of the J-R curves. In addition, the fracture surface analysis using SEM is described.

The chapter closes by discussing the effect of grain size, microstructure and precipitates on the fracture toughness of the tested steel.

6.1 Three Point Bend Test Results

The load=displacement curves obtained during the TPB tests carried out according to ASTM E813 [139] are shown in Figure 6-1 for uncharged and charged steels. The crack-tip energy (J) was calculated from the area under the load-displacement curve at successive unloading points, and plotted against the crack extension (Δa) at these points.

Figure 6-2 and Figure 6-3 present the J-Resistance (J-R) curves (J-based fracture resistance curves) for all samples, before and after hydrogen charging. The calculated J_Q values are plotted in Figure 6-4. The values of J_Q decreased with increasing hydrogen content in all cases with the decrease being approximately linear (Figure 6-4). Assuming a linear relationship between J and hydrogen content, the gradients (in MPa.m/ppm H) for X70 and MX70 are approximately -23 and -19, respectively; -15 for the normalised transfer bar sample and -27 for the simulated HAZ samples of both steels.

The hot rolled X70 samples clearly exhibited the highest fracture toughness in as received condition (Figure 6-2 and Figure 6-4). The J_Q values for the normalised transfer bar showed a similar dependence on hydrogen content, but the magnitudes of the J_Q values were considerably lower than for the hot rolled strip, Figure 6-4. Comparison of the J_Q values for the standard and medium Mn strips (Figure 6-2, Figure 6-3 and Figure 6-4) indicates that the uncharged and charged MX70 samples were slightly, but consistently lower than those for the X70 strip.

The simulated HAZ structures of the X70 and MX70 steels showed significantly lower J_Q values than those of the hot rolled strip steels. These results demonstrate that there was a significant reduction in the toughness of both steels when the fine grained ferrite-pearlite structure of the hot rolled steels was replaced by a coarse bainitic ferrite structure with layers of austenite or martensite that was produced by transformation of coarse austenite grains.

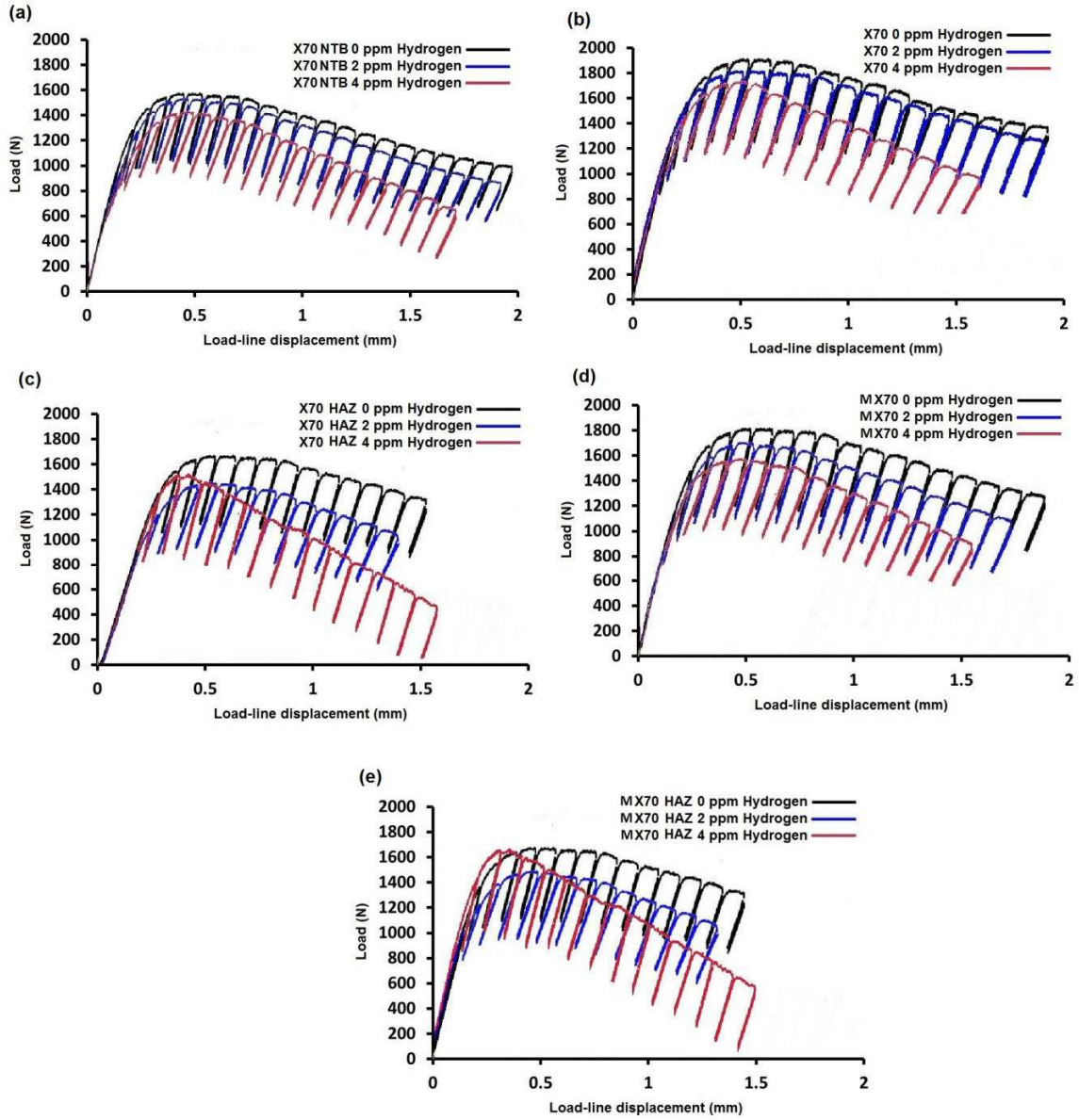

Figure 6-1 J-R curves for (a) NTB, (b) X70, (c) X70 HAZ, (d) MX70 and (e) MX70 HAZ

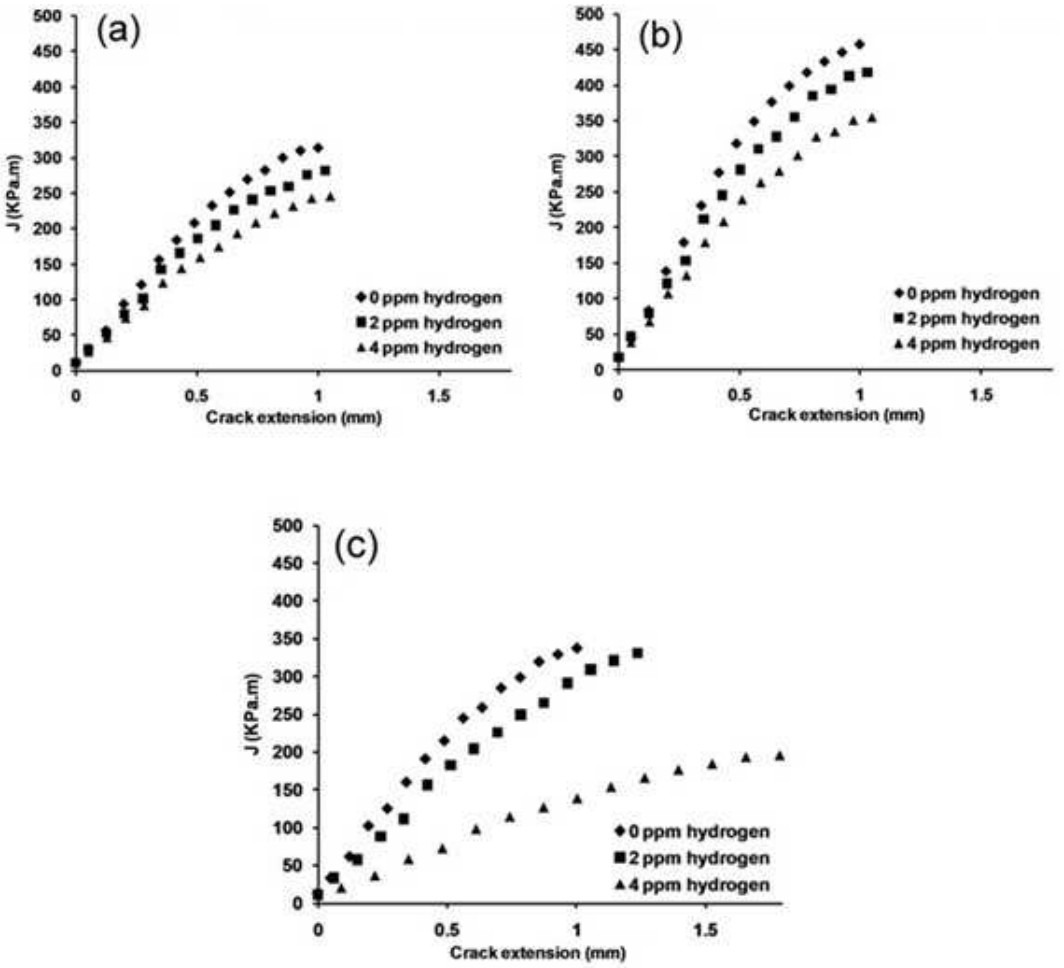

Figure 6-2 J-R curves for X70 samples, before and after charging to 2 and 4 ppm hydrogen: (a) NTB; (b) hot rolled strip; and (c) simulated HAZ.

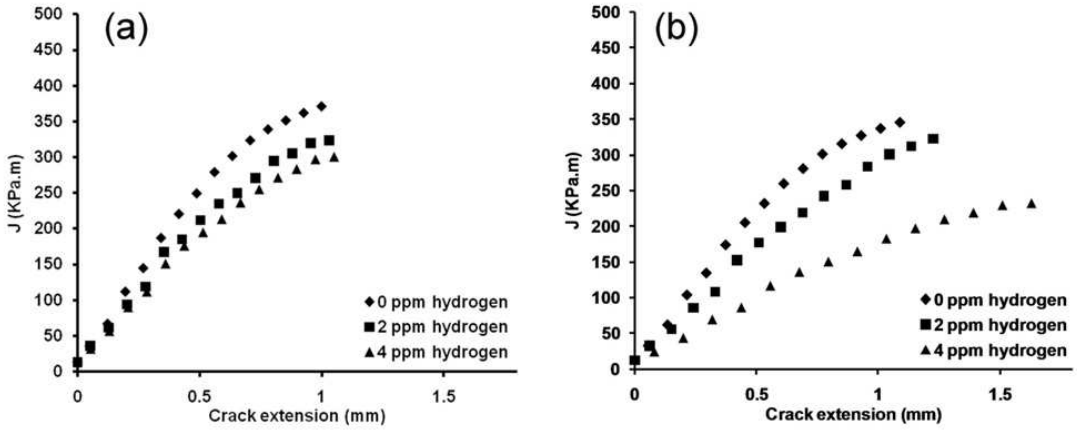

Figure 6-3 J-R curves for MX70 samples, before and after charging to 2 and 4 ppm hydrogen: (a) hot rolled strip; and (b) simulated HAZ.

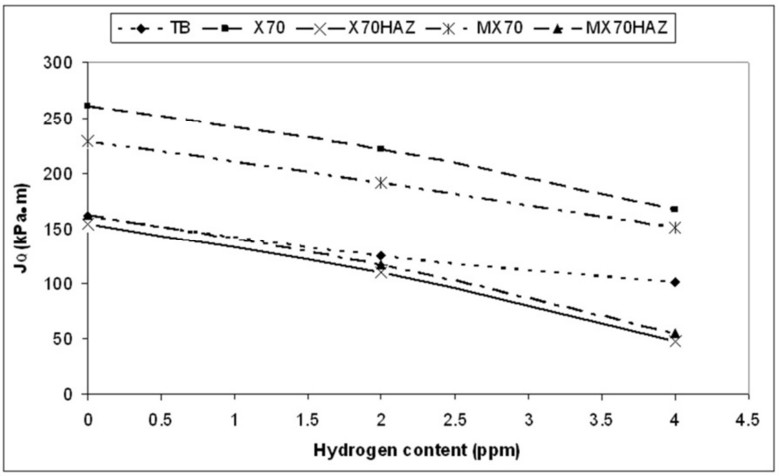

Figure 6-4 Variation of J_Q values with hydrogen content for the tested samples.

6.2 Fractography

The fracture surfaces of the TPB samples were initially studied optically and later in more detail by SEM to analyse the effect of hydrogen. Low magnification views of the fracture surfaces are shown optically in Figure 6-5 and by SEM in Figure 6-6 .

The fracture surface immediately after the fatigue crack changes from mostly ductile in as-received samples to mostly brittle in hydrogen-charged samples.

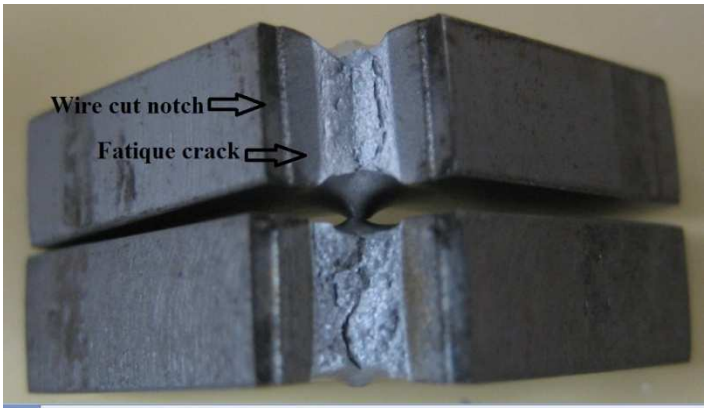

Figure 6-5 Fracture surface of as-received (bottom) and hydrogen charged (top) samples.

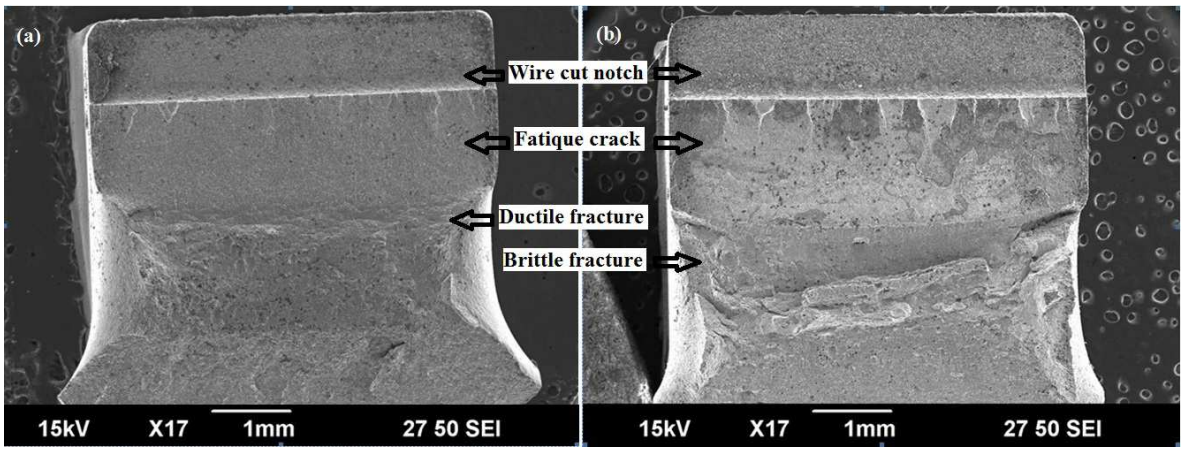

Figure 6-6 SEM images of the cross section of fractured TPB samples (a) as-received sample and (b) hydrogen-charged sample.

Typical SEM images of the fracture surfaces of the normalised TB and the two hot rolled strip steels, before and after charging, are presented in Figure 6-7. The uncharged samples exhibited features characteristic of ductile fracture, such as shear dimples and microvoids, (Figure 6-7d and g) [105, 240, 241]. However, the hot rolled X70 and MX70 strips exhibited a combination of dimples and microvoids, whereas the normalised transfer bar sample showed only elongated dimples without any microvoids, Figure 6-7a. The fracture surface of the MX70 sample presented in Figure 6-7g contains a large inclusion within a large shear/tear dimple.

On charging with 2 ppm hydrogen, the normalised transfer bar and X70 strip specimens showed mixed mode or quasi-cleavage fracture, but with cleavage dominating in the case of normalised transfer bar (Figure 6-7b) and elongated dimples without microvoids being a significant feature of the X70 strip (Figure 6-7e). Furthermore, transverse cracking (cracking perpendicular to the main crack growth direction) was evident in the fracture surface of X70 strip, an effect that was correlated with microstructural banding of pearlite grains parallel to the rolling direction of the strip. With an increase in the hydrogen content to 4 ppm, the fracture appearance of both the normalised transfer bar (Figure 6-7c) and X70 strip (Figure 6-7f) samples exhibited cleavage fracture with facets containing river markings and shear steps or ridges between facets.

The MX70 strip, on the other hand, showed predominantly elongated shear/tear dimples on charging with 2 ppm H (Figure 6-7h); and a fracture surface comprising

microvoids and dimples, as well as cleavage facets for 4 ppm hydrogen (Figure 6-7i). The charged and uncharged MX70 samples consistently showed inclusions either within dimples or at centres of cleavage fracture regions.

From the fractographs shown in Figure 6-7, it is evident that the facets observed in the normalised transfer bar samples are coarser than those in X70 and MX70 strip samples. This difference is likely to arise from the coarser ferrite grain size in the normalised transfer bar samples.

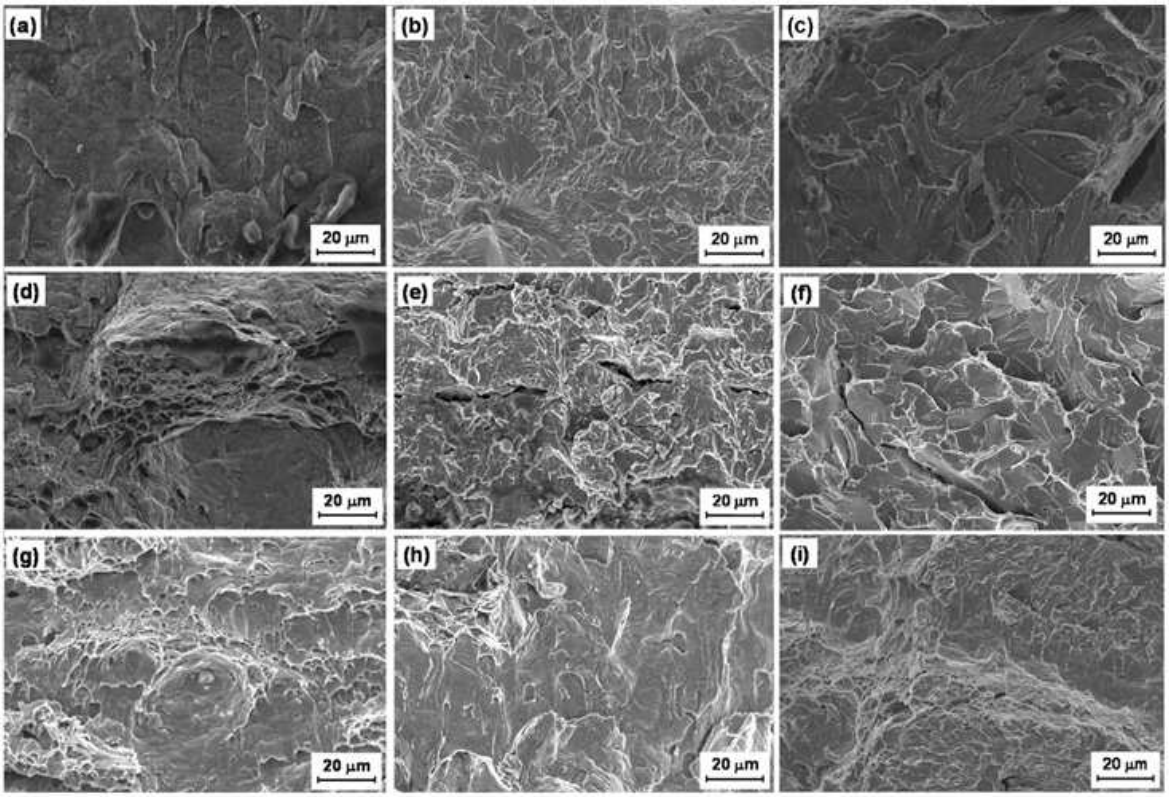

Figure 6-7 SEM fractographs of fracture surfaces before and after charging with hydrogen: NTB - (a), (b), (c); X70 strip - (d), (e), (f); and MX70 strip - (g), (h), (i).

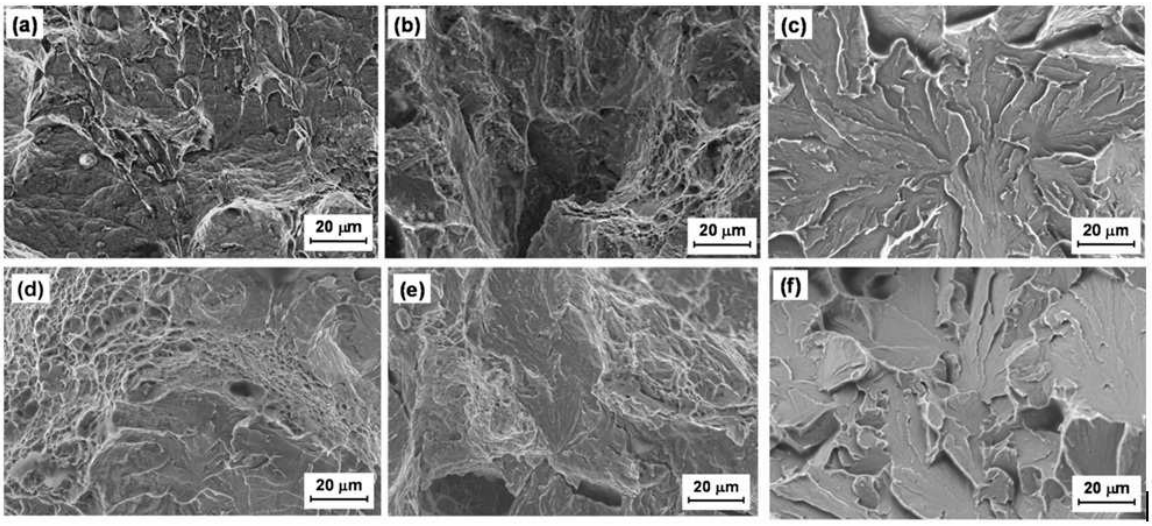

Figure 6-8 SEM fractographs of fracture surfaces before and after charging of the simulated HAZ samples: X70 - (a), (b), (c); and MX70 - (d), (e), (f).

Figure 6-8 shows fractographs of simulated HAZ samples of X70 and MX70, before and after charging. The uncharged MX70 HAZ sample (Figure 6-8d) exhibited a quasi-cleavage morphology with evidence of dimples, microvoids and cleavage facets; whereas only dimples and microvoids were observed for the uncharged X70 HAZ sample (Figure 6-8a). Shear dimple regions of the fractured X70 HAZ samples also showed remnants of fine microvoids that had coalesced to produce coarser shear dimples that were 20-50 μm wide. The presence of 2 ppm hydrogen (Figure 6-8b and e) resulted in similar quasi-cleavage fracture morphologies in both simulated HAZ samples: cleavage facets and regions of microvoids. With 4 ppm hydrogen (Figure 6-8c and f), both steels exhibited large cleavage facets separated by shear steps and tear ridges.

6.3 Discussion

Microstructural features such as reversible and irreversible traps present in the steel reduce the mobility of hydrogen towards regions of stress concentration ahead of the crack tip and thereby influence the susceptibility of the steel to HIC. However, if the hydrogen concentration in the traps increases above the critical value for crack initiation, then traps can act as crack initiation sites. These sites can “trigger” cracking in the stress concentrated zone ahead of the crack front [242, 243]. Micro-fractures around large inclusions were

observed in the present work and it is inferred that particle decohesion is induced by trapped hydrogen, producing sharp cracks and a local stress concentration high enough to promote crack extension by cleavage or void growth around the particle. These "pre-cracked" regions become incorporated in the crack surface on propagation of the crack front [242, 243].

The type, amount, size and distribution of traps affect the HIC susceptibility of the steel remarkably [2]. The observed differences in fracture toughness of the different samples studied here are discussed below in terms of the effects of grain size, microstructure and the type and distribution of precipitates.

6.3.1 Effect of grain size

It is well established that grain refinement of metals and alloys increases the fracture toughness. Consequently, the finer grain size of the X70 strip in the uncharged state results in a higher J_Q value compared with the coarse grained NTB. Furthermore, it has also been reported that grain refinement improves the resistance of materials to HIC [8, 244, 245]. However, when hydrogen is introduced into the material, grain boundaries can either increase the hydrogen diffusion rate [110-112] or decrease it by acting as reversible hydrogen trapping sites at the nodes [115]. As the grain size decreases, the mobility of hydrogen increases because of a larger grain boundary area per unit volume, but the higher density of nodes or junction points can act as potential traps for hydrogen atoms and lead to a reduction in its overall mobility. As a result of these two opposing effects, the hydrogen diffusion coefficient will be a maximum at an optimum grain size, as pointed out by Ichimura [115]. Since the most significant microstructural difference between the NTB sample and the X70 strip was the ferrite grain size, it is likely that in the coarser structure less hydrogen in trapped in nodes and junction points facilitating a higher hydrogen flux to, and build up in, the stress concentrated zone ahead of the crack tip, thus facilitating crack propagation. The fine grained MX70 sample also exhibited higher J_Q values than the NTB sample, before and after hydrogen charging.

It is also well known that dislocations can act as effective traps for hydrogen, thereby reducing the mobility of hydrogen atoms. Therefore, the lower dislocation density

of the ferrite-pearlite microstructure of the normalised transfer bar sample would also be expected to allow faster diffusion of hydrogen to, and its accumulation in, the stress-concentrated zone ahead of the crack tip. Further, the availability of hydrogen atoms would be likely to facilitate hydrogen build-up in particle/defect traps in close proximity to the crack front. Permeation experiments [182] confirm that the diffusivity of hydrogen is higher in the normalised transfer bar steel compared to the X70 strip. Decohesion or particle cracking would occur when the H concentration and local stress reached critical values. Therefore, in terms of microstructural factors, the lower fracture toughness of the NTB sample in the charged state can be attributed to the combined effect of coarser ferrite grains and lower dislocation density. The relatively low fracture toughness in the uncharged condition is considered to be a grain size effect.

6.3.2 Effect of microstructure

The uncharged and charged X70 strip samples exhibited slightly higher J_Q values than the MX70 samples. A possible contributing factor to this result is that more significant ferrite-pearlite banding was observed for the X70 strip. From electrochemical permeation experiments on ferrite-pearlite banded structures, Chan and co-workers [59, 60] have shown that the effective diffusivities of hydrogen in specimens where the banding is perpendicular to the direction of hydrogen entry is an order of magnitude lower than in those specimens where hydrogen entry is along the direction of banding. Since the direction of the loading in the hot rolled X70 strip was perpendicular to the banded structure, reduced mobility of hydrogen towards the crack tip could have contributed to a higher toughness value in charged samples compared with the MX70 strip, which did not show any evidence of banding.

Although the J_Q values in the presence of H were higher for the X70 samples, fracture propagation occurred predominantly by cleavage. Despite this “brittle” mechanism of cracking, more energy was evidently consumed in the crack extension process than for the MX70 samples, which were ostensibly more “ductile”, with the dominance of microvoids and shear dimples. Beachem’s principle [52], that H induces cracking by facilitating the mechanism to which the microstructure is most susceptible, is relevant to

these observations. This principle underpins subsequent development of two general mechanisms for hydrogen embrittlement: hydrogen enhanced local plasticity (HELP) model [246]; and hydrogen enhanced decohesion (HEDE) model [246]. It is therefore concluded that the lower shear strength of the MX70 and the presence of hydrogen facilitates dislocation motion (local plasticity) that contributes to the formation of microvoids and shear dimples, in association with decohesion/cracking of inclusion and precipitate traps. In comparison with relatively "easy" dislocation movement in MX70, the significantly higher solute Mn content in the X70 could restrict dislocation mobility to the extent that, after fracture initiation by particle decohesion, crack propagation occurs by cleavage, albeit with a higher expenditure of energy. The role of particles is discussed in the following section.

The simulated HAZ microstructures of both samples consisted predominantly of coarse bainitic ferrite laths separated by martensite or retained austenite layers. Fracture of bainitic steels along lath boundaries has been reported [247, 248] and the martensite or retained austenite layers are known to provide initiation sites for fracture because of its high hardness and crack susceptibility [249].

When the samples are charged with hydrogen, the bainitic lath boundaries can trap large amounts of hydrogen [125]. Arafin and Szpunar [247] have observed extensive cracking in bainitic microstructures and suggest that the accumulation of a significant amount of hydrogen at the bainitic lath boundaries can eventually lead to the separation of these interfaces and result in cracking when the hydrogen concentration reaches a critical value. Therefore, in the presence of hydrogen, propagation of transgranular cleavage cracks can be facilitated by the presence of bainitic lath interfaces, although the cracks may initiate at local MA regions in the bainitic ferrite structure [247].

The low J_Q values recorded for the simulated HAZ samples are a consequence of the coarse prior austenite grain size, the formation of relatively coarse laths of bainitic ferrite, the presence of elongated MA islands, the high hardness of these structures (Figure 4-16), and the low resistance to crack propagation along lath boundaries in both the charged and uncharged conditions. The more HIC-resistant structures of the parent X70 or MX70 steels consisted mainly of polygonal or quasi-polygonal ferrite.

The ferrite laths formed in the X70 HAZ sample were finer than those present in MX70 HAZ (Figure 4-15 a and b), because the higher hardenability of the X70 steel (see CE (IIW) values in Table 1), resulted in transformation on cooling over a lower temperature range. Nevertheless, the J_Q values were only marginally higher for the X70 HAZ (Figure 6-4), because lath interfaces and MA islands dominate in the fracture process rather than fracture across the thickness of the laths.

6.3.3 Effect of precipitates

In hot rolled steels like those used in this study, hydrogen can be trapped at interfaces between the matrix and non-metallic particles or at the surface of voids and cracks, etc. As the trap activation energies of the interfaces of non-metallic inclusions such as MnS and precipitates of TiC are high, they are regarded as strong irreversible traps for hydrogen [108, 109]. Pressouyre and Bernstein [108] reported that incoherent TiC precipitates are more effective than coherent TiC precipitates, whereas Takahashi *et al.* [120]and Valentini *et al.* [121] found fine coherent TiC particles and Ti(C,N) precipitates to be stronger irreversible traps. According to Wei and Tsuzaki [103], NbC precipitates are stronger traps than TiC in tempered martensitic structures and in API X70 steels, subjected to electrochemical charging in H_2SO_4 solutions. Dong *et al.* [2] have reported that rather than nitrides of Ti and Nb being the main trap sites that cause HIC, coarser inclusions such as oxides play a dominant role. Although Pressouyre and Bernstein [108] considered MnS inclusions to be strong irreversible trapping sites for hydrogen, other researchers have concluded that they have moderate binding energies for hydrogen and can act as reversible trapping sites [119]. The J_Q values for the two strips are discussed below, taking into account relevant reports from the literature and the types and distributions of precipitates observed in this study.

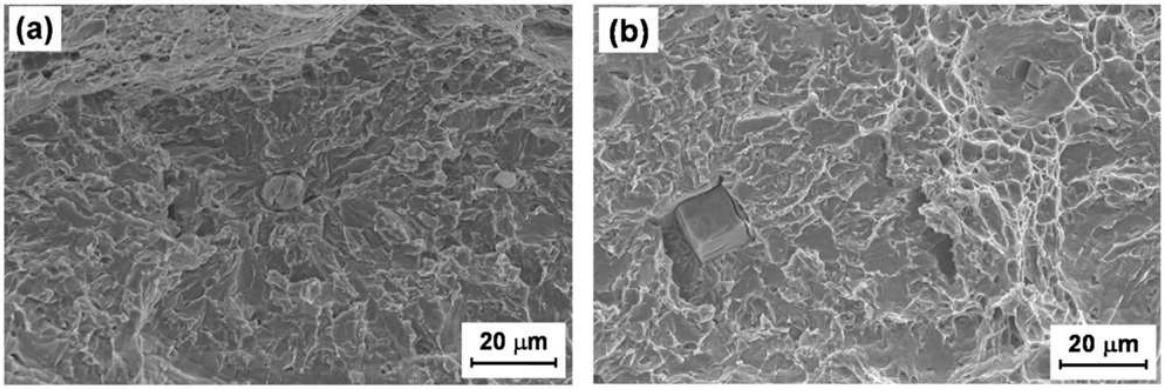

Figure 6-9 SEM fractographs of MX70 samples showing large carbonitride particles that have induced local cleavage fracture.

The current study indicated that the MX70 strip had higher number densities of complex (Ti,Nb)(C,N) precipitates and oxides of Ca and Al, compared to the X70 strip (Figure 4-17). As mentioned above, several authors reported that fine carbonitrides can act as strong traps for hydrogen and significantly reduce the mobility of hydrogen, thereby increasing its resistance to HIC [250-252]. However, the TPB tests results showed that the MX70 strip charged to 2 ppm and 4 ppm hydrogen exhibited slightly lower J_Q values than the X70 strip. This result can be rationalized in terms of the size distribution of the different precipitates in these two steels. The carbonitride precipitates in MX70 strip showed a broad distribution of sizes and some very large precipitates were observed (see Figure 6-9b). Moreover, the MX70 strip had double the number of oxide inclusions compared to X70 strip with most of the inclusions having diameters greater than 2 μm. Dong *et al.* [2] observed cracks originating from large inclusions of Ca-Al oxides, rather than Ti or Nb carbonitrides. They suggested that the larger diameters of the oxides (2-3 μm in diameter) can attract more hydrogen than fine carbonitrides and can therefore play a dominant role in HIC. On this basis, the lower J_Q values observed for the charged MX70 strip may be attributable, at least in part, to the presence of coarse oxide inclusions and/or (Ti,Nb)(C,N) precipitates in these samples. These particles could effectively trap hydrogen to the critical level to induce particle cracking or interfacial decohesion, leading to local void growth and coalescence or to cleavage fracture. This hypothesis is supported by evidence of inclusions/precipitates at the centres of dimples and cleavage fracture sites see for example, Figure 6-7g and Figure 6-9.

The number densities of MnS precipitates are almost the same in both of these strips. However, it can be seen from Figure 4-18b that the distribution of the aspect ratios of MnS precipitates for the MX70 specimen has an extremely long tail with some MnS precipitates exhibiting aspect ratios up to 20:1. Domizzi *et al.* [91] have reported that the presence of even a small number of very elongated inclusions can result in reduced HIC resistance. So this factor could contribute to the lower HIC resistance of the MX70 steel. However, in this study, the elongated MnS inclusions were aligned perpendicular to the loading direction during the three bend tests and therefore it is suggested that they would not have any significant detrimental effect on fracture toughness of the MX70 strip. Rather, it is considered that the lower J_Q values compared to X70 are due mainly to the presence of a higher total density of precipitates/particles (Figure 4-17), particularly oxide inclusions; their susceptibility to hydrogen-induced cracking/decohesion; and decreased resistance to shear fracture mechanisms, by dislocation motion, because of the lower concentration of solute Mn.

6.4 Conclusions

- Increasing the hydrogen content from 0 to 4 ppm resulted in an approximately linear decrease in fracture toughness (J_Q) for all of the samples tested.
- The hot rolled X70 steel consistently exhibited higher J_Q values than the MX70 strip before and after hydrogen charging. Therefore, decreasing the Mn content from 1.2% to 0.5% in the steels investigated resulted in a decrease in fracture toughness.
- In the charged condition, the coarse grained, NTB sample showed much lower J_Q values than both hot rolled strip steels. It is concluded that the coarse ferrite grains and the relatively low dislocation density enhanced hydrogen build-up in the stress-concentrated zone ahead of the crack tip, facilitated decohesion and cracking of particles in this zone.
- The fracture surfaces of X70 and MX70 in the uncharged state were characterised by the more ductile modes of cracking: microvoids and shear dimples. In the

presence of 2 and 4 ppm hydrogen, more brittle modes: quasi-cleavage and cleavage, were evident.

- Although the fracture surfaces of hydrogen-charged MX70 showed that shear mechanisms were more significant than for the corresponding X70 samples, MX70 exhibited slightly lower J_Q values than X70. It is concluded that the presence of a higher volume fraction of coarse oxide and carbonitride particles in MX70 promoted hydrogen-induced decohesion and the lower yield strength facilitated hydrogen-induced local plasticity, with void formation, growth and coalescence.
- Simulated HAZ structures for both the standard and medium Mn steels showed low J_Q values which decreased with increasing hydrogen. There was little effect due to the difference in Mn content. The relatively hard and coarse bainitic-ferrite structure with interlayers of austenite or martensite resulted in a marked decrease in toughness, both with and without hydrogen.

7 GASEOUS CHARGING

Gaseous hydrogen embrittlement of X70, MX70 and NTB samples was studied through tensile tests of sealed hollow cylindrical samples with 10 MPa hydrogen gas pressure at 25, 50 and 100˚C. All samples were also tested under 10 MPa of argon for comparison. It was shown that the strength and ductility in all samples were reduced under 10 MPa of hydrogen. Hydrogen tests at elevated temperature demonstrated reduced strength but increased elongation compared to the room temperature tests. The work hardening behavior of X70 and MX70 was also investigated and is reported in this Chapter.

7.1 Tensile Test Results

The tensile tests revealed the behavioural differences between the steels tested under pressurised hydrogen and under pressurised argon gas at the selected test temperatures of 25, 50 and 100˚C. Macrographs of representative fractured samples are shown in Figure 7-1 for room temperature testing. It can be seen that the samples fractured near the centre of the gauge section and that the hydrogen-charged sample (b) a showed substantially less elongation and necking. Necking is clearly significant in the argon-charged sample.

Figure 7-1 Comparison of fractured tensile test samples for room temperature testing of an argon-charged test piece (a) and a hydrogen-charged test piece (b).

Corrected stress-strain curves obtained from the tensile tests are presented in Figure 7-3. Stress-strain curves were determined using the cross-head displacement. The cross-head displacement consists of a combination of the strains in the machine, the grip fixtures, and the grip and gauge sections of the sample. Because of the circular- shaped sample, it was not possible to install a mechanical extensometer on a sample, nor to use the Instron video extensometer since it was linked to Instron fatigue software not to a tensile test program. Therefore, a video camera was used to record the extension between two standard marks printed on the sample that were longitudinally separated by 35 mm. The video frames were then printed on paper for every two seconds of testing and were related to the load read from the Instron. Figure 7-2 shows the painted and marked sample before and after testing.

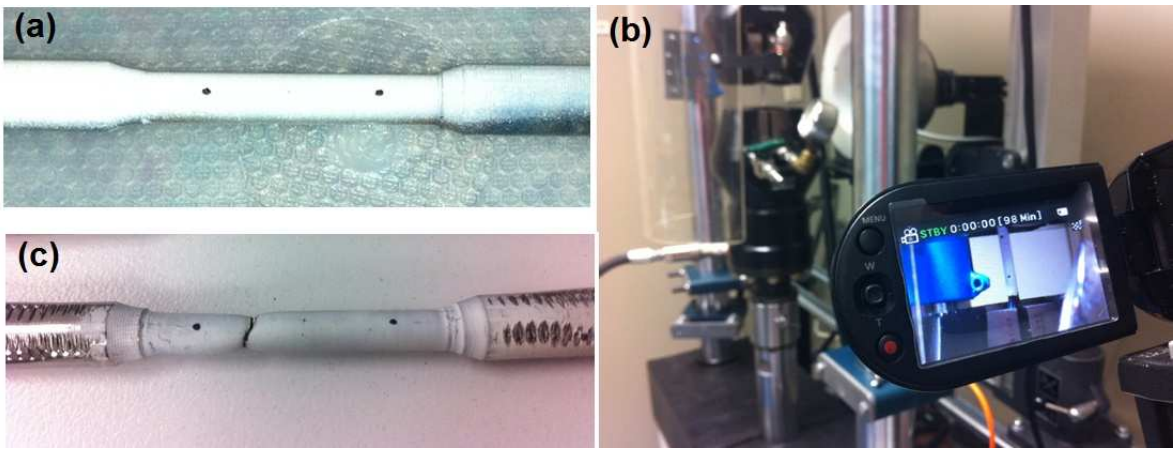

Figure 7-2(a) Example of a white painted sample marked with black dots 35mm apart; (b) photograph of the video camera recording the instantaneous elongation; and (c) the sample after fracture.

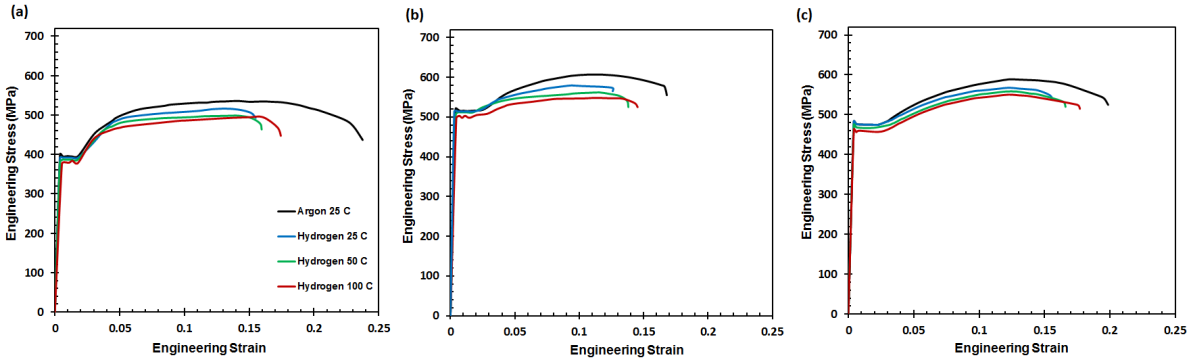

Figure 7-3 Stress-strain curves for NTB (a), X70 (b) and MX70 (c) hollow cylindrical samples with 10 MPa of argon at 25˚C and 10 MPa of hydrogen at 25, 50 and 100˚C.

Uniform strain occurred within the gauge length until the tensile load reached its peak point (or necking point). After the peak point, strain was totally localised at the necking region and accelerated before final fracture. This suggests that the wall thickness outside of the necked region matches that at the peak load. Hence, the final wall thickness measured outside the necking region can be used to calculate the UTS. Specimens were sectioned to measure this final wall thickness optically. The tensile strength of the fractured specimen was calculated by dividing the peak load by the cross-sectional area corresponding to UTS. In addition, the 10 MPa gas pressure was considered as an amount of pre-stress in the calculation of the UTS. For internal pressure within a thin-walled cylinder, the axial stress is defined as Pr/2t [253]. Here, P, r and t are the charging pressure,

the internal radius of the specimen and the wall thickness, respectively. The UTS of specimens was finally calculated by adding the charging pressure to the tensile strength value estimated based on the peak load and final wall thickness.

As shown in Figure 7-3 and

Table 7-1, the specimens charged with 10 MPa of hydrogen gas showed a reduction in their UTS compared to those tested in an argon environment. Interaction of hydrogen gas with the X70 material resulted in 4.5 % reduction in the ultimate tensile strength compared with the argon-charged specimen at 25˚C. These results are consistent with those in previous reports [254, 255] on hydrogen embrittlement. However, the sensitivity of tensile strength to hydrogen depends also on the chemical composition and the microstructures of the steels, since the MX70 and NTB samples showed 3.6% and 3.7% reduction in UTS, respectively.

Table 7-1 Mechanical properties of tested specimens.

Steel/Gas/Temperature	YS (MPa)	TS (MPa)	Total strain (%)	Embrittlement Index
NTB Argon 25˚C	386±8	536±9	23.7±2	-
NTB Hydrogen 25˚C	384±7	516±10	15.5 ±1	0.35
NTB Hydrogen 50˚C	383±8	494±9	16±1	0.33
NTB Hydrogen 100˚C	378±9	493±9	17.4±1	0.27
X70 Argon 25˚C	518±10	606±10	16.8±1	-
X70 Hydrogen 25˚C	517±9	579±8	12.6±1	0.25
X70 Hydrogen 50˚C	511±8	562±7	13.8±1	0.18
X70 Hydrogen 100˚C	503±7	548±7	14.5±1	0.14
MX70 Argon 25˚C	475±6	588±9	19.8±1	-
MX70 Hydrogen 25˚C	475±7	567±8	15.4 ±1	0.22
MX70 Hydrogen 50˚C	467±9	558±9	16.4±1	0.17
MX70 Hydrogen 100˚C	460±8	550±7	17.5±1	0.12

The total strain at fracture in Figure 7-3 was used to calculate a parameter that reflects the extent of hydrogen embrittlement. The total tensile strain for samples tested at 25°C is lower for the hydrogen-charged samples than for those argon-charged specimens, as can be seen in Figure 7-3 and

Table 7-1. An embrittlement index (E_i) is defined as:

$$E_i = 100 \times (\varepsilon_A - \varepsilon_H) / \varepsilon_A \qquad 7\text{-}1$$

where ε_A is the total tensile strain for argon-charged sample and ε_H is the total tensile strain for the hydrogen charged sample. The index for samples tested at 25°C is 35%, 25% and 22% for the NTB, X70 and MX70 samples, respectively. This suggests that NTB has the most susceptibility to hydrogen embrittlement during gaseous charging compared to the strip samples. Also X70 is more affected by gaseous hydrogen than MX70.

One important difference in the stress-strain curves after the peak load is the post-necking strain. The specimens charged with hydrogen gas showed less post-necking strain, while the reference sample charged with argon gas showed extensive post-necking strain and the maximum strain at fracture. Even though the nominal wall thickness of the specimen was 1.0 mm, the real thickness varied by about 100 μm due to the machining followed by polishing of the walls. Thus, a conversion of the load information to the stress value in the Instron software is based on the nominal wall thickness and the accuracy is limited to ±10%.

Table 7-1shows that the yield strengths of X70 and MX70 are higher than that of NTB. As the ferrite grain sizes of the X70 and MX70 are finer compared to NTB (see chapter 5), there is a Hall-Petch effect [253] that leads to an increase in the yield strength, in agreement with the literature [200]. In addition, the higher density of dislocations in X70 and MX70 (Chapter 5) due to controlled thermo-mechanical processing contributes to a rise in the yield strength [256].

It should be noted that for the samples tested at room temperature, hydrogen charging had no apparent effect on the yield stress. However, the ultimate tensile strength was lowered by hydrogen charging. As a result, the yield to tensile ratio is higher for hydrogen-charged samples compared to the argon-charged samples. Detailed analysis of the work hardening characteristics of the hydrogen- and argon-charged samples is presented in section 7.3.

7.2 Effect of Temperature

From Table 7-1 it can be seen that by increasing the testing temperature for hydrogen charged specimens, the total elongation is increased. This phenomenon is in agreement with the literature[257, 258]. Also the results of

Table 7-1 show that yield and tensile strengths are decreased with increasing temperature. This supports the results of Michler's [259] work which covered a much wider range of temperature (-80˚C to 20˚C). Due to limitation in the number of samples, elevated temperature tensile testing was not conducted on argon-charged samples. However Hofmann and Rauls [257] showed that, for air charged normalised plain carbon steel tensile samples, an increase in the temperature from 25˚C to 100 ˚C reduced the reduction in area and total elongation in fractured tensile samples because of aging effect.
Table 7-1 indicates that a temperature increase from 25˚C to 100˚C increased the total elongation of tested samples in the presence of hydrogen in the steels investigated. This observation is consistent with the hypothesis that hydrogen embrittlement would be reduced at higher temperatures because the diffusion and desorption rates of hydrogen are increased, inhibiting hydrogen build-up at potential crack sites such as particle interfaces and other slip barriers [260].

Although the shapes of the stress-strain curves for hydrogen-charged X70, MX70 and NTB samples were similar for all test temperatures, the strength decreased and the ductility increased with increasing temperature. Moreover, both the uniform and total strains under hydrogen gas showed slightly higher values with increasing temperature.

7.3 Work Hardening Behavior

In order to explain the effect of hydrogen on tensile test behavior, the true stress–true strain tensile curves were studied. As mentioned before [261], the work hardening exponent (n), has linear and reverse linear relationships with the uniform strain and yield ratio, respectively. As stated in Chapter 2, a variety of empirical equations for stress–strain

correlation has been used to model the work hardening characteristics of steels. The simplest and the most commonly used relation is that of Hollomon [183] as described in Chapter 2.

In order to investigate the work hardening behaviour using the Hollomon approach, true stress and true strain values were calculated from the following equations [253]:

$$\sigma_T = \sigma_E(1+\varepsilon_E) \quad 7\text{-}2$$

$$\varepsilon_T = ln(1+\varepsilon_E) \quad 7\text{-}3$$

where σ_E, σ_T, ε_E and ε_T are engineering stress, true stress, engineering strain and true strain respectively.

The work hardening rate ($d\sigma/d\varepsilon$) is plotted against true strain (ε) for all samples up to the UTS in Figure 7-4. It is clear that initially the rate of work hardening rapidly declines linearly, whereas later it declines exponentially more slowly. It is associated with first localisation of deformation in the softer phase, e.g. ferrite, in which areas close to hard pearlite work harden first. This is follows by the load transfer to pearlite, in which plastic deformation again is primarily concentrated in the ferrite lamellae.

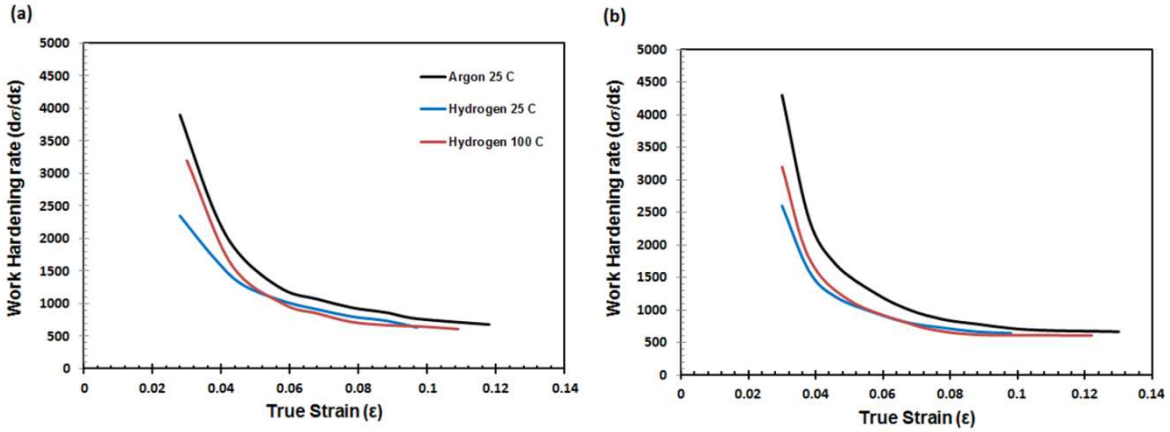

Figure 7-4 Work hardening rate vs. true strain for (a) X70 and (b) MX70.

The Hollomon equation is:

$$\sigma = K_H . \varepsilon^{n_H} \quad 7\text{-}4$$

where n_H is the strain hardening exponent and K_H is a constant.

Taking the logarithm on both sides gives the following linear equation:

$$ln\,\sigma = n_H\, ln\,\varepsilon + ln\,K_H \quad 7\text{-}5$$

The parameters n_H and k_H are determined by linear regression from ln(σ) versus ln(ε) plots. If the experimental data obey the Hollomon power law, these plots are linear. Nevertheless, a small deviation from linearity is seen in Figure 7-5 which is the result of different deformation behaviour during uniform straining. All samples showed two work hardening stages as illustrated schematically in Figure 7-5a (inset). This is in accordance with the typical behaviour of the steels containing soft and hard phases, like ferrite-pearlite or ferrite-martensite steels [262].

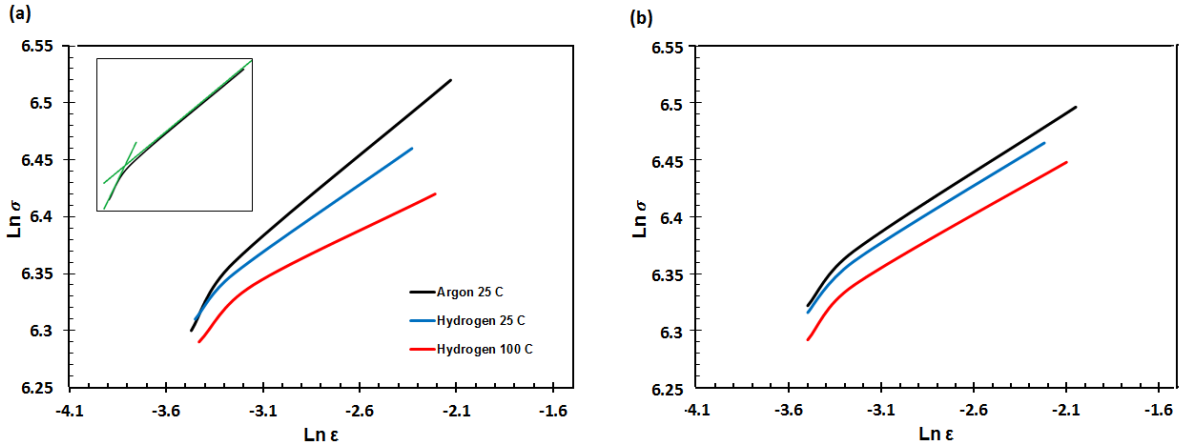

Figure 7-5 ln(σ) versus ln(ε) curves for (a) X70 and (b) MX70. The inset in (a) illustrates schematically the deviation from linearity of the Hollomon power law.

Although the total plastic deformation is reduced in the presence of hydrogen, the different stages are also affected to the same extent. As can be seen in Figure 7-5, a single set of fitting parameters n_H and K_H cannot be allocated to the entire plastic strain range using the Hollomon relationship. However, if the two work hardening regions are outlined as per Figure 7-4a(inset) and the Hollomon equation is re-applied to each of them in Figure 7-5, a good fit is achieved for the whole plastic region (Figure 7-6, Table 7-2).

Considering Table 7-2, in X70 samples the work hardening exponent in stage I decreased to stage II. Exposure to hydrogen at room temperature reduced the work hardening exponent in both stages. In case of MX70 the same trend occurred, however, the work hardening exponent was reduced less in stage II compared to X70. Hydrogen charged samples showed lower work hardening exponent in stage I compared to argon charged samples. The results show that for X70 the effect of hydrogen on reducing the work hardening exponent is more marked than for MX70. Stain hardening exponent is a good

indicator for work hardenability of the steel. The higher the value of exponent, the higher is the rate at which the steel work hardens [263]. The amount of work hardening exponent is within the range of numbers that other researchers reported [264, 265]. Considering the effect of temperature on hydrogen charged samples, the work hardening exponent in both stages was increased with an increase in test temperature from 25 C to 100 C.

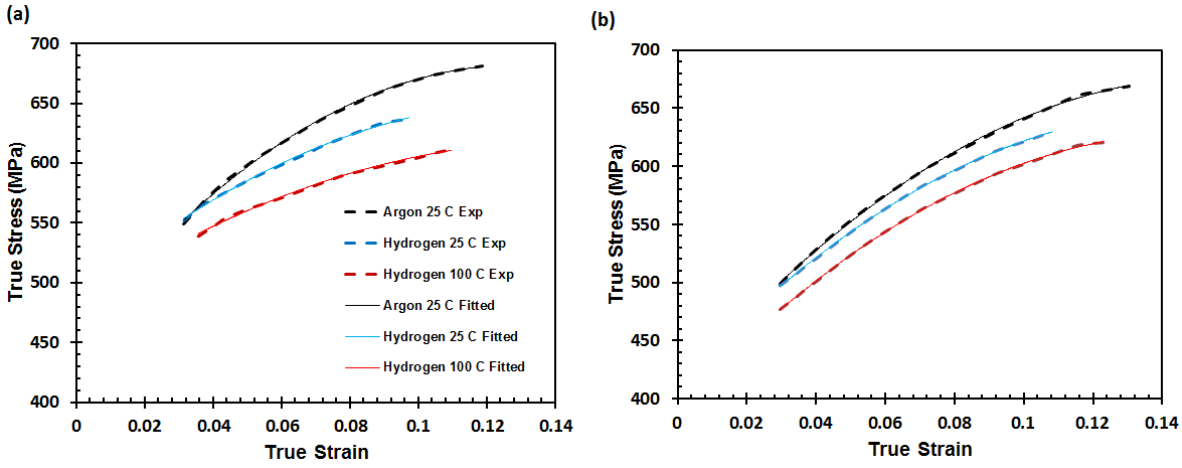

Figure 7-6 Simulated flow curves obtained from Hollomon fitting for the two work hardening stages and experimental curves for X70 (a) and MX70 (b)

Table 7-2 Fitting parameters, predicted uniform strain and associated errors of the Hollomon equations for the various work hardening stages. $\varepsilon_{P,Exp}$ is the uniform true strain at maximum load after subtracting the true strain at the onset of plastic deformation from the maximum uniform true strain.

	$n_{H,I}$	$n_{H,II}$	$\varepsilon_{P,Exp}$	$\varepsilon_{P,Fit}$	Error (%) $=100\times(\varepsilon_{P,Fit}-\varepsilon_{P,Exp})/\varepsilon_{P,Exp}$
X70 argon 25˚C	0.09	0.082	0.085	0.082	-3.5
X70 hydrogen 25˚C	0.066	0.061	0.063	0.061	-3.2
X70 hydrogen 100˚C	0.077	0.07	0.072	0.07	-2.8
MX70 argon 25˚C	0.104	0.096	0.099	0.096	-3
MX70 hydrogen 25˚C	0.087	0.082	0.085	0.082	-3.5
MX70 hydrogen 100˚C	0.094	0.087	0.090	0.087	-3.3

The physical importance of these fitting elements was assessed by assessing their capability to predict the plastic strain at necking (ε_P) at the end of the second stage of work hardening

as proposed in [266]. Based on the instability criterion ($d\sigma/d\varepsilon = \sigma$) the ε_P value is calculated from the following relation [267]:

$$\varepsilon_{PH} = n_H \quad 7\text{-}6$$

where ε_{PH} is the plastic strain as expected by the Hollomon equation and is same as the constant (n_H) gained for stage II from Table 7-2. The errors in the calculated uniform strain are presented in Table 7-2. Variable error estimations with no specific trend were observed, however with maximum deviation of 3.5%, errors are negligible. Thus, the Hollomon equation not only has the capability to define the plastic deformation curve, but also able to calculate the amount of the uniform plastic strain.

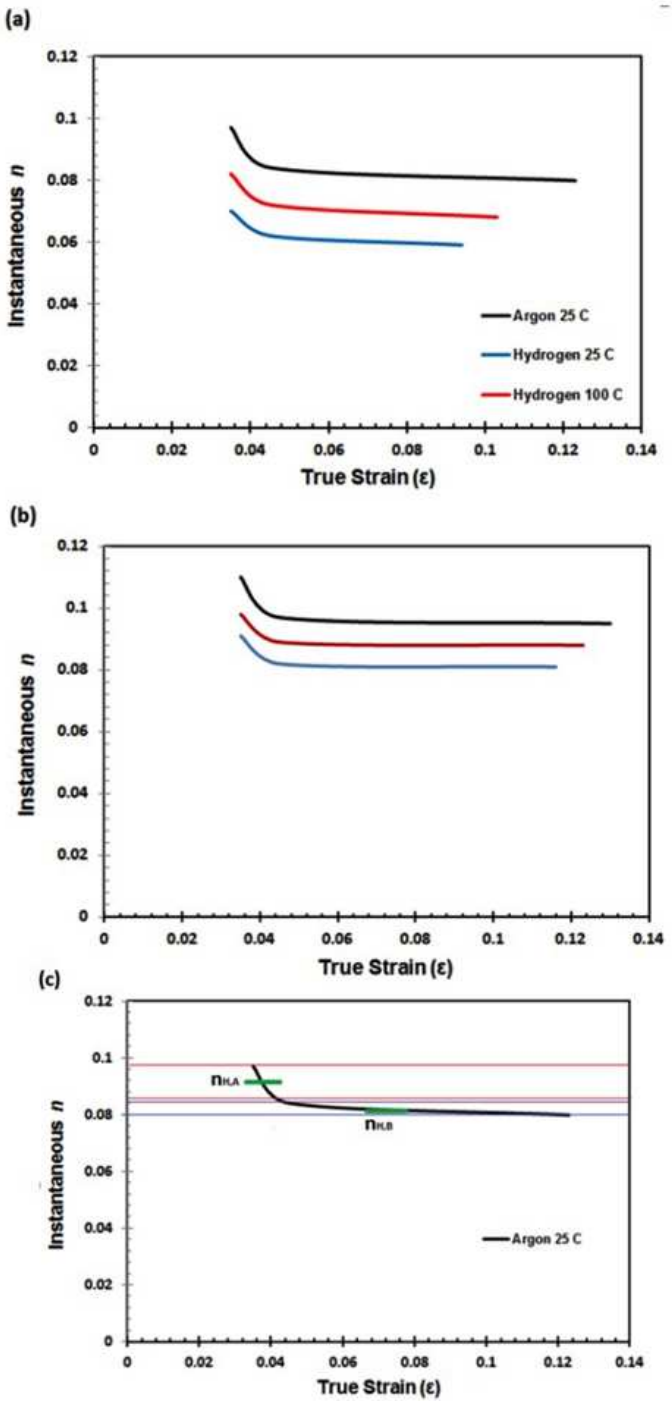

Figure 7-7 Change in instantaneous n throughout the uniform strain range from onset of plastic deformation to UTS for (a) X70, (b) MX70 and (c) representative illustration for the X70 sample charged with argon at room temperature, which compares instantaneous n_i values with the work hardening exponent (n_H) from Hollomon fitting for the two work hardening regions.

The difference between experimental data and empirical relationships is described by comparing the instantaneous strain hardening exponent (n_i) with n_H calculated from Hollomon fitting. The strain hardening exponent is one of the significant elements affecting forming processes as higher n values increase necking resistance and results in formed parts with a greater uniformity of strain distribution across their cross-section. The instantaneous strain hardening exponent is independent of the Hollomon equation or any other power law and is defined as [253]:

$$n_i = d(ln\sigma)/d(ln\varepsilon) \qquad 7\text{-}7$$

On plotting n_i with the true strain (Figure 7-7a and b), it was found to decrease rapidly until about 4% of true strain followed by a gradual decrease. Variation of n_i value is dependent on the applied strain over the entire plastic strain region. If predicted n_H values (Figure 7-7 c) are thought of as an average linear fit to an increasing instantaneous response for stages I and II and are compared to n_i values calculated from Figure 7-7, there is a slight underestimation of the uniform strain, as seen by the negative errors in Table 7-2. The two stages of work hardening for X70 are in agreement with the results of Zimmermann who claimed that Hollomon fitting cannot predict the flow behavior of X70 between yield and 0.5% of strain. [265].

The decrement of work hardening rate from a high initial value possibly relates then to a reordering of the dislocations [207]. The extension of stages 1 and 2 are slightly reduced in the presence of hydrogen, indicating that the mobility of dislocations is decreased by hydrogen. During stage I, the strain-hardening rate is decreased significantly, whereas it decreases slightly during stage II, for which some slip systems are deactivated [268]. Besides the embrittling effect, hydrogen reduces the tensile strength, decreasing the stress level, which in turn delays the attainment of the value of the work hardening rate needed to satisfy Considère's Criterion for necking [253]. It can be seen from Table 7-2 that n_H decreases when the atmosphere is changed from argon to hydrogen at room temperature. However, n increases with increasing temperature under a hydrogen atmosphere in stage II, which occurs over a relatively large strain interval, with a gradual reduction of work hardening rate because of re-arrangement of dislocations generated in the first stage into lower energy configurations, such as dislocation cells or microbands [269-272].

The work hardening exponent results (Table 7-3) indicate that hydrogen strongly lowers the work hardening exponent of both X70 and MX70 for tests conducted at room temperature. However, the effect is more marked for X70, suggesting that it is more prone to gaseous hydrogen embrittlement than MX70 for tensile deformation at room temperature.

7.4 Fractography

The effects of the hydrogen exposure on the fracture behaviour were analysed using fracture surface observations of X70 samples. The comparison of the fracture surface of an X70 sample tested under 10 MPa hydrogen gas with its counterpart tested under argon gas is shown in Figure 7-8.

The main difference in behaviour of the hydrogen and argon-charged specimens is that the argon specimen exhibited typical ductile fracture behaviour with severe necking. In contrast, the hydrogen charged specimen showed only minimal necking before fracture, indicating a substantial loss of ductility.

The fracture surfaces after argon charging are characterised by dimples, as shown in Figure 7-9. The mean diameter of the dimples is 2.5±0.3 µm. However, predominantly brittle fracture was observed in the hydrogen-charged specimen at 25°C (Figure 7-10). In all cases of hydrogen atmosphere testing, partial or complete brittle fracture was observed. However, the area of cleavage surface decreased as the temperature was raised to 100˚C with a corresponding increase the area of dimpled fracture. The size of the dimples was smaller for the X70 sample charged in hydrogen at 100˚C (Figure 7-11) compared to that charged with argon at room temperature (Figure 7-9). This observation is in agreement with the measured tensile strength and elongation (Table 7-1). The mean diameter of dimples for hydrogen-charged X70 tested at 100˚C is 2.1±0.2 µm.

One of the most significant differences shown in Figure 7-9 and Figure 7-10 is the wall thickness: dynamic shear deformation in the neck of the argon-charged specimen (Figure 7-9) substantially reduced the cross-sectional area, with the wall thickness being less than 40 % of the initial wall thickness. In contrast, there was much less necking under hydrogen gas (Figure 7-10) with the wall thickness being about 85 % of the initial

thickness. Further, dynamic shear deformation did not occur at the hydrogen-exposed inner wall of the specimen, contrary to the surfaces exposed to argon gas. The ductile fracture surface in Figure 7-9 has a slope in the loading direction, but the fracture formed in the sample exposed to hydrogen gas (Figure 7-10) shows predominantly brittle, outward crack growth perpendicular to the loading direction.

The X70 specimen that fractured in hydrogen gas at 100˚C (Figure 7-11) also displayed a fracture morphology partially similar to that fractured at 25 ˚C, but the extent of brittle fracture was reduced to about 18 % due to the contribution of ductile fracture. Figure 7-11 shows brittle fracture around the edges of the fracture surface where the material was exposed to hydrogen. Beyond the brittle area the fracture surface of this specimen shows evidence of ductile fracture. The presence of mixed fracture modes (cleavage facets together with dimples), indicates higher plastic deformation levels during the fracture process compared to X70 sample charged with hydrogen at room temperature.

The widths of the brittle fracture surfaces in Figure 7-11 can be related to the critical concentration of hydrogen: at 100˚C, the mobility of hydrogen atoms is higher, with a reduction in the probability of localised accumulation of hydrogen at traps to the critical concentration required to induce hydrogen cracking. Hence, less brittle fracture is to be expected.

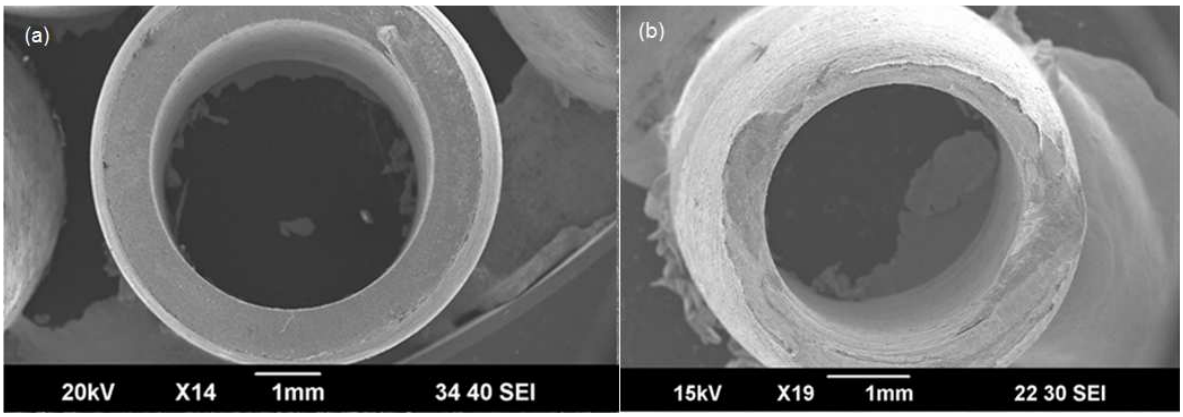

Figure 7-8 SEM images of X70 samples showing a predominantly brittle fracture after tensile testing with hydrogen at 25˚C (a); and mostly ductile fracture after tensile testing with argon at 25˚C (b).

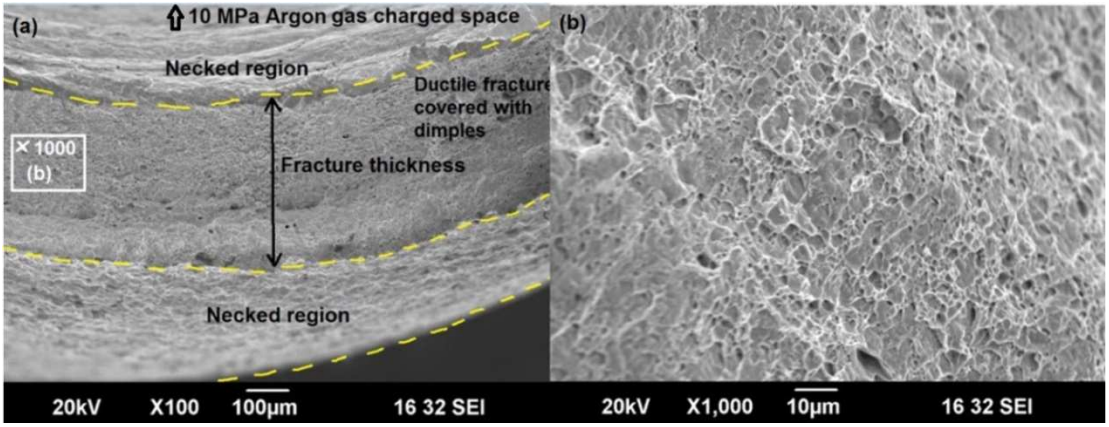

Figure 7-9 SEM images from the fracture surface of an X70 specimen tested with 10 MPa argon at 25˚C.

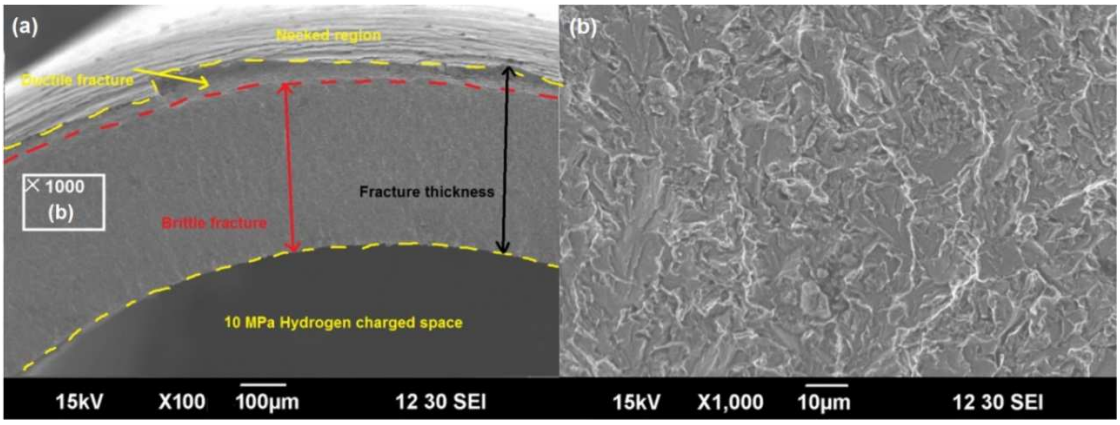

Figure 7-10 SEM images from the fracture surface of an X70 specimen tested with 10 MPa hydrogen at 25˚C.

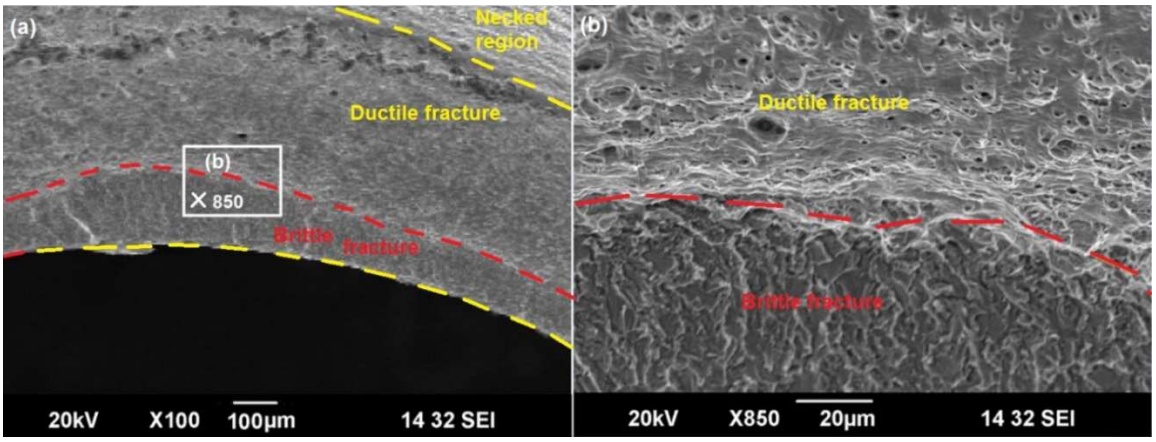

Figure 7-11 SEM images from the fracture surface of an X70 specimen tested with 10 MPa hydrogen at 100˚C, the red line indicates the transition line between ductile and brittle fracture.

The micro-voids in the argon-charged samples are elongated in the tensile loading direction, whereas the voids in the hydrogen-charged at 100˚C sample appear to be nearly spherical. These observations indicate that the hydrogen-charged specimen tested at 100˚C undergoes lower elongation before fracture than the argon-charged specimen at 25˚C.

These are consistent with results of Lee et al. [77], who conducted the same tensile test on X65 hollow cylindrical samples with hydrogen or nitrogen inside. They also found brittle fracture surface with almost no necking under hydrogen charging.

A series of low resolution SEM images were taken from the fracture surface of all samples. The percentages of ductile and predominantly brittle fracture were then calculated for two samples per condition (Figure 7-12).

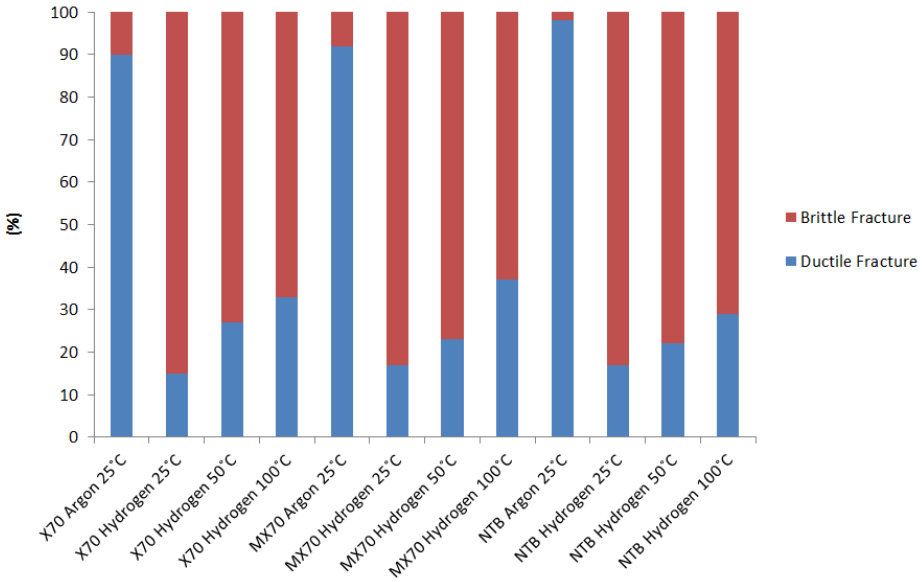

Figure 7-12 Percentages of predominantly brittle and ductile fracture areas (± 12% standard deviation).

7.5 Conclusions

- Tensile testing of the gas-charged tubular specimens resulted in approximately similar stress-strain curves, with nearly the same work-hardening behaviour regardless of the charging gas or temperature. However, the uniform elongations and the total elongations at fracture were significantly lower in the hydrogen-charged specimens than for the argon-charged specimens.

- Since the stress-strain curves of all samples reflected two work hardening stages, Hollomon equation was unable to fit the whole work hardening rate curve using a single set of parameters, however could approximately represent the flow curve using the separate set of parameters for each of work hardening. The work hardening exponent decreased rapidly in the first stage and more gradually in the second stage.
- In presence of hydrogen, the work hardening capacity of X70 was affected more than that of MX70. This is because the balance between void formation and cleavage fracture was slightly shifted towards void coalescence in the MX70 which exhibits a lower strength compared to X70. This can be explained by Beachem model [52].
- Predominantly quasi-cleavage fractures were observed in all samples tested under hydrogen gas conditions whereas ductile fracture surfaces were evident in those tested under argon atmosphere. The fraction of ductile fracture in hydrogen charged samples increased with an increase in test temperature.
- The most significant impact of hydrogen-charged specimens on the tensile behaviour was reduction in the elongation at fracture. The embrittlement indexes estimated from these data were 36%, 25% and 22% for the NTB, X70 and MX70 specimens, respectively.
- Elevated temperatures (up to 100˚C) increased the uniform elongation and decreased the yield and tensile strengths of hydrogen-charged specimens compared to room temperature specimens, due to both the attenuation of the embrittling effect of hydrogen and the increased mobility of dislocations.
- Increase in ferrite grain size from X70 to NTB, raised the susceptibility to gaseous hydrogen embrittlement. Presence of less trapping sites due to lower numbers of dislocation and grain boundaries in NTB, which leads to faster accumulation of hydrogen in traps, could be a reason for this.

8 GENERAL DISCUSSION, CONCLUSIONS AND FUTURE DIRECTIONS

The influence of composition, steel processing and microstructure on susceptibility to HIC has been investigated for high strength pipeline steels with Mn contents of 1.2% (standard X70) and 0.5% (medium X70), designated as MX70 steel. In addition to the as-processed X70 and MX70 strip steels (10 mm thick), X70 transfer bar (28 mm thick) was investigated in the as-processed and normalized conditions. Further, as weld fabrication by ERW is commonly employed in pipe-making, simulated HAZ structures were produced. In addition to these six sample sets representing different composition/processing conditions, three samples of X70 steel were prepared by annealing to produce equiaxed ferrite microstructures with mean grain sizes of 14, 46 and 120 μm.

Therefore, a wide range of ferrite-based microstructures were produced by these nine sets of composition/processing combinations. A major objective of the research was to establish and rationalise differences in hydrogen pick-up, trapping and transport, and particularly, susceptibility to HE.

8.1 General Discussion

8.1.1 Interaction of microstructure and hydrogen

Optical microscopy revealed that the microstructure of the TB sample changed from predominantly polygonal ferrite (PF) with islands of pearlite near the top surface of the bar to a structure of granular bainite towards and in the centre. The presence of a bainitic structure in the bar interior is unexpected as it typically forms at faster cooling rates than that required for transformation to the observed structure of ferrite and pearlite near the surface which cools more rapidly than the interior. Therefore, other hardenability factors, such as an austenite grain size gradient and alloy segregation must counteract the effect of cooling rate in producing a bainitic structure in the core of the bar. After normalising the TB sample, the microstructure was uniform, consisting of equiaxed ferrite grains with small fraction of pearlite.

The as-received X70 and MX70 strip samples displayed inhomogeneous ferrite-pearlite microstructures, whereas HAZ microstructure compromises coarse bainitic ferrite laths and martensite or austenite interlayers. Although pearlite banding was more evident in the hot rolled X70, the number densities of fine precipitates were found to be significantly higher in the MX70 than in X70. The number per unit area of nitrides was more than an order of magnitude higher in MX70 than X70. Further, the number density of oxides in the MX70 strip was almost double that observed for the X70. Since the average sizes of oxide precipitates were similar, the volume fraction of oxides in MX70 was significantly higher than for X70. Therefore, changing the alloy design by decreasing Mn and increasing Cr had a major impact on the precipitate/inclusion distributions, except for the number density of sulphides which was almost the same in both steels.

For the same electrolytic charging conditions (charging time, electrolyte, current density and sample geometry) and no externally applied load, the measured concentrations of diffusible hydrogen for X70 samples increased with the structural sequence: equiaxed ferrite-pearlite microstructure (NTB); as received (banded) ferrite-pearlite microstructure; mixed quasi-polygonal ferrite and bainite microstructure (TB); and simulated HAZ microstructure. In contrast, the HAZ microstructure exhibited the lowest residual (trapped) hydrogen content and the residual hydrogen content increased in the sequence: NTB

microstructure; TB microstructure; and as received strip microstructure. The HAZ microstructure had the highest dislocation density, providing weak traps which readily released diffusible hydrogen during hydrogen measurement. There was evidently little hydrogen available for concentration in strong traps such as particle interfaces, as the residual hydrogen concentration was low. The microstructure that most strongly trapped hydrogen was the as received X70 strip which consisted of fine grained, banded ferrite and pearlite. It is concluded that the ferrite-pearlite interfaces were major contributors to strong trapping.

Accumulation of hydrogen at trapping sites inside the material produced during electrolytical charging without external loading, led to the formation of micro-cracks within the samples and blisters on the surface. Earlier appearance of blisters occurred in the samples with the highest concentrations of residual hydrogen i.e. those with the largest concentration of permanent trapping sites such as the banded ferrite-pearlite structure, as discussed in Chapter 5. The rapid development of hydrogen containing cavities at trap sites resulted in build-up of gas pressure that extended the cracking and produced surface blisters. The crack initiation sites were also associated with Al and Ca oxide particles, consistent with the data in the literature [11]. However, it should be noted that, although it also contained the oxide particles, the simulated HAZ sample did not develop HIC and blisters after 24 hours of charging. In this case the critical hydrogen concentrations required for crack initiation at strong traps were not obtained because of the reduced hydrogen atom mobility arising from the abundance of weak traps (dislocations, lath interfaces and retained austenite).

The investigation of the effect of ferrite grain size on hydrogen transport through the steel samples confirmed that an intermediate grain size exists that maximises the diffusion rate, with smaller grain sizes exerting a stronger trapping function because of the greater density of boundary junctions and coarser grain sizes minimising the surface area of grain boundaries which can act as fast diffusion pathways.

8.1.2 Hydrogen embrittlement and fracture toughness

The observed differences in the fracture toughness behaviour of X70 and MX70, with the latter showing lower HE resistance, can be explained by size distribution of the different precipitates in these two steels. On this basis, the lower J_Q values observed for the charged MX70 strip may be attributable, at least in part, to the presence of higher densities of coarse oxide inclusions and/or (Ti,Nb)(C,N) precipitates, since these particles can effectively trap hydrogen to the critical level to induce particle cracking or interfacial decohesion, leading to local void growth and coalescence or to cleavage fracture. This interpretation is consistent with the literature [2].

The TPB results for the HAZ samples showed a substantial decrease in fracture toughness even though there was no evidence of HIC and blisters in samples charged without any external loading. The high stress concentration induced by the notch and the application of bending stress in the TPB tests interact with the high concentration of diffusible hydrogen atoms to initiate HIC and reduce the fracture toughness. In contrast, the as received strip was characterised by lower diffusible and higher residual hydrogen contents and so the accumulation of hydrogen at points of high stress concentration was more limited. The NTB samples also exhibited a significant loss in fracture toughness upon hydrogen charging, despite lower diffusible and residual hydrogen contents than for the X70 strip, which showed only a small loss in fracture toughness after charging. This result is likely to be caused by the inherently lower strength of NTB structure and its response to the high stress concentrating effect of the notch. Initiation and motion of dislocations in the stress concentration zone, assisted by the presence of hydrogen are likely to enhance the HE effect.

For gaseous charging, the total elongations at fracture were lower in the hydrogen-charged specimens than for the argon-charged specimens even though the stress-strain curves of all samples reflected two work hardening stages. The Hollomon equation can approximately represent the flow curve using two work hardening exponents across the plastic deformation range, but unable to fit the curve with a single set of parameters. However, the work hardening rate exponent decreased rapidly in the first stage and more gradually in the second stage. X70 exhibited a greater loss in work hardening capacity and

a lower total elongation in the presence of gaseous hydrogen than MX70. The lower total elongation for X70 corresponds to an embrittlement index of 25% compared with 22% for MX70 tested at 25˚C. This difference is probably due a higher tendency for crack progress by quasi-cleavage in X70 compared to the slightly lower strength microstructure of MX70. No externally applied stress-concentrating notch was present and, applying the Beachem model [52], the two structures responded to the hydrogen gradient by fracturing in the mode that was most characteristic of the microstructures. The balance between void formation and cleavage fracture was slightly shifted towards void coalescence (micro-plastic failure) in the lower strength structure on MX70. The presence of a higher concentration of hydrogen trapping particles in this steel over X70 did not appear to increase the HE effect in MX70.

While ductile fracture surfaces were observed under an argon atmosphere, quasi-cleavage fractures were identified under hydrogen gas conditions regardless of the test temperature. However, the fraction of predominantly brittle fracture decreased with an increase in test temperature. Hydrogen charged samples at room temperature were characterised by the effective absence of necking and a fully quasi-cleavage fracture surface. Gaseous hydrogen did not have a significant effect on the yield strength of both steels, but slightly lowered the tensile strength. This observation is consistent with the contribution of hydrogen cracking to fracture at a lower stress compared to testing in the absence of hydrogen. The NTB sample showed the maximum embrittlement index, consistent with the results of TPB testing reported in Chapter 6.

Tensile behaviour under 10 MPa hydrogen at elevated temperatures (50 and 100˚C) has not previously been reported for X70 steel. There are only reports for tensile test under gaseous hydrogen of X65 steel at room temperature [77], stainless steel at -20 to -250˚C [273] or medium carbon steel at room temperature [274]. Since pipelines located in desert environment are under slow strain deformation and can reach 50˚C and over, the current work attempted to simulate this service condition.

Elevated temperatures (up to 100˚C) increased the uniform elongation and decreased the yield and tensile strengths of hydrogen-charged specimens compared to room temperature specimens, due to both the attenuation of the embrittling effect of hydrogen

and the increased mobility of dislocations. All tested samples responded similarly to the effect of temperature.

The X70 was less susceptible to HE compared to MX70 when electrolytically hydrogen pre-charged samples were subjected to TPB tests, but it was more susceptible to HE for tensile testing under 10 MPa hydrogen pressure. In the latter case hydrogen diffuses inwards while the sample is being strained. Since hydrogen charging was carried out in the presence of an external stress, hydrogen transport in the specimen was by means of a combination of diffusion mechanism and a dislocation transport mechanism. In the case of for TPB testing of X70 hydrogen atoms have to travel across the layers of pearlite in the normal direction, and therefore diffusivity is low (almost one third of transverse direction according to Lee [60]). However, upon gaseous charging, since hollow cylindrical samples were cut along the rolling direction within thickness of the strip, hydrogen will diffuse in both the transverse and normal directions. It will be much easier for hydrogen to diffuse in the transverse direction. Normal direction diffusion will be much slower for X70 due to pearlite banding causing more hydrogen to diffuse in transverse direction along the pearlite-ferrite bands. With the help of dislocation movement due to plastic deformation, a lot of hydrogen will be trapped at the ferrite-pearlite interfaces and band boundaries where cracks can be initiated [59, 60, 230]. In MX70 samples hydrogen, will diffuse faster in both the transverse and normal directions, but hydrogen will be removed from circulation by the high density of particles and precipitates that can act as traps and cause better HIC resistance compared to X70.

In the case of NTB, the dislocation and grain boundary densities are lower than for X70 and MX70. However, grain boundaries will become hydrogen-saturated quickly and cracks will initiate causing the observed higher HIC index for NTB.

8.2 Conclusions

Two methods of hydrogen charging, electrolytic and gaseous, have been used in this work to study the susceptibility of X70 type pipeline steels to hydrogen embrittlement, both for external loading and under load-free conditions. Electrolytic charging was used to generate conditions appropriate for internal hydrogen embrittlement both for unstressed

samples and for testing of notched samples by TPB test. In contrast, gaseous charging provided conditions for external hydrogen embrittlement during tensile testing of tubular samples.

Electrolytic charging introduced hydrogen concentrations of 2 or 4 ppm, which are typical levels that can occur through arc welding processes used for girth welding and in-service repair of pipelines [215]. The gaseous charging experiments were used to simulate the effect of external tensile stress on the tensile behaviour of X70 pipeline steels under service conditions involving hydrogen gas transportation. Hydrogen at a pressure of 10 MPa hydrogen was used in internally gas-charged cylindrical test pieces, under tensile loading, to ascertain the extent of HE. The pressure was limited to 10 MPa, as it has been reported that higher pressures did not show any significant change in the material's response to HE [275].

Different types of hydrogen charging were used in this work which do not necessarily trap hydrogen with the same mechanism. It was reported [276] that electrolytic charging causes hydrogen trapping near grain boundaries and at the interfaces of small precipitates with relatively low activation energies, on the other hand, charging with the gaseous hydrogen results in hydrogen trapping at incoherent precipitates/matrix interfaces with higher activation energy.

Although one or other of these techniques has been applied previously in investigations of HIC-susceptibility of pipeline steels, there are no reports of the application of both methods, and no studies that have addressed the issue of the effect on HIC-susceptibility of a major X70 alloy re-design in terms of Mn content. In addition to this major research objective, the research addressed differences in the response of a wide range of ferritic microstructures to the take-up, transport and embrittling effect of hydrogen. Different microstructures were produced for the same steel composition and systematically studied.

The main outcomes of the work are as follows.

1. Significant differences have been demonstrated for hydrogen transport and accumulation as a function of the type of the ferritic microstructure. As-received X70 strip with ferrite-pearlite banding displayed the highest trapping capacity

(highest residual hydrogen content), whereas simulated HAZ structure had the lowest residual and the highest diffusible hydrogen contents. TB and NTB samples showed an intermediate diffusible/residual hydrogen contents.

2. The most rapid formation of blisters with underlying HIC occurred for the banded ferrite-pearlite microstructure, whereas no blistering was observed for HAZ structure after 24 hours. These observations can be rationalised in terms of the capacity of the microstructures to allow the build-up of critical hydrogen concentrations at potential crack sites under conditions of no external loading.
3. The standard X70 steel (1.2% Mn) had higher yield and tensile strengths than the medium Mn (0.5%) grade and was much "cleaner" in terms of non-metallic inclusions and nitride precipitates. These factors contributed to superior performance of H-charged notched samples tested by TPB compared to the MX70 grade.
4. For gaseous charging, the total elongations at fracture were lower in the hydrogen-charged specimens than for the argon-charged specimens; and the extent of HE, measured by the embrittlement index, was higher for X70 than MX70. This contradictory result compared to TPB testing arises because of the difference in stress state (tensile as opposed to bending), the presence of a stress-concentrating notch for the TPB tests, and the difference in the hydrogen charging (internal for TPB and external for the tensile testing of tubular samples). These differences are likely to promote a higher tendency for crack progress by quasi-cleavage in X70 compared to the slightly lower strength microstructure of MX70.
5. Exposure of the X70 and MX70 steels to gaseous hydrogen resulted in degradation of their work hardening characteristics, particularly for X70 due to the greater tendency for quasi-cleavage in the presence of hydrogen.
6. The results indicate that the use of a lower Mn alloy design for X70 does not significantly increase the susceptibility to hydrogen embrittlement.

8.3 Future Directions

- Similar gaseous charging tensile tests are recommended to be undertaken for temperatures below ambient in order to determine the susceptibility to HE in colder in-service conditions.
- The current study did not consider hydrogen pick up during girth welding of pipelines in the field. Additional research on the response of MX70 steel to girth welding would provide useful information to assist in its application as pipeline material.
- Analysis of hydrogen-induced cracking after gaseous charging using electron back scattering diffraction is recommended in order to evaluate the effect of texture and grain boundary character. This information could assist in modification of processing schedules to control the required texture.
- Conduct of thermal desorption spectroscopy on X70 steel with different microstructures would be useful in order to distinguish between the different types of microstructural hydrogen traps based on the analysis of the different peak temperatures at which hydrogen desorbs from the material during heating. This can provide important information on the possible mechanisms for hydrogen embrittlement.
- Slow strain rate testing (SSRT) can be utilised to more precisely simulate the condition of pipeline in operation, since in this work the strain rate capacity of hydraulic controlled tensile test machine was not slow enough for such simulation.

References

1. Williams, J.G., *Advances in steels for high strength ERW linepipe application in Australia.* Materials Forum, 2007. **31**: p. 1-10.
2. Dong, C.F., Li, X.G., Liu, Z.Y., and Zhang, Y.R., *Hydrogen-induced cracking and healing behaviour of X70 steel.* Journal of Alloys and Compounds, 2009. **484**(1-2): p. 966-972.
3. Huang, F., Liu, J., Deng, Z.J., Cheng, J.H., Lu, Z.H., and Li, X.G., *Effect of microstructure and inclusions on hydrogen induced cracking susceptibility and hydrogen trapping efficiency of X120 pipeline steel.* Materials Science and Engineering: A, 2010. **527**(26): p. 6997-7001.
4. Dong, C.F., Liu, Z.Y., Li, X.G., and Cheng, Y.F., *Effects of hydrogen-charging on the susceptibility of X100 pipeline steel to hydrogen-induced cracking.* International Journal of Hydrogen Energy, 2009. **34**(24): p. 9879-9884.
5. Yen, S.K. and Huang, I.B., *Critical hydrogen concentration for hydrogen-induced blistering on AISI 430 stainless steel.* Materials Chemistry and Physics, 2003. **80**(3): p. 662-666.
6. Williams, J.G. *New Alloy Design Perspectives For High Strength Steels*. in *Thermomechanical Proceeding of Steel*. 2008. Padua Italy.
7. Carneiro, R.A., Ratnapuli, R.C., and de Freitas Cunha Lins, V., *The influence of chemical composition and microstructure of API linepipe steels on hydrogen induced cracking and sulfide stress corrosion cracking.* Materials Science and Engineering: A, 2003. **357**(1-2): p. 104-110.
8. Thompson, A.W. and Bernstein, I.M., *The role of metallurgical variables in hydrogen-assisted environmental fracture*, in *Advances in corrosion science and technology*. 1980, Springer. p. 53-175.
9. Chatzidouros, E.V., Papazoglou, V.J., Tsiourva, T.E., and Pantelis, D.I., *Hydrogen effect on fracture toughness of pipeline steel welds, with in situ hydrogen charging.* International Journal of Hydrogen Energy, 2011. **36**(19): p. 12626-12643.
10. Nakai, Y., Kurahashi, H., Emi, T., and Haida, O., *Development of steels resistant to hydrogen induced cracking in wet hydrogen sulfide environment.* Transactions of the Iron and Steel Institute of Japan, 1979. **19**(7): p. 401-410.
11. Ren, X., Chu, W.Y., Li, J., Su, Y.J., and Qiao, L., *The effects of inclusions and second phase particles on hydrogen-induced blistering in iron.* Materials Chemistry and Physics, 2008. **107**(2–3): p. 231-235.
12. Beidokhti, B., Koukabi, A.H., and Dolati, A., *Influences of titanium and manganese on high strength low alloy SAW weld metal properties.* Materials Characterization, 2009. **60**(3): p. 225-233.
13. Easterling, K., *Introduction to the physical metallurgy of welding*. Second ed. 1993: Butterworth Publishers, Stoneham, MA.
14. Bailey, N., Coe, F.R., Gooch, T.G., Hart, P.H.M., Jenkins, N., and Pargeter, R.J., *Welding steels without hydrogen cracking*. Second ed. 2004: Woodhead publishing limited.
15. Bhadeshia, H.K.D.H. and Honeycombe, R.W.K., *Steels: microstructure and properties*. 2006: Butterworth-Heinemann.

16. Xiao, F., Liao, B., Ren, D., Shan, Y., and Yang, K., *Acicular ferritic microstructure of a low-carbon Mn-Mo-Nb microalloyed pipeline steel.* Materials Characterization, 2005. **54**(4-5): p. 305-314.
17. Wang, W., Shan, Y., and Yang, K., *Study of high strength pipeline steels with different microstructures.* Materials Science and Engineering: A, 2009. **502**(1-2): p. 38-44.
18. Williams, J.G., Killmore, C.R., Edwards, P.D., and Kelly, P.G., *Thermomechanical processing of Mo-Nb high strength steels for application to X70 and X80 ERW linepipe*, in *2nd International Conference on Thermomechanical Processing of Steels and Other Materials (THERMEC 97)*, T. Chandra and T. Sakai, Editors. 1997, Minerals, Metals & Materials Soc: Wollongong, Australia. p. 475-482.
19. Rampaul, H., *Pipe Welding Procedures*. 2 ed. 2003, New York: Industrial Press. 190.
20. Pressouyre, G.M., Fidelle, J.P., and R., A.-L., *Hydrogen effects in metalls*, in *International conference of Effect of Hydrogen on Behavior of materials*. 1980, Metallurgical society of AIME: Moran,Wyoming. p. 27-36.
21. Anya, C.C. and Baker, T.N., *The effect of silicon on the grain size and the tensile properties of low carbon steels.* Materials Science and Engineering: A, 1989. **118**: p. 197-206.
22. Serajzadeh, S. and Karimi Taheri, A., *An investigation on the effect of carbon and silicon on flow behavior of steel.* Materials & Design, 2002. **23**(3): p. 271-276.
23. Ravi, K., Ramaswamy, V., and Namboodhiri, T.K.G., *Effect of molybdenum on the resistance to H2S of high sulphur microalloyed steels.* Materials Science and Engineering: A, 1993. **169**(1-2): p. 111-118.
24. Kong, J. and Xie, C., *Effect of molybdenum on continuous cooling bainite transformation of low-carbon microalloyed steel.* Materials & Design, 2006. **27**(10): p. 1169-1173.
25. Bhole, S.D., Nemade, J.B., Collins, L., and Liu, C., *Effect of nickel and molybdenum additions on weld metal toughness in a submerged arc welded HSLA line-pipe steel.* Journal of Materials Processing Technology, 2006. **173**(1): p. 92-100.
26. Akben, M.G., Bacroix, B., and Jonas, J.J., *Effect of vanadium and molybdenum addition on high temperature recovery, recrystallization and precipitation behavior of niobium-based microalloyed steels.* Acta Metallurgica, 1983. **31**(1): p. 161-174.
27. Cao, J.-c., Liu, Q.-y., Yong, Q.-l., and Sun, X.-j., *Effect of Niobium on Isothermal Transformation of Austenite to Ferrite in HSLA Low-Carbon Steel.* Journal of Iron and Steel Research, International, 2007. **14**(3): p. 52-56.
28. Katsuki, F., Watari, K., Tahira, H., and Umino, M., *Abrasive wear behavior of a pearlitic (0.4%C) steel microalloyed with vanadium.* Wear, 2008. **264**(3-4): p. 331-336.
29. Ollilainen, V., Kasprzak, W., and Holappa, L., *The effect of silicon, vanadium and nitrogen on the microstructure and hardness of air cooled medium carbon low alloy steels.* Journal of Materials Processing Technology, 2003. **134**(3): p. 405-412.
30. Denpo, K. and Ogawa, H., *Effects of nickel and chromium on corrosion rate of linepipe steel.* Corrosion Science, 1993. **35**(1-4): p. 285-288.

31. Gómez, M., Rancel, L., and Medina, S.F., *Effects of aluminium and nitrogen on static recrystallisation in V-microalloyed steels.* Materials Science and Engineering: A, 2009. **506**(1-2): p. 165-173.
32. Turkdogan, E.T., *Causes and effects of nitride and carbonitride precipitation during continuous casting.* I & SM, 1989. **16**(5): p. 61-75.
33. Narita, K., *Physical chemistry of the groups IVa (Ti, Zr), Va (V, Nb, Ta) and the rare earth elements in steel.* Trans Iron Steel Inst Jap, 1975. **15**(3): p. 145-152.
34. Funnell, G.D., *Observations on effect of aluminium nitride on hot ductility of steel.* AGARD Conference Proceedings, 1980: p. 104-110.
35. Mintz, B. and Arrowsmith, J.M., *Influence of microalloying additions on hot ductility of steels.* AGARD Conference Proceedings, 1980: p. 99-103.
36. Savov, L., Volkova, E., and Janke, D., *Copper and tin in steel scrap recycling.* Materials Geoenvironment, 2003. **50**(3): p. 627-640.
37. Briant, C.L., *The effect of nickel, chromium, and manganese on phosphorus segregation in low alloy steels.* Scripta Metallurgica, 1981. **15**(9): p. 1013-1018.
38. Riecke, E.M., Johnen, B., and Moeller, R., *The effect of phosphorus on hydrogen uptake by iron in acidic sulphate and sulphide solutions.* Corrosion Science, 1987. **27**(10-11): p. 1027-1039.
39. Williams, J.G., Killmore, C.R., and Harris, G.R., *Recrystallisation Behaviour of Fine Grained Nb--Ti Austenite at Low Rolling Reductions,* in *International Conference on Physical Metallurgy of Thermomechanical Processing of Steels and Other Metals. THERMEC-88.* 1988: Iron and steel institue of Japan. p. 224-231.
40. *Making steel at the Port Kembla Steelworks*, BlueScope Steel Port Kembla.
41. Kiefner, J.F., *ERW Line Pipe.* Oil & Gas Journal, 1992: p. 45.
42. Kim, D., Kim, T., Park, Y.W., Sung, K., Kang, M., Kim, C., Lee, C., and Rhee, S., *Estimation of Weld Quality in High-Frequency Electric Resistance Welding with Image Processing.* Welding journal, 2007: p. 71-79.
43. Law, M. and Bowie, G., *Prediction of failure strain and burst pressure in high yield-to-tensile strength ratio linepipe.* International journal of pressure vessels and piping, 2007. **84**(8): p. 487-492.
44. Ueshima, Y., Yuyama, H., Mizoguchi, S., and Kajioka, H., *Effect of Oxide Inclusions on MnS Precipitation in Low Carbon Steel.* Tetsu-to-Hagane, 1989. **75**(3): p. 501-508.
45. Wang, R., *Effects of hydrogen on the fracture toughness of a X70 pipeline steel.* Corrosion Science, 2009. **51**(12): p. 2803-2810.
46. Shipilov, S.A. and Le May, I., *Structural integrity of aging buried pipelines having cathodic protection.* Engineering Failure Analysis, 2006. **13**(7): p. 1159-1176.
47. Olden, V., Thaulow, C., Johnsen, R., Ostby, E., and Berstad, T., *Application of hydrogen influenced cohesive laws in the prediction of hydrogen induced stress cracking in 25%Cr duplex stainless steel.* Engineering Fracture Mechanics, 2008. **75**(8): p. 2333-2351.
48. Nolan, D., Sterjovski, Z., and Dunne, D.P., *Hardness prediction modeles based on HAZ simulation for in-service welded pipeline steels,* in *Science and Technology of Welding and Joining*. 2005, Institue of Materials and Mining. p. 681-693.
49. Barbaro, F.J., Henderson, I.D., Dunne, D.P., Painter, M.J., Norrish, J., and Harrison, R.P., *Quality and productivity improvements in the field welding of high*

strength thin walled pipelines. The 1998 International Pipeline Conference, IPC. Part 2(of 2), 1998: p. 673-687.
50. McKeown, D., *Hydrogen and its control in weld metal.* Metal Construction, 1985. **17**: p. 655-661.
51. Gangloff, R.P., *Hydrogen assisted cracking of high strength alloys*. 2003, DTIC Document. p. 31-34.
52. Beachem, C.D., *A New Model for Hydrogen-Assisted Cracking (Hydrogen "Embrittlement").* Metallurgical Transactions A, 1972. **3**: p. 451.
53. Zapffe, C.A. and Sims, C.E., *Hydrogen embrittlement, internal stress and defects in steel.* Trans. AIME, 1941. **145**(1941): p. 225-271.
54. Troiano, A.R., *The role of hydrogen and other interstitials in the mechanical behavior of metals.* trans. ASM, 1960. **52**(1): p. 54-80.
55. Davis, J.R., Mills, K.M., and Lampman, S.R., *Properties and Selection: Irons, Steels, and High-Performance Alloys*, in *Metals Handbook*. 1990, ASM International, Materials: Park, Ohio, USA, . p. 1063.
56. Bastien, P. and Azou, P., *Effect of hydrogen on the deformation and fracture of iron and steel in simple tension.* Proceedings of the First World Metallurgical Congress, 1951. **49**: p. 837-848.
57. McMahon Jr, C., *Hydrogen Effects in Metals.* TMS-AIME, 1981: p. 219-234.
58. Bernstein, I.M. and Thompson, A.W., *Hydrogen effects in metals.* Metallurgical Society of AIME, 1981: p. 1071.
59. Tau, L. and Chan, S.L.I., *Effects of ferrite/pearlite alignment on the hydrogen permeation in a AISI 4130 steel.* Materials Letters, 1996. **29**(1-3): p. 143-147.
60. Lee, H.-L. and Lap-Ip Chan, S., *Hydrogen embrittlement of AISI 4130 steel with an alternate ferrite/pearlite banded structure.* Materials Science and Engineering: A, 1991. **142**(2): p. 193-201.
61. Chan, S.L.I., *Hydrogen trapping ability of steels with different microstructures.* Journal of the Chinese Institute of Engineers, 1999. **22**(1): p. 43-53.
62. Bechtle, S., Kumar, M., Somerday, B.P., Launey, M.E., and Ritchie, R.O., *Grain-boundary engineering markedly reduces susceptibility to intergranular hydrogen embrittlement in metallic materials.* Acta Materialia, 2009. **57**(14): p. 4148-4157.
63. Oriani, R.A., *Hydrogen embrittlement of steels.* Annual review of materials science, 1978. **8**(1): p. 327-357.
64. McCright, R.D., *Effect of Environmental Species and Metallurgical Structure on the Hydrogen Entry into Steel*, in *Stress Corrosion Cracking and Hydrogen Embrittlement of Iron Base Alloys*. 1973, NACE. p. 306-325.
65. Chou, S. and Makhlouf, M., *The effect of ion implanting on hydrogen entry into metals.* Metallurgical and Materials Transactions A, 1999. **30**(6): p. 1535-1540.
66. Gabrielli, C., Maurin, G., Mirkova, L., Perrot, H., and Tribollet, B., *Transfer function analysis of hydrogen permeation through an iron membrane in a Devanathan cell.* Impedance Contributions Online, 2004. **2**: p. P1.
67. Ren, X., Zhou, Q., Chu, W., Li, J., Su, Y., and Qiao, L., *The mechanism of nucleation of hydrogen blister in metals.* Chinese Science Bulletin, 2007. **52**(14): p. 2000-2005.

68. Rozenak, P., *Hemispherical bubbles growth on electrochemically charged aluminum with hydrogen.* International Journal of Hydrogen Energy, 2007. **32**(14): p. 2816-2823.
69. Vigdorovich, V.I., Tsygankova, L.E., Alekhina, O.V., and D'Yachkova, T.P., *Effect of thiourea on the kinetics of the hydrogen evolution reaction at iron and the transport of hydrogen through a steel membrane in solutions of C2H4(OH)2-H2O-HCl.* Russian Journal of Electrochemistry, 2005. **41**(10): p. 1046-1052.
70. Han, J.N., Pyun, S.I., and Yang, T.H., *Roles of thiourea as an inhibitor in hydrogen absorption into palladium electrode.* Journal of the Electrochemical Society, 1997. **144**(12): p. 4266-4272.
71. Nelson, H.G., *Hydrogen embrittlement.* Treatise on materials science and technology, 1983. **25**: p. 275-359.
72. Liu, H. and Ficalora, P., *Catalytic dissociation, hydrogen embrittlement, and stress corrosion cracking.* International journal of fracture, 1972. **8**(2): p. 223-226.
73. Abraham, D.P. and Altstetter, C.J., *Hydrogen-enhanced localization of plasticity in an austenitic stainless steel.* Metallurgical and Materials Transactions A, 1995. **26**(11): p. 2859-2871.
74. Pan, C., Chu, W.Y., Li, Z.B., Liang, D.T., Su, Y.J., Gao, K.W., and Qiao, L.J., *Hydrogen embrittlement induced by atomic hydrogen and hydrogen-induced martensites in type 304L stainless steel.* Materials Science and Engineering: A, 2003. **351**(1): p. 293-298.
75. Tsong-Pyng, P. and Altstetter, C.J., *Effects of deformation on hydrogen permeation in austenitic stainless steels.* Acta metallurgica, 1986. **34**(9): p. 1771-1781.
76. Iaquaniello, G., Borruto, A., Lollobattista, E., Narducci, G., and Katsir, D., *Hydrogen Palladium Selective Membranes: An Economic Perspective*, in *Membrane Reactors for Hydrogen Production Processes*, M. De Falco, L. Marrelli, and G. Iaquaniello, Editors. 2011, Springer London. p. 57-78.
77. Lee, Y.H., Lee, H.M., Kim, Y., and Nahm, S.H., *Mechanical degradation of API X65 pipeline steel by exposure to hydrogen gas.* Metals and Materials International, 2011. **17**(3): p. 389-395.
78. Weng, C.C., Lin, G.C., and Chen, R.T., *Acoustic emission characterization of a medium strength steel during hydrogen permeation processes.* Materials Science and Engineering A, 1992. **154**(1): p. 51-57.
79. Flis, J. and Smialowski, M., *Hydrogen embrittlement of polycrysstalline iron whiskers.* Scripta Metallurgica, 1979. **13**(7): p. 641-643.
80. Ueda, Y., Funabiki, T., Shimada, T., Fukumoto, K., Kurishita, H., and Nishikawa, M., *Hydrogen blister formation and cracking behavior for various tungsten materials.* Journal of Nuclear Materials, 2005. **337-339**(1-3 SPEC. ISS.): p. 1010-1014.
81. Jin, T.Y., Liu, Z.Y., and Cheng, Y.F., *Effect of non-metallic inclusions on hydrogen-induced cracking of API5L X100 steel.* International Journal of Hydrogen Energy, 2010. **35**(15): p. 8014-8021.
82. Panagopoulos, C.N., El-Amoush, A.S., and Agathocleous, P.E., *Hydrogen-induced cracking and blistering in α-brass.* Corrosion Science, 1998. **40**(11): p. 1837-1844.

83. Solovioff, G., Abramov, E., and Eliezer, D., *The formation of hydrogen induced blisters and their growth in nickel pre-implaned with helium.* Journal of Nuclear Materials, 1994. **217**(3): p. 287-293.
84. Watson, J.W., Shen, Y.Z., and Meshii, M., *Effect of cathodic charging on the mechanical properties of aluminum.* Metallurgical transactions. A, Physical metallurgy and materials science, 1988. **19 A**(9): p. 2299-2304.
85. Ren, X.C., Zhou, Q.J., Shan, G.B., Chu, W.Y., Li, J.X., Su, Y.J., and Qiao, L.J., *A nucleation mechanism of hydrogen blister in metals and alloys.* Metallurgical and Materials Transactions A, 2008. **39**(1): p. 87-97.
86. Huang, H. and Shaw, W.J.D., *Cold work effects on sulfide stress cracking of pipeline steel exposed to sour environments.* Corrosion Science, 1993. **34**(1): p. 61-78.
87. Matsui, H., Kimura, H., and Kimura, A., *The effect of hydrogen on the mechanical properties of high purity iron III. The dependence of softening in specimen size and charging current density.* Materials Science and Engineering, 1979. **40**(2): p. 227-234.
88. Garofalo, F., Chou, Y.T., and Ambegaokar, V., *Effect of hydrogen on stability of micro cracks in iron and steel.* Acta Metallurgica, 1960. **8**(8): p. 504-512.
89. Chen, J., Ai, M., Wang, J., Han, E.H., and Ke, W., *Formation of hydrogen blister on AZ91 magnesium alloy during cathodic charging.* Corrosion Science, 2009. **51**(5): p. 1197-1200.
90. Wilde, B.E., Kim, C.D., and Phelps, E.H., *Some observations on the role of inclusions in the hydrogen induced blister cracking of linepipe steels in sulfide environments.* Corrosion, 1980. **36**(11): p. 625-632.
91. Domizzi, G., Anteri, G., and Ovejero-García, J., *Influence of sulphur content and inclusion distribution on the hydrogen induced blister cracking in pressure vessel and pipeline steels.* Corrosion Science, 2001. **43**(2): p. 325-339.
92. Mertens, G., Duprez, L., De Cooman, B.C., and Verhaege, M., *Hydrogen absorption and desorption in steel by electrolytic charging.* Advanced Materials Research, 2007. **15**: p. 816-821.
93. Escobar, D.P., Minambres, C., Duprez, L., Verbeken, K., and Verhaege, M., *Internal and surface damage of multiphase steels and pure iron after electrochemical hydrogen charging.* Corrosion Science, 2011. **53**(10): p. 3166-3176.
94. McLellan, R.B. and Xu, Z.R., *Hydrogen-induced vacancies in the iron lattice.* Scripta Materialia, 1997. **36**(10): p. 1201-1205.
95. Galvele, J.R., *Reply to E.M. Gutman's: "comments on the "stress corrosion cracking of zirconium and zircaloy-4 in halide aqueous solutions" by S.B. Farina, G.S. Duffo, J.R. Galvele".* Corrosion Science, 2004. **46**(7): p. 1807-1812.
96. Gavriljuk, V., Bugaev, V., Petrov, Y.N., Tarasenko, A., and Yanchitski, B., *Hydrogen-induced equilibrium vacancies in FCC iron-base alloys.* Scripta materialia, 1996. **34**(6): p. 903-907.
97. Osono, H., Kino, T., Kurokawa, Y., and Fukai, Y., *Agglomeration of hydrogen-induced vacancies in nickel.* Journal of Alloys and Compounds, 1995. **231**(1–2): p. 41-45.

98. Elboujdaini, M. and Revie, R.W., *Metallurgical factors in stress corrosion cracking (SCC) and hydrogen-induced cracking (HIC).* Journal of Solid State Electrochemistry, 2009. **13**(7): p. 1091-1099.
99. Asahi, H., Hirakami, D., and Yamasaki, S., *Hydrogen trapping behavior in vanadium-added steel.* ISIJ international, 2003. **43**(4): p. 527-533.
100. Zhao, M.C., Tang, B., Shan, Y.Y., and Yang, K., *Role of microstructure on sulfide stress cracking of oil and gas pipeline steels.* Metallurgical and Materials Transactions A, 2003. **34**(5): p. 1089-1096.
101. Komazaki, S.-i., Koyama, A., and Misawa, T., *Effect of morphology of copper precipitation particles on hydrogen embrittlement behavior in Cu-added ultra low carbon steel.* Materials Transactions(Japan), 2002. **43**(9): p. 2213-2218.
102. Yokota, T. and Shiraga, T., *Evaluation of hydrogen content trapped by vanadium precipitates in a steel.* ISIJ international, 2003. **43**(4): p. 534-538.
103. Wei, F.G., Hara, T., Tsuchida, T., and Tsuzaki, K., *Hydrogen trapping in quenched and tempered 0.42 C-0.30 Ti steel containing bimodally dispersed TiC particles.* ISIJ international, 2003. **43**(4): p. 539-547.
104. Huang, Y., Nakajima, A., Nishikata, A., and Tsuru, T., *Effect of mechanical deformation on permeation of hydrogen in iron.* ISIJ international, 2003. **43**(4): p. 548-554.
105. Villalba, E. and Atrens, A., *Hydrogen embrittlement and rock bolt stress corrosion cracking.* Engineering Failure Analysis, 2009. **16**(1): p. 164-175.
106. Turnbull, A. and Carroll, M.W., *The effect of temperature and H2S concentration on hydrogen diffusion and trapping in a 13% chromium martensitic stainless steel in acidified NaCl.* Corrosion science, 1990. **30**(6–7): p. 667-679.
107. Lee, J.Y. and Lee, S., *Hydrogen trapping phenomena in metals with BCC and FCC crystals structures by the desorption thermal analysis technique.* Surface and Coatings Technology, 1986. **28**(3): p. 301-314.
108. Pressouyre, G.M. and Bernstein, I.M., *An electrical analog model of hydrogen trapping in iron alloys.* Corrosion Science, 1978. **18**(9): p. 819-833.
109. Stevens, M.F. and Bernstein, I.M., *Microstructural trapping effects on hydrogen induced cracking of a microalloyed steel.* Metallurgical Transactions A, 1989. **20**(5): p. 909-919.
110. Calder, R.D., Elleman, T.S., and Verghese, K., *Grain boundary diffusion of tritium in 304- and 316-stainless steels.* Journal of Nuclear Materials, 1973. **46**(1): p. 46-52.
111. Kimura, A. and Birnbaum, H.K., *Hydrogen induced grain boundary fracture in high purity nickel and its alloys—Enhanced hydrogen diffusion along grain boundaries.* Acta Metallurgica, 1988. **36**(3): p. 757-766.
112. Tsuru, T. and Latanision, R.M., *Grain boundary transport of hydrogen in nickel.* Scripta Metallurgica, 1982. **16**(5): p. 575-578.
113. Brass, A.M. and Chêne, J., *Hydrogen uptake in 316L stainless steel: Consequences on the tensile properties.* Corrosion Science, 2006. **48**(10): p. 3222-3242.
114. Yao, J. and Cahoon, J.R., *Experimental studies of grain boundary diffusion of hydrogen in metals.* Acta metallurgica et materialia, 1991. **39**(1): p. 119-126.

115. Ichimura, M., Sasajima, Y., and Imabayashi, M., *Grain Boundary Effect on Diffusion of Hydrogen in Pure Aluminum.* Materials Transactions, 1991. **32**(12): p. 1109-1114.
116. Yazdipour, N., Haq, A.J., Muzaka, K., and Pereloma, E.V., *2D modelling of the effect of grain size on hydrogen diffusion in X70 steel.* Computational Materials Science, 2012. **56**(0): p. 49-57.
117. Kim, W.K., Koh, S.U., Yang, B.Y., and Kim, K.Y., *Effect of environmental and metallurgical factors on hydrogen induced cracking of HSLA steels.* Corrosion Science, 2008. **50**(12): p. 3336-3342.
118. Xue, H.B. and Cheng, Y.F., *Characterization of inclusions of X80 pipeline steel and its correlation with hydrogen-induced cracking.* Corrosion Science, 2011. **53**(4): p. 1201-1208.
119. Garet, M., Brass, A.M., Haut, C., and Guttierez-Solana, F., *Hydrogen trapping on non metallic inclusions in cr-mo low alloy steels.* Corrosion Science, 1998. **40**(7): p. 1073-1086.
120. Takahashi, I., Matsumoto, Y., and Tanada, T., JIMIS-2, 1979: p. 285-289.
121. Valentini, R., Solina, A., Matera, S., and De Gregorio, P., *Influence of titanium and carbon contents on the hydrogen trapping of microalloyed steels.* Metallurgical and Materials Transactions A, 1996. **27**(12): p. 3773-3780.
122. Vökl, J. and Wipf, H., *Diffusion of hydrogen in metals.* Hyperfine Interactions, 1981. **8**(4-6): p. 631-637.
123. Toribio, J., *The role of crack tip strain rate in hydrogen assisted cracking.* Corrosion Science, 1997. **39**(9): p. 1687-1697.
124. Hejazi, D., Haq, A.J., Yazdipour, N., Dunne, D.P., Calka, A., Barbaro, F., and Pereloma, E.V., *Effect of manganese content and microstructure on the susceptibility of X70 pipeline steel to hydrogen cracking.* Materials Science and Engineering: A, 2012. **551**(0): p. 40-49.
125. Park, G.T., Koh, S.U., Jung, H.G., and Kim, K.Y., *Effect of microstructure on the hydrogen trapping efficiency and hydrogen induced cracking of linepipe steel.* Corrosion Science, 2008. **50**(7): p. 1865-1871.
126. Lunarska, E., Ososkov, Y., and Jagodzinsky, Y., *Correlation between critical hydrogen concentration and hydrogen damage of pipeline steel.* International Journal of Hydrogen Energy, 1997. **22**(2-3): p. 279-284.
127. *ISO 3690:2000 Welding and allied processes -- Determination of hydrogen content in ferritic steel arc weld metal*.
128. *AS/NZS 3752:2006 Welding and allied processes - Determination of hydrogen content in ferritic steel arc weld metal*.
129. *AWS A4.3-93 (R2006) Standard Methods for Determination of the Diffusible Hydrogen Content of Martensitic, Bainitic, and Ferritic Steel Weld Metal Produced by Arc Welding*.
130. *JIS Z 3118 Japanese Ondustrial Standard Method for measurement of amount of hydrogen evolved from steel welds*. 2007.
131. Termsuksawad, P., Niyomsoan, S., Goldfarb, R.B., Kaydanov, V.I., Olson, D.L., Mishra, B., and Gavra, Z., *Measurement of hydrogen in alloys by magnetic and electronic techniques.* Journal of Alloys and Compounds, 2004. **373**(1-2): p. 86-95.

132. Sastri, V.S. and McDonnell, D.B., *Analysis of surface hydrogen in high-strength steels.* Canadian Metallurgical Quarterly, 1995. **34**(1): p. 37-41.
133. *Methods for the Analysis of Iron and Steel: As/Nzs 1050.1:1996: Sampling Iron and Steel for Chemical Analysis*. 1996, Sydney: Standards Australia.
134. Banerjee, K. and Chatterjee, U.K., *Hydrogen permeation and hydrogen content under cathodic charging in HSLA 80 and HSLA 100 steels.* Scripta Materialia, 2001. **44**(2): p. 213-216.
135. *ASTM, F1113-87, Standard Test Method for Electrochemical Measurement of Diffusible Hydrogen in Steels (Barnacle Electrode), 1999.*
136. Mao, S.X. and Li, M., *Mechanics and thermodynamics on the stress and hydrogen interaction in crack tip stress corrosion: experiment and theory.* Journal of the Mechanics and Physics of Solids, 1998. **46**(6): p. 1125-1137.
137. *ASTM E399-90, "Standard Test Method for Plane-Strain Fracture Toughness of Metallic Materials", Annual Book of ASTM Standards 3.01, American Society for Testing and Materials, West Conshohocken, PA (1997).*
138. Jung, P., Hishinuma, A., Lucas, G.E., and Ullmaier, H., *Recommendation of miniaturized techniques for mechanical testing of fusion materials in an intense neutron source.* Journal of Nuclear Materials, 1996. **232**(2-3): p. 186-205.
139. *ASTM E813-89: Standard Method for J_{IC}, A Measure of Fracture Toughness*. 1989.
140. Amouzouvi, K. and Bassim, M., *Determination of fracture toughness from stretch zone width measurement in predeformed AISI type 4340 steel.* Materials Science and Engineering, 1982. **55**(2): p. 257-262.
141. Rice, J.R., *A Path Independent Integral and the Approximate Analysis of Strain Concentration by Notches and Cracks.* Journal of Applied Mechanics, 1968. **35**: p. 379-386.
142. Hutchinson, J.W., *Fundamentals of the Phenomenological Theory of Nonlinear Fracture Mechanics.* Journal of Applied Mechanics, 1983. **50**(4b): p. 1042-1051.
143. Chaouadil, R., *An energy-based crack extension formulation for crack resistance characterization of ductile materials.* ASTM Journal of Testing and Evaluation, 2004. **32**(6): p. 469-475.
144. Lucas, G.E., *Review of small specimen test techniques for irradiation testing.* Metallurgical Transactions A, 1990. **21(A)**(5): p. 1105-1119.
145. Mao, X., Shoji, T., and Takahashi, H., *Development of a Miniaturized Specimen Technique for Fracture Toughness JIC Measurement.* Journal of Testing and Evaluation, 1988(16(2)): p. 229-241.
146. Odette, G.R., He, M., Gragg, D., Klingensmith, D., and Lucas, G.E., *Some recent innovations in small specimen testing.* Journal of Nuclear Materials, 2002. **307–311, Part 2**(0): p. 1643-1648.
147. Wakai, E., Ohtsuka, H., Matsukawa, S., Furuya, K., Tanigawa, H., Oka, K., Ohnuki, S., Yamamoto, T., Takada, F., and Jitsukawa, S., *Mechanical properties of small size specimens of F82H steel.* Fusion engineering and design, 2006. **81**(8): p. 1077-1084.
148. *ASTM E 1820-99, Standard test method for measurement of fracture toughness. American Society for Testing and Materials,Philadelphia, 1999*.
149. Hancock, J.W., Reuter, W., and Parks, D.M., *Constraint and toughness parameterized by T.* ASTM special technical publication, 1993. **1171**: p. 21-21.

150. Decamp, K., Bauvineau, L., Besson, J., and Pineau, A., *Size and geometry effects on ductile rupture of notched bars in a C-Mn steel: experiments and modelling.* International journal of fracture, 1997. **88**(1): p. 1-18.
151. Haynes, M. and Gangloff, R., *High resolution R-curve characterization of the fracture toughness of thin sheet aluminum alloys.* Journal of testing and evaluation, 1997. **25**(1): p. 82-98.
152. Henry, B., Luxmoore, A., and Sumpter, J., *Elastic-plastic fracture mechanics assessment of low constraint aluminium test specimens.* International journal of fracture, 1996. **81**(3): p. 217-234.
153. Klemm, W., Memhard, D., and Schmitt, W., *Experimental and numerical investigation of surface cracks in plates and pipes.* Fracture Mechanics Verification by Large-Scale Testing, 1991: p. 139-150.
154. Kordisch, H., Sommer, E., and Schmitt, W., *The influence of triaxiality on stable crack growth.* Nuclear engineering and design, 1989. **112**: p. 27-35.
155. Elliot, C., Emark, M., and Lucas, G., *Development of disk compact tension specimens and test techniques for HFIR irradiation.* Journal of Nuclear Materials, 1991. **179**(Part A): p. 434-437.
156. Alexander, D.J., *Fracture toughness measurements with subsize Disk Compact specimens.* ASTM special technical publication, 1993. **1204**: p. 130-130.
157. Yoon, K.K., Gross, L.B., Wade, C.S., and VanDerSluys, W.A., *Evaluation of disk-shaped compact specimen for determining JR curves.* ASTM special technical publication, 1995. **1256**: p. 272-283.
158. Marschall, C.W., Papaspyropoulos, V., and Landow, M.P., *Evaluation of attempts to predict large-crack-growth JR curves from small specimen tests.* Nonlinear Fracture Mechanics, 1989. **2**: p. 123-143.
159. Eisele, U., Roos, E., Seidenfuss, M., and Silcher, H., *Determination of J-integral-based crack resistance curves and initiation values for the assessment of cracked large-scale specimens.* ASTM special technical publication, 1992. **1131**: p. 37-37.
160. Roos, E., Eisele, U., and Silcher, H., *Effect of stress state on the ductile fracture behavior of large-scale specimens.* ASTM Secial publication, ASTM, Phladelphia, PA(USA), 1993, 1993(1171): p. 41-63.
161. Joyce, J.A. and Link, R.E., *Effects of constraint on upper shelf fracture toughness.* ASTM special technical publication, 1995. **1256**: p. 142-177.
162. Joyce, J.A. and Link, R.E., *Application of two parameter elastic-plastic fracture mechanics to analysis of structures.* Engineering Fracture Mechanics, 1997. **57**(4): p. 431-446.
163. Faleskog, J., *Effects of local constraint along three-dimensional crack fronts—a numerical and experimental investigation.* Journal of the Mechanics and Physics of Solids, 1995. **43**(3): p. 447-493.
164. Kikuchi, M., *Study of the effect of the crack length on the J_{IC} value.* Nuclear engineering and design, 1997. **174**(1): p. 41-49.
165. Shan, G.X., Kolednik, O., and Fischer, F.D., *A numerical study on the crack growth behavior of a low and a high strength steel.* International journal of fracture, 1996. **78**(3): p. 335-346.

166. Xia, L., Shih, C.F., and Hutchinson, J.W., *A computational approach to ductile crack growth under large scale yielding conditions.* Journal of the Mechanics and Physics of Solids, 1995. **43**(3): p. 389-413.
167. Yan, C. and Mai, Y.W., *Effect of constraint on ductile crack growth and ductile-brittle fracture transition of a carbon steel.* International journal of pressure vessels and piping, 1997. **73**(3): p. 167-173.
168. Cialone, H., Scott, P., Holbrook, J., Sieradzki, K., and Bandyopadhyay, N., *Hydrogen effects on conventional pipeline steels*, in *Proc. 5th World Hydrogen Energy Conf.* 1984: Toronto, Canada. p. 15-20.
169. Gutierrez-Solana, F. and Elices, M., *High-pressure hydrogen behavior of a pipeline steel.* Current Solutions to Hydrogen Problems in Steels, 1982: p. 181-185.
170. Hoover, W., Robinson, S., Stoltz, R., and Spingarn, J., *Hydrogen compatibility of structural materials for energy storage and transmission.* NASA STI/Recon Technical Report N, 1981. **81**: p. 29598.
171. Kussmaul, K., Deimel, P., Fischer, H., and Sattler, E., *Fracture mechanical behaviour of the steel 15 MnNi 6 3 in argon and in high pressure hydrogen gas with admixtures of oxygen.* International journal of hydrogen energy, 1998. **23**(7): p. 577-582.
172. Kussmaul, K., Deimel, P., and Sattler, E., *Tensile Properties of the Steel X 70 TM in High Pressure Hydrogen Gas with Admixtures of Oxygen at Different Strain Rates.* Advances in Hydrogen Energy, 1994. **10**: p. 285-285.
173. Nelson, H.G., *Hydrogen-induced slow crack growth of a plain carbon pipeline steel under conditions of cyclic loading.* Effect of hydrogen on behavior of materials, 1976: p. 602-611.
174. Fukuyama, S. and Yokogawa, K., *Prevention of Hydrogen Environmental Assisted Crack Growth of 2. 25 Cr--1 Mo Steel by Gaseous Inhibitors.* Pressure Vessel Technology., 1992. **2**: p. 914-923.
175. Nguyen-Duy, P. and Bayard, S., *Fracture toughness of 4130 quenched and tempered steel.* Journal of Engineering Materials and Technology(Transactions of the ASME), 1981. **103**(1): p. 55-61.
176. Hayes, D. and Turner, C., *An application of finite element techniques to post-yield analysis of proposed standard three-point bend fracture test pieces.* International journal of fracture, 1974. **10**(1): p. 17-32.
177. Tarpani, J.R., Bose, W.W., and Spinelli, D., *Backscattered electron microscopy technique enhancing stretch zone width imaging for initiation fracture toughness measurements.* Materials Characterization, 2003. **51**(2–3): p. 159-170.
178. Olden, V., Alvaro, A., and Akselsen, O.M., *Hydrogen diffusion and hydrogen influenced critical stress intensity in an API X70 pipeline steel welded joint – Experiments and FE simulations.* International Journal of Hydrogen Energy, 2012. **37**(15): p. 11474-11486.
179. ISO, I., *12135 Metallic materials–Unified method of test for the determination of quasistatic fracture toughness.* International Organization for Standardization, Geneva, 2007.
180. Tang, Z. and Stumpf, W., *The effect of microstructure and processing variables on the yield to ultimate tensile strength ratio in a Nb–Ti and a Nb–Ti–Mo line pipe steel.* Materials Science and Engineering: A, 2008. **490**(1–2): p. 391-402.

181. Liessem, A., Knauf, G., and Zimmermann, S. *Strain Based Design—What the Contribution of a Pipe Manufacturer Can Be*. in *Proceedings of the 17th International Offshore and Polar Engineering Conference (ISOPE), Lisbon, Portugal*. 2007.
182. Mohr, W., *Strain-Based Design for Materials with HAZ Softening*, in *2006 International Pipeline Conference*. 2006, American Society of Mechanical Engineers. p. 529-536.
183. Hollomon, J.H., Trans. Amer. Inst. Min. Met. Eng. Iron Steel Div., 1945. **162**: p. 268.
184. Ludwik, P., *Elements of the technological mechanics*. 1909: Springer.
185. Swift, H.W., *Plastic instability under plane stress.* Journal of the Mechanics and Physics of Solids, 1952. **1**(1): p. 1-18.
186. Hockett, J. and Sherby, O., *Large strain deformation of polycrystalline metals at low homologous temperatures.* Journal of the Mechanics and Physics of Solids, 1975. **23**(2): p. 87-98.
187. Voce, E., *The relationship between stress and strain for homogeneous deformation.* J Inst Met, 1948. **74**: p. 537-562.
188. Ghosh, A., *Tensile instability and necking in materials with strain hardening and strain-rate hardening.* Acta metallurgica, 1977. **25**(12): p. 1413-1424.
189. Jaoul, B., *Study and application to metal plasticity.* J. Mech. Phys. Solid., 1957. **5**: p. 95-114.
190. Monteiro, S.N. and Reed-Hill, R.E., *On the double-n behavior of iron.* Metallurgical Transactions, 1971. **2**(10): p. 2947-2948.
191. Jha, B.K., Avtar, R., Dwivedi, V.S., and Ramaswamy, V., *Applicability of modified Crussard-Jaoul analysis on the deformation behaviour of dual-phase steels.* Journal of Materials Science Letters, 1987. **6**(8): p. 891-893.
192. Samuel, F.H., *Tensile stress-strain analysis of dual-phase structures in an Mn-Cr-Si steel.* Materials Science and Engineering, 1987. **92**(0): p. L1-L4.
193. Ramos, L., Matlock, D.K., and Krauss, G., *On the deformation behavior of dual-phase steels.* Metallurgical Transactions A, 1979. **10**(2): p. 259-261.
194. Jiang, Z., Lian, J., and Guan, Z., *Effects of microstructural variables on the deformation behaviour of dual-phase steel.* Materials Science and Engineering: A, 1995. **190**(1): p. 55-64.
195. Nes, E., *Modelling of work hardening and stress saturation in FCC metals.* Progress in Materials Science, 1997. **41**(3): p. 129-193.
196. Nes, E. and Marthinsen, K., *Modeling the evolution in microstructure and properties during plastic deformation of f.c.c.-metals and alloys – an approach towards a unified model.* Materials Science and Engineering: A, 2002. **322**(1–2): p. 176-193.
197. Zehetbauer, M., *Cold work hardening in stages IV and V of FCC metals—II. Model fits and physical results.* Acta metallurgica et materialia, 1993. **41**(2): p. 589-599.
198. Kocks, U.F. and Mecking, H., *Physics and phenomenology of strain hardening: the FCC case.* Progress in Materials Science, 2003. **48**(3): p. 171-273.
199. Tomita, Y., *Effect of morphology of second-phase martensite on tensile properties of Fe-0.1C dual phase steels.* Journal of Materials Science, 1990. **25**(12): p. 5179-5184.

200. Afrin, N., Chen, D.L., Cao, X., and Jahazi, M., *Strain hardening behavior of a friction stir welded magnesium alloy.* Scripta Materialia, 2007. **57**(11): p. 1004-1007.
201. Christopher, J., Choudhary, B.K., Isaac Samuel, E., Srinivasan, V.S., and Mathew, M.D., *Tensile flow and work hardening behaviour of 9Cr–1Mo ferritic steel in the frame work of Voce relationship.* Materials Science and Engineering: A, 2011. **528**(21): p. 6589-6595.
202. Lian, J., Jiang, Z., and Liu, J., *Theoretical model for the tensile work hardening behaviour of dual-phase steel.* Materials Science and Engineering: A, 1991. **147**(1): p. 55-65.
203. Farabi, N., Chen, D.L., and Zhou, Y., *Tensile Properties and Work Hardening Behavior of Laser-Welded Dual-Phase Steel Joints.* Journal of Materials Engineering and Performance, 2012. **21**(2): p. 222-230.
204. Umemoto, M., Tsuchiya, K., Liu, Z.G., and Sugimoto, S., *Tensile stress-strain analysis of single-structure steels.* Metallurgical and Materials Transactions A, 2000. **31**(7): p. 1785-1794.
205. Byun, T. and Kim, I., *Tensile properties and inhomogeneous deformation of ferrite-martensite dual-phase steels.* Journal of Materials Science, 1993. **28**(11): p. 2923-2932.
206. Bag, A., Ray, K.K., and Dwarakadasa, E.S., *Influence of martensite content and morphology on tensile and impact properties of high-martensite dual-phase steels.* Metallurgical and Materials Transactions A, 1999. **30**(5): p. 1193-1202.
207. Paruz, H. and Edmonds, D.V., *The strain hardening behaviour of dual-phase steel.* Materials Science and Engineering: A, 1989. **117**(0): p. 67-74.
208. Kessler, L. and Gerlach, J., *The impact of materials testing strategies on the determination and calibration of different FEM material models*, in *IDDRG*. 2006: Porto Portugal p. 113-120.
209. Bergström, Y., *A dislocation model for the stress-strain behaviour of polycrystalline α-Fe with special emphasis on the variation of the densities of mobile and immobile dislocations.* Materials Science and Engineering, 1970. **5**(4): p. 193-200.
210. Van Liempt, P., *Workhardening and substructural geometry of metals.* Journal of materials processing technology, 1994. **45**(1): p. 459-464.
211. Totten, G.E., Xie, L., and Funatani, K., *Modeling and simulation for material selection and mechanical design*. Vol. 166. 2003: CRC.
212. Tome, C., Canova, G.R., Kocks, U.F., Christodoulou, N., and Jonas, J.J., *The relation between macroscopic and microscopic strain hardening in FCC polycrystals.* Acta metallurgica, 1984. **32**(10): p. 1637-1653.
213. Nolan, D., Sustarsic, B., Bruce, W., and Grace, P., *Small-scale fracture testing of heat-affected zones of in-service welds of pipeline steels.* Australasian Welding Journal, 2007. **52**(3): p. 41-48.
214. *ASTM E112-10: Standard Test Methods for Determining Average Grain Size* 2010.
215. Grong, O., *Metallurgical Modelling of Welding*, ed. H.K.D.H. Bahadeshia. 1994: The Institute of Materials London.

216. Williams, R.S. and Homerberg, V.O., *Principles of metallography* Metallurgy and metallurgical engineering series. 1948, New York. 319.
217. *ASTM E562-11 Standard Test Method for Determining Volume Fraction by Systematic Manual Point Count.*
218. ; Available from: http://www.eltragmbh.com/onh2000/information.shtml.
219. Al Shahrani, A., Schambron, T., Dehghan-Manshadi, A., Williams, J.G., and Pereloma, E.V., *Effects of Processing Parameters on Microstructure Development in X70 Pipeline Steel.* Materials Science Forum, 2010. **654**: p. 298-301.
220. Schambron, T., Phillips, A.W., O'Brien, D.M., Burg, J., Pereloma, E.V., Killmore, C.C., and Williams, J.A., *Thermomechanical Processing of Pipeline Steels with a Reduced Mn Content.* ISIJ International, 2009. **49**(2): p. 284-292.
221. Dehghan-Manshadi, A. and Dippenaar, R., *The Behavior of Precipitates during Hot-Deformation of Low-Manganese, Titanium-Added Pipeline Steels.* Metallurgical and Materials Transactions A, 2010. **41**(13): p. 3291-3296.
222. Lee, S.M. and Lee, J.Y., *The effect of the interface character of tic particles on hydrogen trapping in steel.* Acta metall, 1987. **35**(11): p. 2695-2700.
223. Escobar, D.P., Duprez, L., Verbeken, K., and Verhaege, M., *Identification of the hydrogen trap sites in a high strength TRIP steel by means of Thermal Desorption Spectroscopy.* Effects of Hydrogen on Materials, ASM International, Ohio, USA, 2009: p. 485-492.
224. Farrell, K., *Cathodic hydrogen absorption and severe embrittlement in a high strength steel.* Corrosion, 1970. **26**(3): p. 105-110.
225. Qi, Y., Luo, H., Zheng, S., Chen, C., and Wang, D., *Effect of immersion time on the hydrogen content and tensile properties of A350LF2 steel exposed to hydrogen sulphide environments.* Corrosion Science, 2013. **69**(0): p. 164-174.
226. Kim, S.J., Jung, H.G., and Kim, K.Y., *Effect of tensile stress in elastic and plastic range on hydrogen permeation of high-strength steel in sour environment.* Electrochimica Acta, 2012. **78**(0): p. 139-146.
227. Escobar, D.P., Depover, T., Wallaert, E., Duprez, L., Verhaege, M., and Verbeken, K., *Thermal desorption spectroscopy study of the interaction between hydrogen and different microstructural constituents in lab cast Fe–C alloys.* Corrosion Science, 2012. **65**(0): p. 199-208.
228. Escobar, D.P., Verbeken, K., Duprez, L., and Verhaege, M., *Experimental evaluation of the hydrogen distribution in steel by thermal desorption spectroscopy*, in *Proceedings International Conference on Effects of Hydrogen on Materials, ASM international*. 2009. p. 477-484.
229. Stroe, M.E., *Hydrogen embrittlement of ferrous materials*. 2006, Université Libre de Bruxelles: Belgium.
230. Hardie, D., Charles, E.A., and Lopez, A.H., *Hydrogen embrittlement of high strength pipeline steels.* Corrosion Science, 2006. **48**(12): p. 4378-4385.
231. Escobar, D.P., Miñambres, C., Duprez, L., Verbeken, K., and Verhaege, M., *Hydrogen damage in multiphase steels after electrochemical charging*, in *Hydrogen-materials, stress corrosion, corrosion fatigue*. 2010, Mines Paris Tech. p. 133-138

232. Oriani, R., *Hydrogen degradation of ferrous alloys.* Noyes Publications, Mill Rd. at Grand Ave, Park Ridge, New Jersey 7656, USA, 1985. 886, 1985: p. 561-578.
233. International, N., *Standard Test Method: Evaluation of Pipeline and Pressure Vessel Steels for Resistance to Hydrogen-induced Cracking*. 2003: Nace International.
234. Kushida, T., Okaguchi, S., Hamada, M., Yamamoto, A., and Ohnishi, K., *Study of X80 grade high strength line pipe for sour service.* Sumitomo Metal Industries, Ltd., Japan, 1997(24).
235. Van der Burg, M.W.D., van der Giessen, E., and Brouwer, R.C., *Investigation of hydrogen attack in 2.25Cr-1Mo steels with a high-triaxiality void growth model.* Acta Materialia, 1996. **44**(2): p. 505-518.
236. Krom, A.H.M., Bakker, A., and Koers, R.W.J., *Modelling hydrogen-induced cracking in steel using a coupled diffusion stress finite element analysis.* International Journal of Pressure Vessels and Piping, 1997. **72**(2): p. 139-147.
237. Griesche, A., Dabah, E., Kannengiesser, T., Kardjilov, N., Hilger, A., and Manke, I., *Three-dimensional imaging of hydrogen blister in iron with neutron tomography.* Acta Materialia, 2014. **78**(0): p. 14-22.
238. Albarran, J.L., Martinez, L., and López, H.F., *The Sour Gas Susceptibility of an X-80 Steel for Oil and Gas Transport.* Scripta Materialia, 1998. **38**(5): p. 749-755.
239. Hejazi, D., Saleh, A.A., Haq, A.J., Dunne, D.P., Calka, A., Gazder, A.A., and Pereloma, E.V., *Role of Microstructure in Susceptibility to Hydrogen Embrittlement of X70 Microalloyed Steel.* Materials Science Forum, 2014. **783**: p. 961-966.
240. Liang, P., Li, X., Du, C., and Chen, X., *Stress corrosion cracking of X80 pipeline steel in simulated alkaline soil solution.* Materials & Design, 2009. **30**(5): p. 1712-1717.
241. Rivalin, F., Pineau, A., Di Fant, M., and Besson, J., *Ductile tearing of pipeline-steel wide plates: I. Dynamic and quasi-static experiments.* Engineering Fracture Mechanics, 2000. **68**(3): p. 329-345.
242. Rosenfield, A.R. and Majumdar, B.S., Nuclear Engineering and Design, 1987. **105**: p. 51-57.
243. Rosenfield, A.R. and Majumdar, B.S., *Micromechanisms and toughness for cleavage fracture of steel.* Nuclear Engineering and Design, 1987. **105**(1): p. 51-57.
244. Bernstein, I.M. and Thompson, A.W., *Effect of metallurgical variables on environmental fracture in steels.* Int. Metals Reviews, 1976. **21**: p. 269-287.
245. Cain, W.M. and Troiano, A.R., *Steel Structure and Hydrogen Embrittlement.* Petrol eng, 1965. **37**: p. 78.
246. Gerberich, W.W., Stauffer, D.D., and Sofronis, P., *A coexistent view of hydrogen effects on mechanical behavior of crystals: ductile or brittle*, in *Inter. Hydrogen Conference*. 2008. p. 38-45.
247. Arafin, M.A. and Szpunar, J.A., *A new understanding of intergranular stress corrosion cracking resistance of pipeline steel through grain boundary character and crystallographic texture studies.* Corrosion Science, 2009. **51**(1): p. 119-128.
248. Kim, Y.H. and Morris, J.W., *The Nature of Quasicleavage Fracture in Tempered 5.5Ni Steel after Hydrogen Charging.* Metallurgical and Materials Transactions A, 1983. **14**(9): p. 1883-1888.

249. Lee, S., Kim, B.C., and Lee, D.Y., *Fracture mechanism in coarse grained HAZ of HSLA steel welds.* Scripta Metallurgica, 1989. **23**(6): p. 995-1000.
250. Zhao, M.C., Liu, M., Atrens, A., Shan, Y.Y., and Yang, K., *Effect of applied stress and microstructure on sulfide stress cracking resistance of pipeline steels subject to hydrogen sulfide.* Materials Science and Engineering: A, 2008. **478**(1-2): p. 43-47.
251. Ramírez, E., González-Rodriguez, J.G., Torres-Islas, A., Serna, S., Campillo, B., Dominguez-Patiño, G., and Juárez-Islas, J.A., *Effect of microstructure on the sulphide stress cracking susceptibility of a high strength pipeline steel.* Corrosion Science, 2008. **50**(12): p. 3534-3541.
252. Hurtado Noreña, C. and Bruzzoni, P., *Effect of microstructure on hydrogen diffusion and trapping in a modified 9%Cr–1%Mo steel.* Materials Science and Engineering: A, 2010. **527**(3): p. 410-416.
253. Dieter, G.E. and Bacon, D., *Mechanical metallurgy*. Vol. 3. 1986: McGraw-Hill New York.
254. Chang, T.L., Tsay, L.W., and Chen, C., *Influence of gaseous hydrogen on the notched tensile strength of D6ac steel.* Materials Science and Engineering A, 2001. **316**(1-2): p. 153-160.
255. Michler, T. and Naumann, J., *Hydrogen embrittlement of Cr-Mn-N-austenitic stainless steels.* International Journal of Hydrogen Energy, 2010. **35**(3): p. 1485-1492.
256. Luo, J., Mei, Z., Tian, W., and Wang, Z., *Diminishing of work hardening in electroformed polycrystalline copper with nano-sized and uf-sized twins.* Materials Science and Engineering: A, 2006. **441**(1–2): p. 282-290.
257. Hofmann, W. and Rauls, W., *Ductility of steel under the influence of external high pressure hydrogen(Hydrogen embrittlement of plain steel and Armco iron).* Welding journal, research supplement, 1965. **44**.
258. Wu, X., Katada, Y., Kim, I.S., and Lee, S.G., *Hydrogen-involved tensile and cyclic deformation behavior of low-alloy pressure vessel steel.* Metallurgical and Materials Transactions A, 2004. **35**(5): p. 1477-1486.
259. Michler, T., Yukhimchuk, A.A., and Naumann, J., *Hydrogen environment embrittlement testing at low temperatures and high pressures.* Corrosion Science, 2008. **50**(12): p. 3519-3526.
260. Senkov, O.N. and Jonas, J.J., *Dynamic strain aging and hydrogen-induced softening in alpha titanium.* Metallurgical and Materials Transactions A, 1996. **27**(7): p. 1877-1887.
261. Jang, J.-i., Choi, Y., Lee, Y.-H., and Kwon, D., *Instrumented microindentation studies on long-term aged materials: work-hardening exponent and yield ratio as new degradation indicators.* Materials Science and Engineering: A, 2005. **395**(1–2): p. 295-300.
262. Huh, H., Kim, S.-B., Song, J.-H., and Lim, J.-H., *Dynamic tensile characteristics of TRIP-type and DP-type steel sheets for an auto-body.* International Journal of Mechanical Sciences, 2008. **50**(5): p. 918-931.
263. Akbarpour, M.R. and Ekrami, A., *Effect of temperature on flow and work hardening behavior of high bainite dual phase (HBDP) steels.* Materials Science and Engineering: A, 2008. **475**(1–2): p. 293-298.

264. Hashemi, S.H. and Jalali, M.R., *Experimental study of Charpy impact characteristics of high-strength spiral welded gas pipeline*, in *2006 International Pipeline Conference*. 2006, American Society of Mechanical Engineers. p. 57-63.
265. Zimmermann, S., Brauer, H., and Löbbe, H. *Assessment of work hardening behavior of HFI-welded pipes for strain based design approaches*. in *17th Joint Technical Meeting on Pipeline Research*. 2009. Milan, Italy.
266. Reed-Hill, R.E., Cribb, W.R., and Monteiro, S.N., *Concerning the analysis of tensile stress-strain data using log dσ/dεp versus log σ diagrams.* Metallurgical Transactions, 1973. **4**(11): p. 2665-2667.
267. Tomita, Y. and Okabayashi, K., *Tensile stress-strain analysis of cold worked metals and steels and dual-phase steels.* Metallurgical Transactions A, 1985. **16**(5): p. 865-872.
268. Ludwigson, D.C., *Modified stress-strain relation for FCC metals and alloys.* Metallurgical Transactions, 1971. **2**(10): p. 2825-2828.
269. Embury, J. and Fisher, R., *The structure and properties of drawn pearlite.* Acta Metallurgica, 1966. **14**(2): p. 147-159.
270. Dollar, M., Bernstein, I., and Thompson, A., *Influence of deformation substructure on flow and fracture of fully pearlitic steel.* Acta Metallurgica, 1988. **36**(2): p. 311-320.
271. Tomota, Y., Suzuki, T., Kanie, A., Shiota, Y., Uno, M., Moriai, A., Minakawa, N., and Morii, Y., *In situ neutron diffraction of heavily drawn steel wires with ultra-high strength under tensile loading.* Acta materialia, 2005. **53**(2): p. 463-467.
272. Tomota, Y., Lukaa, P., Neov, D., Harjo, S., and Abe, Y.R., *In situ neutron diffraction during tensile deformation of a ferrite-cementite steel.* Acta materialia, 2003. **51**(3): p. 805-817.
273. Deimel, P. and Sattler, E., *Austenitic steels of different composition in liquid and gaseous hydrogen.* Corrosion Science, 2008. **50**(6): p. 1598-1607.
274. Fricke, E., Stüwe, H., and Vibrans, G., *Dissolution of hydrogen from the gas in steel at room temperature.* Metallurgical Transactions, 1971. **2**(9): p. 2697-2700.
275. Moro, I., Briottet, L., Lemoine, P., Andrieu, E., Blanc, C., and Odemer, G., *Hydrogen embrittlement susceptibility of a high strength steel X80.* Materials Science and Engineering: A, 2010. **527**(27–28): p. 7252-7260.
276. Wallaert, E., Depover, T., Arafin, M., and Verbeken, K., *Thermal Desorption Spectroscopy Evaluation of the Hydrogen-Trapping Capacity of NbC and NbN Precipitates.* Metallurgical and Materials Transactions A, 2014. **45**(5): p. 2412-2420.

List of Publications

- Hejazi, D., Haq, A. J., Yazdipour, N., Dunne, D. P., Barbaro, F. and Pereloma, E. V. (2010). Role of microstructure in susceptibility of X70 pipeline steel to hydrogen embrittlement. A. Morton and J. Nie (Eds.) in Pacific Rim International Conference on Advanced Materials and Processing, 2-6 August 2010, Cairns, Australia. Materials Science Forum.
- Hejazi, D., Haq, A.J., Yazdipour, N., Dunne, D.P., Calka, A., Barbaro, F., and Pereloma, E.V., Effect of manganese content and microstructure on the susceptibility of X70 pipeline steel to hydrogen cracking. Materials Science and Engineering: A, 2012. 551(0): p. 40-49.
- Hejazi, D., Saleh, A.A., Haq, A.J., Dunne, D., Calka, A., Gazder, A.A., and Pereloma, E.V., Role of Microstructure in Susceptibility to Hydrogen Embrittlement of X70 Microalloyed Steel. Materials Science Forum, 2014. 783: p. 961-966